GEOLOGICA ULTRAIECTINA

Mededelingen van de
Faculteit Aardwetenschappen
Universiteit Utrecht

No. 166

Temporal constraints on the kinematics of the destabilization of an orogen;

syn- to post-orogenic extensional collapse of the Northern Aegean region

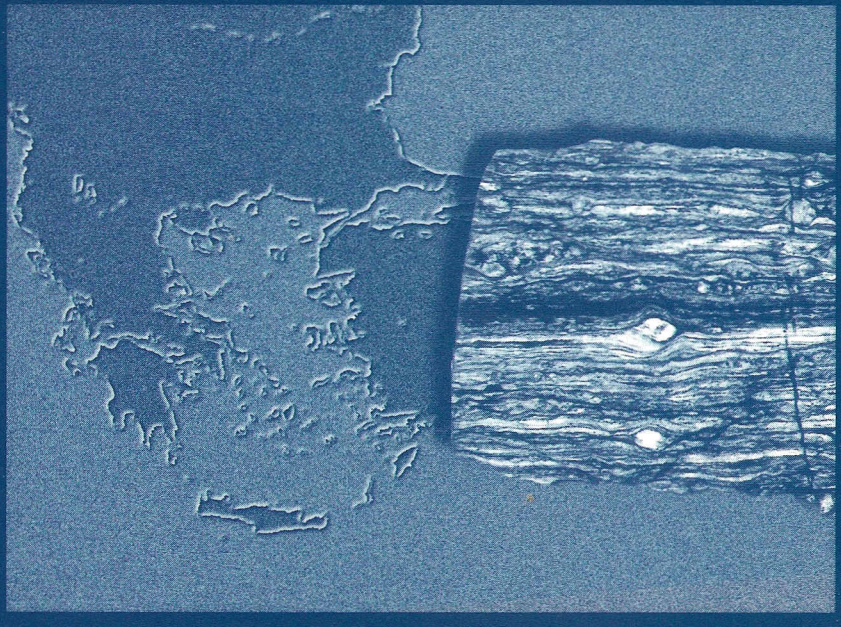

Andor L.W. Lips

GEOLOGICA ULTRAIECTINA

Mededelingen van de
Faculteit Aardwetenschappen
Universiteit Utrecht

No. 166

Temporal constraints on the kinematics of the destabilization of an orogen;

syn- to post-orogenic extensional collapse of the Northern Aegean region

Andor L.W. Lips

Temporal constraints on the kinematics of the destabilization of an orogen;

syn- to post-orogenic extensional collapse of the Northern Aegean region

Tijdscontrole op de kinematiek van de destabilisering van een orogeen;

syn- en post-orogene, extensie gedomineerde, instorting van het noordelijk Egeïsch gebied

(met een samenvatting in het Nederlands)

PROEFSCHRIFT

ter verkrijging van de graad van Doctor aan de Universiteit Utrecht

op gezag van de Rector Magnificus Prof. Dr. H.O. Voorma

ingevolge het besluit van het College voor Promoties in het openbaar te verdedigen op

woensdag 11 november 1998, des namiddags te 12.45 uur

door

Adrianus Leonardus Wilhelmus Lips

Geboren op 5 maart 1971 te Breda

Promotor:

Prof. Dr. S.H. White
Projectgroep Structurele Geologie & Tektoniek,
Vening Meinesz Onderzoeksschool voor Geodynamica,
Faculteit Aardwetenschappen, Universiteit Utrecht

Co-promotor:

Dr. J.R. Wijbrans
Vakgroep Petrologie & Isotopen Geologie
Nederlandse Onderzoeksschool voor Sedimentaire Geologie,
Vrije Universiteit Amsterdam

Leden van de beoordelingscommissie:

Prof. J-P. Brun
Géosciences Rennes, Université de Rennes, France
Prof. K.V. Hodges
Department of Earth, Atmospheric, and Planetary Sciences,
Massachusetts Institute of Technology, Cambridge, MA, USA
Prof. G.S. Lister
Australian Crustal Research Centre, Department of Earth Sciences,
Monash University, Melbourne, Australia
Prof. J.E. Meulenkamp
Nederlandse Onderzoeksschool voor Sedimentaire Geologie,
Faculteit Aardwetenschappen, Universteit Utrecht
Prof. M.J.R. Wortel
Vening Meinesz Onderzoeksschool voor Geodynamica,
Faculteit Aardwetenschappen, Universiteit Utrecht

Het onderzoek beschreven in dit proefschrift werd uitgevoerd aan de faculteiten Aardwetenschappen van de Universiteit Utrecht en de Vrije Universiteit Amsterdam en gesubsidieerd door de Nederlandse Organisatie voor Wetenschappelijk Onderzoek (NWO), en de, voormalig, Stichting Geologisch Oceanografisch en Atmosferisch Onderzoek (GOA), projectnummer 750.194.11

ISBN 90-5744-024-5

CONTENTS

SAMENVATTING

Op het contactvlak van de Afrikaanse en Euraziatische continentale platen ligt de Middellandse Zee. Het gebied in en rond de Middelandse Zee dankt zijn huidige vorm aan de interactie van beide platen. Deze zijn sinds de laatste circa honderd miljoen jaar, tijdens de Alpiene gebergtevorming, naar elkaar toe geschoven en tegen elkaar gebotst. In het algemeen wordt de Alpiene ontwikkeling van de regio door de tijd gescheiden in twee fasen. Tijdens een fase van Alpiene compressietektoniek (de "Alpiene Orogenese") vormden de gebergten welke aaneengeschakeld te vinden zijn van de Pyreneeen in het westen, via de Alpen, de Helleniden (Griekenland), tot Turkije in het oosten van de Middellandse Zee en verder via de Kaukasus tot in de Himalaya. Een fase van laat Alpiene extensietektoniek volgde na de gebergtevorming en resulteerde in de ontwikkeling van gebieden waarvan de lithosfeer (welke de aardkorst en het bovenste deel van de aardmantel beslaat) sterk verdund werd. In en rond de Middellandse Zee zijn deze gebieden te vinden in het uiterst westelijke deel van de Middellandse Zee (de Alboran), in de Tyrrheense Zee, in het Pannoonse bekken (in de Karpaten gebergtegordel) en in de Egeïsche Zee in het oostelijk deel van de Middellandse Zee.
In de huidige studie is het gebied rond de Egeïsche Zee geselecteerd om de geodynamische processen te bestuderen, die een rol speelden tijdens de interactie van de Afrikaanse en Euraziatische platen. Het gebied in en rond de Egeïsche Zee beslaat het huidige Griekenland en west-Turkije en wordt begrensd in het zuiden (ten zuiden van Kreta) en westen (in de Ionische Zee) door een subductiezone, de Helleense boog, waar de Afrikaanse plaat onder de Europese plaat schuift. De nadruk van deze studie ligt op de karakterisering van de geodynamische processen die een rol speelden tijdens de overgang van de twee traditionele tektonische fasen; de, compressieve, Alpiene gebergtevorming en de laat-Alpiene extensietektoniek. De karakterisering gebeurt door te onderzoeken wanneer en op welke manier gesteenten, welke afkomstig zijn van verschillende delen van de diepere delen van de aardkorst (meer dan circa 20-30 km diep), uiteindelijk aan de oppervlakte zijn gekomen (exhumatie) en nu in verschillende delen van Griekenland en Turkije terug te vinden zijn. Het doel van dit onderzoek is om het inzicht te verbeteren in de geodynamische processen die gerelateerd kunnen worden aan de vorming (de metamorfose) van deze gesteenten ten gevolge van de heersende druk en temperatuur in de middenkorst tijdens de Alpiene gebergtevorming, alsmede in de processen die een rol speelden bij de exhumatie van deze gesteenten.
Het onderzoek heeft zich voornamelijk gericht op de Pelagonische Zone op het vasteland van Griekenland ten noordwesten van de Egeïsche Zee. Aanvullende veldonderzoeken zijn uitgevoerd in de Rhodope Zone (noord-Griekenland; ten noorden van de Egeïsche Zee) en de Kazdag en Menderes massieven (west-Turkije; ten oosten van de Egeïsche Zee). Al de hier boven genoemde gebieden worden gekenmerkt door het voorkomen van metamorfe gesteenten, welke na hun metamorfose in de diepere delen van de aardkorst stapsgewijs op geringere diepte in de korst werden gepositioneerd en

uiteindelijk aan de oppervlakte kwamen te liggen. De integratie van veldwerk met microstructureel en metamorf petrologisch onderzoek en de $^{40}Ar/^{39}Ar$ dateringsmethode heeft het mogelijk gemaakt om de individuele tektonische gebeurtenissen te onderscheiden welke plaatsvonden tijdens het naar boven manoeuvreren van deze gesteenten. Dit onderzoek heeft aangetoond dat deze individuele tektonische gebeurtenissen direct gedateerd kunnen worden. Hiervoor dient echter eerst de regionale thermische geschiedenis van het gesteente nauwkeurig bepaald te worden en moeten de mineralen die geselecteerd zijn voor de datering eerst gerelateerd zijn aan de correcte tektonische gebeurtenis, welke de (re-) kristallisatie van deze mineralen heeft veroorzaakt.
Het ontrafelen van de tektonische geschiedenis in het Egeïsch gebied heeft geleid tot de identificatie van een samenspel van synchrone en diachrone geodynamische processen in het gebied tijdens de laatste circa 70 miljoen jaar. Het belangrijkste diachrone process is gerelateerd aan het beëindigen van een episode van hoge druk metamorfose, waarbij gesteenten op diepten geringer dan circa 15 km terecht kwamen. Dit proces vond circa 52 miljoen jaar geleden plaats in de Pelagonische Zone en migreerde door plaats en tijd naar de Cycladen en Kreta, alwaar het respectievelijk circa 40 miljoen en 20 miljoen jaar geleden plaatsvond. De migratierichting laat zien dat de exhumatie van deze hoge druk gesteenten telkens op een later tijdstip plaatsvond naarmate de huidige subductiezone genaderd werd. Terwijl het proces van exhumatie van hoge druk facies gesteenten migreerde richting de subductie zone werd het beinvloed door synchrone periodes van regionale compressie, rond circa 120 tot 100 miljoen en 45 tot 40 miljoen jaar geleden, en regionale extensie sinds circa 20 miljoen jaar geleden tot het heden.
De interactie van de diachrone en synchrone geodynamische processen die betrokken zijn geweest bij de ontwikkeling van het Egeïsch gebied wordt gedomineerd door de variaties in snelheid waarmee Afrika en Europa elkaar naderden en door de gesteenten welke tijdens de subductie van de Afrikaanse plaat aan de Europese plaatrand bleven steken en onderdeel werden van het Egeïsch gebergte (accretie). De snelheid waarmee Afrika en Europa elkaar naderen bepaalt de snelheid waarmee de Afrikaanse plaat onder de Europese plaat schuift. Is de naderingssnelheid hoog, dan wordt de overschuivende Europese plaat voornamelijk samengedrukt en kan het Egeïsch gebergte worden opgebouwd. Is de naderingssnelheid laag, dan kan de reeds gesubduceerde Afrikaanse plaat terugzakken in de bovenmantel, omdat de onderschuivende Afrikaanse plaat zwaarder is dan de onderliggende mantelgesteenten. Tijdens het terugzakken van de gesubduceerde plaat zal de overschuivende Europese plaat uiteengetrokken worden. De afwisseling van periodes van lage naderingssnelheden (circa 70 tot 55 miljoen jaar geleden en 20 miljoen jaar geleden tot heden) met periodes van relatief hogere snelheden hebben geresulteerd in het herhaaldelijk samendrukken en weer uittrekken van het Egeïsch gebergte. Bovendien bleef meer dan 50 miljoen jaar geleden een serie van platformcarbonaten steken aan de rand van de Europese plaat tijdens het onderschuiven van de Afrikaanse plaat. Deze carbonaten waren afgezet op een dik pakket Trias evaporieten (voornamelijk gips). Het Egeïsch gebergte verloor de interne sterkte nadat zich schuifzones hadden ontwikkeld in de relatief zwakke evaporieten. Door het verlies van de interne sterkte in het gebergte neigde het gebergte naar een minder hoge maar veel bredere opbouw. In

combinatie met het samendrukken en uiteentrekken tengevolge van de varierende bewegingen van Afrika ten opzichte van Europa, heeft dit ervoor gezorgd dat het Egeïsch gebergte sinds minstens 55 miljoen jaar geleden gedestabiliseerd raakte. Het is zelfs zeer goed mogelijk dat het Egeïsch gebergte nooit meer een stabiele opbouw bereikte en stapsgewijs instortte. Tijdens het instorten spreidde de overschuivende Europese plaat zich voornamelijk in de richting van de subductie zone uit. Dit gebeurde omdat de opbouw van het gebergte, waarbij fragmenten van de Europese plaat aan de Europese zijde op het gebergte leunden, nauwelijks een verspreiding in een andere richting toestond. De beweging van materiaal in de richting van de subductiezone zorgde ervoor dat hoge druk metamorfose bleef aanhouden in de buurt van de subductiezone, terwijl in het achterland de hoge druk metamorfe gesteenten reeds geleidelijk naar de oppervlakte gebracht werden.

Dit onderzoek heeft geleid tot een sterk verbeterd inzicht in de geodynamische processen welke een rol hebben gespeeld tijdens de vorming en het instorten van het Egeïsch gebergte. Het toont aan dat de tektonische ontwikkeling van het gebied zich niet laat karakteriseren door een fase van Alpiene gebergtevorming welke werd opgevolgd door een fase van laat-Alpiene extensietektoniek. Het sterven van een gebergte kan beschouwd worden als een geleidelijke destabilisering ten gevolge van het regionaal en lokaal samenwerken van verschillende, synchrone en ook diachrone, geodynamische processen. Deze destabilisering kan reeds vroeg in de geschiedenis van het orogeen geinitieerd worden en al plaats vinden voordat de opbouw van het orogeen door compressietektoniek voltooid is.

Abstract

The Mediterranean region is situated at the interface of the African and Eurasian plates and has been shaped by the Alpine Orogeny and the subsequent post-orogenic extension during the convergence and collision of the African and Eurasian plates. Numerous tectonic studies have focussed on the role of the African - Eurasian interaction and its effect on the development of the Mediterranean region. One of the prime areas where this interaction has been investigated is the Aegean region in the Eastern Mediterranean. The study which is reported in this thesis has investigated the tectonic development of the ductile Aegean crust which was involved in the Alpine Orogeny and in its post-orogenic history. The aims of this thesis are to obtain a detailed record of the Alpine kinematic history in the Pelagonian Zone in the northern Aegean region, focussing on the timing of, and the interaction between, compressional and extensional tectonics and on their effect on the development of the Aegean region and to temporally constrain the correlation between the Alpine Orogeny and the post-orogenic extension. The study will help to understand the geodynamic controls of the extensional processes that have characterized the development of the Aegean orogenic wedge. The aims have been achieved by combined field, microstructural and $^{40}Ar/^{39}Ar$ laserprobes studies of terrains of exposed Aegean basement, which have been metamorphosed and ductily deformed during the Alpine Orogeny. The research has mainly focussed on the Pelagonian Zone in the northwestern Aegean with additional field based studies in the Rhodope Zone (northern Aegean) and Kazdag and Menderes Massifs (eastern Aegean). The field based studies and $^{40}Ar/^{39}Ar$ laserprobe dating of deformational fabrics from selected samples have resulted in temporal constraints on the deformational and kinematic events which affected the basement, when it was still positioned at ductile levels within the crust. The wealth of published data from the Cyclades area and from Crete, in the central and southern Aegean respectively, has been integrated with the results from this study to characterize the Alpine tectonic development of the Aegean region, as a whole.

The study has shown that direct dating of deformational and kinematic events with the $^{40}Ar/^{39}Ar$ laserprobe technique can only yield meaningful results when regional thermal conditions are well constrained and the analysed minerals have been related to the correct metamorphic assemblage and to the correct deformational and kinematic fabric. The integration of microstructural, petrological and geochronological research has provided a detailed record of deformational and kinematic events in the Pelagonian Zone. This record covers the Middle Cretaceous to Recent tectonic history and is characterized by an alternation of compressional and extensional events, which affected the Pelagonian basement. The Alpine tectonic history of the Pelagonian Zone records cooling of basement thrust slices, which are mostly Hercynian granites and metamorphics, below circa 350°C by 100 Ma, while lower tectonostratigraphic levels of the basement had already cooled below these temperatures at around circa 285 Ma. Blueschist facies mylonite fabrics yield ages as old as 84.5 ± 3.3 Ma, while exhumation of the blueschist facies sequences was initiated at circa 54 Ma and involved a bivergent tectonic activity along blueschist facies and greenschist facies

mylonites. Final WSW-ward transport of the metamorphic sequence across the structurally lowest, and supposed, autochthonous, series of the Olympos-Ossa region in the Pelagonian Zone occurred at around 45 Ma, and was shortly followed by a termination of the ductile deformation history in this region. In contrast, ductile deformation continued to affect the Pelion Massif, south of the Olympos-Ossa region, till circa 15 Ma. The prolonged episode of ductile deformation in the Pelion Massif has resulted in the formation of an Oligocene-Early Miocene ductile extensional dome.

The research in the Pelagonian Zone has identified an Early to Middle Alpine cycle, lasting over 30 million years and involving crustal shortening, high pressure metamorphism and exhumation. It confines the onset of high pressure metamorphism to an interval between 100 Ma and 85 Ma and has shown that high pressure metamorphism had terminated by circa 54 Ma. The new detailed record of the Alpine kinematic history in the Pelagonian Zone allows a re-evaluation of P-T-t data from Aegean HP rocks to characterize the regional thermotectonic history. It is shown that, on a regional scale, termination of HP metamorphism is a diachronous process in the Aegean region, being circa 54 Ma in the north (Pelagonian Zone) and shifting to younger ages, chiefly circa 40 Ma in the Cyclades, and circa 20 Ma on Crete, as the present-day subduction zone is approached. In contrast to the diachronous exhumation of Aegean HP assemblages, the published Early Miocene phase of regional extension appears to be synchronous across the whole Aegean region. The studies in the Pelagonian and Rhodope Zones and the Kazdag and Menderes Massifs all show that the onset of exhumation by regional extension had initiated by circa 35 Ma in the northern Aegean. They also indicate that the widely recognized phase of Early Miocene extension is not the only period during which the Aegean region was affected by extension. It is concluded that the Aegean tectonic history is dominated by a complex interplay of tectonic events, some of which are synchronous, whereas others may be diachronous. The above diachronous event, related to the termination of HP metamorphism, becomes progressively younger towards the present-day active subduction zone and is superimposed on the synchronous events, which are characterized by regional compression at circa 120-100 Ma and 45-40 Ma and by regional extension from circa 20 Ma to Recent. It is argued here that subduction and related HP metamorphism was a continuous process since at least the Early Cretaceous. There is little evidence to suggest that three separate HP events occurred. The interplay of synchronous and diachronous tectonic processes in the Aegean region requires specific controlling geodynamic processes. A tentative tectonic history is proposed which identifies the interplay between several geodynamic processes in the destabilization of the Aegean orogenic wedge during overall convergence of the African and Eurasian plates in the last circa 100 Ma. Stagnation of the convergence rates between the two main plates at circa 70-55 Ma and 20-0 Ma has enhanced roll-back of the subducted lithosphere and its associated acceleration of extension in the back-arc location of the overriding plate. The effect of the increased roll-back of the subducted plate in the Paleogene, plus the drive of the orogenic wedge to restore its critical wedge geometry after formation of an evaporitic decollement in the base of the accreted carbonate sequences in Early Eocene times, has caused a destabilization of the orogenic wedge from Paleocene - Early Eocene onwards. The destabilization of the orogenic wedge was continued during the final extensional col-

lapse of the orogen at early Miocene times. The Miocene period of roll-back and the superimposed detachment of the subducting slab and westward expulsion of Turkey resulted in a total fragmentation of the orogen. Exhumation of high pressure metamorphic sequences in the Aegean region is associated with the recognized phases of syn- to post-orogenic extension. During the overall convergence, outward migration of the subduction related compressional front gradually caused exhumation of high pressure metamorphic sequences in the internal parts of the wedge, while in the external parts of the wedge, the metamorphic sequences were continuously repositioned closer to the active subduction zone and reworked with younger accreted material. As a result, the age of the termination of high pressure metamorphism progressively youngs towards the subduction zone.

Chapter 1

Introduction

1.1 Preamble

During the history of the earth, the global plate tectonics have been characterized by several phases of collision and break-up of the continents. After the most important recent break-up, namely the break-up of the Pangea supercontinent and the subsequent formation of the Tethys Ocean in the Late Paleozoic - Early Mesozoic, the southern margin of the Eurasian continent has been shaped by the convergence of Eurasia with the African and Indian plates and associated gradual closure of the Tethys Ocean (Ricou, 1994; Hsü, 1995; Smith, 1996). The stages of convergence and the ultimate collision of these plates has led to the formation of the Alpine-Himalayan chain, which strikes roughly E-W and runs semi-continuously from Indo-China to southwestern Europe. In the western part of the Alpine-Himalayan chain, the Mediterranean region is situated on the interface of the African and Eurasian plates (figure 1.1). The Mediterranean region has been shaped by the Alpine Orogeny and subsequent intense extension during continued convergence, which has been referred to as the "post-orogenic extensional collapse" (Dewey, 1988).

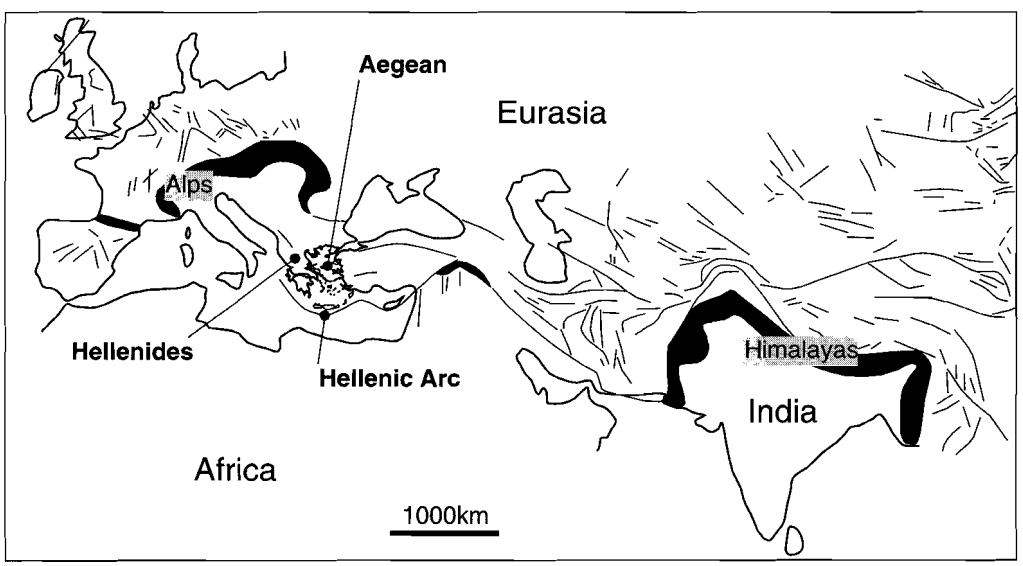

Figure 1.1. - Simplified tectonic map of the Alpine-Himalayan chain (modified after Dewey et al, 1986) showing the dominant linear elements associated with the development of the Alpine Himalayan system. Black zones characterize main thrust belts.

The concept of post orogenic extensional collapse has been widely accepted (Dewey, 1988; Platt & Vissers, 1989; Houseman & England, 1993). Since then the number of recent studies which have investigated the dominant controlling and operating mechanisms of such extensional collapse has increased relative to the number of concurrent studies which concern the characterization of the Alpine collision in the Mediterranean region. As the post-orogenic collapse and associated extension has led to the present-day geometrical configuration of the Mediterranean region, much recent research has also concentrated on the role of the African - Eurasian plate interaction in the distribution of the rates and directions of present-day motions in the Mediterranean region. The Aegean region in the Eastern Mediterranean has been a key area in three sets of studies; i.e. to study the Alpine collision (e.g. Schermer, 1993; Robertson, 1994; Okay et al, 1996; Vandenberg & Lister, 1996), the late-orogenic extension (e.g Dewey, 1988; Dinter & Royden, 1993; Jolivet et al, 1994b, 1998; Seyitoglu & Scott, 1996) and the present-day motions (Jackson, 1994; Le Pichon et al, 1995; Meijer & Wortel, 1997). The Aegean region is characterized by an Alpine collisional belt which underwent severe extension, related to the post-orogenic extensional collapse, at the southernmost margin of the European plate above a clearly identifiable subducting African plate (following first descriptions in the Mediterranean region of the horizontal motions by McKenzie, 1970, and of the lithospheric structure by Caputo et al, 1970).

1.2 Aims of this research

The study that is presented in this thesis investigates the tectonic development of the ductile Aegean crust which was involved in the compressional tectonic regimes related to the Alpine Orogeny and the extensional tectonic regime in its post-orogenic history. The prime aims of this study are:

i) To obtain a detailed record of the Alpine kinematic history in the Pelagonian Zone of the northern Aegean region, focussing on the interaction of the periods of compressional and extensional tectonics and their effect on the development of the Aegean region as a whole.
ii) To provide the temporal and spatial correlation between the classically termed "Alpine Orogeny" and the "post-orogenic extensional collapse".

Understanding of the geodynamic controls of the extensional processes that have characterized the development of the Aegean orogenic wedge and their relation to known subduction zone dynamics is thus improved.
The data have been derived from terrains of exposed basement in the Aegean region. The exposed basement has been metamorphosed and ductily deformed during the Tertiary tectonic history and subsequently positioned at the surface. The integration of field based studies, microstructural analyses and metamorphic petrology with $^{40}Ar/^{39}Ar$ laserprobe dating of deformational fabrics has resulted in temporal constraints on the deformational and kinematic events which affected the basement, when it was still positioned at ductile levels

within the crust. The temporal constraints on the kinematics are a crucial link between processes at ductile crustal levels and their surficial expression at brittle crustal levels as they provide insights into the dynamics of collisional zones and of orogenic wedges. A detailed recording of the kinematic events in the Aegean region will help to further understand the present-day dynamics and the periods of the Alpine collision and of the late-orogenic extension and will allow the characterization of the transitional phases of these three events. The integrated approach will help to further understand the last circa 100 m.y. of the evolution of the dynamic Aegean system.
The following subsidiary objectives helped to provide a detailed record of the Alpine kinematic history of the Pelagonian Zone in the northwestern Aegean region:

1. To determine the extent to which direct dating of deformational and kinematic events with the $^{40}Ar/^{39}Ar$ laserprobe can be undertaken in the multiply deformed and metamorphosed rocks of the Aegean region.
2. To place temporal constraints on the kinematic events and on the metamorphic episodes which affected the allochthonous basement in the Pelagonian Zone.

The following additional objectives allowed the Pelagonian data to be extended regionally:

3. To relate the kinematic and metamorphic evolution of the Pelagonian Zone to the thermotectonic evolution of other parts of the Aegean region.
4. To determine the dominant operating mechanisms which controlled the exhumation of basement in the Aegean area.
5. To characterize the kinematics of the transitional episode between the "Alpine Orogeny" and the "post-orogenic extensional collapse".

After characterization the kinematics in the Aegean region and after establishing the temporal constraints, a tentative model is proposed for the Tertiary evolution of the Aegean orogenic wedge.

1.3 Approach taken

The research has been undertaken by integration of detailed field based studies in the Pelagonian Zone in the northwestern Aegean with field based studies in the Rhodope Zone (northern Aegean) and Menderes and Kazdag Massifs (eastern Aegean). The studies involved field mapping combined with detailed microstructural and metamorphic studies. After kinematic and metamorphic characterization of the main structural elements, $^{40}Ar/^{39}Ar$ laserprobe dating has been applied to selected deformational fabrics in order to directly date the main kinematic events. The study in the Pelagonian Zone forms the backbone of this thesis and has been carried out in conjunction to the PhD research study of Walcott (1998) which concerned a lithological, structural and metamorphic characterization of the same region. Earlier published structural and geochronological investigations in the

Pelagonian Zone have been carried out by Schermer (1990, 1993) and Schermer et al (1990) in the Olympos region, which is situated north of the region in this study. Their results have been incorporated into this study. After detailed investigations in the Pelagonian Zone, additional studies have been carried out in the Rhodope Zone and the Kazdag and Menderes Massifs, in the northern and eastern Aegean, to investigate the regional correlation of the kinematic events which were recognized in the Pelagonian Zone. Ultimately, the results from the studies,which are obtained from the northern and eastern Aegean, are linked in with published data from the central and southern Aegean to characterize the tectonic development of the Aegean region as a whole.

1.4 Organization of this thesis

This thesis is organised into eight chapters, the first three chapters provide an introduction to the thesis (chapter 1), to Aegean tectonics and metamorphism (chapter 2) and to the $^{40}Ar/^{39}Ar$ laserprobe systematics and its application to multiply deformed rocks (chapter 3). The next chapters (chapters 4 to 6) present data from the studies in the Pelagonian Zone (chapters 4 and 5) and nearby locations in the Aegean region (chapter 6) and their conclusions which have been directly based on the presented data. The final chapters present an integrated discussion on the geodynamic implications related to the development of the Aegean region which arise from this study (chapter 7) and the main conclusions of the research (chapter 8). Details of these chapters are listed below.

Chapter 2 presents a review on some principles which characterize the tectonic setting of the Aegean region and related occurrences of high pressure metamorphic assemblages. The chapter provides an introduction to several concepts which form a basis for further discussions in the subsequent chapters.

Chapter 3 presents a detailed review and discussion on $^{40}Ar/^{39}Ar$ systematics in order to clarify the limits of $^{40}Ar/^{39}Ar$ laserprobe dating of white mica generations from multiply deformed and metamorphosed basement sequences.

In chapter 4 a field based study of the Ossa Massif in the Pelagonian Zone has been combined with the $^{40}Ar/^{39}Ar$ laserprobe technique on selected samples from the tectonostratigraphic sequence of the Ossa Massif. The laserprobe technique is applied to directly date the kinematic events related to the prevailing metamorphic conditions at the time when characteristic deformational fabrics formed. The study in the Ossa Massif has been undertaken, firstly, to characterize its Early to Mid Alpine tectonothermal history and, secondly, to characterize the role of blueschist facies deformational structures in the tectonic evolution of the Pelagonian Zone.

In chapter 5 $^{40}Ar/^{39}Ar$ laserprobe studies have been combined with structural and metamorphic investigations in order to characterize the Middle to Late Alpine tectonothermal history of the Pelion Massif in the Pelagonian Zone. As for the Ossa Massif, the study in the Pelion Massif has dated kinematic events related to the prevailing metamorphic conditions at the time of the formation of the deformational fabrics. The results from the studies in the Pelion Massif (chapter 5) and in the Ossa Massif (chapter 4) summarize the temporal con-

straints on the kinematic events and metamorphic episodes in the Pelagonian Zone and allow correlation with reported events from high pressure metamorphic assemblages in the central and southern Aegean regions (the Cyclades Archipelago and the island of Crete).
Chapter 6 presents the results of three field based studies which concerned the temporal and geometrical characterization of the tectonic settings in the northern and eastern Aegean region in order to correlate the results of these studies with the conclusions from the Pelagonian Zone and to differentiate between the effects of regional versus local tectonic events. All three areas are characterized by the presence of mid-crustal rocks and by the reported occurrences of eclogite facies assemblages and they have all been affected by documented phases of extension. The first study is located in the Rhodope Massif, which is situated in a more internal position within the Hellenides than the Pelagonian Zone with respect to the active subduction zone. The second study has been located in the Kazdag Massif in northwestern Turkey which is interpreted to be located in a similar position to the Pelagonian Zone with respect to its regional Aegean setting, but on the eastern side of the Aegean sea. The third study has been undertaken in the Menderes Massif and Cine Submassif, which are located in southwestern Turkey and has been correlated with the extensively studied Cycladic region in the central and southern Aegean sea. The characterization and timing of the main kinematic events in these three regions elaborate the regional significance of the detailed deformational and kinematic events which have been identified in the Pelagonian Zone and allow the investigation of their correlation across the Aegean Sea in time and space.
Chapter 7 discusses the regional significance of the studies which have been reported in the earlier chapters and combines the main conclusions with published data in order to place temporal constraints on the regional kinematic evolution of the Aegean region during compressional tectonics related to the Alpine Orogeny and the late-orogenic extensional tectonics. Additionally, the temporal and geometrical characterization of the areas discussed in chapters 4, 5 and 6 leads to a tectonic scenario which not only discusses the dominant controlling mechanisms of the exhumation of the high pressure sequences, but also introduces a tentative model of the Tertiary evolution of the Aegean region and which places geometrical constraints on the development of the Aegean orogenic wedge.
Chapter 8 summarizes the main conclusions of the research and highlights the fields for further research.

Chapter 2

An introduction to the tectonics and the evolution of high pressure metamorphic sequences in the Aegean region

2.1 Introduction

The study reported in this thesis focuses on the interaction between extensional and compressional tectonics and their relation to the development of the Aegean orogenic wedge during the Alpine orogenic event. In this chapter several aspects from published studies are discussed and summarized to provide a basis which allows the optimal integration of the results from the present study with the existing literature. Before presenting the data from the field based studies, microstructural analyses, metamorphic petrology and $^{40}Ar/^{39}Ar$ laserprobe dating of deformational fabrics (chapters 4, 5, and 6), this chapter will introduce the tectonic setting of the Aegean region in its present-day configuration and during its Alpine history. In addition, as most data in this study have been collected from the exposed basement in which occurrences of blueschist and/or eclogite facies metamorphic assemblages are reported, the second part of this chapter concerns the general tectonic development of, and exhumation mechanisms for, high pressure metamorphic assemblages. Finally, it has been recognized by several studies (since Lister et al., 1984) within the Aegean region that low angle normal fault systems, or detachment fault systems, which operated at circa Early Miocene times, have contributed to the final exhumation of the exposed basement. As it is known that detachment fault systems may exhume high pressure (HP) rocks from crustal depths of > 30 km to the surface (Hill & Baldwin, 1993), the theoretical evolution of detachment fault systems is discussed, which will allow further investigation of their specific role in the evolution of Aegean tectonics.
Ultimately, the full integration of the concepts discussed in this chapter and the results presented in the next chapters will provide temporal and spatial constraints on the deformational and kinematic events which affected the Aegean basement at ductile crustal levels and which will provide the platform for the further discussion on the tectonic development of the Aegean region as a whole.

2.2 Present-day configuration of the Aegean region

The Aegean region is situated in the eastern Mediterranean and forms part of the interface between the overriding Eurasian plate and the subducting African plate. In the present-day configuration the western and southern boundaries of the Aegean region are formed by the Hellenic subduction system, or Hellenic Arc (figures 1.1 and 2.1). Closest to the subduction system are the predominantly southwest vergent thrust belts of the Hellenides and Dinarides, which are situated on mainland Greece, Albania, and former Yugoslavia, and which are separated from each other by the Scutari-Pec Line (figure 2.1). The Hellenic fold-and-thrust belt is composed of several structural units, i.e. *isopic zones* (after Aubouin et al., 1963), which parallel the strike of the orogen and are, from southwest (external) to north-east (internal) (figure 2.2, modified after Robertson, 1994): i) the pre-Apulian Zone, ii) the Ionian Zone, iii) the Pindos Zone, partially separated from the Ionian Zone by the platform carbonates of the Gavrovo-Tripolitza Zone, iv) the Pelagonian Zone, v) the Vardar Zone, vi) the Serbo-Macedonian Massif, and vii) the Rhodope Massif. In general, the pre-Apulian, Ionian, Gavrovo-Tripolitza, and Pindos Zones are referred to as the *External Hellenides*. They are characterized by non-metamorphosed Mesozoic to Tertiary platform carbonates and Eocene to Miocene flysch sequences. The Pelagonian, Vardar,

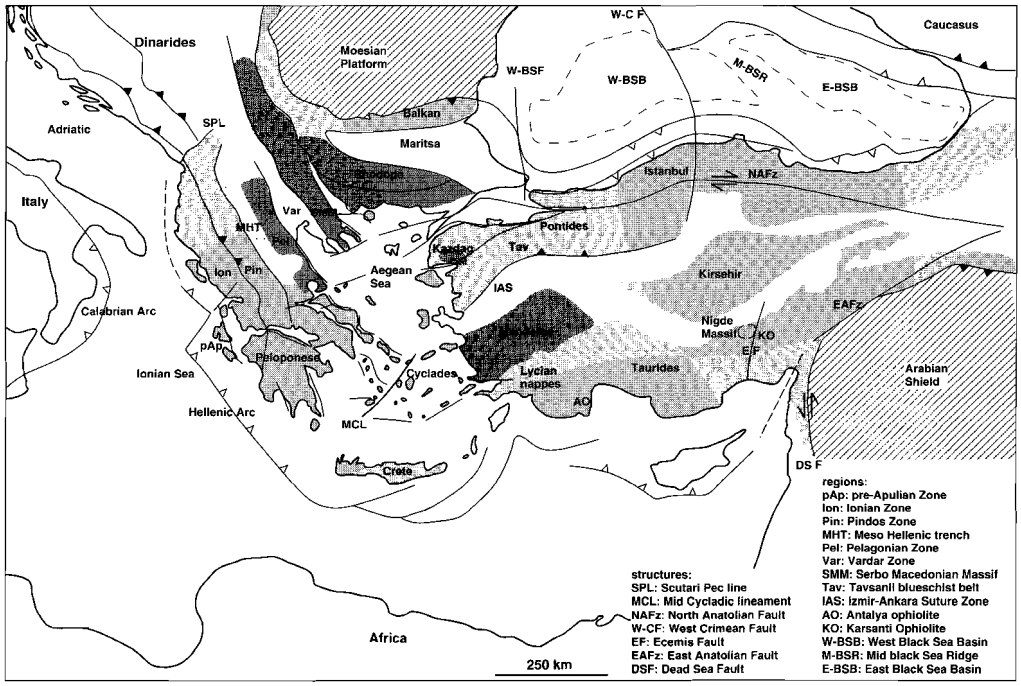

Figure 2.1. - Aegean region and surrounding areas, showing main tectonic domains, main basins and main fault zones in the region surrounded by the (stable) Moesian and Arabian platforms, the Calabrian and Hellenic Arcs, and the Black Sea and Caucasus region.

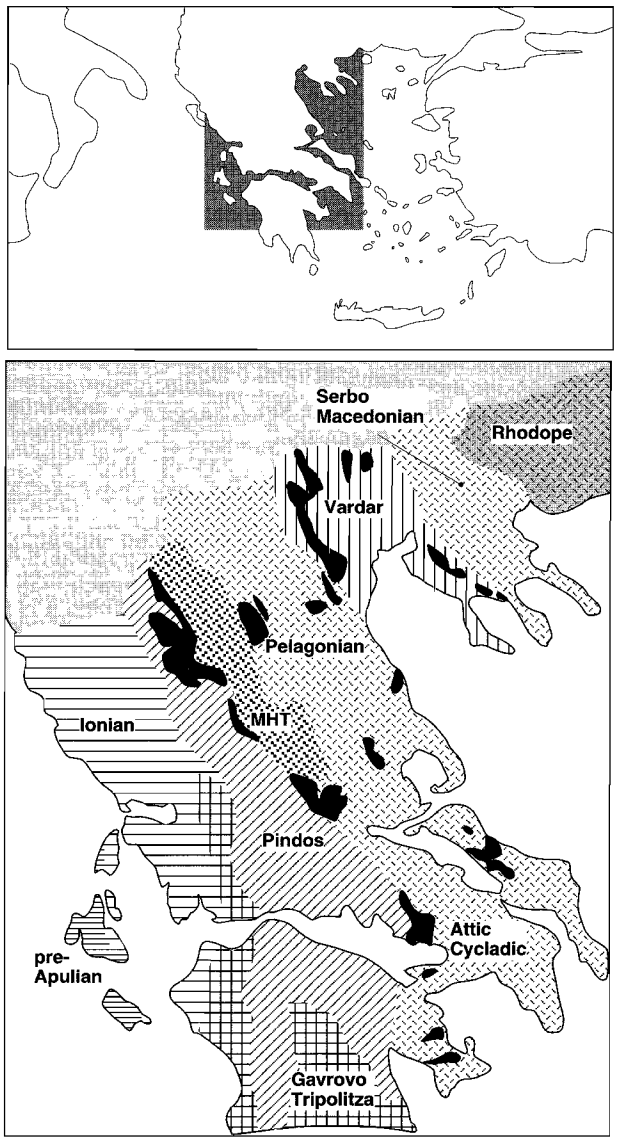

Figure 2.2. - Spatial distribution of the main isopic zones of Aubouin et al. (1963) on mainland Greece. Black regions indicate the occurrence of ophiolite sequences. Abbreviations: MHT = Meso Hellenic Trench (Diagram modified after Robertson, 1994).

Serbo- Macedonian and Rhodope Zones are referred to as the *Internal Hellenides*, and are in map view separated from the External Hellenides by the Meso Hellenic Trench, an Eocene-Oligocene regional basin, which parallels the main strike of the Hellenic Orogen (Caputo & Pavlides, 1993). The Pelagonian Zone is characterized by blueschist and greenschist facies metamorphosed, relic Hercynian basement units, which tectonically overly Mesozoic platform carbonates and Tertiary flysch sequences (summarized in Schermer, 1993; Walcott, 1998). The Serbo-Macedonian Belt and Rhodope Zone are characterized by imbricated basement, which has been metamorphosed to eclogite, am phibolite, and/or greenschist facies metamorphic conditions, and which is intruded by Tertiary granitoids (summarized by Burg et al., 1996). The Vardar Zone is characterized by the occurrence of ophiolite sequences, which have been related to the Neotethys and have been obducted in the Jurassic (Spray & Roddick, 1980). Similar remnants of ophiolite sequences are also present in the Pindos and Pelagonian Zones (figure 2.2).

The regional correlation of units between the Hellenides on mainland Greece and the Pontides and Taurides in, respectively, northern Turkey and southern Turkey is obscured by the limited exposure of regionally correlatable units in the Cyclades and on Crete and by inherited differences in paleogeo-

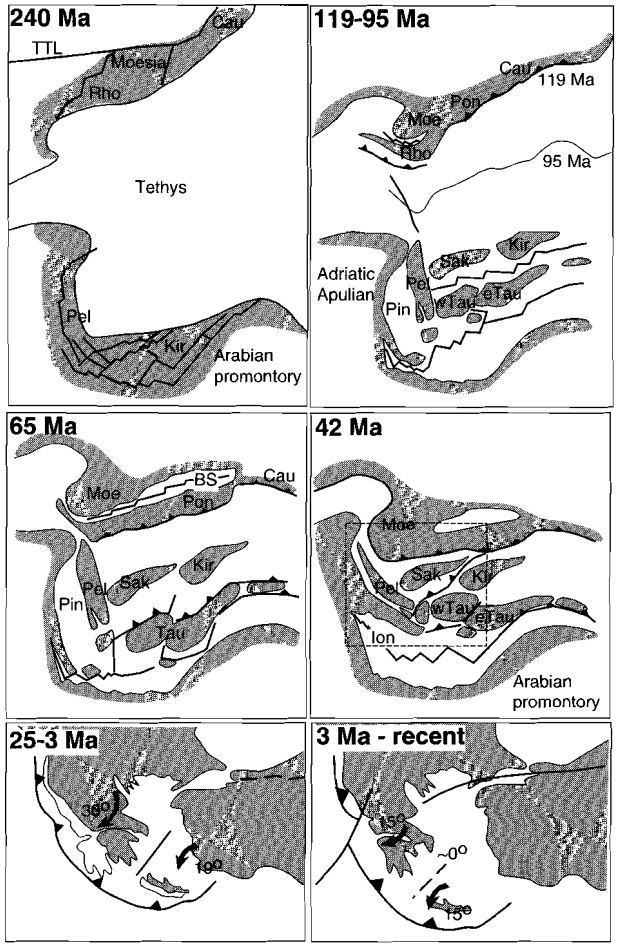

Figure 2.3. - Paleogeographic reconstructions (240-42 Ma; after Robertson & Dixon, 1984) showing reconstructed development of the eastern Mediterranean and the role of continental fragments and secondary basins of the Tethys seaway in the development of the southern Eurasian margin during the African-Eurasian convergence. *2.3a*: Proposed location of continental fragments in the Triassic configuration. *2.3b*: 119-95 Ma reconstruction shows the overall narrowing of the Tethys ocean due to N-S convergence of the African and Eurasian plates (position of southern margin of Europe relative to the position of Africa has been drawn for the 119 and 95 Ma location). *2.3c*: Gradual closure of the Tethys ocean and accretion of continental fragments. *2.3d:* Collision of most fragments, closure of Pindos basin and formation of Ionian basin. The inset in figure 2.3d, 42 Ma reconstruction, is further presented in 25 Ma (figure 2.3e) to Recent (figure 2.3f) reconstructions (summarized after Walcott, 1998, with paleomagnetic data after Kissel & Laj, 1988; Duermeijer et al, 1998). *2.3e*: Development of the present-day Aegean configuration during extension of the overriding Eurasian plate above the subducting African plate. Clockwise rotation of mainland Greece and northern Cyclades, anticlockwise rotation of southern Cyclades. Development of Mid Cycladic Lineament (after Walcott, 1998). *2.3f:* Further outward migration of the overriding plate and associated rotation of individual blocks. Abbreviations: TTL = Tornquist Teisseyre Line, Rho = Rhodope, Pel = Pelagonian, Kir = Kirsehir, Moe = Moesian, Pon = Pontides, Cau = Caucasus, Pin = Pindos Basin, Sak = Sakarya, Tau = Taurides, wTau = western Taurides, eTau = eastern Taurides, Ion = Ionian Sea.

graphic origin and subsequent tectonic development (figure 2.3, see Robertson & Dixon, 1984, and Smith, 1996, for Aegean reconstructions; and Ricou, 1994, for Tethyan scale configurations). Roughly, the Taurides appear to occur in an equivalent structural setting to the External Hellenides and are characterized by imbricated non-metamorphosed thrust sheets with a vergence towards the present-day active subduction zone (Lycian nappes, Collins & Robertson, 1997). The northern parts of the Pontides have been correlated to the Rhodope Massif (Okay et al., 1996).
The Moesian platform is situated north of the Rhodope zone (figure 2.1) and is regarded to be part of stable Eurasia (as shown on the paleogeographic reconstructions, figure 2.3). To the east of the Taurides and Pontides is the relatively stable Arabian platform located, which forms part of a separate Arabian plate (figure 2.1 and 2.3). On a regional scale the northern and eastern boundary of the Aegean system, which should be incorporated in its Alpine development, have to be located further away from the Aegean Sea and appear to be defined by the Moesian platform, the Black Sea region and the Arabian platform (figure 2.1). The presence of the relatively stable Arabian and Moesian platforms at the northern and eastern boundaries of the Aegean system contrasts with the free boundary of the active subduction zone forming its western and southern boundary.

As mentioned previously, ophiolites and related sequences are found at several locations (see e.g. figure 2.2 and Smith & Woodcock, 1982, for locations). The main occurrences are in the Pindos Zone (Pindos and Othris ophiolites), in the Vardar Zone (Vardar ophiolites), in the Izmir-Ankara Suture Zone, and in the Taurides (Antalya and Karsanti ophiolites and locations in the Lycian nappes; figure 2.1). The widespread occurrence of ophiolitic rocks has led to a discussion about the number and the location of oceanic basins, that played a role in the tectonic development of the Aegean region. Although a clear root zone to the ophiolite sequences has not been definitely identified, it is generally accepted that the Vardar zone has been the northern side of the oceanic basin(s) that separated the Eurasian plate in the north from the African plate further in the south (Smith & Woodcock, 1982). Apart from reported meta-ophiolite gneisses (Burg et al., 1996) no other ophiolitic sequences have been found over the northeastern side of the Vardar zone. Most ophiolite sequences form part of allochthonous thrust sheets which have been interpreted to be emplaced during intra-oceanic obduction, with ages of metamorphic soles varying from circa 170-180 Ma (Pindos,

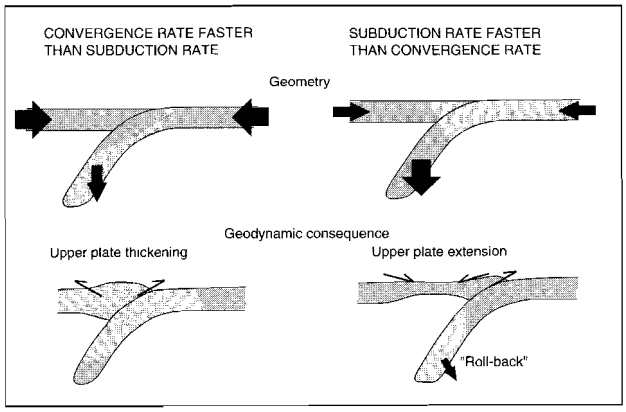

Figure 2.4. - The role of the relation between convergence and subduction rates in the distribution of compressional and extensional regimes in the overriding plate (after Royden, 1993b).

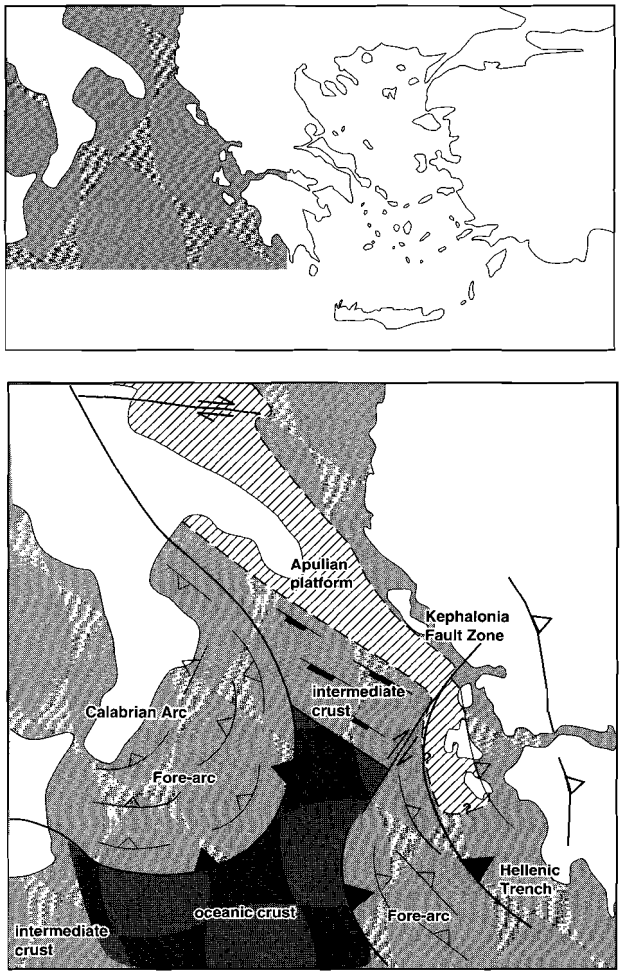

Figure 2.5. - Simplified map of western margin of the Hellenic subduction complex (after Underhill, 1989) showing the distribution of oceanic and thinned continental lithosphere in the western margin and the close appearance of the curvatures in the Calabrian arc and the Hellenic arc and associated structures related to roll-back and the retreating subduction boundary of the subducting African plate (after Royden, 1993a).

Othris and Guevgueli ophiolites in the Pindos and Vardar Zones, Spray & Roddick, 1980; Spray et al., 1984) to circa 90 Ma (Kiziltepe ophiolite in the Central Taurides, Dilek & Whitney, 1997).

Investigations of the mechanisms that controlled the present-day extensional regime, which has been interpreted to have operated since the Early- to Mid-Miocene (Jackson, 1994; Jolivet et al., 1994b; Le Pichon et al., 1995; Meijer, 1995; summarized by Walcott, 1998) have concluded that the dominant controlling mechanism which caused extensive extension of the overriding plate has been a combination of the roll-back of the subducting slab (figures 2.4 and 2.5) and superimposed local dynamics. The roll-back of the subducting slab is caused by the rapid subduction of the dense subducted lithosphere relative to the overall convergence rate (figure 2.4). It causes a retreat of the subduction zone and, by the associated outward migration of the overriding plate, it results in the development of a pronounced curvature in the subduction arc. The surficial expression of the roll-back process is illustrated in figure 2.5 (after Underhill, 1989) and shows the outward migration of the Calabrian and Hellenic Arcs, due to the roll-back of the dense oceanic lithosphere which subducts below these two arcs. The above mentioned local dynamics, which are superimposed on the process of roll-back, are the gradual detachment of the subducting slab in the Hellenic subduction zone (Wortel & Spakman, 1992; Meijer, 1995) and the westward expulsion of Turkey in the Latest Miocene - Pliocene. The westward expulsion of Turkey has been

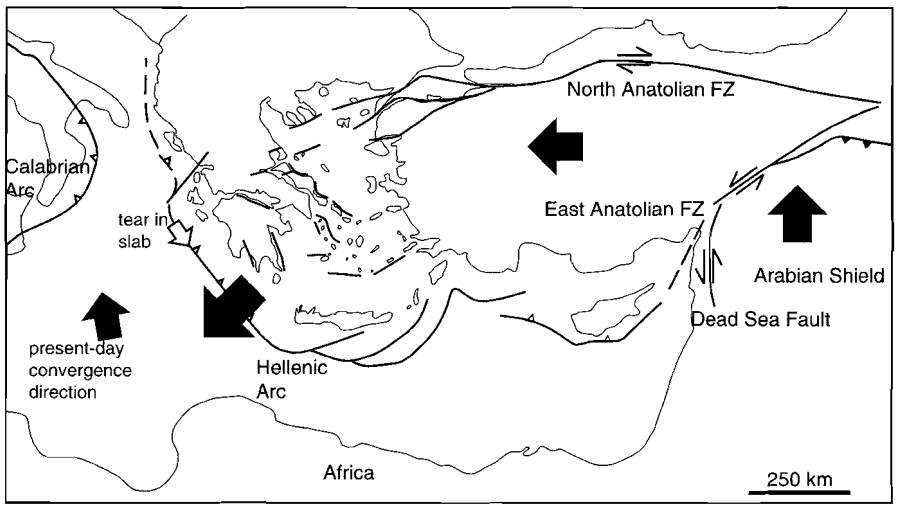

Figure 2.6. - Surficial expression of the current kinematics which control the present-day extension in the Aegean region (Jackson, 1994; Le Pichon et al, 1995). Black arrows indicate relative motions, white arrow indicate position and propagation direction of tear in subducted slab (Spakman et al, 1988, Meijer & Wortel, 1997).

caused by the final collision of Arabia and Eurasia, and was accommodated by the development of the North Anatolian and East Anatolian Fault Zones (McKenzie, 1978). It has been concluded that the contribution of the above processes of roll-back, slab detachment and westward expulsion of Turkey has resulted in the geodetically determined regional crustal velocities as observed today (Le Pichon et al., 1995; Meijer & Wortel, 1997). These regional velocities show a W-ward movement of Turkey and a SW-ward movement of the SW Aegean at a rate of ~20-30 mm/yr and over 30 mm/yr respectively (figure 2.6; see also Le Pichon et al., 1995).

The subducted portion of the African plate is expressed seismically by earthquake activity to depths of circa 200 km (Makropoulos & Burton, 1984). Seismic tomography suggests the presence of a subducting slab to depths of circa 600-800 km (Spakman et al., 1988), which have been interpreted to reflect at least circa 60 m.y. of subduction activity along the Hellenic subduction system (Hatzfeld, 1994). A well defined subduction related volcanic arc, associated with the present-day active subduction zone is found in the southern Cyclades and southwest Turkey and is only as old as circa 3 Ma (Fytikas et al., 1984; Pe-Piper & Piper, 1989). Older, Oligocene to Middle Miocene, calc-alkaline magmatism is found further north and might reflect earlier stages of the developing Hellenic subduction zone (Pe-Piper & Piper, 1989), or, alternatively, might have been emplaced in an extensional regime related to the extensional collapse of the region and associated elevation of thermal gradients (Jones et al., 1992).

The present-day Aegean crust is characterized by large variations in thickness, which range from over 45 km below the External Hellenides of mainland Greece and less than 20 km in the northern Cycladic region (figure 2.7, after Tsokas & Hansen, 1997). The large differences in thickness of the crust are most likely the result of crustal thinning as a response to

initial reduction of the thickness of the lithospheric mantle, driven by excess potential energy in regions that originally had undercompensated crustal thicknesses (see Platt & England, 1993, for discussion of the concepts). The relevance of the crustal extension after initial thinning or removal of part of the mantle lithosphere will be discussed in section 2.5 and in chapter 7.

2.3 Paleogeographic reconstructions of the Aegean region

The paleogeographic development of the Eastern Mediterranean has been extensively studied (Dewey et al., 1973; Le Pichon & Angelier, 1979; Burchfiel, 1980; Smith & Woodcock, 1982; Robertson & Dixon, 1984; Sengör et al., 1984a; Dercourt et al., 1986; Ricou, 1994; Robertson, 1994). The studies have led to a generally consistent, but still limitedly constrained, history for the evolution of the Aegean region (figure 2.3). Problems remaining with paleogeographic reconstructions were pointed out by Smith and Woodcock (1982): "...puzzling aspects of the region that are not adequately accounted for by current models include; large extensional areas contemporaneous with regional compression, the disappearence of significant amounts of continental crust, the metamorphism of shallow water continental sequences to blueschist and higher pressure facies, and the rare occurrence of calc-alkaline igneous activity at former compressional plate margins." In the past decade the "puzzling aspects" of Smith & Woodcock (1982) have been studied extensively and important contributions to the solution of these aspects have been made.

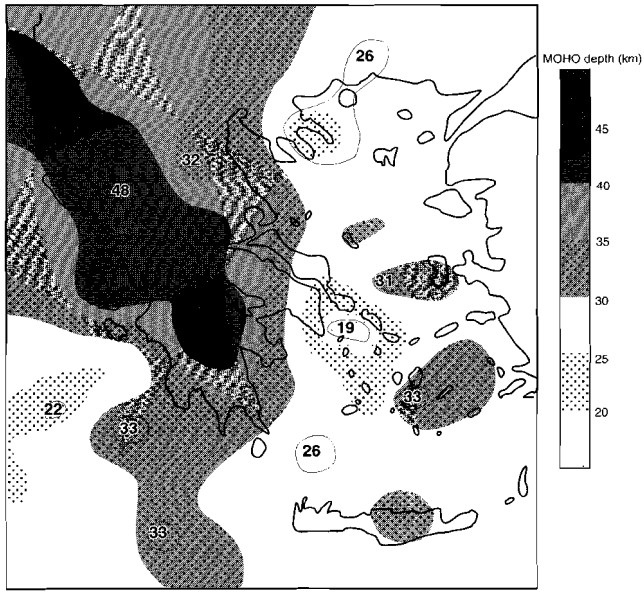

Figure 2.7. - Schematic presentation on crustal thicknesses in the Aegean region, based on the Moho depth data by Tsokas & Hansen (1997).

The geological history of the Aegean region starts after the Caledonian-Hercynian collision between Gondwana and Laurasia that resulted in the Pangea supercontinent (Ricou, 1994). The breakup of Pangea led to the development of the Tethys Ocean (figure 2.3a). Although there is general consensus that the Tethys ocean consisted of a complex array of continental fragments and marginal basins, generally two

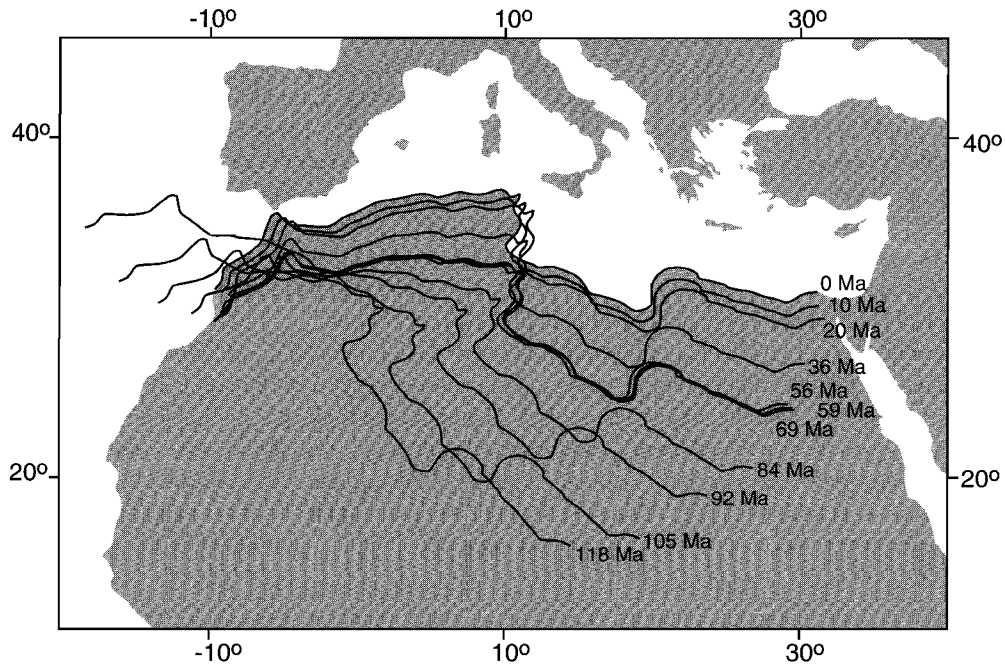

Figure 2.8. - Presentation of the convergence of the African and Eurasian plates, based on the relative motion and poles of rotation of Africa-North America versus Eurasia-North America (after data from Müller & Roest, 1992). The presentation shows the change from oblique convergence to dominant N-S convergence of the African and Eurasian plates since circa 92 Ma and indicates the differences in overall convergence rates since the past circa 100 Ma (further discussed in chapter 7).

major Tethyan Oceans have been proposed (Dewey et al., 1973; Robertson & Dixon, 1984; Smith, 1996); a late Paleozoic to early Mesozoic Paleotethys in the north and a Late Triassic - Early Jurassic Neotethys in the south, separated by the Kimmerian continent (Sengör, 1984). Numerous remnant Tethyan ophiolite, and related, sequences have been identified and have been ascribed to the Neotethys. Of the Paleotethys only remnants of an accretionary wedge system have been identified by Pickett & Robertson (1996). Generally; it has been assumed that both Paleotethys and Neotethys were subducting towards the north, underneath Eurasia. The Paleotethyan accretionary complex however, as identified by Pickett & Robertson (1996), has been related by these authors to minor southward subduction along the southern margin of the Paleotethys. Sedimentary basins of the Neotethys which formed following rifting of the northern margin of Gondwana were progressively closed and incorporated into the evolving orogenic belt (figures 2.3b to 2.3d). Within what is now the Vardar Zone, separating the Pelagonian and Rhodopian fragments, Late Jurassic flysch has been found. Orogenic activity accelerated in the Late Cretaceous when relative motions between the African and Eurasian plates changed to roughly north-south convergence (evidenced by relative locations of Eurasian and African margins, figures 2.3b, 2.3c and 2.3d, and by figure 2.8). Shortening started with the emplacement of oceanic lithos-

phere and continued with the formation of a tectonic imbricate after which thrusting subsequently migrated towards the more external parts, forming a typical fold-and-thrust belt of the External Hellenides (figure 2.9, right columns). At the front of the advancing thrust sheets, thick flysch sequences accumulated in flexurally controlled foreland basins (Underhill, 1989). In the Latest Cretaceous and Early Paleocene (Maastrichtian-Danian) 1800 m of flysch accumulated in the Vardar Zone. Also in the Pindos and Ionian Zones, substantial amounts of Eocene to Miocene flysch were deposited (figure 2.9). During ongoing convergence of the African and Eurasian plates, the Aegean region was affected by regional extension since Miocene times, which led to the present-day configuration as discussed in the previous section (figure 2.3f, after Walcott, 1998).
The paleomagnetic evolution of the Hellenides (basically mainland Greece) from the Pindos to the Serbo-Macedonian Zones has been summarized by Kissel & Laj (1988) and Edel et al. (1992). The paleomagnetic evolution is characterized by a N-S orientation of the Hellenic Zones in the Early Cretaceous (figure 2.3b and 2.3c), which was followed by a large counterclockwise rotation of about 80 degrees during the Early Tertiary and resulted in a WNW-ESE and W-E orientation of the Pindos-Pelagonian-Vardar zones (figure 2.3d). A later clockwise rotation led to the presentday NNW-SSE orientation (figures 2.3e and 2.3f).

2.4 Occurrences of high pressure metamorphic sequences

2.4.1 Introduction

During the Alpine orogenic cycle in the Aegean region, high pressure, low temperature, metamorphism affected parts of the orogen, of which metamorphosed sequences have been reported on the Peloponese Peninsula (Seidel et al., 1982), Crete (Jolivet et al., 1996), the Pelagonian Zone (Schermer, 1993), the Cyclades (Okrusch & Bröcker, 1990) and the Tavsanli region (Pontides belt, Okay, 1984). Although blueschist facies metamorphic assemblages have been reported from intracontinental locations (Till & Snee, 1995), high pressure sequences are generally interpreted to be associated to subduction complexes (Ernst, 1973). The study of the high pressure metamorphic assemblages in the Aegean region, which are composed of both sediments and basement sequences, should provide insights into the evolution of the Hellenic subduction zone and its development during Aegean compressional and extensional tectonics.

2.4.2 Concepts on the formation and development of subduction complexes

Movement of oceanic crust plus (micro-) continental terrains toward continental margins are processes that take place today and have taken place in the past and are accompanied by accretion at and beneath those margins (Cloos, 1993). It is generally recognised that blueschists and related high pressure, low temperature metamorphic rocks have formed in these subduction zones (Ernst, 1973). A long standing problem in the evolution of convergent plate margins is the manner of preservation and exhumation of high pressure metamorphic rocks from depths of greater than 25-50 km to the surface of the earth. Thermal

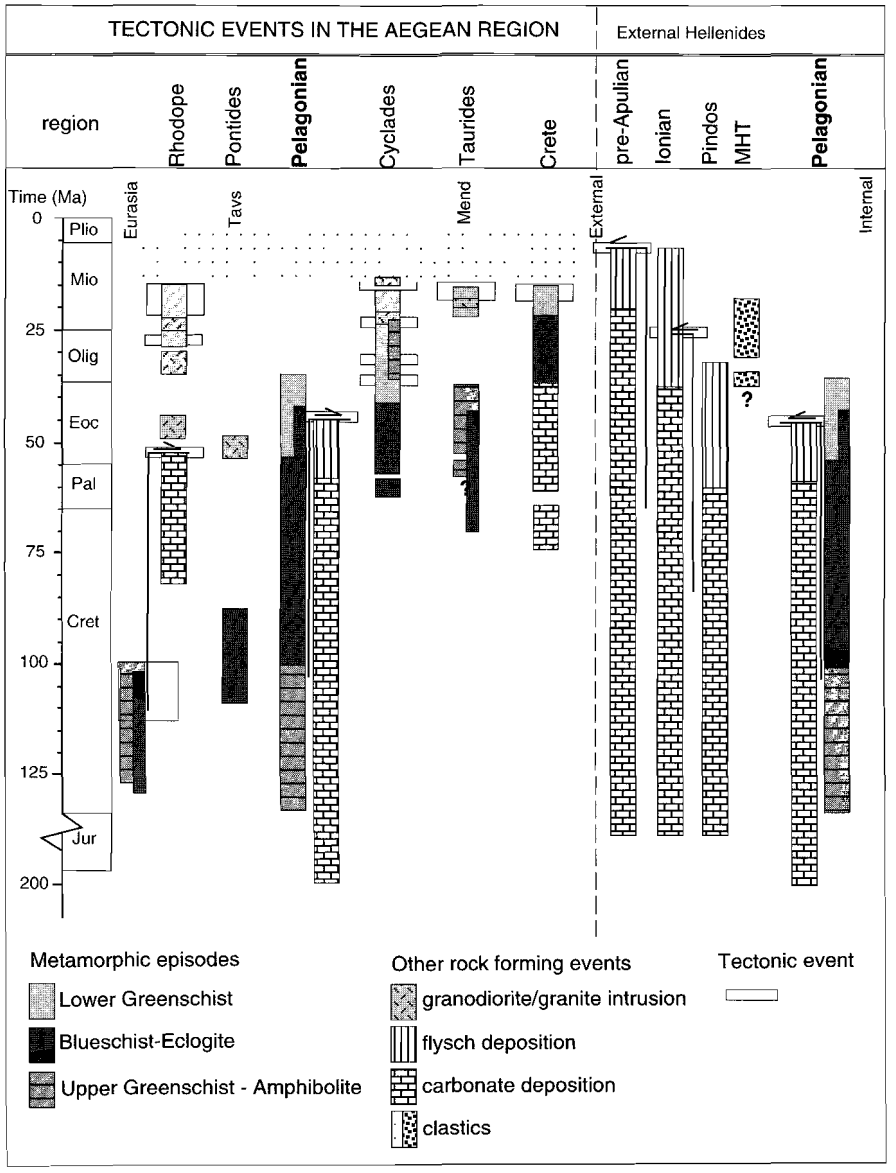

Figure 2.9. - Diagram summarizing the recognized metamorphic episodes and tectonic events in the Aegean region (left column, summarized N-S from internal zones (left) towards active subduction zone (right)), and in the External Hellenides (right column, summarized W-E from internal (right) to external (left)). Abbreviations; Tavs, Tavsanli region; Mend, Menderes and Cine Massifs; MHT, Meso Hellenic Trench. Data from Wijbrans & McDougall, 1988; de Wet et al, 1989; Wijbrans et al, 1990; Schermer, 1993; Harris et al, 1994; Okay, 1994; Dinter et al, 1995; Hetzel et al, 1995b; Hetzel & Reischmann, 1996; Jolivet et al, 1996; Okay et al, 1996; Raouzaios et al, 1996; Wawrzenitz, 1997; Thomson et al, 1998, External Hellenides data primarily after Aubouin et al, 1963; Underhill, 1989; Jones & Robertson, 1991).

modeling by Wang & Shi (1984) and many petrologic studies on high pressure metamorphic rocks demonstrate that unusually low geothermal gradients (<10°C/km) may characterize subduction related shear zones. These low thermal gradients are classically interpreted to be the product of the downward deflection of the isotherms in the subducting plate (Turcotte & Oxburgh, 1972; Cloos, 1985). The exhumation histories of high pressure terrains are determined by the interplay of numerous factors (see also Platt, 1993; Royden, 1993c; Jolivet et al., 1994a; Stüwe & Barr, 1998), which involve i) changes in the rate and direction of convergence and associated subduction, ii) frontal accretion, underplating and nappe displacement and iii) subsequent extension, uplift, erosion, and sedimentation. Careful characterization of metamorphic assemblages formed during collision and uplift, accurate determination of their pressure and temperature conditions, and the timing of the metamorphic processes, which will be presented in the following chapters of this thesis, thus form a major component of the geodynamic interpretation of orogenic belts. Such research might quantify the contribution of the above mentioned factors which influence the exhumation history of a high pressure metamorphic terrain.

2.4.3 General structure and exhumation mechanisms of a high pressure metamorphic belt

Average uplift rates of 0.01 cm/yr have been proposed for parts of subduction complexes (e.g. the Franciscan complex, Baldwin & Harrison, 1989). In contrast to these proposed values, Draper & Bone (1981) concluded that minimum uplift rates of 0.04 cm/yr to 0.14 cm/yr are required to expose preserved high pressure metamorphic sequences, without obliteration of the original low temperature mineral assemblage by relaxation and radioactive self heating. With the given parameters, this implies that it takes at least 25 m.y. to exhume high pressure metamorphic sequences to surface levels after formation at depths over circa 35 km. The higher rates of uplift are required when radioactive heating within the complex needs to be accounted for. The low uplift rate of Baldwin & Harrison (1989), together with the complete preservation of high pressure metamorphic sequences requires syn-subduction uplift through a dynamic accretionary wedge setting characterised by low geothermal gradients (such as observed for the Fransiscan complex in the western USA; Cloos, 1985; Baldwin & Harrison, 1989; Platt, 1986). Equivalently, Ernst (1988) proposed that the decrease of the rate of plate convergence could cause an overprint of the HP metamorphic assemblage by lower pressure and/or higher temperature metamorphic assemblages accompanying upthrusting, whereas continued underflow beneath the high pressure metamorphic belt allowed a continued cooling and thus retention of the high pressure prograde assemblages during gradual decompression.

The uplift rates can be attributed solely to erosional processes (Draper & Bone, 1981), but tectonic mechanisms are likely to have contributed to the exhumation of high pressure metamorphic sequences. Ernst (1975) already noted that high pressure metamorphic sequences are strongly deformed, with abundant thrust faults and/or recumbent folds showing vergence and tectonic transport towards the low-grade side of the terrane. Platt (1986; 1993) concluded that exhumation of high pressure metamorphic rocks could have occurred during overall convergence, and pointed out that unmetamorphosed rocks may occur directly over high pressure metamorphic rocks, indicating that tectonic unroofing had taken

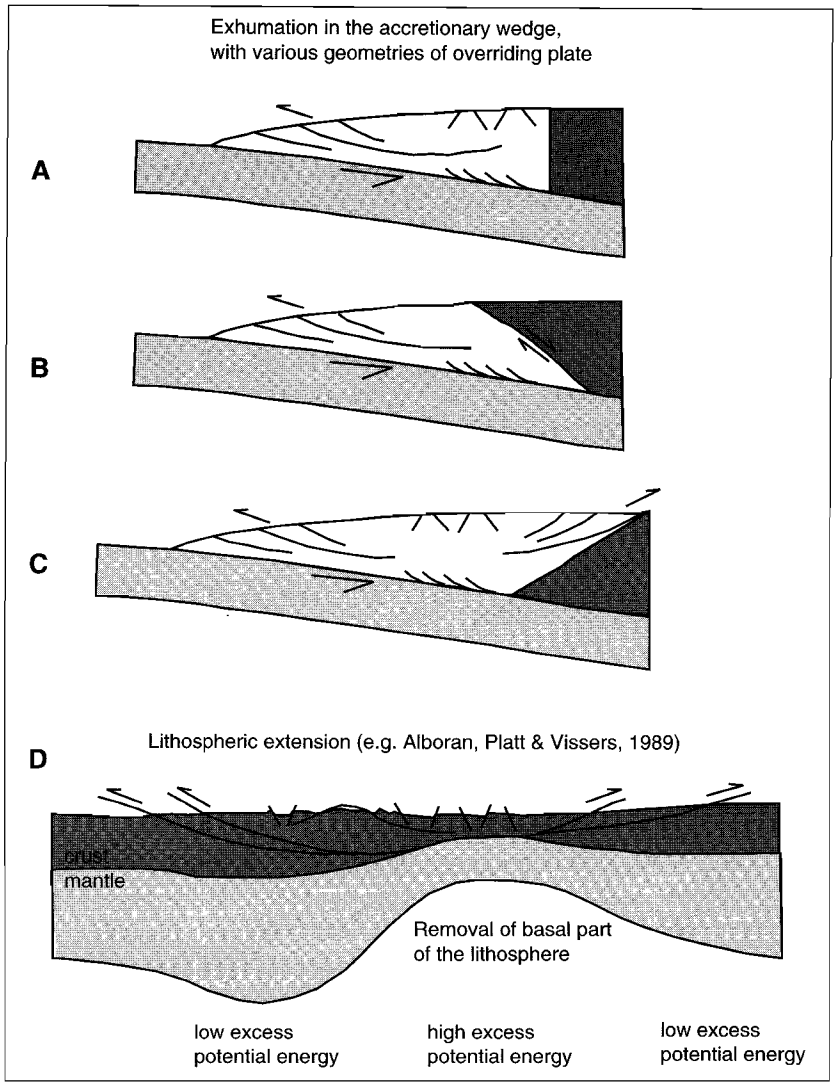

Figure 2.10. - Schematized exhumation of mid-crustal rocks and net direction of flow of wedge material in an accretionary wedge setting with varying geometries of the overriding plate, as presented in figures 2.10a to 2.10c, or by lithospheric extension as presented in figure 2.10d(after Platt, 1993).

place within the tectonostratigraphic pile. The syn-convergence exhumation can be dominated by corner flow processes in the accretionary wedge, which causes flow of material controlled by the geometries of the involved wedge and of the overriding plate (figure 2.10a to 2.10c, after Platt, 1993; see also Merle, 1994). Tectonic mechanisms responsible for exhumation in the accretionary wedge controlled by corner flow of material trapped

between the upper and lower plates in a subduction zone may cause upward flow of deeply buried rock, and may explain the occurrences of high pressure metamorphic blocks in a tectonic melange (Cloos, 1985), or may result in the occurrence of high pressure metamorphic blocks in diapiric intrusions of low-density mud or serpentinite (Platt, 1993). Alternatively, the syn-convergence exhumation might be caused by overall lithospheric extension which is driven by a gradient in excess potential energy following removal of the basal part of an initially overthickened lithosphere (figure 2.10d; see also, Platt & Vissers, 1989; Platt & England, 1993; Vissers et al., 1995). Associated with (continental) lithospheric extension, metamorphic core complexes may have developed (see section 2.5.2 for geometrical constraints on core complex formation). The metamorphic core complexes have been recognized across the whole globe (see for example, Lister et al., 1984; Lister & Davis, 1989; Hill & Baldwin, 1993; Holm & Lux, 1996) and may have a significant contribution to the exhumation of rocks from deep crustal levels by fault activity along low angle normal (detachment) fault systems (see also Lister et al., 1984, Hill & Baldwin, 1993). The significance of detachment faulting and associated formation of metamorphic core complexes will be further discussed below and in chapters 6 and 7.

2.5 Style of Aegean tectonics

2.5.1 Alpine compression

Alpine compression during the Late Mesozoic and Tertiary, due to the closure of the Neotethyan ocean(s) and continent-continent collision of the Apulian-Adriatic microplate(s) with Eurasia (see figure 2,3 and paragraph 2.3), created a strong tectonic grain in the form of folds, thrust faults and occurrences of emplaced ophiolite sequences that trend NW-SE in mainland Greece and change to an overall E-W orientation across the Central Aegean into Turkey (see figures 2.1 and 2.2; and Burchfiel, 1980; Robertson & Dixon, 1984; Sengör et al., 1984). The overall shortening is interpreted to have initiated with obduction of ophiolite sequences by circa 170-180 Ma (i.e. the oldest age of the metamorphic soles of the Hellenic ophiolites determined by Spray & Roddick, 1980; Spray et al., 1984; see also paragraph 2.3). The overall shortening during the Alpine convergence has been estimated from a minimum of circa 135 km to a maximum of circa 500 km and has been derived from a transect from the Rhodope Zone to the present day subduction zone (Zimmerman & Ross, 1976; Burchfiel, 1980; Dewey et al., 1986). The Alpine compressional structures in the western Aegean region are preserved in a set of WSW-ward verging thrust sheets; the External Hellenides (figure 2.9, right column). A similar fold-and-thrust belt geometry is found in the soutward verging Lycian Nappes of the Tauride Belt in southern Turkey. In general, an inverted metamorphic gradient is observed in the Hellenides, e.g. evidenced by weakly metamorphosed sedimentary sequences overlain by metamorphosed basement in the Pelagonian Zone (Schermer, 1993), and by amphibolite to eclogite facies metamorphic units overlying greenschist facies metamorphic units in the Rhodope Zone (Liati & Mposkos, 1990; Burg et al., 1996), and which are associated with northeastward dipping thrusts (in the present day configuration).

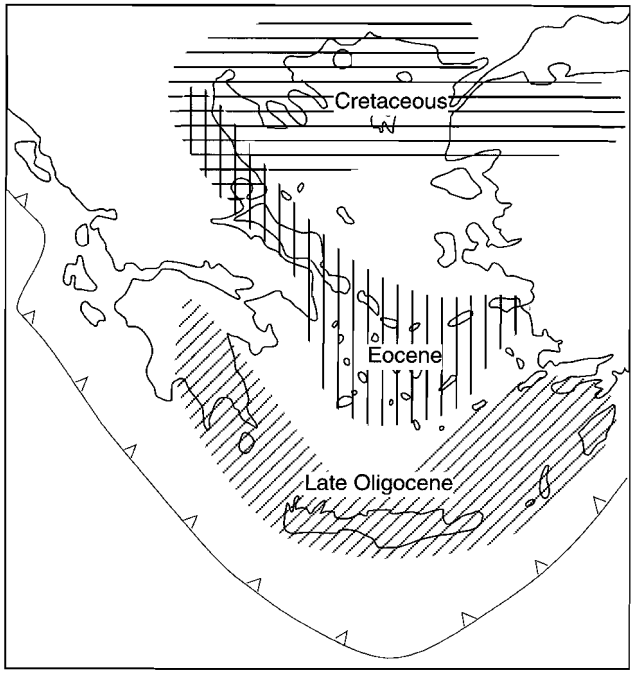

Figure 2.11. - Spatial distribution of the three proposed HP metamorphic belts in the Aegean region, which are related to the Alpine Orogeny, following data and/or postulations from Blake et al, 1981; Bonneau & Kienast, 1982; Seidel et al, 1982; Okay, 1984; Papanikolaou, 1984; Schermer et al, 1990; Gautier & Brun, 1994; Okay & Kelley, 1994; Jolivet et al, 1996.

In the Aegean region, the occurrence of three regional high pressure metamorphic belts has been proposed, which have been related to different stages of the Alpine tectonic history (Blake et al., 1981; Bonneau & Kienast, 1982; Papanikolaou, 1984; Gautier & Brun, 1994; Jolivet et al., 1996). The proposed belts are summarized in figure 2.11 and are exposed in the Rhodope Zone, Pontides and Pelagonian Zone (relic Early Cretaceous HP belt), the Pelagonian Zone, Cyclades and Menderes Massif (Eocene HP belt) and the Peloponese Peninsula and Crete (Oligocene-Early Miocene HP belt). The formation of the HP metamorphic fabric and associated proposed HP metamorphic belts of varying ages has been related to different phases of regional compression during the Alpine Orogeny (Seidel et al., 1982; Avigad et al., 1997; Dora et al., 1997; Oberhansli et al., 1997), although some workers noted the correlation between HP metamorphic fabrics and later extensional structures and suggested an extensional regime which occurred during the latest stages of HP metamorphism (Gautier & Brun, 1994).

2.5.2 Miocene extension and detachment systems

In the Aegean region, low angle normal fault systems (detachment zones), which operated at Early Miocene times and caused exhumation of ductile basement rocks to surface levels, have been widely identified (Lister et al., 1984; Gautier & Brun, 1994; Dinter et al., 1995; Hetzel et al., 1995; Jolivet et al., 1996; Vandenberg & Lister, 1996; Wawrzenitz, 1997). As numerous authors have concluded that these detachment zones were the dominant mechanisms for exhumation of high pressure metamorphic assemblages (Gautier & Brun, 1994; Jolivet et al., 1994b; Avigad et al., 1997), it is important to investigate the characteristics of these zones in order to understand their role in the exhumation process.

The theoretical geometric characteristics of detachment zones have been discussed by Davis (1983), Wernicke (1985), and Lister et al. (1986) and, since their first description, they have

been globally recognized in extended terrains of different ages (see also section 2.4.3). The model geometry is based on the different rheological response to the mantle and crustal sections of the lithosphere to extension. The effect of extension of the entire lithosphere by simple shear is illustrated in figure 2.12a (after Wernicke, 1985). The diagram at the bottom of figure 2.12a shows the extension factors of the mantle lithosphere (β_{ml}) and the crust (β_{cr}), and, thus, the contribution of added/subtracted mass to the isostatic column. Additionally, the domains of uplift versus subsidence are indicated, which are caused by i) extensional (tectonic) strain alone (lighter shading), and by ii) conductive cooling of the mantle lithosphere, responding to extensional strain (tectonic + thermal), following instantaneously extending of the lithosphere (darker shading). The model shows that subsequent conductive cooling of the mantle lithosphere is sufficient to compensate the initial possible "tectonic" uplift of parts of the region; i.e. the hanging wall of detachment (following figure 2.12a). Footwall rocks of such an extended lithosphere might be subject to rapid unloading, which will promote melting as dry melting curves typically have shallower slopes than adiabatic paths on PT diagrams (see also Spear, 1993). Consequently, the footwalls of the detachment zones are often characterized by the emplacement of syn-tectonic intrusions (see chapter 7 for a further discussion)

In reality, detachment zones are far more complex than those shown in the theoretical models. The detachment zones which have been recognized in the Aegean region also reflect this complexity. Often, pre-existing zones of weakness (e.g. old thrust planes) are inherited and exploited by detachment zones (recognized in the study by Emre & Sözbilir, 1997 and discussed in chapter 6). Detachment zones in the Aegean may develop as single zones in an asymmetric extensional setting (see also Gautier & Brun, 1994; figure 2.12b), and as double dipping zones in a bivergent extensional setting, which developed simultaneously (see also Hetzel et al., 1995a; figure 2.12b), or which developed as a southdipping detachment overprinting a north dipping detachment which finally resulted in an overall bivergent extensional setting (Hetzel et al., 1995a; Vandenberg & Lister, 1996). The schematic sections presented in figure 2.12b, show the exhumation mechanisms of rock sequences from crustal depths of circa 25 km. As some of the recognized detachment zones in the Aegean region exhume high pressure sequences, which initially formed at depths over 40 to 50 km (eclogite assemblages indicating pressure equivalents of 14-16 kbar, as summarized for the Aegean by Okrusch & Bröcker, 1990), the detachment zones either continued till deeper crustal levels than the depths indicated in figure 2.12b, or alternative mechanisms had operated in the Aegean region which positioned high pressure sequences to shallower crustal depths (ca 20-25 km) relative to their depth of crystallization (ca 40-50 km). If additional exhumation mechanisms would have operated, it is clear that the first part of the exhumation history is partly hidden in the pre-Miocene history. Wijbrans (1985)

Figure 2.12. - 2.12a. Schematic geometry of a detachment zone which formed under normal simple shear of the entire lithosphere (after Wernicke, 1985). *2.12b.* Different styles of detachment formation; asymmetric extension accomodated by a single detachment zone (after Gautier & Brun, 1994), bivergent extension accomodated by two synchronously operating detachment zones (after Hetzel et al, 1995). *2.12c.* Temporal development of detachment zones and their role in the exhumation of high pressure sequences (dark grey zones) (after Avigad et al, 1997).

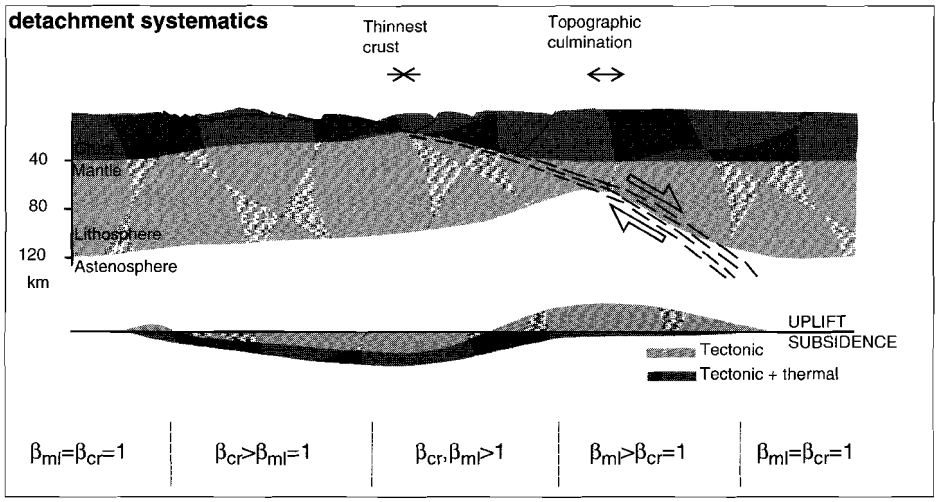
detachment systematics
Thinnest crust
Topographic culmination
40
80
120
km
Mantle
Lithosphere
Astenosphere
UPLIFT
SUBSIDENCE
Tectonic
Tectonic + thermal
βml=βcr=1
βcr>βml=1
βcr,βml>1
βml>βcr=1
βml=βcr=1

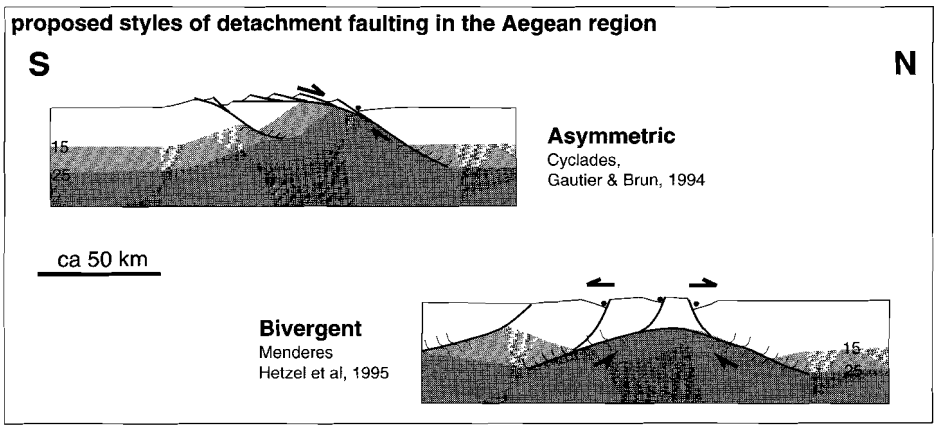
proposed styles of detachment faulting in the Aegean region
S
N
15
25
Asymmetric
Cyclades,
Gautier & Brun, 1994
ca 50 km
Bivergent
Menderes
Hetzel et al, 1995
15
25

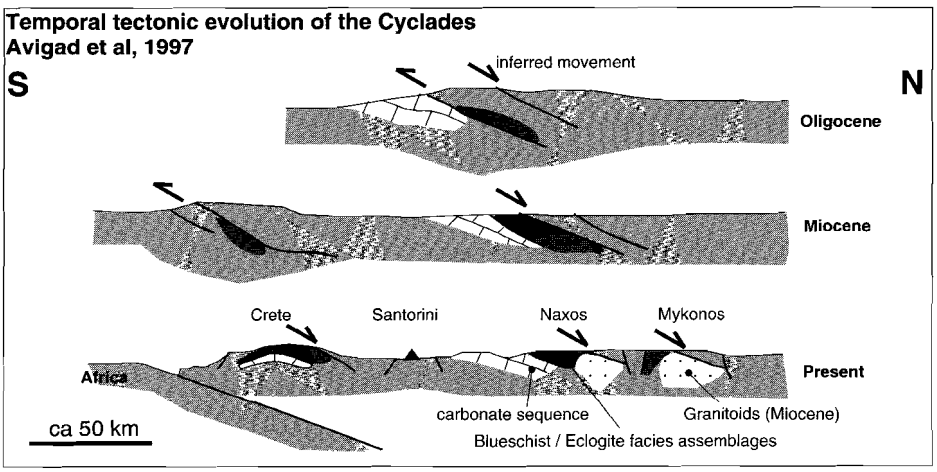
Temporal tectonic evolution of the Cyclades
Avigad et al, 1997
S
N
inferred movement
Oligocene
Miocene
Crete
Santorini
Naxos
Mykonos
Present
Africa
carbonate sequence
Granitoids (Miocene)
Blueschist / Eclogite facies assemblages
ca 50 km

pointed out that there was a circa 20 Ma period of apparent quietness between the termination of HP metamorphism and the onset of Miocene overprinting (see also Wijbrans et al., 1993). Avigad et al. (1997) also met this problem and stated that "...an important phase of unroofing affected the eclogite in the Cyclades between the Eocene and the Miocene, but extensional structures are practically undocumented". The authors inferred a phase of Oligocene thrusting plus extensional sliding which contributed to the initial stage of eclogite exhumation, as indicated in their schematic temporal tectonic evolution, which is presented figure 2.12c. The figure summarizes the two extensional events, at Oligocene and Miocene times respectively, which have been proposed by Avigad et al. (1997) to exhume eclogite facies metamorphic rocks (dark shaded areas) after their formation.

2.6 Summary

The general accepted concepts for the formation of high pressure metamorphic assemblages in the Aegean region during the Alpine Orogeny and the driving mechanisms of the Miocene to Recent extension and the development of associated Early Miocene detachment fault systems, which have been discussed in this chapter provide a working platform to allow optimal integration with the results from the present study (chapters 4, 5 and 6).
The Aegean region in the Eastern Mediterranean Sea has witnessed a prolonged history of convergence between the African and Eurasian plates and the associated closure of the Tethys ocean/oceans. The convergence and collision of the African and Eurasian plates, and of continental fragments, microplates, and/or platform carbonates between the two main continental plates, have shaped the Aegean region over the past circa 200 Ma. This has been visualized in published paleogeographic reconstructions, of which the reconstruction of Robertson and Dixon (1984) is still the most detailed, but not the most recent one (more recent ones, e.g. Ricou, 1994; Smith, 1996, concerned the reconstructions of the Tethyan Oceans as a whole and of Europe, respectively).
The present-day configuration of the Aegean region is characterized by pronounced extension, classically related to the post-orogenic extensional collapse, which might have initiated in the Early Miocene. It has been proposed that the driving mechanism of the regional extension is related to the roll-back of the African plate, caused by a high subduction rate of the dense subducting lithosphere relative to the overall convergence rate, in combination with superimposed dynamics, controlled by westward movement of the Anatolian block and gradual detachment of the subducting slab (Le Pichon et al., 1995; Meijer & Wortel, 1997). The Early Miocene extension has been accommodated by low-angle normal fault systems which have been recognized throughout the Aegean region (since Lister et al., 1984) and which have developed at crustal levels conducive to ductile deformation and gradually exhumed from mid-crustal levels to upper crustal, more brittle, levels and finally to the surface.
In contrast to the late-orogenic extensional tectonics of the region which have been extensively studied in the past decade, the "period of Alpine compression" has received less recent attention. Consequently the tectonic scenario which was acting during the Alpine

period and its correlation to the phase of late-orogenic extension is still under debate and forms one of the key questions in this thesis (see chapter 1). The study of high pressure metamorphic sequences and related subduction type settings in the present study will contribute to the understanding of the Alpine tectonic history in the Aegean region. The high pressure sequences are a principal interest because they occur throughout the orogen, dominantly at the interface of unmetamorphosed (external) zones and amphibolite facies metamorphosed (internal) zones. Also, it has been argued that the early part of the exhumation of high pressure metamorphic sequences and of other mid crustal basement rocks is hidden in the pre-Miocene tectonic history before the development of the widely recognized Early Miocene detachment fault systems (further discussed in chapters 5, 6 and 7).
The present study will integrate the data from field studies, microstructural analyses, metamorphic petrology and $^{40}Ar/^{39}Ar$ laserprobe dating of deformational fabrics of exposed basement rocks in order to resolve the pre-Miocene tectonic history and correlate this history to the better understood Miocene to Recent tectonic history. After characterization of the pre-Miocene tectonic scenario, the study will also attempt to provide insights in the driving mechanisms of Alpine dynamics which operated in the Aegean region during the Tertiary.

Chapter 3

$^{40}Ar/^{39}Ar$ laserprobe dating; Background and its application to the multiply deformed Aegean basement

3.1 Introduction

In order to place temporal constraints on the metamorphic episodes and on the deformational and kinematic events which have been identified in the Aegean region, $^{40}Ar/^{39}Ar$ laserprobe dating experiments have been carried out on white mica generations from the basement sequences. Before the datasets from the studies in the Aegean region are presented and discussed in chapters 4, 5 and 6, the principles of the $^{40}Ar/^{39}Ar$ technique and its analytical limits will be briefly summarized and discussed with respect to the samples from the present study. Basic principles of the $^{40}Ar/^{39}Ar$ method and of laserprobe characteristics are further outlined in detail in appendix 1. The summary enables the quantification of the application limits of $^{40}Ar/^{39}Ar$ laserprobe dating of minerals from multiply deformed and metamorphosed rocks. Following this summary, the operating mechanisms which theoretically control Ar diffusion are discussed. In addition to the well known factor of thermally activated volume diffusion which causes loss of Ar in white mica during metamorphism (or gain of Ar when the material is positioned in an Ar oversaturated environment), the discussion will also investigate the control of recrystallization on the diffusion of Ar in white mica. It is expected that deformation and chemical alteration are dominant recrystallization controlling factors in high strain mylonite zones which operate at relatively low metamorphic temperatures (i.e. below circa 350°C, when thermally activated volume diffusion becomes less significant). As these mylonite zones are known to be present in the Pelagonian Zone (Schermer, 1993; Walcott, 1998), these factors are further characterized in terms of their contribution to the generation of preferred diffusion pathways of Ar in white mica. The investigations are carried out on a microstructural and crystal chemical basis, and will commence with some results from $^{40}Ar/^{39}Ar$ laserprobe experiments on white mica generations from samples of the Pelagonian Zone. To investigate to what extent the presence of such a multigeneration white mica population in the selected samples limits the analysis and preservation of reasonable and objective absolute age information, the experiments in this study have been carried out on small white mica separates (incremental heating experiments on single crystals and small populations of white mica crystals) and white mica in thick-section (spot fusion experiments on sections of circa 20 mm in diameter and circa 100 μm thickness).

3.2 Principles of $^{40}Ar/^{39}Ar$ geochronology

3.2.1 Introduction to the $^{40}Ar/^{39}Ar$ technique

The $^{40}Ar/^{39}Ar$ dating technique is now the most commonly used variant of the conventional K-Ar method and is based on the natural decay of ^{40}K to ^{40}Ar (see figure 3.1 for the decay scheme; details of the basics of K-Ar decay and of the principles of the $^{40}Ar/^{39}Ar$ technique are further explained in sections A1.1 and A1.2 of appendix 1). The $^{40}Ar/^{39}Ar$ technique permits precise dating of very small samples (down to single-grain size, Layer et al., 1987; Wijbrans et al., 1990) and samples of very low potassium content (less than 80 ppm; Hanes et al., 1985). The theory and technique of the $^{40}Ar/^{39}Ar$ method are extensively described in the textbook of McDougall & Harrison (1988). The development of the laser microprobe technique, whereby a laser with very small spot diameters is used to provide point-source heating of minerals, was originally developed to investigate the distribution of noble gases in meteorites (Megrue, 1967) and subsequently used for $^{40}Ar/^{39}Ar$ dating of lunar rocks (Plieninger & Schaeffer, 1976). The laser step heating method (or incremental heating method) to extract Ar from irraditiated terrestrial samples was first demonstrated by York et al. (1981) and has subsequently been applied to mineral populations from multiply deformed rocks (Wijbrans et al., 1990; Scaillet et al., 1990; Reddy et al., 1996). The introduction of the laser-probe technique has also furthered research on the dominant mechanisms which control argon diffusion in deformed K-bearing minerals (Hames & Hodges, 1993), parallel to studies which applied furnace heating to extract Ar from the selected material to investigate the argon diffusion behaviour (Heitzler & Harrison, 1988; Kirschner et al., 1996). In the case of white mica, diffusion controlling factors are not only temperature, cooling rate, and grainsize, but also deformation induced recrystallization, which might lower the effective diffusion pathlength (Reddy et al., 1996) and chemical alteration (Scaillet et al., 1992). The diffusion controlling factors will be further discussed in the next sections.

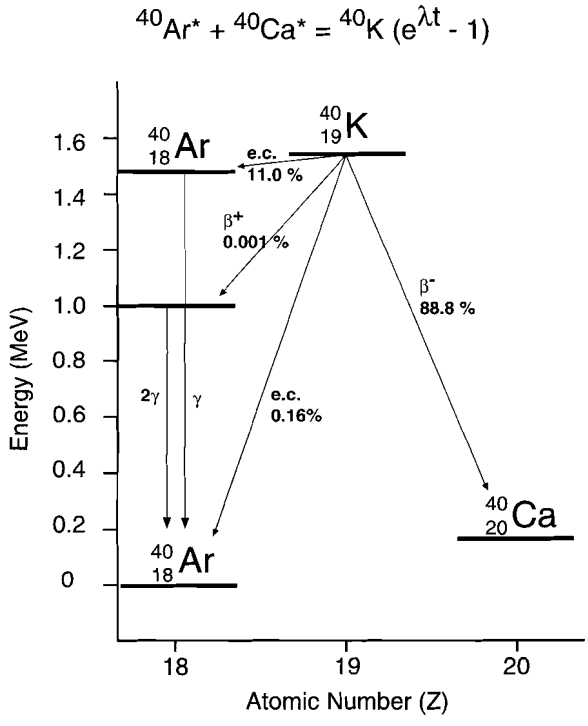

Figure 3.1. - Decay scheme of the branched decay of ^{40}K to ^{40}Ca and ^{40}Ar (modified after Faure, 1986).

3.2.2 Analytical constraints

In the $^{40}Ar/^{39}Ar$ age dating technique, several analytical steps contribute to the analytical uncertainty of the final absolute age. Correction factors which have to be taken into account are presented and discussed in section A1.2 of appendix 1 (see also McDougall & Harrison, 1988, for an extensive presentation on the correction factors). In brief, the main factors which contribute to the final analytical uncertainty of the established absolute age concern the measurement of; i) the relative quantities of the three naturally occurring isotopes of potassium, ii) the decay constant of ^{40}K decay to ^{40}Ar, iii) the irradiation parameter J, iv) the uncertainty on the mass spectrometric analysis of the Ar intensities (including the error on the blanks), v) the mass interferences of radiogenic Ar with atmospheric Ar and potassium, calcium and chlorine derived Ar, and, additionally, vi) the error on the weighted mean of the individual steps which contribute to the plateau age, established from an age spectrum after completion of an incremental heating experiment. Generally, the first three factors, which are related to the estimation of the abundance of ^{40}K in the unknown sample and the natural decay of ^{40}K, contribute to an analytical error which is expected to be less than circa 1% of the absolute age. As these uncertainties are the same for all K-Ar age measurements, it is justified to exclude these factors if the results are compared within the K-Ar system only (see also Renne et al., 1998, for an extensive discussion). As the $^{40}Ar/^{39}Ar$ analyses in the present study have been carried out on very small samples, and thus containing very small quantities of Ar, the error on the analysed Ar intensities is another main contribution to the analytical error. The mass spectrometric analysis in this study results in typical "sample over system blank" ratios of 50 to 250, 35 to 250, 2 to 6, circa 1, and 1 to 5, for ^{40}Ar, ^{39}Ar, ^{38}Ar, ^{37}Ar and ^{36}Ar, respectively (see figure 3.2). The ratios show that in this study, mass interference due to additional Ar isotope production during irradiation is limited. The white micas that were analysed contain little or no calcium, which resulted in very little to no production of calcium derived ^{36}Ar, ^{37}Ar, and ^{39}Ar and consequently, an analysed ^{37}Ar intensity which is near system blank values. Also, little chlorine derived ^{38}Ar is present (2 to 6 times the blank value) and hence $^{36}Ar_{Cl}$ is negligible. As a result, potassium derived Ar (both by natural ^{40}K decay and by irradiation) and minor atmospheric Ar are the most significant components of the bulk Ar analysis. If ^{40}Ar intensities are low with respect to the system blanks (i.e. $\leq$ 50 times the blank) the error in the ^{36}Ar intensity contributes significantly to the correction of ^{40}Ar for atmospheric Ar (as the atmospheric ratio of $^{40}Ar/^{36}Ar$ is 295.5). As a consequence, stringent controls of system blanks are essential for the success of the analysis. Figure 3.2 also presents the typical analytical errors (2σ) which were obtained in this study, projected on the intensity of the ^{40}Ar analysis (lower diagram in figure 3.2). The figure illustrates that, after all corrections have been applied, analytical errors per individual step become acceptable when the ^{40}Ar mass intensity exceeds hundred times its corresponding blank.

In the present study, system blanks were determined after every second unknown analysis. At the end of every day the system blanks were plotted as a function of time of the measurement and their variation was determined at a 2σ significance level. The unknowns were corrected for the interpolated blank at the time of analysis of the unknown and the 2σ error on the blank was further used for the error calculation of the unknown (see also section 4.8

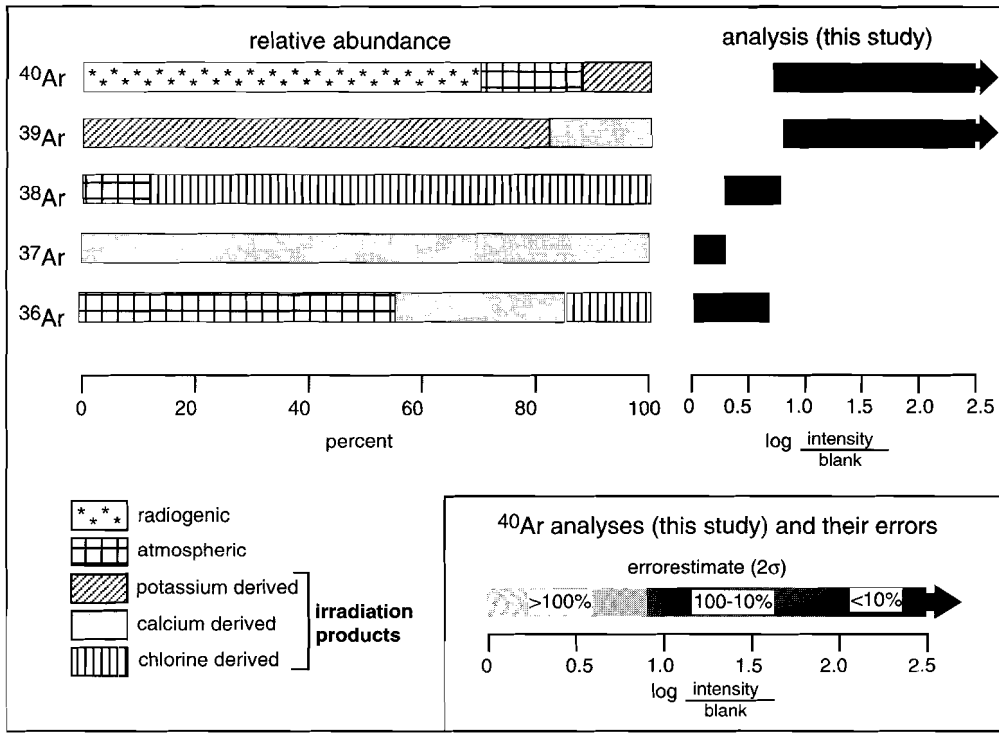

Figure 3.2. - Schematic presentation of argon isotope sources after irradiation (left, after Wijbrans et al, 1995), and schematic presentation of typical argon isotope intensity intervals in white mica, obtained in this study (right, presented in "sample over system blank ratio".

for further discussion on the data processing). In general, analytical errors (2σ level) on final absolute ages (i.e. including all individual steps of an incremental heating experiment) were in the order of circa 1-2% when a sufficient amount of material was analysed (results of chapters 4 and 5) and increase rapidly to 5-10% or higher when too small quantities of material are analysed (as expressed by large analytical errors on some analyses in chapter 6). Too small quantities of material might have been selected when the age of the sample is younger than expected (i.e. less radiogenic ^{40}Ar), the sample is very poor in K content (e.g. irradiation of paragonitic or margaritic white micas will result in less K derived Ar) and / or irradiation times have been too short to convert sufficient ^{39}K to ^{39}Ar.

3.2.3 The closure temperature concept

When the absolute age of a sample has been determined by a $^{40}Ar/^{39}Ar$ laserprobe experiment (see the above paragraphs and sections A1.3 and A1.4 of appendix 1 for details on the experiment) it is important to interpret the obtained numerical "age" value in terms of its geological relevance. Given the case of a stable mineral, the most important process of controlling the isotopic composition of a crystal is thermally activated volume diffusion. At low temperatures, diffusion is slow and radiogenic Ar may be retained quantitatively after it has

formed (*closed system*). At high temperatures, diffusion is rapid and radiogenic Ar may be lost by diffusion from the crystal after it has formed (*open system*). It has been recognized that there is a critical temperature range over which the mineral goes from completely open to being a completely closed system to argon loss during cooling, which is called the *closure temperature range* (after Dodson, 1973). The closure temperature is dependent on the activation energy for diffusion, the geometry and size of the diffusion domain and the cooling rate (see also Dodson, 1973; and McDougall and Harrison, 1988, for an extensive discussion). The basic equation used to quantify the closure temperature, T_c, is expressed by the formula (Dodson 1973);

$$T_c = (R)/(E\ (\ln A\tau D_o/a^2))$$

with R the gas constant, E the activation energy, A a numerical constant related to the geometry and decay constant, τ a time constant with which the diffusion coefficient, D, diminishes related to the cooling rate, and a a characteristic diffusion size. The basic equation shows that the closure temperature is mostly dependent on the activation energy, as the closure temperature is a linear function of the activation energy for diffusion relative to a dependence on the logarithm of the cooling rate and geometry of diffusion. The faster the cooling rate and/or the larger the effective radius for diffusion, the higher the closure temperature (see also Hames & Hodges, 1993; Hodges et al., 1994, and a recent discussion by Dunlap, 1998; and Lister, 1998). Many studies have been carried out to investigate diffusion domains and diffusion rates of Ar in different minerals (summarized in McDougall & Harrison, 1988, broadened in more recent articles on diffusion domains; Lovera, 1992, on hornblende; Baldwin et al., 1990, on alkali feldspars; Foster et al., 1990; Harrison et al., 1991, on white mica; Hames & Bowring, 1994). In addition to theoretical calculations of closure temperatures, estimates of closure temperature ranges have also been inferred from the pattern of age discordance in minerals from a single locality using different dating methods. Examples of natural experiments to obtain semi-quantitative values of closure temperatures are the calculation of the thermal effects on argon loss in a mineral due to heat conduction from an intrusion into the rocks of the contact aureole (Harrison & McDougall, 1980), and the interpolation of absolute age information with pressure-temperature information (e.g. by thermobarometry) of metamorphic mineral assemblages (von Blanckenburg et al., 1989). The generally accepted closure temperature ranges for the main K-bearing

K-bearing mineral	Closure Temperature	References
Hornblende	525 ± 25°C	e.g. Harrison, 1981
White mica	350 ± 30°C	figure 3.3
Biotite	300 ± 20°C	e.g. Harrison et al, 1985
K-feldspar	200 ± 50°C	Berger & York, 1981; Harrison & McDougall, 1982; Onstott et al, 1989

Table 3.1. Average argon closure temperatures of main K-bearing minerals (used in this study).

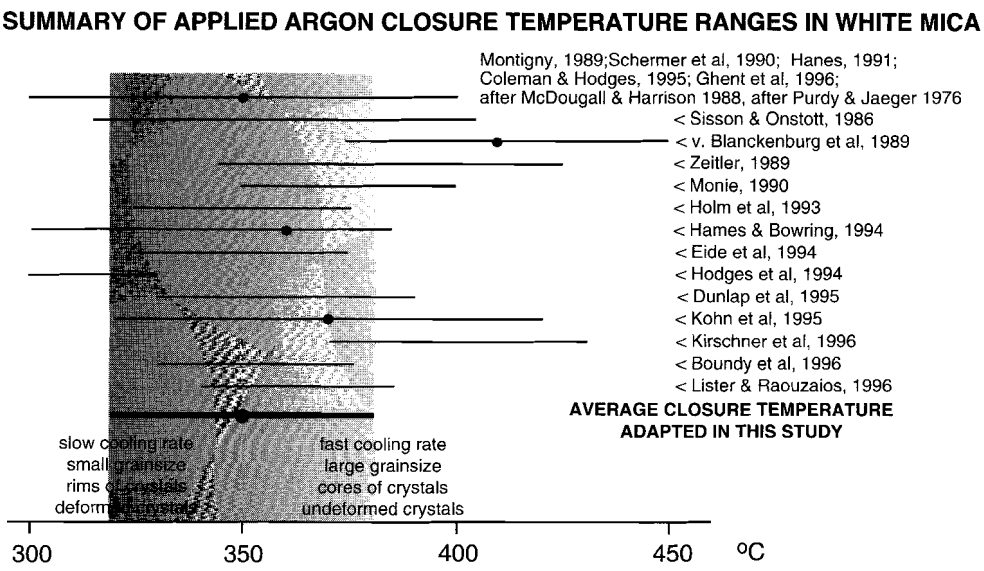

Figure 3.3. - Summary of closure temperature ranges of the argon isotopic system in white mica as used in recent publications on $^{40}Ar/^{39}Ar$ geochronology and average closure temperature range adapted in the present study: 350±30°C.

minerals are presented in table 3.1. As white mica is the K-bearing mineral, which is dominantly used in the present study, its published closure temperature ranges, derived from both interpolation of petrological information (e.g. von Blanckenburg et al., 1989) and experimental studies (e.g. Hames & Bowring, 1994), is presented in figure 3.3.

To establish meaningful interpretations of obtained absolute ages, studies which concern the geochronological evaluation of a multiply deformed and metamorphosed sequence should always investigate what dominant diffusion controlling mechanism has affected the selected mineral generations. The mechanisms are related to the ambient metamorphic temperature, cooling rate, deformation controlled recrystallization, and/or chemical alteration, and might operate synchronously. The results from the Pelagonian Zone show the regional preservation of Hercynian and Early Cretaceous cooling ages in protolith muscovites (see chapters 4 and 5 and Schermer et al., 1990). The preservation of the Hercynian isotopic signature suggests that thermally activated argon loss in white mica was slow or even absent in the protolith white mica generation, which was subjected to subsequent Alpine deformational events, and indicates that these events operated at ambient metamorphic temperatures below circa 350±30°C. The samples, which were selected from the tectonostratigraphic sequence of the Pelagonian Zone, have been affected by ambient metamorphic temperatures between circa 400 and 250°C for most of the Alpine history (Schermer et al., 1990). Consequently they have experienced low cooling rates during the Alpine history, which still might have caused some Ar loss from parts of the crystal where diffusion is relatively easy due to high argon gradients (e.g. at rims of crystals). The Ar loss caused by slow cooling might be evidenced by a typical "diffusion loss spectrum", which is characterized by

younger ages in the first steps of the age spectrum (see McDougall & Harrison, 1988 for further discussion). Further insights in the investigations on dominant diffusion controlling mechanisms related to deformation and chemical alteration will be further discussed below (section 3.4).

3.2.4 Crystal chemistry of white mica

The basic structural feature of the mica group is a composite sheet of two phyllosilicate layers of linked (Si, Al)O_4 tetrahedra, which sandwich layers of large alkali cations or Ca^{2+} ions (X-positions in figure 3.4). The two layers with sandwiched alkalis are linked by a plane of cations (octahedral sites, Y-positions in figure 3.4) and additional hydroxyl ions. In the case of pure muscovite, the central plane of cations consists fully of Al^{3+} ions, resulting in the chemical formula of $K_2Al_4[Si_6Al_2O_{20}](OH, F)_4$, which is based on the general formula $X_2Y_{4-6}[Z_8O_{20}](OH, F)_4$. The occurrence of respectively Na^+ or Ca^{2+} at the X-position results in a paragonitic or margaritic component in the muscovite. Metamorphic white mica can incorporate $(Mg\text{-}Fe)^{2+}Si^{4+}$ at the expense of 2 Al^{3+} (i.e. Mg^{2+} and Fe^{2+} from octahedral sites, and Si^{4+} from tetrahedral sites in expense of 1 octahedral Al^{3+} and 1 tetrahedral Al^{3+}), which changes the bulk composition to $K_2Al_3(Fe,Mg)[Si_7AlO_{20}](OH, F)_4$ and is the basic formula for phengitic white mica (Ernst, 1963).

Cation partitioning data for coexisting muscovite and biotite provide a useful crystal-chemical view on argon retention in these minerals, which has been extensively studied and summarized by Dahl (1996). Dahl's main observations suggest that the relative weaker/longer K-O bonds of biotite will be more easily stretched (during volume diffusion) or broken (during recrystallization) relative to muscovite. Firstly, the preferences of large alkali ions in biotite (e.g. Rb and Cs) and of small ions in muscovite (e.g. Li and Na) indicate a relatively spacious interlayer volume in biotite (the X-position in figure 3.4) at the site where radiogenic argon is produced. Secondly, the preferred occurrence of interlayer vacancies in biotite suggests that the two surrounding sheet-silicate layers are connected by fewer interlayer bonds, which might enhance argon diffusion pathways. An important conclusion of the study by Dahl (1996) is that interpretations of isotopic age information may be obtained irrespective of the dominant processes of isotopic loss in a metamorphic terrane (e.g. volume diffusion, recrystallization, chemical reaction, etc.). Additionally, the domi-

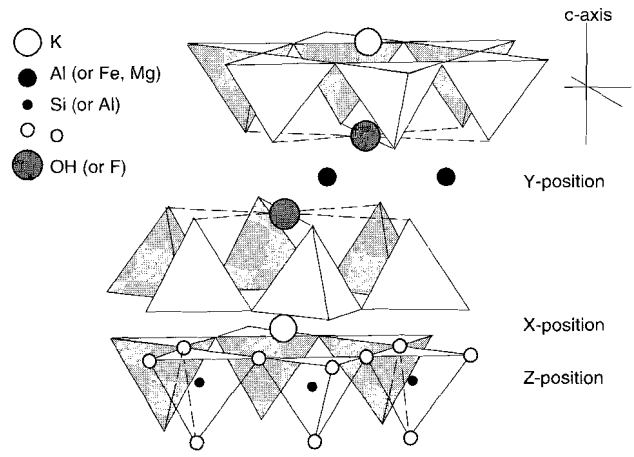

Figure 3.4. - Schematic presentation of the crystal structure of white mica (di-octahedral). Showing location of main cations in relation to the sheet-silicate orientation (modified after Dahl, 1996).

nant isotopic mass-transfer process may vary spatially and temporally within and among metamorphic terrains, and might result in a range of isotopic dates in a region which has experienced a single thermal history. Dunlap (1997) suggests that variations in ionic porosity (the interlayer bond strength of Dahl, 1996) might be an order of magnitude less important in controlling diffusion rates than some microstructural features. The microstructural features, like dislocation networks, kink boundaries or subgrains, limit lattice diffusion length scales or act as higher diffusivity pathways and are too large or too irregular to be defined in terms of the mineral lattice. It is suggested that the presence of these microstructural features will lower the total crystal strength of muscovite and shorten the effective diffusion radii of the crystals.

3.3 Absolute dating of deformational events and metamorphic episodes

Initial papers treating the general concept of closure temperatures and the dating of crystallization to reconstruct the tectonothermal evolution in metamorphic belts have been presented by Armstrong et al. (1966) and followed by Jäger (1973). In summary, $^{40}Ar/^{39}Ar$ dating in metamorphic terrains is most important in outlining domains, from local to regional scale, with distinctly different thermal histories and characterized by different P-T-t histories. The sensitivity of the $^{40}Ar/^{39}Ar$ system to thermal perturbations means that this system can be useful for estimating the age, temperature and duration of discrete metamorphic episodes. Knowledge of the closure temperature ranges of the different minerals, both during cooling (the classical closure temperature concept), and during heating (which might differ from the cooling related closure temperature), coupled with the extent of argon loss, allows an estimation of the combined time and temperature of the event. In theory, such calculations, however, should incorporate not only the closure temperature concept, but

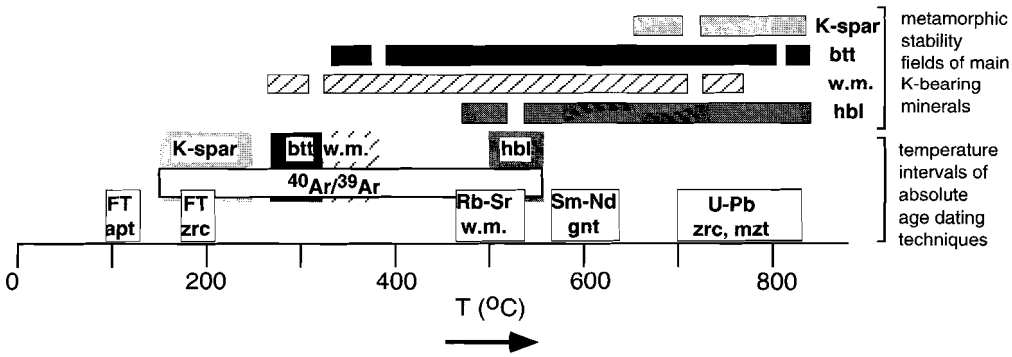

Figure 3.5. - Diagram showing the temperature intervals of the metamorphic stability fields of main K-bearing minerals (upper horizontal bars) and of the closure temperature ranges of $^{40}Ar/^{39}Ar$ technique compared to other isotope systems (lower intervals). FT= Fission track analysis, Mineral abbreviations: apt = apatite, zrc = zircon, K-spar = K-feldspar, btt = biotite, w.m. = white mica, hbl = hornblende, gnt = garnet, mzt = monazite.

also should remember that argon loss (or gain) can be affected by fluid interaction, chemical alteration, and/or deformation rather than simple heating or cooling. Most $^{40}Ar/^{39}Ar$ studies, which have been carried out to establish the thermotectonic evolution of metamorphic belts have dominantly used mineral cooling ages to deduce thermal histories of metamorphosed sequences. The correlation of mineral cooling ages to tectonic events can be deceitful as the ages obtained from this approach only reflect the timing of the closure of the analysed material to isotope diffusion. The argon systematics for the main K-bearing minerals and the temperature ranges of other applied isotope systems are presented in figure 3.5. The figure shows the metamorphic stability fields (vertical columns) and the argon closure temperature ranges (upper horizontal bars) of the main K-bearing minerals and indicates that there are two temperature intervals at which white mica and hornblende might have crystallized near or below their relevant closure temperature, below circa $350\pm30°C$ and $525\pm25°C$ respectively. These temperature intervals form potential windows to directly date crystallization events with the $^{40}Ar/^{39}Ar$ technique. Of the two minerals, white micas have been recognized to crystallize in low grade rocks well below their closure temperatures, and this mineral phase has been used in numerous studies to directly date tectonic events (see for example, Dunlap et al., 1991; West & Lux, 1993; Coleman & Hodges, 1995; Dallmeyer et al., 1995; Reddy et al., 1996).

3.4 The deformational control on argon distributions in white mica

3.4.1 Cooling ages versus crystallization ages

A natural experiment on white mica recrystallization has been studied by Dunlap et al. (1991) and Dunlap (1997). The authors conclude that recrystallization of white mica might occur below its argon closure temperature range. This means that direct dating can be carried out on the recrystallized white mica fabric which formed *during* ductile deformation, if recrystallization is syn-tectonic, or, *after*, if recrystallization is post tectonic. As the authors analysed bulk samples by furnace heating, which is often applied to larger sample quantities than laserprobe dating, they obtained age spectra from the low-grade deformed rocks, which are not completely flat or concordant. The irregular spectra most likely reflect outgassing of relic, partially recrystallized, white mica and show that fabric forming white mica separates are often contaminated by fragments of older white mica generations. The small volumes of individual fabric forming mica (e.g. with diameters of less than circa 50 μm) often obstruct the analysis of these individual grains, as the $^{40}Ar/^{39}Ar$ technique requires larger gas amounts to be analysed than present in a single crystal of the fine grained white mica.

Many authors (e.g. Scaillet et al., 1990; Hames & Hodges, 1993; Hames & Bowring, 1994; Hodges et al., 1994; Reddy et al., 1996) have concluded that dominant diffusion of argon in white mica occurs perpendicular to the C-axis (figure 3.4). Their research also shows that the effective diffusion dimension for argon in white mica is dominantly occurring at a similar scale as the physical grainsize. As diffusion pathways might divide the mica crystals into a domainal structure, it is evident that only perfectly developed crystals may have diffusion

dimensions equal to the physical grainsize, while other crystals might exhibit a domainal structure, in which the diffusion length scale is controlled by the superposition of preferred diffusion pathways and the physical grainsize (e.g. see Scaillet et al, 1992). The results of the research by Hames & Hodges (1993) shows that age zoning in white mica crystals is broadly parallel to the crystal faces but an age contour map contains valleys of ages that correspond with fast diffusion pathways. Some authors (e.g. Lister & Raouzaios, 1996) claim that Ar diffusion rates might be dominated by the very short pathway parallel to the C-axis. This was already hinted by Robbins (1972), albeit that the experimental data of Robbins (1972) carried too large uncertainties to discriminate between diffusion parallel or perpendicular to the C-axis (see also Dunlap, 1998, and Lister, 1998). Preferred diffusion pathways might be introduced in the crystal during deformation, or (incomplete) recrystallization at low grade metamorphic conditions. Subtle chemical variations would seem to be much less important in controlling argon diffusion, since recrystallized micas tend to exhibit limited chemical variation (e.g. Dunlap, 1997), although isotopic discordance occurring in HP metamorphosed metapelites (from the Dora-Maira Massif in the western Alps) has been suggested to be mainly controlled by the compositional re-equilibration of the HP phengites during greenschist overprinting (i.e. the effect of the transition from Mg phengite to Fe phengite on the Ar retention, discussed by Scaillet et al, 1992).

3.4.2 Microstructural and microchemical controls on (re-)crystallization

At low metamorphic temperatures, i.e. below the argon closure temperature range in white mica, deformation and fluid circulation can trigger *(neo-)crystallization* of micas, i.e. growth of newly formed metamorphic minerals. A detailed microstructural and microchemical study on recrystallized white mica has been carried out by Behrmann (1984), which differentiated three distinguishable white mica generations in the progressively deformed rocks of the Betic Cordilleras of SE Spain (figure 3.6). In the samples of the Pelagonian Zone (figure 3.7 and see chapters 4 and 5), which is quite similar in tectonic setting to the Betic Cordilleras in terms of metamorphic conditions and deformation, it is seen that the deformational control on white mica (re-)crystallization is similar to the study by Behrmann

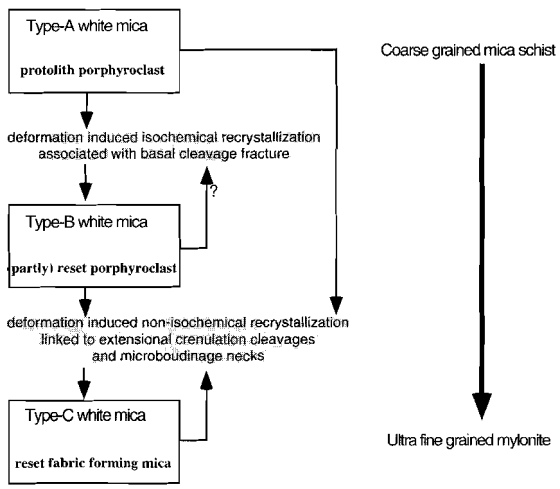

Figure 3.6. - Summary diagram of microstructural and microchemical processes during the recrystallization of white mica in mylonitic sequences of low metamorphic grade in the Betics, southeastern Spain, after Behrmann (1984). The figure illustrates the formation of several white mica generation during progressive deformation of a muscovite bearing protolith.

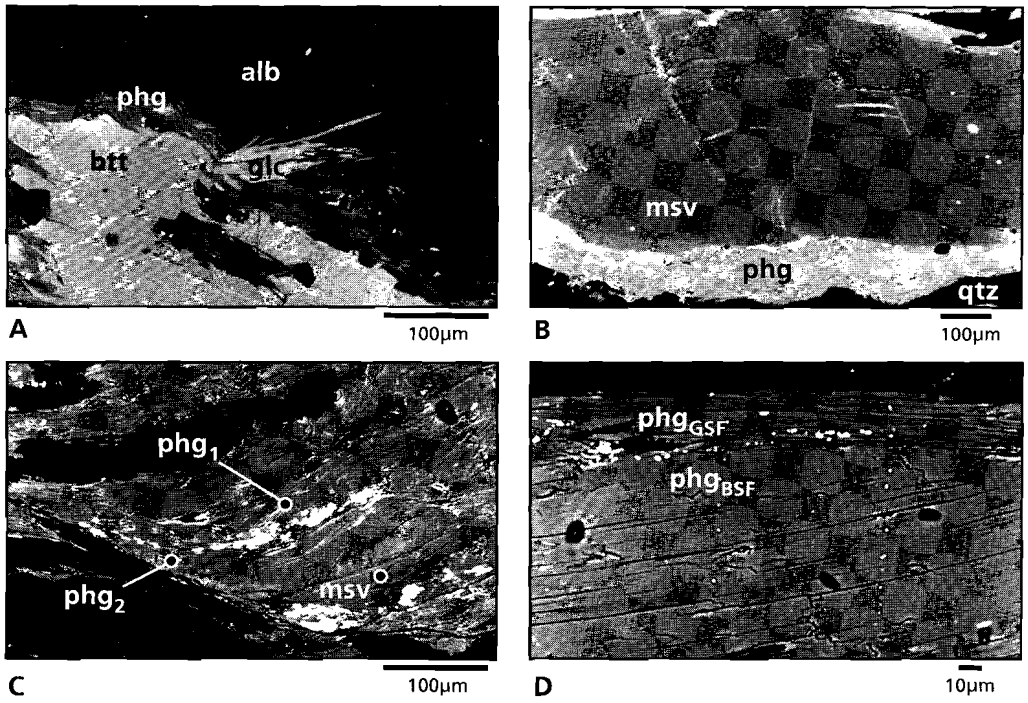

Figure 3.7. - Back scattered electron micrographs showing the dominant crystalization and recrystallization characteristics of white mica in samples from the Pelagonian Zone. *3.7a*: micrograph showing static recrystallization of phengitic white mica (phg), together with radial glaucophane (glc) under blueschist facies conditions in a metagranite at the interface of metastable biotite (btt) and plagioclase (alb) (Ossa Massif, Pelagonian Zone, sample 5; chapter 4). *3.7b*: micrograph showing preferred recrystallization of phengitic white mica (phg) around muscovite porphyroclast (msv) in a granite mylonite (West Volos, Pelagonian Zone, sample 7, chapter 5). Also note the deformation induced isochemical kink-formation within the mucovite porphyroclast. *3.7c*: micrograph showing passive rotation of relic muscovite grains (msv) and (re-) crystallized phengitic white mica (phg_1) in a mylonitic foliation crosscut by a phengitic white mica bearing shear band foliation (phg_2) in a granite mylonite (West Volos, Pelagonian Zone, sample 7, chapter 5). *3.7d*: micrograph showing syntectonic crystallization of phengitic white mica in greenschist facies mylonite foliation (phg_{GSF}), overprinting coarse phengites related to a blueschist facies mylonitic foliation (phg_{BSF}) (Ossa Massif, Pelagonian Zone, sample 4, chapter 4).

(1984; figure 3.6). As presented in figure 3.6, the final white mica population in a progressively deformed rock consists of muscovite porphyroclasts, occurring as deformed crystals and/or fragments, and newly formed white mica generations, which are subject to further deformation induced (re-)crystallization. The samples from the Pelagonian Zone show that (neo-)crystallization of white mica occurs *statically*, i.e. growth of mica in an assemblage which is unaffected by deformation (figure 3.7a), or *dynamically*, i.e. growth of white mica by grainsize reduction and neocrystallization during the deformation of existing white mica (figure 3.7b). It is evident that the formation of a white mica bearing mylonitic foliation is controlled by dynamic recrystallization. Under the given metamorphic conditions in the Pelagonian Zone, namely low grade blueschist and greenschist facies conditions, the devel-

opment of a mica mylonitic foliation is dominated by two main microstructural features; i) passive rotation of existing mica grains (figure 3.7c), and ii) syntectonic (re-)crystallization in association with oriented grain growth (figures 3.7b, c, and d). It is also commonly shown that destruction of white mica porphyroclasts is most efficient when quartz forms a high percentage of the sample. Mica rich layers might shield some micas from the deformation process by localizing the deformation, which gives rise to contamination of the recrystallized mica population with remnants of older mica generations (see also Dunlap, 1997). The above mentioned mechanisms may compete with each other during the development of a mylonitic foliation. The dominant mechanism will determine the presence (or absence) of a mineral fraction containing partially Ar reset white mica crystals. Only the mechanism which involves (neo-)crystallization, or complete argon loss by recrystallization (mechanism ii) will result in a mica population, exhibiting a $^{40}Ar/^{39}Ar$ fabric age, which is directly related to the deformational event.

3.4.3 Spot fusion analyses of multiply deformed samples

The combination of observed microstructures and $^{40}Ar/^{39}Ar$ laserprobe incremental heating experiments (IHE) and spot fusion experiments (SFE) can provide insights in the dominant mechanisms of white mica (re-)crystallization and of argon loss in the samples from the Pelagonian Zone. It is shown that for the Pelagonian samples the effect of argon loss on IHE results differs from sample to sample (chapters 4 and 5). After careful characterization and separation of different white mica generations, mixed phase spectra are obtained in cases of only partial succes or meaningful fabric ages may be obtained when separation was succesful (figure 3.8; see figures 3.7d and 4.5 for the microstructural relationships of samples 4 and 152). Not only the meaningful IHE results (upper spectra, samples 3 and 4) are confirmed by SFE results (upper right column in figure 3.8), but also the mixed phase spectra (lower spectra, sample 152) are confirmed by a similar distribution of SFE ages, albeit with almost unacceptably large analytical errors (in general, 40 to 90 Ma ages with 4 to 30 Ma, 2σ, analytical errors). Irrespective of the large analytical errors in SFE results from sample 152, the distribution of SFE ages in the sample and the IHE results of the two foliations show that the mixed phase spectrum is not the result of poor separation, but is the result of the presence of a partially recrystallized white mica generation in the mylonitic foliations,

Figure 3.8. - Illustration of different quality of incremental heating results on white mica generations in multiply deformed samples. Upper spectrum shows incremental heating experimental (IHE) results of two mica separates of a blueschist mylonite (sample 4, Ossa Massif, Pelagonian Zone), which contains a total of three characteristic white mica generations (also shown in right micrograph), muscovite prophyroclast (108 ± 3 Ma), blueschist facies mylonitic foliation forming white mica (85 ± 3 Ma), and a greenschist facies mylonitic foliation forming white mica, which was too fine grained in sample 4 and has been separated from a greenschist mylonite from a nearby location (sample 3; 45 ± 1 Ma). Right column of upper spectrum shows the spot fusion experimental (SFE) results, which confirm the ages of the three mica generations in sample 4. Lower spectrum shows IHE results of three mica separates of a blueschist mylonite (sample 152, Ossa Massif, Pelagonian Zone), which contains three characteristic white mica generations (presented in left photograph) muscovite porphyroclast in both mylonitic foliations (286 ± 7 Ma) and two blueschist mylonitic foliations which were first split by diamond sawing, subsequently separated, and resulted in mixed phase spectra.

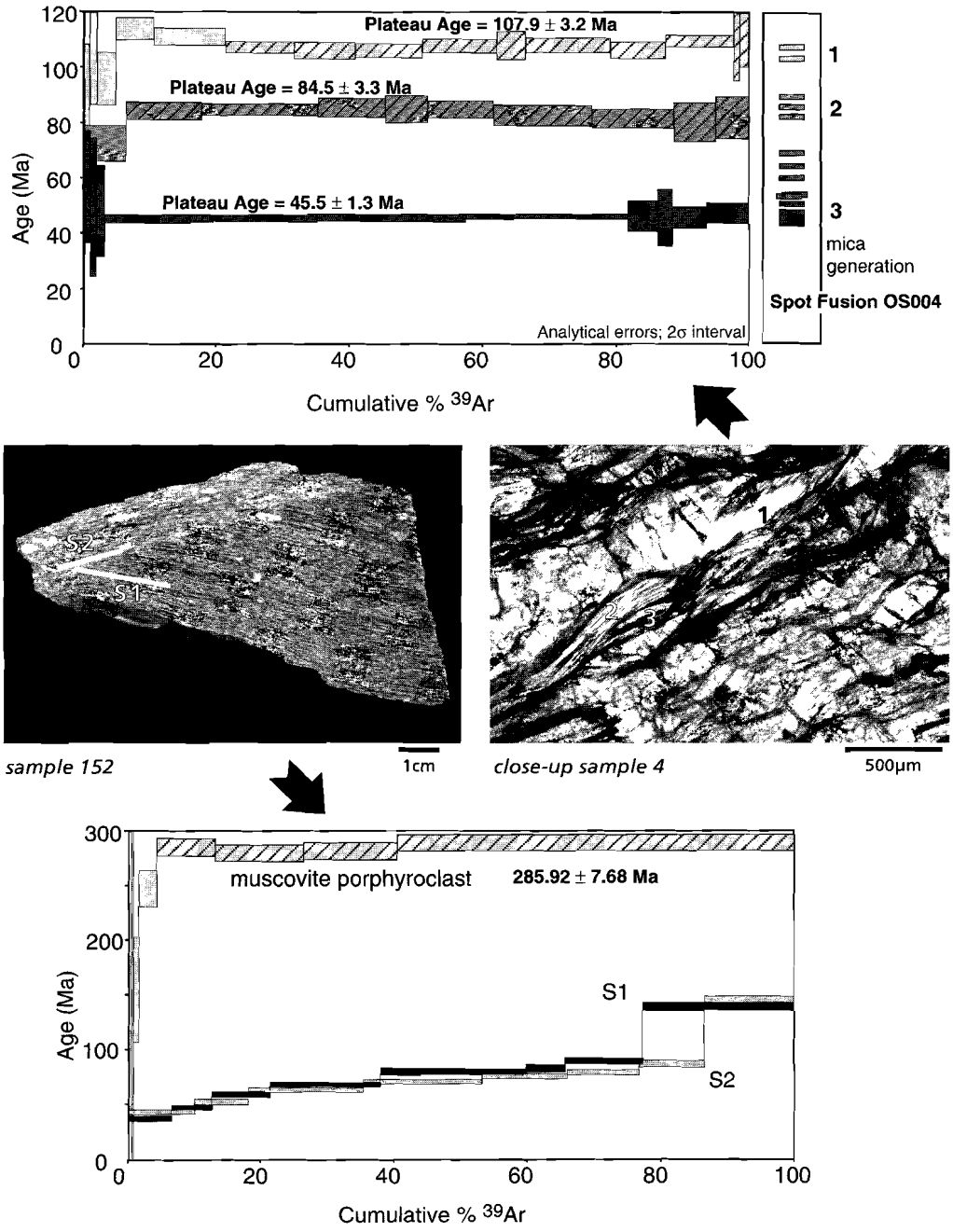
Plateau Age = 107.9 ± 3.2 Ma
Plateau Age = 84.5 ± 3.3 Ma
Plateau Age = 45.5 ± 1.3 Ma
Analytical errors; 2σ interval
Age (Ma)
Cumulative % 39Ar
1
2
3
mica generation
Spot Fusion OS004
S2
S1
sample 152
1cm
close-up sample 4
500μm
muscovite porphyroclast
285.92 ± 7.68 Ma
S1
S2
Age (Ma)
Cumulative % 39Ar

or, alternatively, the mylonitic micas have been affected by chemical alteration or re-equilibration which caused *incomplete resetting* of the argon signature. It can be concluded from sample 152 that the partial recrystallization of the mylonitic mica generation, which also forms S_1, might have been caused by the low angle at which the two mylonitic foliations crosscut each other (figure 3.11). To further investigate the degree of deformation in relation to the orientation of the overprinting foliation, additional SFE were carried out on a crenulated blueschist foliation, with the newly formed foliation being perpendicular to the relic foliation (sample 151). $^{40}Ar/^{39}Ar$ laserprobe experiments on this sample (sample 151,

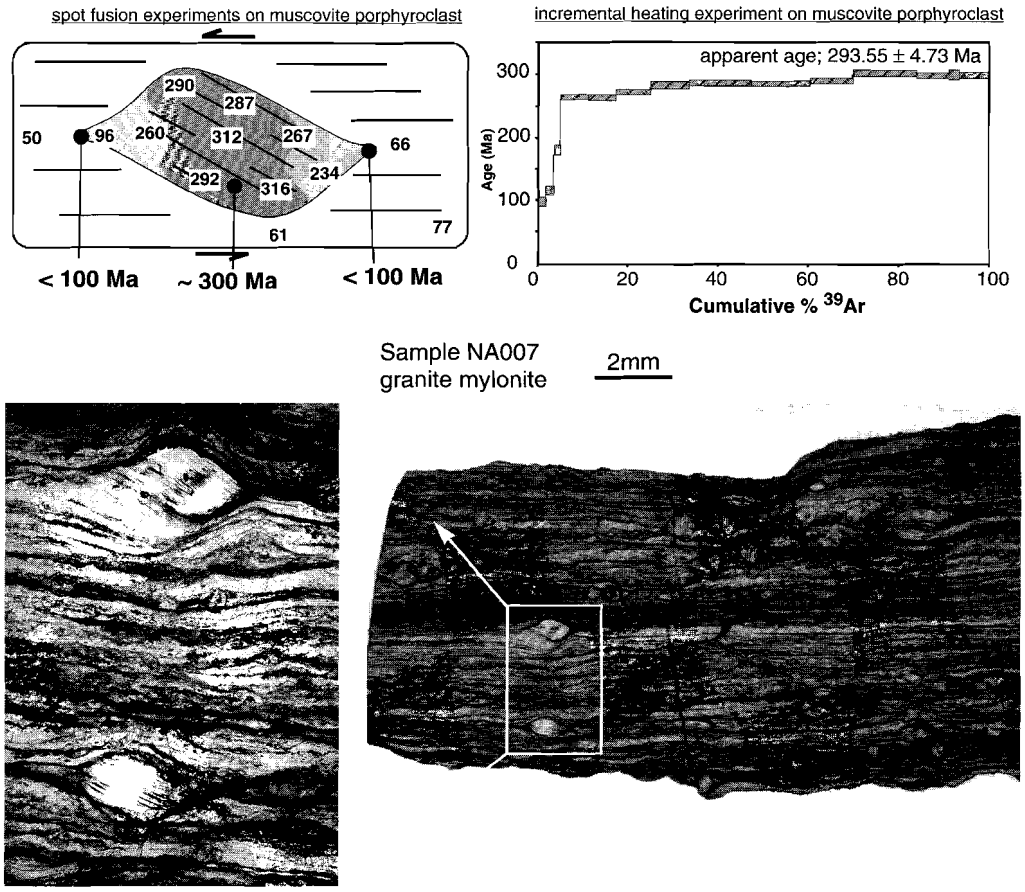

Figure 3.9. - Overview of geochronological data of sample 7 (West Volos, Pelagonian Zone). Bottom figures show micrograph of thick section of sample 7, used for spot fusion dating (right micrograph), and close-up of muscovite porphyroclasts (average diameter is circa 600 µm) in sample 7 which were analysed by spot fusion experiments (SFE) and incremental heating experiments (IHE) (left micrograph). Upper figures show incremental heating experimental (IHE) results from the muscovite porphyroclast in sample 7, with an apparent age of circa 294 Ma (right diagram) and simplified spatial distribution of spot fusion ages within the porphyroclasts (summarized in left diagram).

see chapter 4, and figure 3.11), have resulted in two undifferentiated sets of SFE ages for the two distinct foliations, albeit that the two undifferentiated sets of fabrics ages for sample 151 are partly obscured by very high analytical errors, due to analysis of very small gas fractions (i.e. relic S_1: 50 to 65 Ma fabric ages with 9 to 40 Ma, 2σ, analytical errors, S_2: 46 to 66 Ma fabric ages with 1 to 4 Ma, 2σ, analytical errors). In summary, the results show that metamorphosed samples with clear relative age relationships, indicated by overprinting foliations, might contain white mica generations which exhibit a partially reset Ar isotopic system. In such a case, IHE on mica separates and SFE in thick sections cannot resolve the timing of recrystallization as the fine grain size and, thus, a small Ar quantity introduces unacceptably large analytical errors.

In contrast to the poor isotopic distinction between the overprinting foliations, the effect of very high strains (and related recrystallization) shows some remarkable results. Figure 3.9b shows IHE results from muscovite porphyroclasts from the W-Volos granite mylonite (sample 7, also presented in figures 3.7b and 3.7c and discussed in chapter 5), with an apparent age of 293.5 ± 4.7 Ma and significant low ages at low temperature steps. Additional spot fusion experiments on this sample (white circles in lower diagram of figure 3.9b show laserprobe spot locations) illustrate domains of partially reset argon signatures. The gradually younger ages towards the tails of the Hercynian muscovite porphyroclasts can be explained by either preferred re-crystallization at the tails of the muscovite or chemical alteration due to fluid infiltration in the deformed tails. The youngest ages in the tails of the muscovite clast are similar to those from the mylonitic foliation, which is chemically different from the muscovite with circa 60 to 80 Ma SFE ages (high analytical errors).

An example which illustrates the preservation of older white mica fabric ages in young white mica bearing deformational structures comes from the Neohori (Pelion) granite mylonite, where white mica separates have yielded circa 95 to 100 Ma muscovite porphyroclast cooling ages and circa 54 and 39 Ma fabric ages (figure 3.10 and chapter 5, samples 140, 141 and 142). Detailed structural investigations in the outcrop and in thin section have shown that the two fabric ages are related to two distinct kinematic settings, the circa 54 Ma fabric related to top-to-NE tectonic transport, and the circa 39 Ma fabric related to top-to-SW tectonic transport. The partial preservation of the 54 Ma fabric in the 39 Ma mylonitic structure is confirmed by SFE on sample 141 (right column and diagram in figure 3.10). The SFE results show the presence of circa 54 and younger ages in the relic foliation and the presence of circa 39 Ma and younger ages in the shear band foliation related to top-to-SW tectonic transport (C'-type shear band cleavage of Passchier & Trouw, 1996). The results characterize the overprint of a 54 Ma top-to-NE mylonitic foliation and associated asymmetric microstructures by 39 Ma white mica bearing structures which evidence opposite kinematics. Although shear band foliations are usually interpreted to have formed at a relatively later stage but still during the same kinematic event as the dominant mylonitic foliation (see also White et al., 1980; Lister & Snoke, 1984; Passchier & Trouw, 1996; for discussion) the recognition of a 15 m.y. time lag between formation of the top-to-NE mylonitic foliation and associated microstructures and the top-to SW shear band foliation within a single mylonitic interval illustrates that these structures are not always related to the same kinematic event.

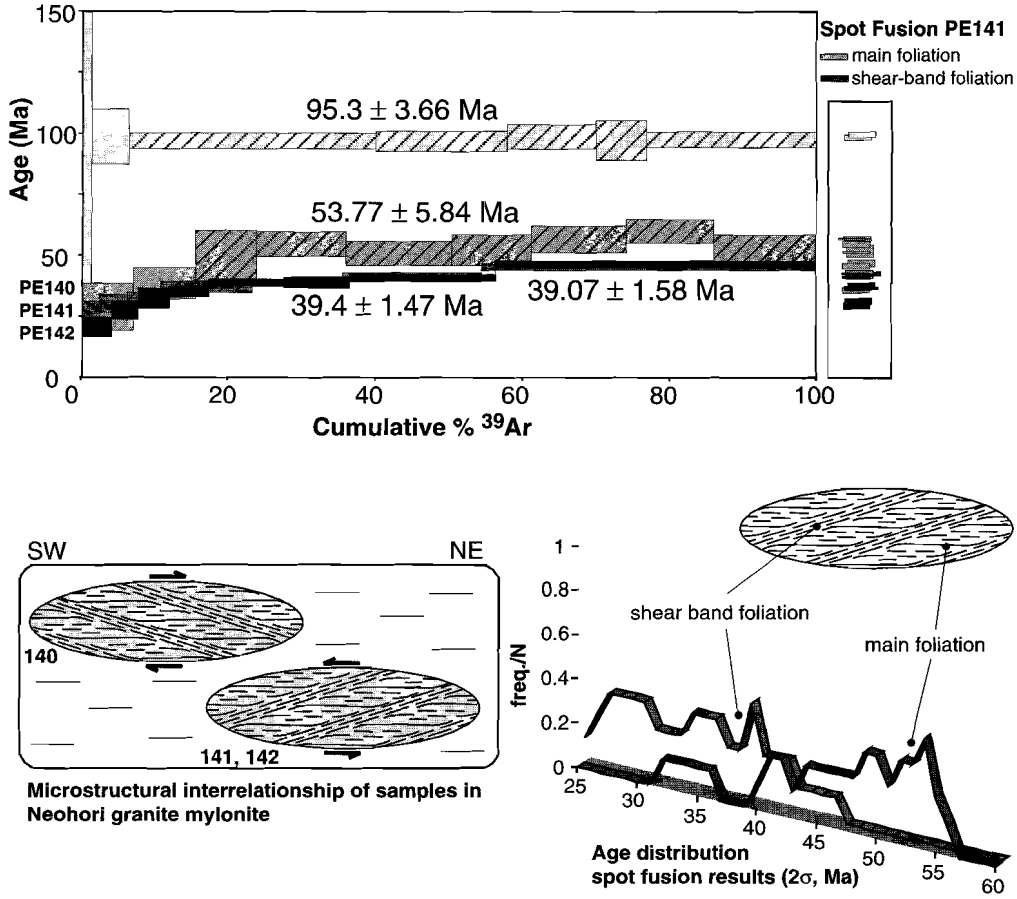

Figure 3.10. - Summary of combined geochronology and (micro-) structural data from samples 140, 141 and 142 (Neohori, Pelion, Pelagonian Zone). Upper spetrum shows Incremental heating experimental (IHE) results from muscovite porphyroclast (95 ± 4 Ma) and from greenschist mylonitic foliation forming micas of the different samples from the same mylonitic interval. Column right of IHE spectrum presents spot fusion (SFE) results of sample 141 (light grey; mylonitic foliation, dark grey; shear band foliation). Bottom diagrams present schematic structural interrelationship (left diagram), and frequency plot of SFE results from sample 141, related to the analysed microstructural fabric (right diagram).

In summary, the SFE results, and their relation to IHE results, can provide an imporant contribution to the microstructural analysis of deformed rocks and allow an investigation of the control of deformation on argon loss in white mica. The SFE results are obscured, partly, by extremely high analytical errors, which are related to the small crystal size (and thus low bulk Ar gas quantities) in combination with the characteristics of the applied laser system, the laser spot size, and the thickness of the section used for SFE (see also appendix 1.3 and 1.4). Other studies which applied SFE to deformed micas required either circa 60-250

μm spot sizes, in 100/200 μm thick sections (Scaillet et al., 1992), using an argon lasersystem (quite similar to the VULKAAN laserprobe used in this study), or, alternatively, probably smaller (perhaps circa 50 μm) diameter spot size, in 200 μm thick sections (Reddy et al., 1996), using a pulsed UV laser. Currently the available laserprobe and mass spectrometric set-up do not allow single crystals of very fine grained white mica fabrics (i.e. circa 10-20 μm) to be analysed with acceptable analytical errors (within circa 1%). Thus experiments need to be carried out on larger amounts of white mica of such diameters. Because of this, analysis of a mixed generation white mica population cannot always be avoided. The results also show that high strains and related dynamic recrystallization appear to be required to reset the argon isotopic signatures in recrystallized fabrics. The above investigations have shown that multiply deformed samples which were metamorphosed at relatively low ambi-

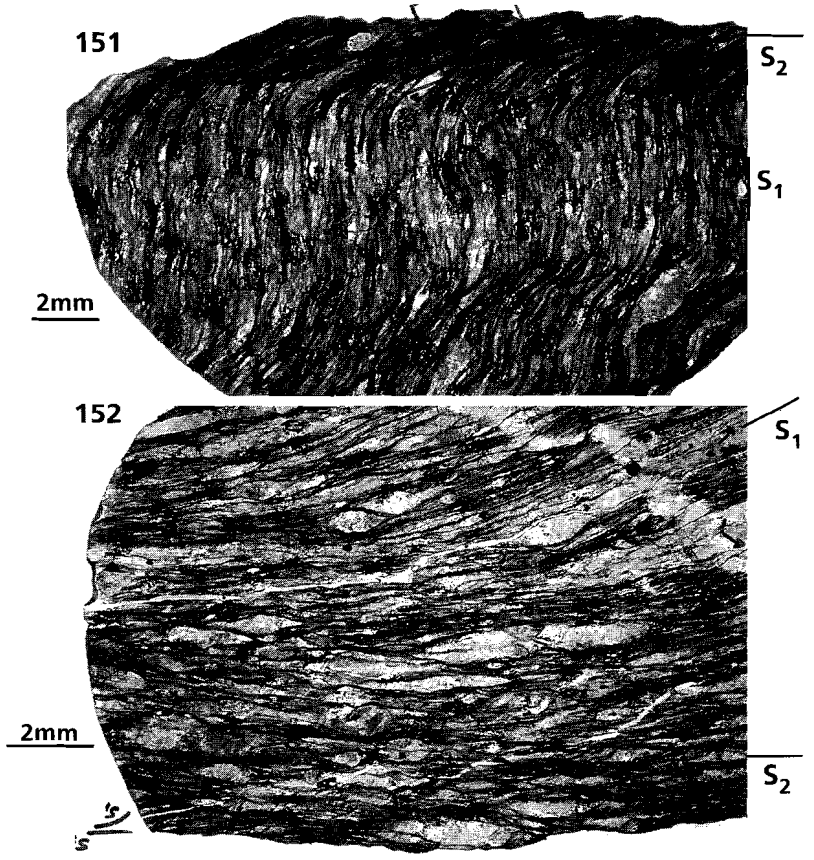

Figure 3.11. - Micrographs of 100 μm thick sections of samples 151 and 152 (Ossa Massif, Pelagonian Zone), which were used for spot fusion experiments. The micrographs illustrate the difference in microstructural orientation of overprinting foliation generations, which are at an angle of circa 90 degrees and circa 30 degrees for sample 151 and 152 respectively.

ent temperatures not only can provide relevant white mica cooling ages from protolith micas and white mica fabric ages related to the dominant mylonitic fabric, but also might provide relic white mica fabric ages, if the white mica generation related to the older fabric has not recrystallized. The relic fabric forming white mica may cause the analysis of white mica mixed ages due to their presence as a partially recrystallized or re-equilibrated mica generation in the analysed white mica population.

3.5 Conclusions

In the Aegean region, basement rocks are exposed which have been metamorphosed and deformed under blueschist to eclogite facies and subsequent retrograde conditions. White mica may have a primary magmatic origin in granitic rocks (muscovite composition). White mica is stable and may (re-)crystallize at almost any point on the metamorphic PT loop (phengite composition). If the rocks remain below the relevant closure temperature range in white mica (ca 350 ± 30°C), they provide the potential to directly date the events during which the white mica formed. Theoretically, $^{40}Ar/^{39}Ar$ laserprobe dating experiments can be applied to different white mica generations in the basement sequences in the Aegean region and can be used to establish; i) the cooling history of pre-Alpine protoliths, ii) the timing and duration of Alpine metamorphic episodes (as long as corresponding metamorphic temperatures failed to reset argon isotopic signatures in white mica), iii) the timing of tectonic events which are related to the initiation and/or termination of metamorphic episodes, and iv) the duration of these events with respect to the overall tectonic history of the Aegean region.

It is shown that, depending on the degree of recrystallization, the combination of incremental heating experiments (IHE) and spot fusion experiments (SFE) can resolve the timing of different tectonic events and metamorphic episodes of regional importance down to a circa 2-5 m.y. interval. The SFE experiments on multiply deformed samples illustrate various degrees of resetting during deformation at various metamorphic conditions. The results show that white mica fabric ages are not always present as completely preserved fabric ages which are related to the dominant fabric, but can also be present as partially overprinted fabric ages without any geological temporal significance or even as preserved fabric ages from relic deformational fabrics which have not been reset by later deformational processes (e.g. due to strain partitioning during younger events).

Chapter 4

$^{40}Ar/^{39}Ar$ laserprobe direct dating of discrete deformational events in the Ossa Massif: a continuous record of Early Alpine tectonics in the NW Aegean

Accepted for publication in Tectonophysics special issue, edited by A.H.F. Robertson, as: Lips, A.L.W., S.H. White and J.R. Wijbrans: $^{40}Ar/^{39}Ar$ laserprobe direct dating of discrete deformational events: a continuous record of Early Alpine tectonics in the Pelagonian Zone, NW Aegean area, Greece.

4.1 Abstract

The Pelagonian Zone of the Hellenides, which occurs in the north-western Aegean region of the Eastern Mediterranean, contains remnants of a high pressure metamorphic belt which subsequently underwent localized reworking during low temperature deformational events. Formation of Alpine deformational structures in the Ossa Massif (northern Pelagonian Zone) occurred at metamorphic temperatures which failed to reset most pre-Alpine $^{40}Ar/^{39}Ar$ cooling ages in muscovite porphyroclasts. The low metamorphic temperatures at Alpine times have preserved the argon isotopic signature in white mica bearing deformational structures, which allows direct dating of these structures and refinement of the Alpine tectonic history in the region. After separation of the carefully selected and characterized mica generations, application of sensitive $^{40}Ar/^{39}Ar$ laserprobe dating has resulted in a continuous record of the Alpine tectonic history of the Ossa Massif from the Early Cretaceous well into the Eocene.

The Early Alpine history of the Ossa Massif records cooling of basement thrust slices, which are mostly Hercynian granites and metamorphics, below circa 350°C by 100 Ma, while lower tectonostratigraphic levels of the basement had already cooled below these temperatures at around circa 285 Ma. Blueschist facies mylonite fabrics, related to a top-to-ENE direction of tectonic transport, yield ages as old as 84.5 ± 3.3 Ma. Exhumation of the blueschist facies sequences was initiated at circa 54 Ma and involved tectonic activity along blueschist facies and greenschist facies mylonites zones. Final WSW-ward transport of the

metamorphic sequence across the structurally lowest, and supposed, autochthonous, series occurred at around 45 Ma, and resulted in termination of the ductile deformation history in the studied area.
This study confines the onset of high pressure metamorphism in the Pelagonian Zone to an interval between 100 Ma and 85 Ma and has shown that high pressure metamorphism had terminated by circa 54 Ma. The recognition of an Early to Middle Alpine cycle, lasting over 30 million years and involving crustal shortening, high pressure metamorphism, exhumation and subsequent crustal shortening is a key contribution to a better understanding of the Early Alpine tectonic history of the Aegean region and eastern Mediterranean.

4.2 Introduction

In most past geochronological studies of the Alpine Belt, absolute age data have not been directly related to tectonic events or tectonic episodes but have been obtained from episodes of cooling of the metamorphic sequence (e.g. Betics, Monié et al., 1991; Alps, references in Hunziker et al., 1992; Aegean region, references in Lips et al., 1998b, chapter 5). Problems which arise from this approach are that i) cooling of a metamorphic sequence is not an instantaneous process and ii) closure temperatures of isotope systems cover ranges of temperatures rather than fixed values. The absolute ages which have been obtained by the metamorphic studies have often been assigned to tectonic events, but actually reflect the response of the metamorphic sequence to a tectonic event, rather than the timing of the event itself. The result is that tectonic events dated by this approach are poorly constrained although the quoted age may be of high precision. An example of such an application of cooling ages to deduce tectonic events in the Mediterranean comes from the Aegean region (Gautier & Brun, 1994; Vandenberg & Lister, 1996; Avigad et al., 1997). In this region, Middle Eocene cooling ages (ca 40-45 Ma) derived from white mica crystals have been generally interpreted as the age of high pressure metamorphism (peak PT around 1.6 Gpa and 450-500°C), yet these Eocene ages in fact only reflect the time interval when metamorphic temperatures dropped below the argon closure temperature range in white mica (i.e. circa 350±30°C; see chapter 3 and also McDougall & Harrison, 1988; von Blanckenburg et al., 1989; Kohn et al., 1995).
Further refinement of the age ranges that are proposed for the main metamorphic episodes and deformational events is required to constrain the exact timing of the kinematic evolution of metamorphic rocks throughout the Mediterranean. Absolute age dating of deformational events in metamorphic rocks is possible when the minerals, selected for absolute age dating have (re-)crystallized at temperatures below their relevant closure temperature range of the used isotopic system. In this study $^{40}Ar/^{39}Ar$ laserprobe age dating experiments have been applied to white mica bearing fabrics in blueschist facies rocks because i) the high sensitivity and low blank characteristics of the laserprobe technique allows small sample fractions or single crystals to be analysed (Wijbrans et al., 1990), ii) white mica may crystallize in deformation fabrics below its argon closure temperature (Dunlap et al., 1991; Dunlap, 1997), iii) the degree of deformation of white mica is an important factor in the resetting of

the argon isotopic system (Costa & Maluski, 1988; Monié, 1990; Scaillet et al., 1990; West & Lux 1993; Kirschner et al. 1996), and iv) metamorphic temperatures in blueschist facies rocks tend to fall around the argon closure temperature in white mica.
Blueschist facies rocks are reported throughout the Alpine Belt in the Mediterranean region (Betic Cordilleras, Calabria, Corsica, Western and Central Alps, and in the Aegean region; in mainland Greece, Cyclades and Crete). In the Aegean region the early Alpine tectonic history is still poorly constrained. In this paper, results of the combined (micro-) structural,

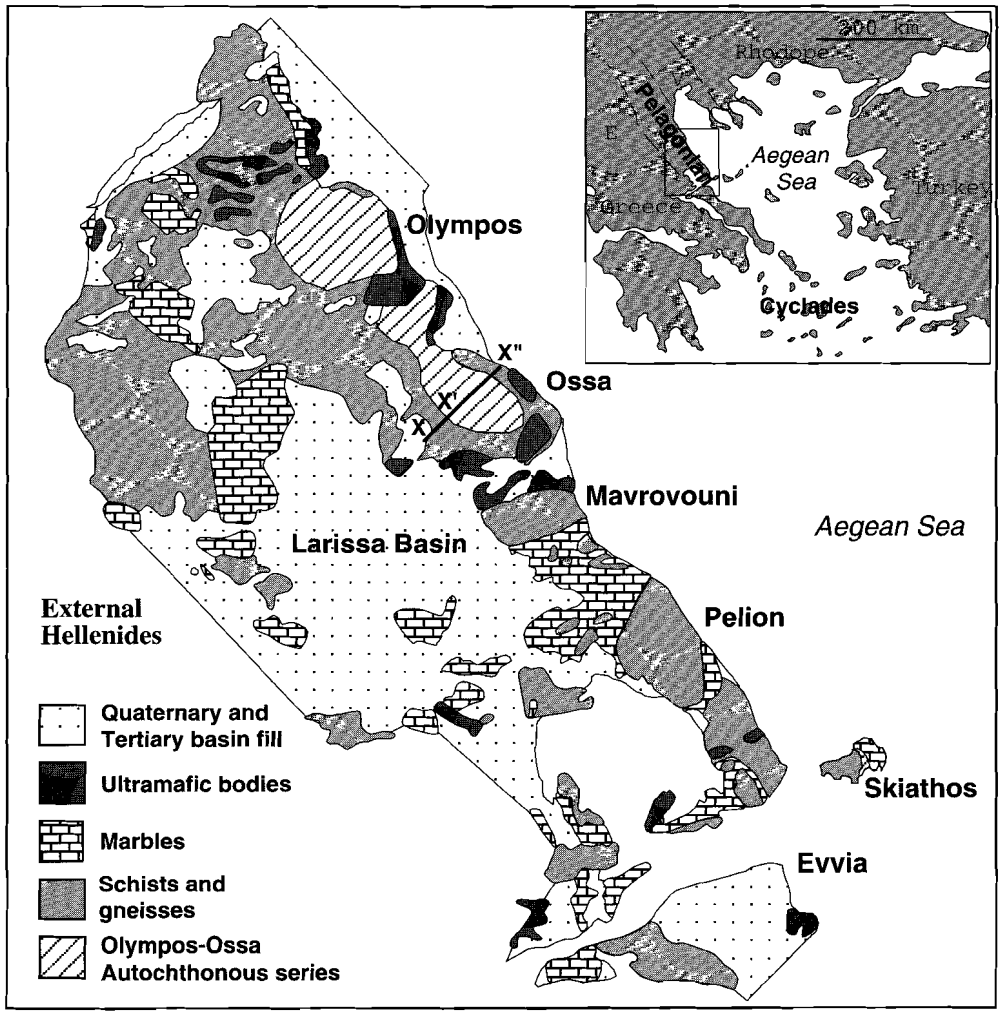

Figure 4.1. - Location of the Pelagonian Zone in the Aegean region (inset) and schematic distribution of lithologies in the Pelagonian Zone (after IGME, 1983). (In inset: E = External Hellenides, V = Vardar Zone). Section X-X'-X" through Ossa Massif is presented in figure 4.2.

petrological studies and $^{40}Ar/^{39}Ar$ laserprobe analyses are presented for the tectonic sequence of the Ossa Massif in the Pelagonian Zone of mainland Greece. The Ossa Massif which is located in the Pelagonian Zone of the Internal Hellenides (figure 4.1) is situated immediately south of the Olympos Massif (Schermer, 1990, 1993; Schermer et al., 1990). A limited, reconnaisance level, study of the Ossa Massif formed part of Schermers work (Schermer et al., 1990). In our study, the Ossa Massif was selected because of the occurrence of blueschist facies assemblages, which appear to have escaped the well-documented Early Miocene phase of regional deformation under greenschist facies conditions, as reported for the Aegean region (Gautier & Brun, 1994), because the metamorphic sequence in the Olympos-Ossa region was already at brittle crustal levels around mid-Alpine times (Schermer et al., 1990; Schermer, 1993). The escape from the Early Miocene phase of greenschist facies deformation suggests that blueschist facies fabrics might be better preserved in the Ossa Massif. The good preservation of the blueschist facies assemblages and the indication that the rocks have been subjected to metamorphic temperatures around, and below, the argon closure temperature in white mica might provide a window into the early Alpine tectonic history.

4.3 Characterization of the geological setting

The Pelagonian Zone (figure 4.1) is the westernmost zone of the Internal Hellenides. It separates the basin fill of the Meso-Hellenic Trench together with the unmetamorphosed rocks of the External Hellenides in the west, from the weakly metamorphosed rocks in the Vardar Zone, and the greenschist to granulite facies rocks of the Rhodope Zone in the east. The Pelagonian Zone extends south into the Cyclades and both are characterized by the occurrence of blueschist facies rocks, with higher peak metamorphic conditions in the latter area.

The tectonostratigraphic sequence of the Pelagonian Zone is characterized by a weakly metamorphosed sequence overlain by an allochthonous basement sequence. The weakly metamorphosed sequence, which is exposed in the tectonic windows of the Olympos and Ossa Massifs (figure 4.1), is at the deepest observed tectonostratigraphic level and is characterized by platform carbonates, overlain by phyllites, thought to resemble Middle Eocene (~ 45-50 Ma) flysch (Godfriaux, 1968). In most structural studies of the region (Barton, 1976; Nance, 1981; Schermer, 1993) the platform carbonates and phyllites are regarded as an autochthonous sequence, although they may be underlain by a thrust fault which caused ramping of the whole sequence (Schermer, 1993). In this paper the weakly metamorphosed sequence in the Ossa and Olympos Massifs will be further referred to as the autochthonous series. The allochthonous sequence consists of felsic basement rocks, including Hercynian granites and gneisses, marbles and ultramafics, and has been affected by blueschist and greenschist facies metamorphism (Schermer, 1990, 1993). A tectonostratigraphic subdivision of the allochthonous basement sequence has been erected by Schermer et al. (1990) for the Olympos Massif and is also in general applicable to the Ossa Massif. The Ambelakia Unit, which has been used by Schermer et al. (1990) and Schermer (1993) and which occurs at

the interface of the autochthonous series and the overlying allochthonous basement, is named after the village of Ambelakia at the northern margin of the Ossa Massif. In the current study, individual mylonite zones have been studied which occur in the Ambelakia and Infrapierien Units (after Schmitt 1983) of Schermer et al. (1990).

4.4 Previous geochronology and thermotectonic studies

There have been several geochronological studies of the Pelagonian Zone in the past 25 years. These include K-Ar (Hynes et al., 1972; Borsi and Ferrara in Mercier, 1973), Rb-Sr (Barton, 1976; Yarwood & Dixon, 1977), U-Pb (Yarwood & Aftalion, 1976) and $^{40}Ar/^{39}Ar$ absolute age dating experiments (Schermer et al., 1990). A compilation of the results of these studies is presented in table 4.1.

In an extensive geochronological and structural study of the Olympos Massif Schermer (1990, 1993) and Schermer et al. (1990) document the successive deformation events which change from ductile conditions in the early stages of deformation, to lower temperature semi-ductile and finally to brittle conditions in the later stages of deformation. Schermer (1993) has distinguished seven deformation stages; D1-D4 have been related to phases of crustal shortening which resulted in thrust faulting and folding at blueschist facies conditions, whereas D5-D7 have been related to phases of crustal extension which resulted in unroofing of the blueschist facies rocks.

Schermer et al. (1990) used relatively large sample fractions (ca 100 mg) for conventional $^{40}Ar/^{39}Ar$ age dating experiments which often resulted in staircase pattern spectra due to outgassing of multiple generation white mica populations. By correlating upper and lower age limits from mixed phase spectra, Schermer (op cit) interpreted D1 as being Lower Cretaceous in age (98-100 Ma). She suggests that D2 and D3 might be related to a broadly continuous period of deformation and concludes that D2 and D3 have occurred between 61 and 36 Ma, while final uplift during and after D5 was constrained by $^{40}Ar/^{39}Ar$ K-

Age	Event	*Reference*
302 to 293 Ma	Crystallization of granites.	*1, 2*
125 to 98 Ma	Upper greenschist facies to blueschist facies metamorphism,mylonitization in the allochthonous sequence and imbrication of thrust sheets.	*2, 3, 4*
61 to 53 Ma	blueschist facies metamorphism and thrusting.	*2*
40 to 36 Ma	greenschist facies metamorphism and thrusting.	*2, 3*
23 to 16 Ma	uplift and cooling below 150°C.	*2*

Table 4.1. Summary of thermotectonic events in the Pelagonian Zone (references: *1* Yarwood and Aftalion, 1976; *2* Schermer et al, 1990; *3* Barton, 1976; *4* Yarwood and Dixon, 1977).

feldspar dating to be in the interval from 23 to 16 Ma. The results of Schermer et al. (1990) will be used in conjunction with the $^{40}Ar/^{39}Ar$ laserprobe results of the present study to summarize the regional thermotectonic setting.

4.5 Structural setting of the studied area

To establish and date the tectonic history, samples were carefully selected from the kinematically and microstructurally characterized tectonites of the Ossa Massif in the Pelagonian Zone (figures 4.1 and 4.2). A brief description of each sample together with relevant structural data is given in table 4.2. As mentioned in the previous section, the tectonic setting of the Ossa Massif is comparable to the Olympos Massif (Schermer, 1993) on a regional scale, although local differences have been observed.
A section through the lower structural levels of the allochthonous basement sequence is well exposed on the west flank of the Ossa massif (Sikourio-Spilia road) and has been investigated in detail (scale 1:5000; see figure 4.1 for section location). The section (X-X'-X", figure 4.2b) shows the spatial distribution of blueschist facies structures at the basal part of the allochthonous sequence which comprises an intensely mylonitized interval (Ambelakia unit of Schermer, 1993). The mylonitized interval has a present thickness of circa 2 km and shows a well developed blueschist mylonitic foliation accompanied by a glaucophane mineral lineation (azimuth to circa 200°-260°, figure 4.2) and in many cases by an albite / quartz stretching lineation which is parallel to the glaucophane mineral lineation (figures 4.5a, 4.5b and 4.7). The blueschist facies mylonites show evidence for reactivation under retrograde conditions, during which strain has partitioned into bands of greenschist facies mylonites which wrap around domains of the blueschist facies mylonites. This has resulted in the presence of high strain greenschist facies mylonites which are in narrower zones than the blueschist mylonites, and which become more abundant towards the base of the allochthonous sequence (figure 4.2c). Discrete mylonite zones (1 cm to 10 cm wide) have been observed which crosscut the dominant mylonitic fabric (e.g. figure 4.5c). The discrete zones show blueschist facies or greenschist facies mylonitic foliations, both of which are accompanied by a well defined quartz-albite stretching lineation (figure 4.2c, 2d). Directions of tectonic transport within mylonites, both from the overall mylonitic interval and from the discrete mylonite zones, discussed above, have been derived from asymmetric structures such as shear-bands and asymmetric clasts, both in outcrop and in thin-section (see also White et al., 1980; Lister & Snoke, 1984; Passchier & Trouw, 1996; for discussion of the method). All directions of tectonic transport which are presented in this study are presented in their present-day observed orientation. It was found that the blueschist facies kinematic indicators in different levels of the mylonitized zone give an ambiguous direction of tectonic transport but which appears nevertheless to be dominantly a top-to-ENE direction of tectonic transport. The top-to-ENE direction of tectonic transport is overprinted by a consistent top-to-WSW direction of tectonic transport in retrograde blueschist and greenschist facies mylonites (figure 4.2c). A systematic variation with structural height in the direction of tectonic transport is not apparent in stereographic projections (figure 4.2d) but

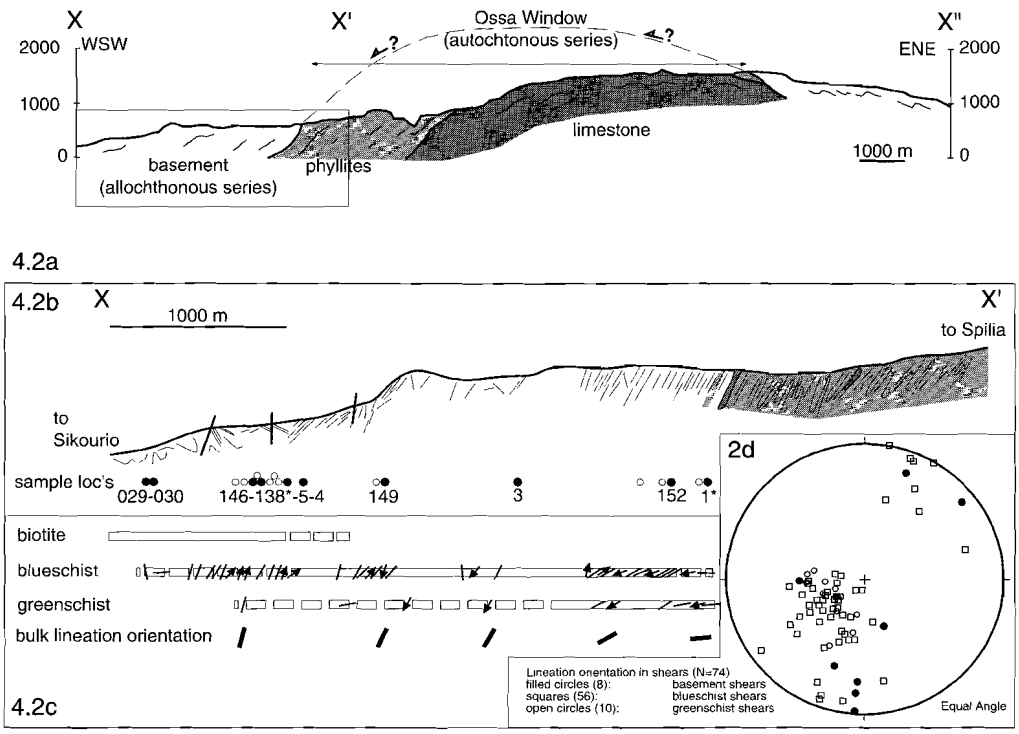

Figure 4.2. - 4.2a. Schematic WSW-ENE cross section through the Ossa Massif, indicating tectonostratigraphic distribution of allochthonous basement series and relative autochthonous series (the Ossa Window) of platform carbonates overlain by phyllites. *4.2b.* Detailed cross section of the area boxed in figure 4.2a through the basement rocks on the western flank of the Massif showing locations of samples used for microstructural and petrological studies (all circles) and samples used for microstructural, petrological and geochronological studies (filled circles, with corresponding sample numbers, table 4.2; sample numbers with star symbols have been collected from similar tectonostratigraphic levels in adjacent areas (see figure 4.8a for locations)). Relevant structural data for the samples above are given in table 4.2. *4.2c.* The distribution of relic biotite, of blueschist facies assemblages together with orientation of glaucophane mineral lineation, of greenschist facies assemblages together with the orientation of stretching lineations and, where observed, the direction of tectonic transport, are, together with a summary of the general trend of the (bulk) lineation orientation, projected along the line of section. Glaucophane mineral lineation, stretching lineations in greenschist facies rocks and overal lineation orientation strikes are projected in plan view. *4.2d.* Orientations of stretching lineations summarized in the stereographic projection (equal angle projection).

is clearly shown in figure 4.2c (bulk lineation orientation). Near the contact between the allochthonous series and the underlying phyllites, the glaucophane mineral lineations parallel the greenschist facies stretching lineation and rotate into a near E-W orientation which is related to the final transport of the metamorphosed basement across the underlying autochthonous series. This observed variation in bulk lineation orientation with structural position indicates that older lineation orientations may have been reorientated by younger deformational events, which has also been suggested by Vandenberg & Lister (1996) in the Cyclades region.

The contact between the autochthonous series and the allochthonous sequence is intensely deformed and characterized by greenschist facies and semi-brittle mylonites. It is defined by an imbrication of alternating deformed slices of metamorphosed basement, phyllites and limestones. The weakly metamorphosed character of the phyllites (prehnite-pumpellyite grade), which have become interleaved with the structurally higher metamorphosed basement slices and structurally lower limestones together with the semi-brittle nature of the deformation, suggest that imbrication of these units occurred at semi-brittle crustal levels.

No.	Sample description	porph. clasts	myl. fol.
	westflank Ossa Massif		
1	greenschist facies mylonite at contact with underlying series, observed tectonic transport to WSW (256)	X	X
3	greenschist facies mylonite, no clearly observed tectonic transport direction. (WSW ?)		X
4	blueschist facies mylonite, relic biotite, observed transport to ENE (060)	X	X
5	biotite muscovite granite gneiss, incipient glaucophane growth	X	
29	biotite muscovite granite gneiss	X	
30	biotite muscovite granite gneiss, incipient glaucophane growth	X	
138	greenschist facies mylonite with blue-green amphibole mineral lineation parallel to stretching lineation, observed transport to NNE (030)		X
146	greenschist facies mylonite, relic glaucophane, observed tectonic transport to NE (055)	X	X
149	blueschist facies mylonite, transport to NE (045)	X	X
152	blueschist facies mylonite, crosscut by (steeper) discrete blueschist facies shear, both tectonic transports to SW (240)	X	X
	eastflank Ossa Massif		
24	granite gneiss	X	
26	biotite muscovite gneiss with fine grained glaucophane	X	
	(random orientation)		
	southflank Ossa Massif		
106	crenulated biotite muscovite gneiss	X	
109	quartz vein with muscovite in two mica gneiss	X	
159	greenschist facies mylonite near contact with underlying series, transport to SW (235)	X	X

Table 4.2. Summary of the petrological and structural characteristics of the samples selected for $^{40}Ar/^{39}Ar$ laserprobe experiments. The right colums refer to the generation of white mica selected. Locations of the samples are indicated in figure 4.2 and figure 4.8.

4.6 Characterization of the metamorphic assemblages

The metamorphic sequence in the allochthonous units of the Ossa Massif is dominated by medium to fine grained felsic to intermediate basement rocks with the following protolith minerals as their principal constituents: plagioclase, quartz, microcline (often albitised), muscovite, biotite and opaque minerals. The development of blueschist assemblages varies throughout the sequence. It is absent in the higher tectonostratigraphic levels (e.g. sample 29), while in other samples randomly oriented fine grained blue amphibole (10 to 100 μm in size) is observed along the grainboundaries between the different mineral phases (e.g. samples 5 and 30). In yet other samples a well developed blueschist facies assemblage has developed (e.g. samples 4, 24). The blueschist facies assemblage is characterized by the occurrence of albite, white mica (phengitic in composition), epidote, glaucophane and quartz; locally lawsonite is found. Jadeitic pyroxene and garnet are absent in the assemblage. PT conditions of the blueschist facies assemblage have been estimated around 0.8 GPa and 350°C, applying PT estimates of the lawsonite blueschist (LBS) - epidote blueschist (EBS) transition reaction of Evans (1990; figure 4.3). The position of this transition reaction is dependent on the Fe/Al ratio of epidote and sodic amphibole. The observed lithology dependent occurrence of, locally, lawsonite-glaucophane versus, regionally, epidote-glaucophane parageneses and the absence of jadeitic pyroxene positions the PT conditions of the high pressure assemblages near the overlap of LBS and EBS fields, below the jadeite stability range. The LBS-EBS boundary is most affected by variations

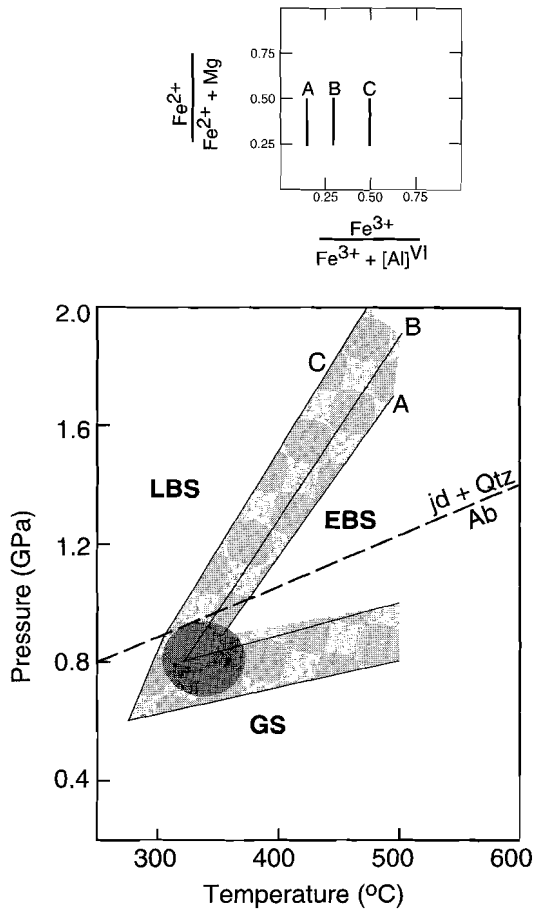

Figure 4.3. - PT estimation of the peak metamorphic assemblage in the Ossa Massif. Positions of the transition reaction lines which bound the epidote blueschist field and location of the albite to jadeite + quartz transition reaction (dashed line) are after Evans (1990). Reaction lines A-B-C represent transition reaction lines in lithologies with increasing Fe content (upper diagram). Metamorphic stability fields; LBS, lawsonite-blueschist; EBS, epidote-blueschist; GS, greenschist (Evans, 1990).

in H_2O activity. The reaction lines presented in figure 4.3 are calculated for an adopted H_2O activity of 0.9 (as presented by Evans, 1990) to allow limited dilution of the content of H_2O by other fluid species (e.g. carbonic volatiles, salts). Greenschist facies assemblages are characterized by the occurrence of albite, chlorite, epidote, white mica (phengitic in composition) ± actinolite ± quartz. In the greenschist facies assemblages relic minerals of older assemblages may be found (e.g. relic biotite, relic glaucophane). Considering again the position of the transition reactions of the EBS field of Evans (1990), it is seen that epidote-glaucophane and greenschist assemblages may coexist at 350°C over a range of circa 0.2 GPa, namely between 0.60 and 0.80 GPa.
The metamorphic assemblage of the autochthonous phyllites is defined by a prehnite-pumpellyite assemblage in which lawsonite has been reported (Godfriaux, 1968), which confines minimum pressures to 3 kbar and maximum temperatures to 300°C (Frey et al., 1991, Bröcker & Day, 1995). The lithostatic equivalent of the minimum pressure of 3 kbar corresponds to the overall thickness of the overthrusting allochthonous basement sequence.

4.7 Application of the $^{40}Ar/^{39}Ar$ laserprobe technique and the direct dating of deformational fabrics

Generally, three types of events can be dated with the $^{40}Ar/^{39}Ar$ technique; i) crystallization from a melt, ii) thermal resetting, and iii) metamorphic crystallization (i.e. both neocrystallization and recrystallization). Considering the metamorphic stability field and the closure temperature ranges for the main K-bearing minerals that can be used for $^{40}Ar/^{39}Ar$ age dating (figure 4.4), it is shown that in greenschist and blueschist facies settings, with corresponding metamorphic temperatures of circa 300 to 400°C, white mica is the only main K-

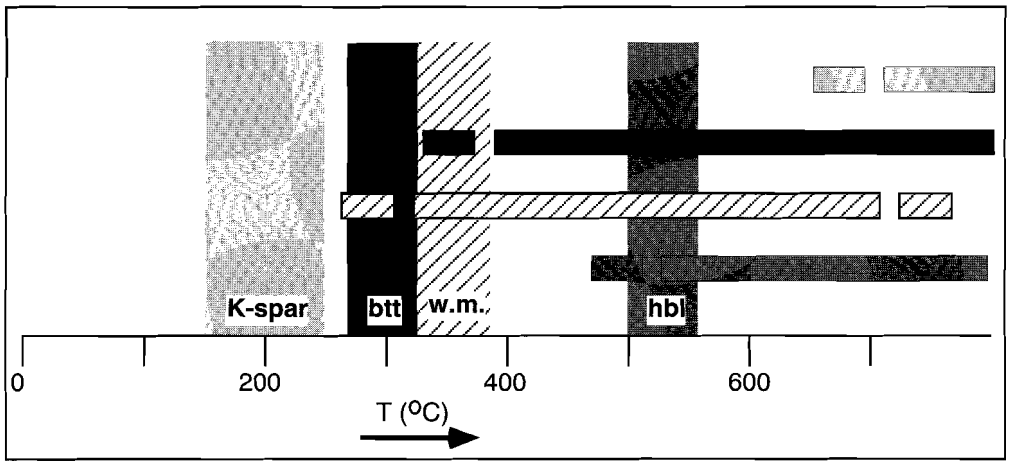

Figure 4.4. - Schematic diagram illustrating the metamorphic stability fields (horizontal bars) and average argon closure temperature ranges (vertical columns) of the main K-bearing minerals; from left to right, K-feldspar, light grey; biotite, black; white mica, diagonal bars; hornblende, dark grey.

bearing mineral which may crystallize at these conditions. It is also illustrated that a temperature range exists at which white mica may (re-)crystallize below the closure temperature range (i.e. circa 350°C), which is of interest as discrete fabric forming events might be directly datable (Dunlap, 1997). Consequently white mica was selected as key mineral in this study.

Hercynian cooling ages have been obtained from basement muscovites of the Olympos region (Schermer et al., 1990). The indication that regional metamorphic temperatures which affected the rock sequence of the Olympos region in Alpine times generally failed to reset the Hercynian muscovite porphyroclast ages thermally, suggests that the argon isotopic signature in white mica which formed in Alpine deformational structures might have been preserved. The newly formed white mica is more phengitic in chemical composition than the muscovite porphyroclasts which allows it to be distinguished in back-scattered scanning electron microscope images. As the tectonic history of the metamorphic sequence in the Pelagonian is characterized by several deformation events, it is likely that more than one mica generation will be present in most samples (figure 4.5). From our careful investigation of the structural setting in the Ossa Massif and from the results from the Olympos Massif (Schermer et al., 1990; and Schermer, 1993), the following white mica generations can be

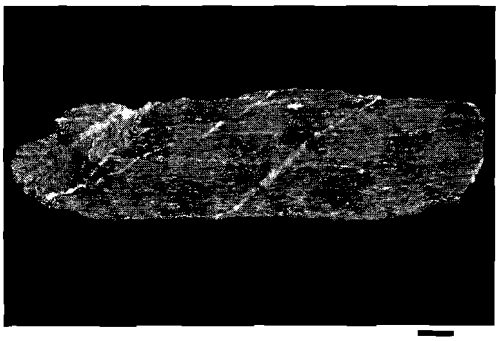

4.5a: sample 4 1cm

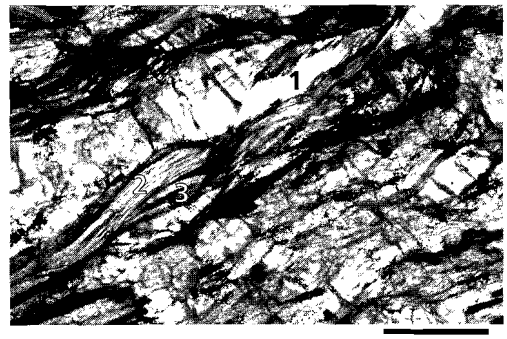

4.5b: close-up sample 4 500µm

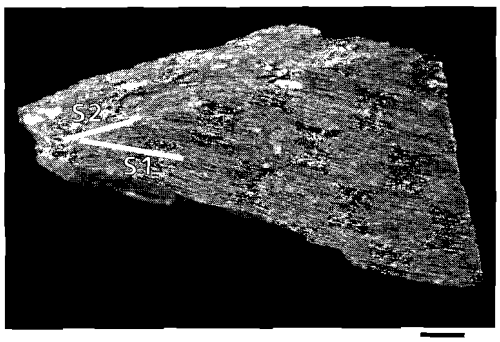

4.5c: sample 152 1cm

Figure 4.5. - Characterization and identification of different white mica generations. *4.5a.* Polished surface of blueschist mylonite sample cross cut by post-mylonitic tensional veins (sample 4), scalebar; major divisions are cm scale. *4.5b.* Micrograph from a polished thin section (100 µm thick) of sample 4, illustrating three different white mica generations; 1) muscovite porphyroclasts, 2) white mica in blueschist facies mylonitic foliation, and 3) secondary white mica in retrograde mylonitic foliation. See also figure 4.7 for schematic presentation of figures 4.5a and 4.5b. *4.5c.* Polished surface of blueschist mylonite sample (sample 152), crosscut by discrete shear (ca 1 cm wide). The two mylonitic foliations could be processed separately after sawing of the sample, scalebar; major divisions are cm scale.

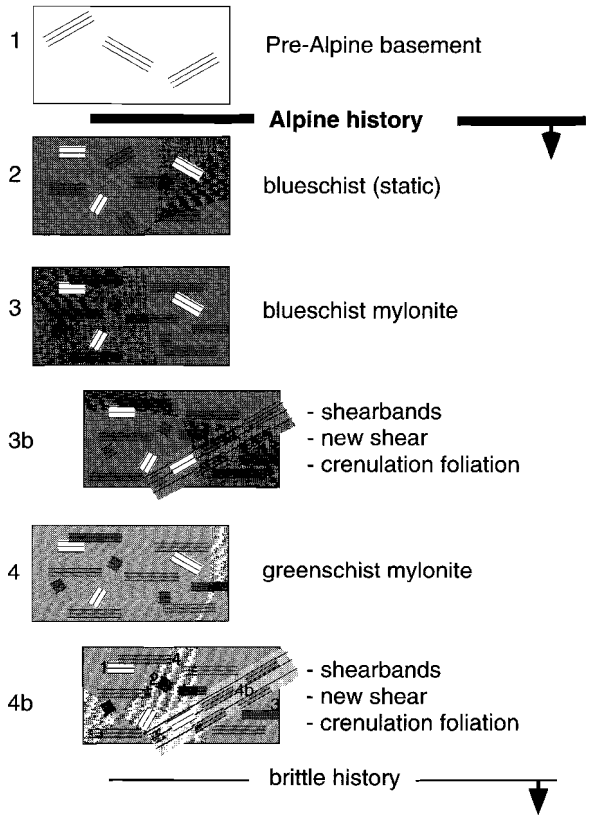

Figure 4.6. - Schematic diagram summarizing the idealized microstructural relationships for white mica which have formed in the metamorphic sequence of the Ossa Massif. White structures illustrate pre-Alpine fabrics (1), dark grey structures indicate blueschist facies fabrics, which include an early static (2), a main deformational (3), and alate deformational phase (3b) light grey structures indicate greenschist facies fabrics, which include a main (4) and late deformational phase (4b).

expected to be present in the metamorphic sequence (figure 4.6): i) muscovite porphyroclasts, ii) white micas in blueschist facies metamorphic assemblages, iii) white micas in blueschist facies mylonitic foliations which formed by recrystallization of the older assemblages and by neocrystallization, iv) white micas in greenschist facies metamorphic foliations, and v) white micas in greenschist facies mylonitic foliations which formed by recrystallization of the older assemblages (preferably after reactivation of older structures) and by neocrystallization. In actual fact up to three white mica generations were observed per individual sample; porphyroclasts, white micas which formed the mylonitic foliation and white micas which formed after reactivation of the structure by recrystallization of the existing white mica generations (figure 4.5). Accurate mineral separation and analysis of small mineral fractions is required to reduce the chance that more than one mica population is present in the analysed mica separate. Analysis of such a multipopulation will often result in a staircase pattern spectrum (Schermer et al. 1990, Kirschner et al. 1996), in which pseudo-plateau ages might be observed which have no geologically meaningful significance (Wijbrans & McDougall, 1986). The muscovite porphyroclasts were selected to map out regional thermal conditions in the Ossa Massif, whereas micas from the metamorphic fabrics were selected to directly date the fabric forming events. A brief description of the samples used, plus their structural relevance, is presented in table 4.2.

4.8 Analytical techniques

4.8.1 Identification and selection of mica generations

White mica generations were identified and characterized in the field and, subsequently, in thin section by optical microscopy and SEM studies (figure 4.7-I). The metamorphic assemblages related to the mylonitic fabrics were determined in thin section (figure 4.7-II) and the different mica generations were selected (figure 4.7-III). In the present study a maximum of two mica generations were separated for every sample. Large sized muscovite porphyroclasts in mylonites were used to deduce the protolith thermal histories. After establishing these, recrystallized white micas, associated with the mylonitic foliation were selected to date the fabric development of the mylonite. The fabric forming white micas are finer grained (i.e. lower thickness-diameter ratio) but are also more phengitic in composition showing higher Si/Al ratios (ca 1.5 to 2) and a lower Ti content. The muscovite porphyroclasts have an average diameter of circa 500-1000 μm (thickness-diameter ratio of circa 0.5), the largest recrystallized white micas in the mylonitic foliation have average diameters which range from circa 100 μm to circa 600 μm (thickness-diameter ratio of circa 0.2). Secondary generations of fabric forming white micas were excluded for further analysis, to avoid analysis of multiple mica generations.

4.8.2 Mica separation

After selection, the samples were gently crushed and then sieved firstly into size intervals of < 250 μm, 250 to 500 μm, 500 to 1000 μm and > 1000 μm. Subsequently, the micas were separated in these sieve intervals using a Faul vibration table and sieved a second time into narrower 50 μm size intervals. Before final handpicking, some samples were further separated using a Frantz magnetic separator and heavy liquids to minimise any contribution from a multigeneration white mica population in the final mica separate (figure 4.7). The analysed biotite separates were obtained by the same procedure. Final handpicking from the final mineral separate was carried out under the microscope. The muscovite porphyroclasts can be optically distinguished from the fabric forming white mica on grainsize (muscovite is larger in grainsize), colour and transparency (muscovite is less colored and more transparent), lustre (muscovite is more "silvery" in glaze), and cleavage (muscovite has a better developed cleavage). The foliation forming micas contain more inclusions than the muscovites. Inclusion bearing micas were not selected for age dating experiments, but the optical characteristics of these micas were used as comparison to select inclusion free micas of the same generation.

4.8.3 Irradiation procedure

The hand-picked crystals were put into a 3 mm thick Al tablet with 20, 2 mm diameter, holes. Sixteen holes were loaded with circa 0.5 mg of sample (varying from single crystals for coarse micas (i.e. diameters ≥ 500 μm) to circa 16 crystals for the finest mica fractions (i.e. diameter sizes ~ 160 μm)), the other four positions were loaded with a flux monitor (USGS standard 85G003 TCR sanidine, age 27.92 Ma, relative to an K-Ar age of 162.9 Ma for SB3, USGS standard biotite). To this end it was chosen to analyse extremely small min-

I **(micro-) structural + petrological investigations**

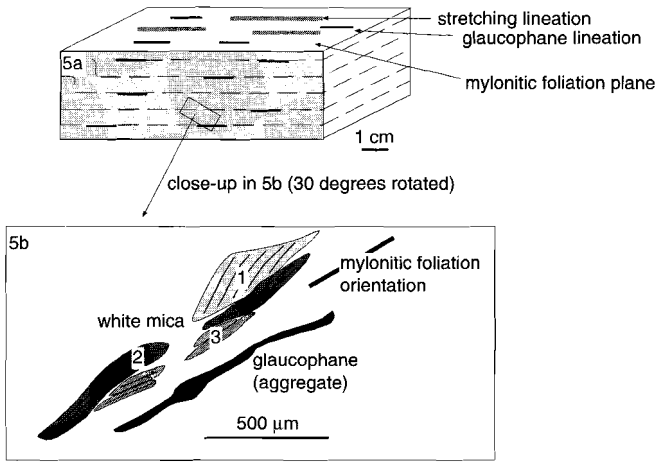

II **Characterization of mica generations:**
1. muscovite porphyroclasts
2. white mica (phengitic) in blueschist facies mylonitic foliation
3. white mica (phengitic) in greenschist facies overprinting foliation

III **Selection of mica generations:**
1. porphyroclasts to investigate the protolith thermal history (moment of cooling below ca 350°C)
2. largest mylonitic foliation forming white mica (fabric age of blueschist facies mylonite)

excluded:
3. smaller mylonitic foliation forming white micas (risk of contamination; multipopulation analysis)

IV **crushing + separation**

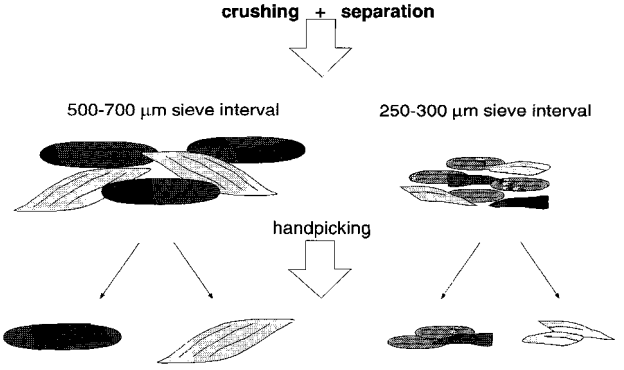

V **$^{40}Ar/^{39}Ar$ analysis**

Fabric age **Cooling age** mixed fabric age Cooling age

Figure 4.7. - Schematic overview of the employed characterization and separation of white mica generations. Sample 4 is taken as example (corresponding (micro-) photographs in figure 4.5a and 4.5b).

eral fractions, which requires a $^{40}Ar/^{39}Ar$ laserprobe set-up which is characterized by high sensitivities and low blanks. The use of small mineral fractions gives rise to a greater analytical error but gives meaningful absolute ages by minimising analysis of mixed populations. A set of trays was irradiated with fast neutrons in the CLICIT facility of the TRIGA reactor at the Oregon State University.

4.8.4 $^{40}Ar/^{39}Ar$ analyses and data processing

The $^{40}Ar/^{39}Ar$ laserprobe experiments were carried out with the VULKAAN laserprobe facility at the Vrije Universiteit of Amsterdam (see also appendix 1, and Wijbrans et al., 1995). After irradiation, a single fusion experiment was applied to analyse every flux monitor. Horizontal variations in irradiation values of the flux monitors and their analytical errors resulted in a final error on the calculated irradiation values of the unknowns of 0.8 to 1.2%, which contributes to the total analytical error of the analyses of the unknowns. The samples to be dated were analysed by an incremental heating experiment. The experiment consists of a total of 10 to 15 analyses with a stepwise increase of the laserpower for every analysis. Typical incremental heating experiments consist of 1 minute of laser heating with a defocussed beam, followed by 4 minutes additional clean-up time, per analysis. After every two analyses, the system blanks were measured. The isotopic composition of the argon gas was measured using a double focussed noble gas mass spectrometer (MAP215-50) in static mode. Beam intensities were measured on a secondary electron multiplier detector and switchable pre-amplifier resistor settings (10, 100 and 1000 MOhm) by peak jumping at half mass intervals down from mass 40 to 35.5. The blank correction applied to every unknown was a blank (and its analytical error) which had been integrated to the time of analysis of the unknown, after calculating a third order best fit of all the blank analyses over the day. System mass discrimination was measured by letting clean air Ar (ca 4 x 10^{-15} moles of ^{40}Ar) into the mass spectrometer from an air reservoir (10 l) using a 1 ml gas pipette.

4.9 Results and discussion of $^{40}Ar/^{39}$ Ar experiments

As mentioned in chapter 3, age calculations should incorporate not only the closure temperature concept, but also should remember that argon loss (or gain) can be affected by fluid interaction, chemical alteration, and/or deformation rather than simple heating or cooling. The discussion of the, possible, contribution of these factors is important to question the relevance of the obtained age and, if the age is concluded to be relevant, to question its regional significance. It is shown by the correlation of spot fusion data and incremental heating data (section 3.4.3) that deformation induced recrystallization and/or chemical alteration might introduce the presence of a partially reset argon signature in a white mica generation, which becomes evident in either a staircase pattern 40Ar/39Ar release spectrum (see sample 152 in figure 3.8) or a diffusion loss profile (see sample 7 in figure 3.9). The diffusion loss profile might also be caused by the gradual cooling of the sample and associated gradual decrease of argon diffusion rates with latest argon loss at the rims of crystals or through, possibly existing, fast diffusion pathways. Argon gain during or after recrystallization of white mica is often harder to detect. As stated in appendix 1 (A1.4) argon

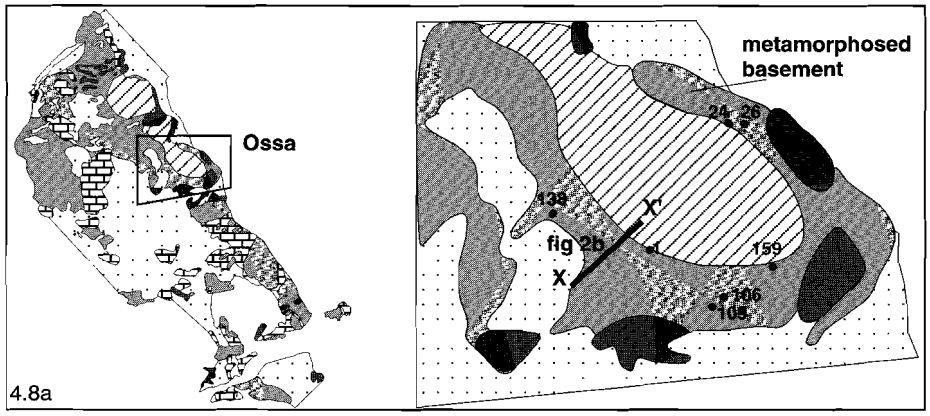

4.8b upper half

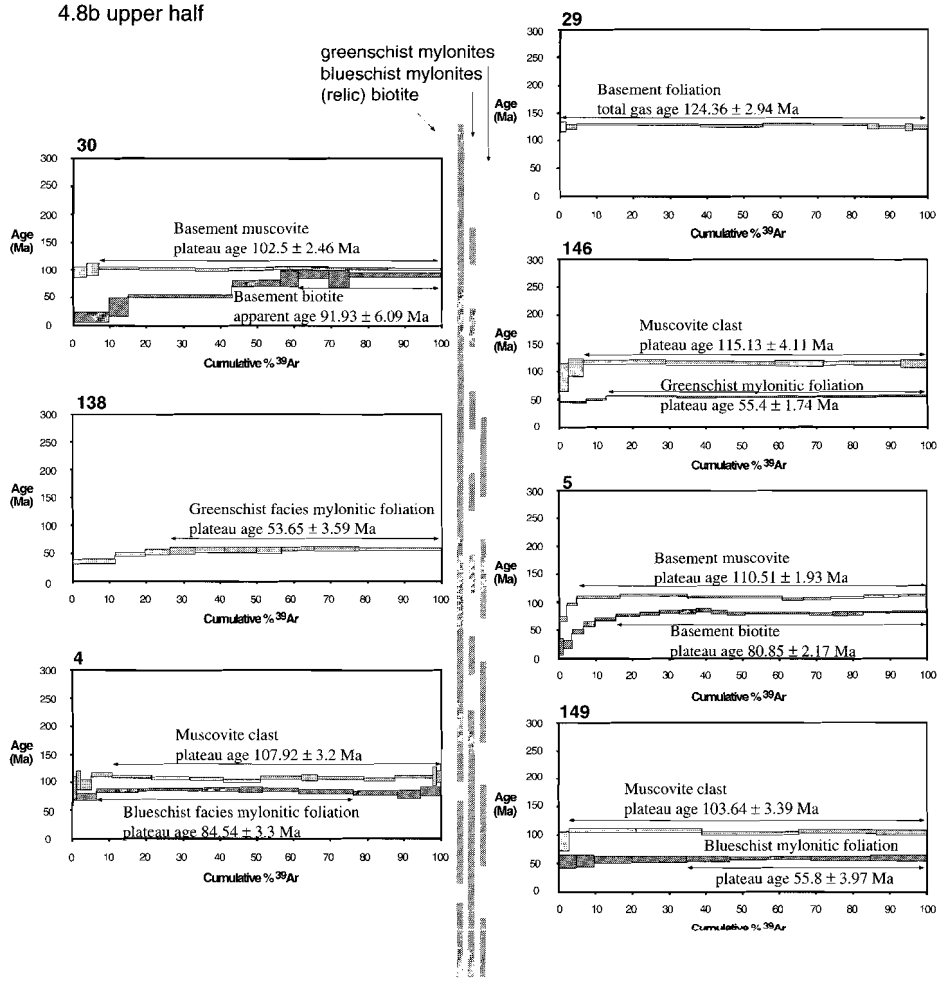

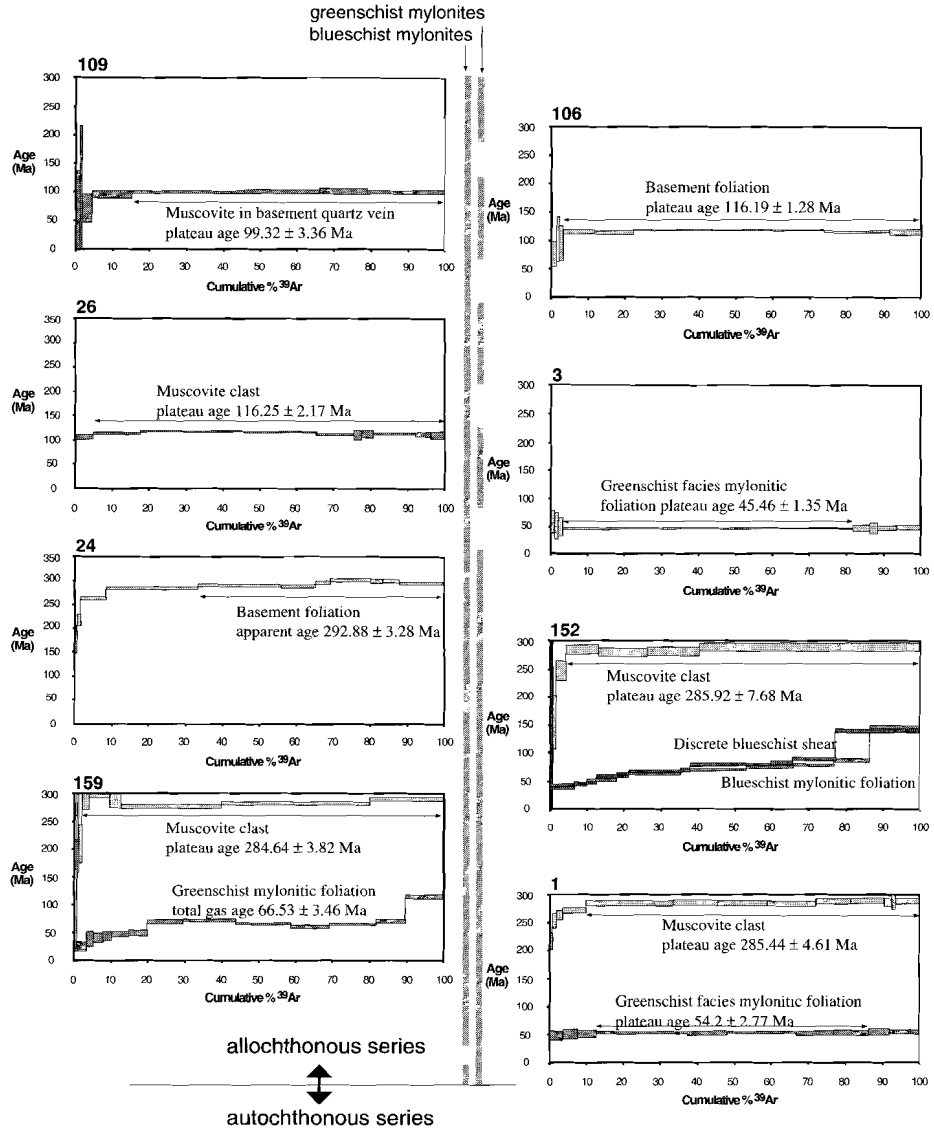

Figure 4.8. - Results of $^{40}Ar/^{39}Ar$ laserprobe dating. *4.8a.* Simplified map of the Ossa Massif (after IGME, 1983) with locations of the samples selected other than along the section X-X' (for which the reader is referred to figure 4.2). *4.8b.* Results of $^{40}Ar/^{39}Ar$ laserprobe dating in tectonostratigraphical order. Results of structurally highest sample first. Observed distribution of biotite, blueschist mylonites and greenschist mylonites are included (as presented in figure 4.2c). All age spectra are presented with a 2σ analytical error and summarized in table 4.3. Two spectra in one diagram represent analyses from two mica generations in the same sample (muscovite and biotite analyses, e.g. sample 30; or porphyroclast and fabric analyses, e.g. sample 146). Three spectra in one diagram (sample 152) are derived from analyses on muscovite porphyroclast and two mylonite fabrics (S1 and S2, structural relationship shown in figure 4.5c).

preferably partitions into the fluid phase and subsequently into biotite over white mica. With other words, if the fluid phase is oversaturated with argon (the initial cause of excess argon to be present in minerals), then the excess argon might be present in biotite before it becomes present in white mica. As the incremental heating experiment on the biotite sample (e.g. sample 5) still shows a diffusion loss profile and not any evidence of the presence of an excess argon component it is concluded to be unlikely that the white micas in the same mylonitic interval have incorporated an excess argon component.
Based on the above, it is concluded that the age spectra produced by incremental heating experiments can be interpreted in terms of cooling ages and fabric ages, unless the presence of a partially reset mica population is evidenced in the spectrum. There is no evidence of any excess

No.	Analysed fabric (mica generation)	grnsize (μm)	crystals (No.)	total gas (Ma, 2σ)	plateau (Ma, 2σ)	%^{39}Ar (in plt)	significance
1	muscovite porhyroclast	~600	1	283.7±4.7	285.4±4.6	90%	cooling age
	greenschist mylonite	~200	10	53.9±3.9	54.2±2.8	74%	fabric age
3	greenschist mylonite	~400	4	45.7±2.5	45.5±1.4	79%	fabric age
4	muscovite porphyroclast	~600	1	106.7±3.6	107.9±3.2	50%	cooling age
	blueschist mylonite	~500	1	82.2±4.2	84.5±3.3	70%	fabric age
5	basement muscovite	~600	1	109.2±1.9	110.5±1.9	95%	cooling age
	basement biotite	~600	1	76.5±2.5	80.9±2.2	84%	cooling age
29	basement foliation	~500	1	124.4±3.0	124.4±2.9	100%	cooling age
30	basement muscovite	~600	1	102.2±3.0	102.5±2.5	93%	cooling age
	basement biotite	~500	1	66.7±7.0	91.9±6.1	39%	cooling age
138	greenschist mylonite	~250	8	49.7±4.0	53.7±3.6	67%	fabric age
146	muscovite porphyroclast	~500	1	114.1±5	115.1±4.1	94%	cooling age
	greenschist mylonite	~250	8	54.5±1.8	55.4±1.7	87%	fabric age
149	muscovite porphyroclast	~500	1	103.3±3.6	103.6±3.4	100%	cooling age
	blueschist mylonite	~200	12	54.8±5.2	55.8±4.0	65%	fabric age
152	muscovite porphyroclast	~600	1	283.4±8.0	285.9±7.7	96%	cooling age
	blueschist mylonite (S1)	~150	16	77.7±2.6	—	—	multipopulation
	blueschist mylonite (S2)	~150	16	85.6±2.6	—	—	multipopulation
24	basement muscovite	~500	1	288.4±3.3	292.9±3.3	92%	cooling age
26	basement muscovite	≥500	1	114.9±2.2	116.3±2.2	96%	cooling age
106	basement foliation	~500	1	114.4±2.6	116.2±1.3	97%	cooling age
109	muscovite in quartzvein	~600	1	97.7±5.8	99.3±3.4	85%	cooling age
159	muscovite porphyroclast	≥500	1	281.8±4.6	284.6±3.8	98%	cooling age
	greenschist mylonite	~250	6	65.4±3.6	—	—	multipopulation

Table 4.3. Summary of ^{40}Ar/^{39}Ar laserprobe age dating results.
Columns from left to right: sample number (see also: table 4.2 and figures 4.2 and 4.8); characterization of analysed mica generation; grainsize of selected mica(s); number of crystals analysed; total gas age (2σ analytical error); plateau age (2σ analytical error); %^{39}Ar used in plateau age; interpretation of result.

argon being present in the samples. The regional significance of the obtained ages is further expressed by the summarizing diagram (figure 4.9), which also shows the age information of the individual samples and the (regional) frequency of the obtained age. In such way the regionally significance of the ages can be easily recognized, as they occur in clusters (regional significant) and also individually (less significant, and little suspicious).The age spectra of the samples are presented in tectonostratigraphical order in figure 4.8, all with a 2σ analytical error. Because $^{40}Ar/^{39}Ar$ incremental heating experiments have been carried out on extremely small fractions of crystals (less than circa 0.5 mg) to minimise analysis of mixed populations most spectra show fairly large 2σ analytical errors, ranging between 1% and 7% of the absolute age.

Most of the incremental heating experiments on the muscovite porphyroclasts resulted in fairly flat spectra with minor to substantial diffusion loss of argon in the lower temperature steps. The plateau ages which have been obtained from these experiments are all interpreted as being cooling ages. The experiments on the muscovite porphyroclasts yield well defined plateau ages which cluster at 290-285 Ma (samples 1, 24, 152 and 159) and 125-100 Ma (samples 4, 5, 26, 29, 30, 106, 109, 146 and 149). Incorporation of the structural position of the samples shows that all samples which yield Hercynian cooling ages are found at the structurally lower parts of the sequence, while the samples which yield 125-100 Ma cooling ages are derived from the structurally higher parts of the sequence. Two incremental heating experiments have been carried out on biotite porphyroclasts (sample 5 and 30). Both spectra show substantial diffusion loss of argon in the low temperature steps. The spectrum from sample 5 shows a fairly well defined plateau with an age around 80.9 ± 2.2 Ma, while the spectrum from sample 30 shows a poorly defined plateau with an apparent age of 92 ± 6 Ma. The ages reflect the time of cooling of the sequence below the closure temperature range of the argon isotopic system in biotite (i.e. circa 300±20°C; see chapter 3 and Hanes, 1991; Harrison et al., 1985).

In contrast with the spectra from the mica porphyroclasts, which show some diffusion loss of argon, the age spectra derived from the white mica populations defining the mylonitic fabrics show little to no diffusion loss of argon in the low temperature steps. The plateau ages obtained from these spectra all give a direct age of the formation of these fabrics. Incremental heating experiments on white mica populations, which define the mylonitic foliations, result in flat spectra for most of the samples (samples 1, 3, 4, 138, 146 and 149) and staircase pattern spectra for a few samples (samples 152 and 159). The staircase pattern spectra of samples 152 and 159 are caused by outgassing of a mixed population, which most likely consisted of newly formed white mica and recrystallized porphyroclasts with partially preserved Hercynian ages. The spectra derived from experiments on blueschist facies mylonite fabrics yield well defined plateau ages of 84.5 ± 3.3 Ma (sample 4) and 55.8 ± 4.0 Ma (sample 149), and a mixed phase spectrum (sample 152). The circa 85 Ma and 56 Ma are related to crystallization of a blueschist facies mylonitic fabric with a clearly observed direction of tectonic transport towards ENE, i.e. top-to-060° (sample 4) and top-to-045° (sample 149) respectively. The ages related to the mylonitic fabrics of sample 152 are indeterminable. The mixed population spectrum of the blueschist mylonitic foliation is indistinguishable from the mixed population spectrum of the discrete blueschist shear. The latter fabric has formed by recrystallization of the former but appears to have not partially reset the argon isotopic signature of the mylonitic foliation. The

spectra derived from experiments on greenschist facies mylonite fabrics yield well defined plateau ages of circa 54 ± 2 Ma (samples 1, 138 and 146) and 45.5 ± 1.4 Ma (sample 3), and a mixed phase spectrum (sample 159). The circa 54 Ma age is related to crystallization of a greenschist facies mylonitic fabric with both an observed tectonic transport direction towards NE (030° and 055° for samples 138 and 146 respectively) and an observed tectonic transport direction towards SW (256°, sample 1). The mixed phase spectrum of sample 159 might be caused by mixing of partial recrystallized muscovites with Hercynian cooling ages and white mica forming the greenschist facies mylonitic fabric with an age around circa 50 Ma (steps 2-6 in the spectrum). This is the upper age limit of the crystallization of the mylonitic fabric and is comparable to the 54 ± 2 Ma. The observed direction of tectonic transport of sample 159 is top-to-235°. The circa 45 Ma (sample 3) is related to crystallization of a greenschist facies mylonitic fabric which gave a poorly defined direction of tectonic transport top-to-220°.

4.10 Thermotectonic evolution of the Ossa Massif

The integration of the results from microstructural, petrological and geochronological studies in the Ossa Massif have defined several thermotectonic events which are summarized in figure 4.9. The $^{40}Ar/^{39}Ar$ analyses on muscovite porphyroclasts in the Ossa Massif have uniformly yielded Hercynian cooling ages (i.e. 290-285 Ma) from the structurally lower parts of the metamorphosed basement and Lower Cretaceous (i.e. 125-100 Ma) cooling ages from the structurally higher parts of the sequence. The age distribution suggests a phase of basement imbrication during which parts of the basement were transported to levels at which temperatures were low enough to close the argon isotopic system in white mica. None of the Alpine structures appear to have been affected by the structure that caused this preferred jump in cooling ages which suggests that the phase of basement imbrication occurred before the development of the Alpine structures. The structure that separates the two sets of cooling ages has not been observed in the field and might be obscured by development of younger structures. By circa 100 Ma metamorphic temperatures in all levels of the allochthonous sequence had dropped below circa 350°C.

The onset of blueschist facies metamorphism in the Ossa Massif is confined to the time interval between the 125-100 Ma cooling ages and the 84.5 ± 3.3 Ma fabric age (sample 4). The top-to-NE direction of tectonic transport (with respect to the present-day orientation), which has been obtained from the circa 85 Ma mylonitic fabric is related to the dominant observed

Figure 4.9. - Thermotectonic events in the Ossa Massif. *4.9a.* Summary of thermotectonic events identified in this study. Size of age intervals (shaded horizontal columns; light grey, cooling age; dark grey, fabric age) are defined by number of samples (individual sample information; $^{40}Ar/^{39}Ar$ laserprobe ages with 2σ analytical errors). The fabric ages have been related to the observed tectonic transport directions (white arrows indicate top-block tectonic transport). *4.9b.* The summary of events of the Olympos Massif from Schermer et al (1990); illustrated by vertical black bars; which allow to be compared to the results from the Ossa Massif (4.9a). *4.9c.* Events around the Pelagonian: 1. First detection of detrital glaucophanes in clastics of External Hellenides (Faupl et al, 1996); 2. Termination of HP metamorphism in Cyclades (discussed in Lips et al, 1998b, chapter 5); 3. regional phase of granodiorite emplacement in western Rhodope (after de Wet et al, 1989); 4. Onset of clastics deposition in Meso Hellenic Trench (western boundary, Caputo & Pavlides, 1993).

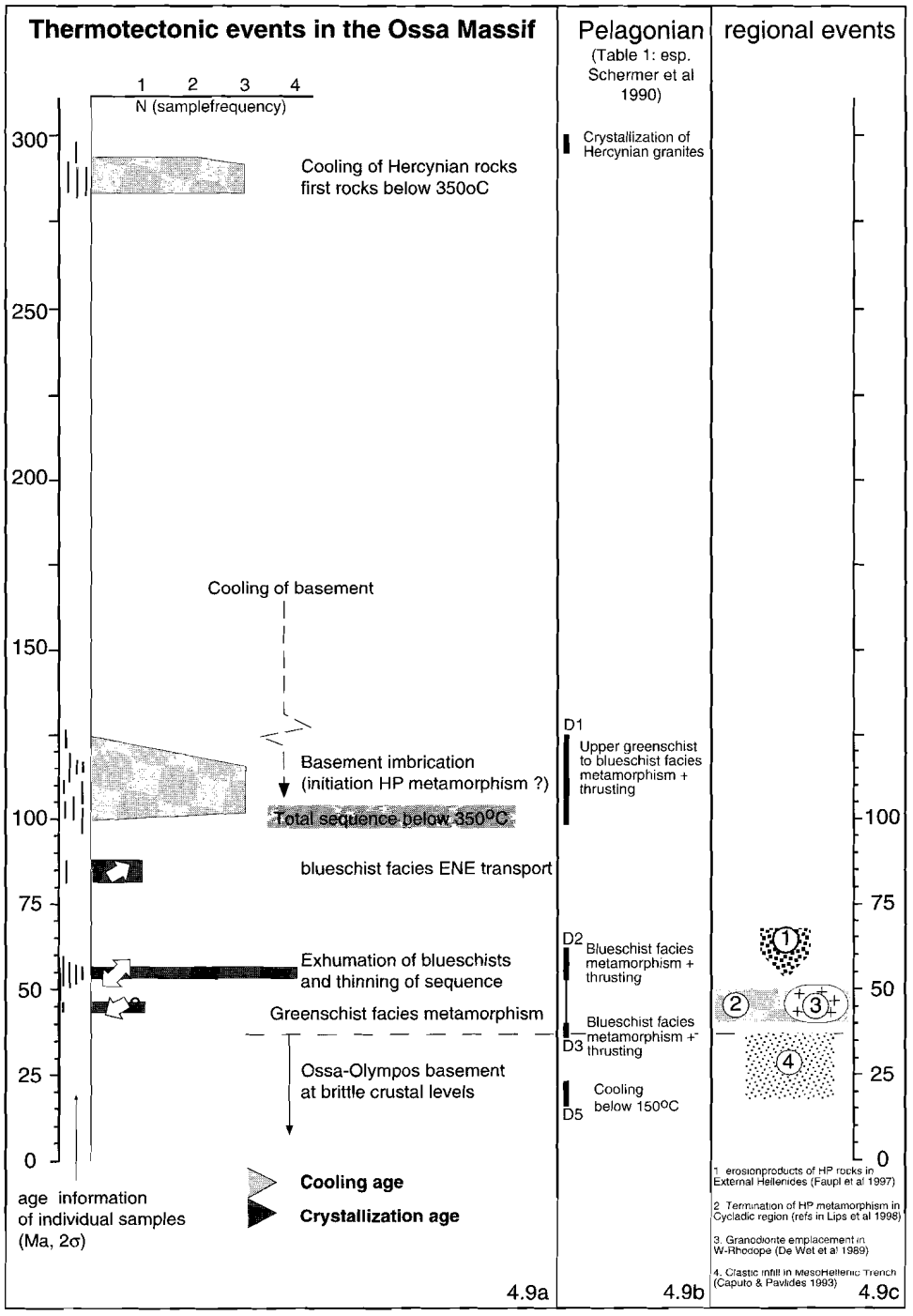
Thermotectonic events in the Ossa Massif
1 2 3 4
N (samplefrequency)
300
250
200
150
100
75
50
25
0
Cooling of Hercynian rocks
first rocks below 350oC
Cooling of basement
Basement imbrication
(initiation HP metamorphism ?)
Total sequence below 350°C
blueschist facies ENE transport
Exhumation of blueschists
and thinning of sequence
Greenschist facies metamorphism
Ossa-Olympos basement
at brittle crustal levels
Cooling age
Crystallization age
age information
of individual samples
(Ma, 2σ)
4.9a
Pelagonian
(Table 1: esp.
Schermer et al
1990)
Crystallization of
Hercynian granites
D1
Upper greenschist
to blueschist facies
metamorphism +
thrusting
D2
Blueschist facies
metamorphism +
thrusting
Blueschist facies
metamorphism +
thrusting
D3
Cooling
below 150°C
D5
4.9b
regional events
100
75
50
25
0
1
2
3
4
1. erosionproducts of HP rocks in
External Hellenides (Faupl et al 1997)
2. Termination of HP metamorphism in
Cycladic region (refs in Lips et al 1998)
3. Granodiorite emplacement in
W-Rhodope (De Wet et al 1989)
4. Clastic infill in MesoHellenic Trench
(Caputo & Pavlides 1993)
4.9c

direction of tectonic transport in the blueschist facies mylonites (i.e. to 040°-060°). However, the opposite directions of tectonic transport have been observed. Blueschist facies metamorphism had terminated by circa 54 Ma. Mylonite fabrics which were dated at circa 56-53 Ma, involve both blueschist facies mylonites (sample 149) and greenschist facies mylonites (samples 1, 138, 146). The circa 54 Ma event is also characterized by a bivergent direction of tectonic transport and is the time of transition from a NE-ward direction of tectonic transport during blueschist facies metamorphism to a WSW-ward direction during subsequent events (with respect to the present-day orientation). It is concluded that this phase of deformation is related to thinning of the metamorphic sequence and exhumation of the blueschist facies rocks, during which some blueschist facies rocks had been exposed. From Paleocene times onwards detrital blue amphiboles have been reported in the flysch sequences of the Hellenides (Faupl et al., 1996), indicating that some blueschist facies rocks were at the surface.
Following the circa 54 Ma event, the total metamorphic sequence was at relatively shallow crustal levels, at which time ductile deformation of the basement sequence continued under greenschist facies conditions. By circa 45 Ma, the metamorphosed basement was transported across the autochthonous series and escaped from further ductile deformation. The reorientation of mineral lineations and extension lineations into an E-W orientation near the contact of the metamorphosed basement is interpreted to be related to the latest stages of tectonic transport under semi-ductile conditions and which might have continued under brittle conditions. The post circa 45 Ma tectonic history of the Ossa Massif has not been further recorded by $^{40}Ar/^{39}Ar$ laserprobe analyses on white mica, as the period is characterized by brittle deformation.

4.11 Regional importance of dated events

The muscovite porphyroclasts from the basement sequence of the Ossa Massif show two clusters of cooling ages. The phase of basement imbrication which might explain the spatial distribution of the two sets of cooling ages could have affected the Hercynian basement around 125-100 Ma. Such an event was first proposed by Yarwood & Aftalion (1975) and Yarwood & Dixon (1976) for the Pieria region (NW of the Ossa region) and re-introduced by Schermer (1993) for the Olympos Massif (figure 4.9, column b). A phase of basement imbrication would have resulted in higher pressure conditions in the lower nappes and an increase in metamorphic temperatures during restoration of the geothermal gradient. In contrast to an expected elevation of metamorpic temperatures after a phase of basement imbrication, the imbrication in the Pelagonian Zone was followed by further cooling of the total metamorphic sequence below circa 350°C by 100 Ma (figure 4.9, column a; and Schermer 1993, figure 4.9, column b), after which blueschist facies metamorphism was initiated.
In the Ossa Massif the high pressure metamorphic episode has been confined to a 30 to 40 m.y. interval, namely from pre 85 Ma to circa 54 Ma. High pressure metamorphism had initiated after the phase of basement imbrication and cooling by circa 100 Ma and before the circa 85 Ma recorded blueschist mylonite fabric age. Termination of high pressure metamorphism occurred around circa 54 Ma, when the metamorphic sequence was exhumed and continued

to be affected by deformation under greenschist facies conditions. The top-to-NE direction of tectonic transport, observed in the blueschist mylonites of the Ossa Massif conflicts with the observations by Schermer (1993) for the Olympos Massif. Schermer (op cit) concluded tectonic transport to be SW-ward directed at all times in the Alpine history. The exact age of termination of high pressure metamorphism was not recorded by Schermer et al. (1990) in the sequence of the Olympos Massif, but is indirectly evidenced by their spread in fabric ages between D2 and D3, at 61-53 Ma to 42-36 Ma. The cause of this spread in ages is almost certainly due to analyses of mixed populations and incomplete recrystallization of blueschist facies fabrics during younger deformational events under retrograde blueschist facies (D2) and younger greenschist facies (D3) metamorphic conditions.

The circa 54 Ma event, related to termination of high pressure metamorphism and exhumation of the blueschist facies sequence in the Pelagonian Zone, might be correlated on a regional scale to the cluster of cooling ages which are related to the termination of high pressure metamorphism of the Cyclades (figure 4.9, column c; see Lips et al., 1998b, chapter 5) and to another set of cooling ages which point to the emplacement of granodiorites in the Rhodope region (figure 4.9, column c; de Wet et al., 1989). The age difference between the circa 54 Ma tectonic event in the Pelagonian and the 50 Ma and younger cooling ages from the Cyclades may reflect a diachronous uplift of the high pressure metamorphic sequence from the northern Aegean to the south. Alternatively the age difference could be related to the time interval between the exhumation of the metamorphic sequence in the Cyclades, which was initiated by the 54 Ma event but which was only recorded circa 5-10 Ma later at the time of closure of the argon isotopic system in white mica.

Following the circa 54 Ma event, during which tectonic transport shifted from a NE-ward direction to a WSW-ward direction, the basement sequence was affected by deformation under greenschist facies conditions and subsequent semi-brittle and brittle conditions. The regional correlation of the change in the overall direction of tectonic transport, shifting from NE-ward to WSW-ward (with respect to the present-day orientation) is poor, due to limited input data for paleogeographical reconstructions of the Northern Aegean in this time interval (e.g. Ricou 1994). The above shift in vergence might be related to the 80 degrees counterclockwise rotation of the Hellenic system, from a NNE-SSW orientation to a WNW-ESE orientation, at Late Cretaceous-Paleocene times and to further collision of the Pelagonian fragment with the Rhodopian Massifs, as suggested by Edel et al. (1992).

The youngest reported ductile fabric ages of 45 Ma from the Ossa Massif (figure 4.9a) and circa 42-36 Ma from the Olympos Massif, related to the W-ward thrusting of the basement series over the autochthonous units (figure 4.9b) show that by circa 40 Ma the tectonostratigraphic sequence of the Ossa and Olympos Massifs was in the brittle part of the crust and escaped younger phases of ductile deformation. Subsequently in the Oligocene and Miocene, the Meso Hellenic Trench had developed on the western margin of the Pelagonian basement sequence in a graben system controlled by NNW-SSE trending high angle brittle normal faults (figure 4.9, column c; Caputo & Pavlides, 1993), due to local extension during the E to W tectonic transport. This Oligocene-Miocene phase of extension is reflected in the Ossa-Olympos region by $^{40}Ar/^{39}Ar$ cooling ages on K-feldspar (figure 4.9, column b, D5; Schermer et al., 1990), which is again related to brittle fault activity and cooling of the

sequence below circa 200°C. Further south, in the Cyclades region, ductile deformation was continued and has been reflected in the recording of an Oligocene-Miocene phase of regional extension (Wijbrans & McDougall, 1988; Gautier & Brun, 1994).

4.12 Conclusions

The $^{40}Ar/^{39}Ar$ laserprobe age dating technique can be successfully used to directly date deformational and kinematic events in the Ossa Massif of the Pelagonian Zone in the north-western Aegean region. These events can only be dated when regional thermal conditions are well constrained, the deformational fabrics and kinematics have been carefully characterized, and, above all, meaningful ages can only be obtained when the white mica that is selected for dating experiments is related to a well characterized fabric in the identified metamorphic assemblage.

A record of ductile deformational events in the Ossa Massif is obtained from the Early Cretaceous well into the Eocene, after which deformation became semi-brittle. Cooling ages have been obtained from muscovite porphyroclasts and yield Hercynian ages (i.e. 290-285 Ma) at the base of the metamorphosed basement and Early Cretaceous ages (i.e. 125-100 Ma) at higher structural levels of the metamorphosed basement. Subsequent to the cooling of basement sequences below the closure temperature range of argon in white mica, fabric forming events have been directly dated and have resolved that blueschist facies metamorphism in the Pelagonian Zone is as old as 84.5 ± 3.3 Ma. The onset of tectonic activity under blueschist facies conditions is confined to the time interval between the circa 125-100 Ma cooling ages and the 85 Ma blueschist facies fabric age. Tectonic transport directions in blueschist facies mylonites are top-to-NE (with respect to the present-day orientation), although the direction of tectonic transport determined from kinematic indicators is not always inambiguous. Termination of tectonic activity under blueschist facies conditions and exhumation of the blueschist facies rocks occurred at circa 54 Ma, as it involves both blueschist facies mylonites and greenschist facies mylonites. Tectonic transport directions during this event have been top-to-NE and top-to-WSW and have resulted in the exhumation of the sequence. Following exhumation of the blueschist facies rocks at circa 54 Ma, an episode of greenschist facies deformation has been recorded till circa 45 Ma. Tectonic transport directions during the phase of greenschist facies metamorphism and subsequent semi-brittle conditions is more consistent than transport directions in blueschist facies mylonites and is directed towards SW to W.

In summary, this study not only recognizes an early Alpine cycle involving crustal shortening (ca 120-100 Ma), high pressure metamorphism (pre 85 Ma to 54 Ma), exhumation (ca 54 Ma) and subsequent crustal shortening (ca 45-40 Ma), but also a shift in dominant direction of tectonic transport from NE-ward to WSW-ward (with respect to the present-day orientation) at circa 54 Ma, both of which might serve as key input to paleogeographical reconstructions of the Late Cretaceous-Paleocene setting in the Eastern Mediterranean.

Chapter 5

$^{40}Ar/^{39}Ar$ laserprobe dating of white mica fabrics from the Pelion Massif, Pelagonian Zone: Implications for the timing of metamorphic episodes and tectonic events in the Aegean region

Accepted for publication in Geological Society of London / Institut Français du Petrole Special Publication, on "The Mediterranean Basins - Tertiary Extension within the Alpine Orogen", co-edited by L. Jolivet, as: Lips, A.L.W., J.R. Wijbrans and S.H. White: New insights from $^{40}Ar/^{39}Ar$ laserprobe dating of white mica fabrics from the Pelion Massif, Pelagonian Zone, Internal Hellenides, Greece: Implications for the timing of metamorphic episodes and tectonic events in the Aegean region.

5.1 Abstract

$^{40}Ar/^{39}Ar$ laserprobe dating of mylonites fabrics from the Pelion Massif in the Pelagonian Zone of mainland Greece has characterized its Middle to Late Alpine deformation history. Following high pressure (HP) metamorphism, ductile deformation occurred under greenschist facies conditions from circa 54 Ma, and continued to affect the Pelion Massif till circa 15 Ma. The prolonged episode of ductile deformation in the Pelion Massif has resulted in the formation of an Oligocene-Early Miocene ductile domal structure. The new geochronological data obtained for the Pelion contribute to a detailed record of the Alpine kinematic history in the Pelagonian Zone and allow a discussion of P-T-t data from Aegean HP rocks to characterize the regional thermotectonic history. Comparison with the P-T-t data from the Cycladic region reinforces the point that Middle Eocene phengite ages, commonly taken as the age of peak HP metamorphism in the Cyclades, do not always reflect the metamorphic culmination but rather the retrograde paths of the HP rocks. It is shown that, on a regional scale, termination of HP metamorphism is a diachronous process in the Aegean region, being circa 54 Ma in the north (Pelagonian Zone) and shifting to younger ages, chiefly circa 40 Ma in the Cyclades, and circa 20 Ma on Crete, as the present-day subduction zone is approached. In contrast to the diachronous exhumation of Aegean HP assemblages, the well documented Miocene phase of ductile regional extension appears to be synchronous across the whole Aegean region and affected basement rocks until circa 15 Ma.

5.2 Introduction

The Hellenic Orogen in the Aegean region (figure 5.1) contains a high pressure, low temperature, (HP) metamorphic belt which occurs at the interface of the largely unmetamorphosed External Hellenides in the (south-)west and the amphibolite grade metamorphic rocks of the Internal Hellenides in the (north-) east (Blake et al., 1981; Seidel et al., 1982). In the northern part of the Aegean region, the HP metamorphic belt crops out in the Pelagonian Zone, where it runs semi-continuously along the eastern coast of the Greek mainland (figure 5.1a), and has been thrust over weakly metamorphosed rocks, which are exposed in the Olympos and Ossa tectonic windows (figure 5.1b) (Godfriaux, 1970; Derycke & Godfriaux, 1976). In the southern part of the Aegean region, the belt crops out in the Cyclades Archipelago, where it changes its overall strike from northwest-southeast to roughly east-west and can be traced further to the east into western Turkey. South-and southwest of the Cyclades and closest to the present-day subduction zone, high pressure metamorphic sequences have been documented from the Peloponese and Crete.
The HP metamorphic belt in the Hellenides reflects the temporal and spatial evolution of the convergent tectonics between the African and Eurasian plates. Although characterized by overall convergence, involving the subduction of both oceanic and continental crust, much of the Late Alpine tectonic history of the belt is dominated by regional extension (Jolivet et al., 1994b). Since the exact timing of peak HP metamorphism and the subsequent uplift and exhumation of HP assemblages is an integral part of the understanding of the orogenic history of the Hellenides, a combination of detailed structural/petrological studies and sensitive dating techniques is required to characterize the metamorphic and deformational events that affected the polydeformed HP belt. The application of the $^{40}Ar/^{39}Ar$ laserprobe technique not only allows dating of individual grains, using the incremental heating technique (Wijbrans et al., 1990), but also allows the spot dating of individual crystals to characterize the resetting of the argon isotopic system during recrystallization (Scaillet et al., 1990) and to investigate the argon gradients in single crystals (Reddy et al., 1996). This paper demonstrates that the high sensitivity and low blank characteristics of the laserprobe dating is a significant advance in the dating of multiple tectonothermal events.

Numerous petrological studies in the Cyclades over the past decades provide a good coverage of data constraining the petrological evolution of the HP rocks in the central-southern part of the Aegean region (van der Maar & Jansen, 1983; Okrusch et al., 1984; Ridley, 1984; Schliestedt & Matthews, 1987; Buick & Holland, 1989; Okrusch & Bröcker, 1990; Avigad et al., 1992; Franz & Okrusch, 1992). Pressure and temperature estimates of the HP metamorphism range from blueschist facies conditions (7-9 kbar, circa 400-450°C) to eclogite facies conditions (14-17 kbar, circa 450-500°C). Tectonic studies in the Cyclades suggest that the HP rocks are part of a composite stack of thrust sheets that have experienced variable PT histories (Avigad, 1993; Vandenberg & Lister 1996). In the past, several studies have concentrated on the geochronology of the HP rocks in various parts of the Cyclades by the $^{40}Ar/^{39}Ar$ age dating technique (Maluski et al., 1981, 1987; Wijbrans & McDougall, 1986, 1988; Wijbrans et al., 1990; Bröcker et al., 1993; Raouzaios et al., 1996). The peak of HP

metamorphism is dominantly interpreted as being Middle Eocene (ca 40-45 Ma) in age, which was established by early K-Ar and Rb-Sr studies (Altherr et al., 1979; Andriessen et al., 1979). Although older ages have been reported (Maluski et al., 1987) and recent work has argued that the culmination of HP metamorphism in the Cyclades is not directly constrained by the published geochronological data (Wijbrans et al., 1990, 1993; Raouzaios et al., 1996), many papers have continued to use the Middle Eocene ages for the peak of HP metamorphism in the Cycladic area (Avigad et al. 1992; Avigad, 1993; Gautier & Brun,

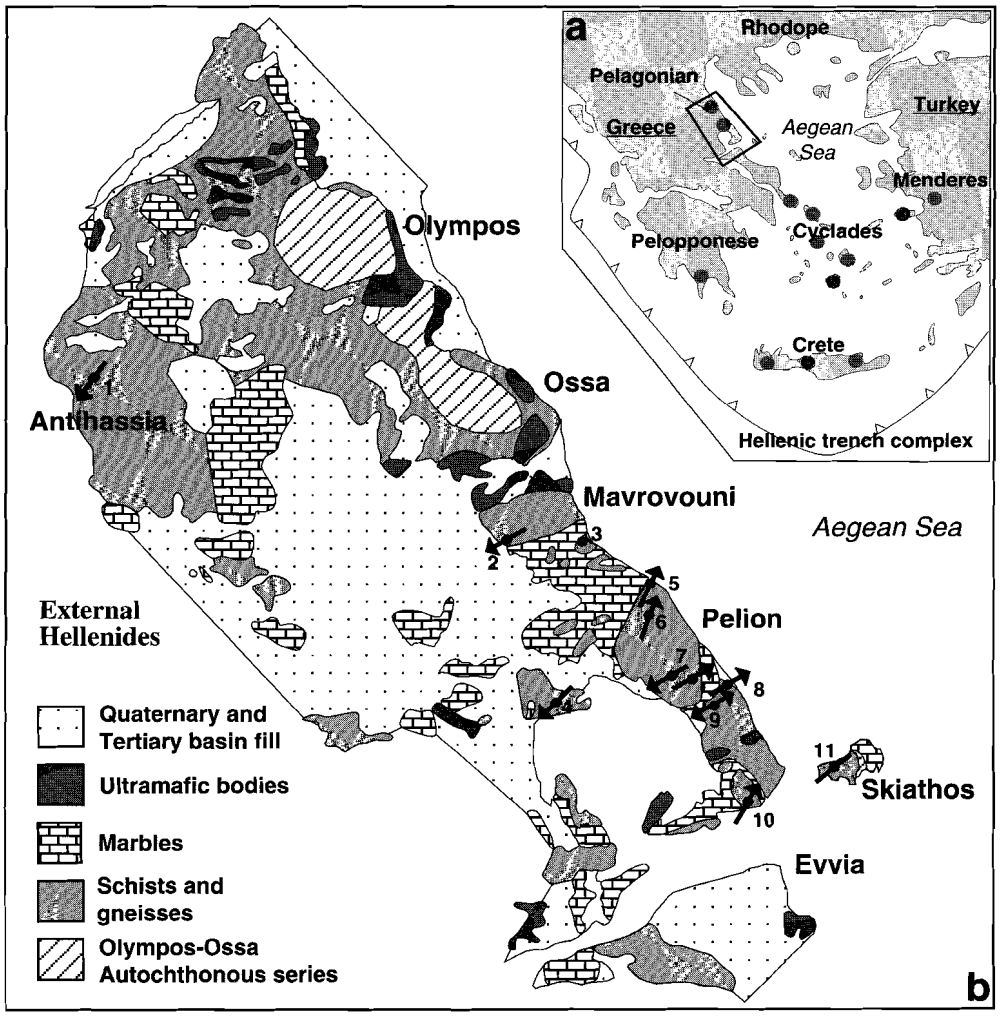

Figure 5.1 - 5.1a. Locations of exposed HP assemblages (dots) in the Circum-Aegean region. *5.1b.* Simplified geological map of the Pelagonian Zone (modified after IGME, 1983), showing $^{40}Ar/^{39}Ar$ sample locations (numbered) and observed directions of tectonic transport.

1994; Vandenberg & Lister, 1996).
In contrast to the extensive literature published on the HP rocks of the Cyclades, fewer publications exist on the northern and southern parts of the HP belt. Petrological and geochronological work on Crete, south of the Cycladic region, has resulted in Oligocene to Early-Miocene ages (i.e. pre-24 Ma to circa 20 Ma) for the HP metamorphism (Seidel et al., 1982; Triboulet & Bassias, 1988; Skarpelis, 1989; Theye et al., 1992; Fassoulas et al., 1994; Jolivet et al., 1996). The results of an extensive study around the Olympos tectonic window in the northern Pelagonian Zone (figure 5.1) have been presented by Schermer (1990; 1993) and Schermer et al. (1990), following first recognition of high pressure assemblages in the seventies (e.g. Derycke & Godfriaux, 1976). Schermer (1993) established that peak metamorphic pressure and temperature conditions for HP metamorphism in the Olympos region occurred at circa 5-8 kbar and circa 300-350°C. Conventional $^{40}Ar/^{39}Ar$ age dating on bulk samples (ca 100 mg) resulted in Paleocene (53-61 Ma) ages for the peak of the HP metamorphism in the Olympos Massif. The PT conditions of HP metamorphism and its timing in the Pelagonian Zone have been further refined after detailed structural, microstructural and petrological studies, combined with $^{40}Ar/^{39}Ar$ laserprobe experiments on mica separates (ca 0.5 mg) from selected samples of the Ossa Massif (Lips et al., 1998a; chapter 4), which had been subject of a limited investigation by Schermer et al. (1990) and is similar in style to the Olympos Massif (Schermer et al. 1990; Schermer 1993). The occurrence of either lawsonite bearing blueschists or epidote bearing blueschists depending on host lithology in the Ossa Massif (Lips et al., 1998a; chapter 4) further constrain the metamorphic conditions in the area to 7-8 kbar and 320-360°C for the Pelagonian HP event (PT estimates following Evans, 1990). Laserprobe dating on samples from the Ossa Massif has constrained the episode of HP metamorphism to a period from pre-85 Ma to circa 54 Ma (Lips et al., 1998a; chapter 4), following final cooling of the basement rocks to circa 350±30°C (taken as average closure temperature range of argon in white mica) by circa 100 Ma. The local identification of lawsonite porphyroblasts in Tertiary flysch (first reported by Derycke & Godfriaux, 1978), indicates that at least parts of the flysch sequence, which forms part of the autochthonous Olympos-Ossa sequence has experienced elevated pressures and low temperatures by circa 45 Ma (PT estimates in Lips et al., 1998a; chapter 4). It is emphasized that the recognized lawsonite occurrences by Dercyke & Godfriaux (1978) have been reported for flysch thrust slices in the metamorphic sequence, which originally were interpreted to have a slightly older age (ca Paleocene) than the autochthonous flysch with an estimated Lutetian-Priabonian biostratigraphical age (Derycke & Godfriaux, 1978).

This chapter presents the results of an integrated structural, petrological, and $^{40}Ar/^{39}Ar$ laserprobe study in the Pelion Massif and adjacent areas (figure 5.1b) of the southern Pelagonian Zone. Here, basement rocks have been affected by blueschist facies metamorphism and have been severely overprinted by greenschist facies deformational fabrics (Walcott & White 1998; Walcott 1998). A more intense greenschist facies ductile overprint in the Pelion Massif suggests that ductile deformation continued in the Pelion Massif after it had terminated in the Olympos-Ossa Massifs. This might give insight into the timing of ductile fabric forming events at younger Alpine times. Careful application of $^{40}Ar/^{39}Ar$

laserprobe dating to structurally well defined white micas will help to constrain the timing of the fabric forming events during the ductile deformation and the possible temporal difference in the observed directions of tectonic transport in the Pelion Massif. Additionally, the integration of the $^{40}Ar/^{39}Ar$ laserprobe and kinematic data for the Pelion Massif, with the results of Schermer et al. (1990) and Lips et al. (1998a; chapter 4) for the Ossa-Olympos region will produce a more complete overview of the thermotectonic evolution of the Pelagonian Zone. This in turn provides a platform to re-evaluate the thermotectonic evolution for the Aegean region as a whole.

5.3 Structural setting of the Pelion Massif

The basement sequence in the Pelion Massif has been studied in the past (Ferriere, 1976; Jacobshagen & Wallbrecher, 1984) and consists of gneisses and schists of felsic to intermediate compositions, tectonically interlayered with marble and serpentinite units (see also Walcott & White, 1998; Walcott, 1998). In contrast to a well defined lithotectonostratigraphy for the Olympos and Ossa Massifs (Schermer, 1993, following dominantly, Ferriere et al., 1988; Godfriaux et al., 1988), the sequence of rocks in the Pelion Massif occurs in a regionally mylonitised interval in which the lithologies have been severely intermixed tectonically to produce a mylonitic melange. This mylonitised interval might be correlated with the lower structural levels of the metamorphic sequence in the Ossa Massif (Ambelakia and lower Pierien units, following terminology by Schermer, 1993, after Schmitt, 1983), albeit that in the Pelion Massif the sequence is drastically thinned and partly dismembered and no units at structurally lower positions than the relic blueschists are exposed (i.e. potential existence of an autochthonous series as observed in the Ossa-Olympos Massifs). Remnants of blueschist facies assemblages have been observed in the lower structural levels and are characterized by epidote-albite blueschists and rare lawsonite-albite blueschists, depending on parent lithologies. As concluded for the Ossa Massif, these blueschist rocks constrain the peak metamorphic pressure and temperature conditions to circa 7-8 kbar and 320-360°C respectively (following Evans, 1990). The mylonitic melange in the Pelion Massif is characterized by a strong greenschist facies overprint, which largely obliterates the blueschist facies fabrics.

The tectonic characteristics of the Pelion Massif are basically similar to those of the Ossa and Olympos Massifs (Schermer, 1993; Lips et al., 1998a; chapter 4) and are extensively discussed by Walcott & White (1998) and Walcott (1998). In the intensely deformed sequence of rocks of the Pelion Massif a well developed extension lineation is often observed. It parallels mineral lineations defined by aligned (blue or green) amphiboles and is characterized by stretched recrystallized quartz aggregates or stretched albite crystals. Where extension lineations are well developed, kinematic indicators such as shear band foliations or asymmetric strain shadows around rigid clasts have been used to obtain a direction of tectonic transport which indicates both a top-to-the-northeast and a top-to-the-southwest sense of shear (figure 5.1, figure 5.5). Samples with well developed mica bearing mylonitic foliations

and clear kinematics were selected for micro-structural analyses and for the characterization of the white mica populations as a prelude to $^{40}Ar/^{39}Ar$ laserprobe experiments to directly date the fabric forming events, an approach which was successful for a similar setting in the Ossa Massif (Lips et al., 1998a; chapter 4). Samples were also collected from the eastern and western margins of the Pelagonian Zone (most likely to be correlated with levels of the Pierien unit); in the Antihassia Mountains, near the village of Longa (figure 5.1, location 1), and from the island of Skiathos, near Troulos (figure 5.1, location 11), because the margins appear to have been totally overprinted by greenschist facies metamorphism or, alternatively, have escaped blueschist facies metamorphism. Sample locations and their deduced directions of tectonic transport are indicated in figure 5.1. Following $^{40}Ar/^{39}Ar$ laserprobe experiments, the kinematic data and $^{40}Ar/^{39}Ar$ fabric ages are combined to characterize the temporal and regional distribution of the directions of tectonic transport.

5.4 $^{40}Ar/^{39}Ar$ laserprobe dating

5.4.1 Analytical techniques

The selection and separation of white mica single crystals and multigrain populations for $^{40}Ar/^{39}Ar$ laserprobe analyses have been carried out in a similar way as described by Lips et al. (1998a; presented in chapter 4). In summary, different white mica generations were identified and characterized in the field and, subsequently, in thin section by optical microscopy and SEM studies. The metamorphic assemblage of the mylonitic fabric was determined in thin section and the mica generations were selected. In the present study a maximum of two mica generations were separated for every sample. Large sized muscovite porphyroclasts in mylonites were used to deduce the protolith thermal histories. After establishing these, recrystallized white micas (phengitic in composition), associated with the mylonitic foliation were selected to date the fabric development of the mylonite. The muscovite porphyroclasts have an average diameter of circa 500-800 μm, the largest recrystallized white micas in the mylonitic foliation have average diameters which range from circa 100 μm to circa 500 μm. After selection, the samples were crushed and then sieved firstly into 250 μm size intervals. Subsequently, the micas were separated in these sieve intervals using a Faul vibration table and sieved a second time into narrower 50 μm size intervals. Before final handpicking, some samples were further separated using a Frantz magnetic separator and heavy liquids to minimise any contribution from a multigeneration white mica population in the final mica separate. $^{40}Ar/^{39}Ar$ laserprobe analyses and data regression techniques were also carried out in a similar way as described by Lips et al. (1998a; chapter 4). It is essential that contamination with fragments of micas belonging to other populations, is minimized. To achieve this, it was decided to work with the smallest possible amount of material (i.e. less than circa 0.5 mg). A side effect is that some low temperature steps of the stepwise heating experiments contained very little argon and hence, show rather large uncertainties.

5.4.2 Results of $^{40}Ar/^{39}Ar$ laserprobe dating on samples from the Pelion Massif

The age spectra of the $^{40}Ar/^{39}Ar$ laserprobe experiments on samples from the locations are

presented in figure 5.2 with a two sigma analytical error. Age spectra from muscovite porphyroclasts and from mylonitic fabrics or spectra from the same sampling area have been combined in single diagrams. The relevance of the obtained ages is further outlined in table 5.1 and presented in figure 5.4. To arrive at the initial regional thermal conditions, the $^{40}Ar/^{39}Ar$ laserprobe ages which were obtained from the muscovite porphyroclasts have been combined with published data from Schermer et al. (1990) and Lips et al. (1998a; chapter 4) in figure 5.3. The results show a regional preservation of pre-Alpine and Early

loc#	sample description	analysed	transport direction	age ± 2σ (Ma)	comments
A:1.	greenschist mylonite	porphyroclast	-	108.2±5.1	cooling age
		mylonitic foliation	SW	89.0±2.7	fabric age
M:2.	greenschist mylonite[1, 2]	porphyroclast	-	149.9±5.4	cooling age
		mylonitic foliation	SW	143.1±4.2	cooling age
M:3.	greenschist4	foliation	-	121.2±4.0	cooling age
P:4.	greenschist mylonite	porphyroclast	-	293.6±4.7	cooling age
		mylonitic foliation	ambiguous	—	too fine grained[5]
P:5.	greenschist mylonite	mylonitic foliation	ambiguous	37.1±1.1	fabric age
	greenschist mylonite	mylonitic foliation	NE	21.5±1.8	fabric age
	greenschist mylonite	mylonitic foliation	NE	15.5±3.2	fabric age
P:6.	greenschist mylonite[2]	mylonitic foliation	NE	34.9±2.6	fabric age
	calc-mylonite	mylonitic foliation	NE	15.5±2.0	fabric age
P:7.	greenschist mylonite	porphyroclast	-	293.1±3.5	cooling age
		mylonitic foliation	NE	20.7±2.7	mixed age
	greenschist mylonite[3]	mylonitic foliation	SW	26.8±4.1	fabric age
P:8.	greenschist mylonite	porphyroclast	-	304.8±4.9	cooling age
		mylonitic foliation	NE	—	too fine grained[5]
P:9.	greenschist mylonite	porphyroclast	-	95.3±3.7	cooling age
		mylonitic foliation	NE	53.8±5.9	fabric age
	greenschist mylonite	mylonitic foliation	SW	39.1±1.6	fabric age
	greenschist mylonite	mylonitic foliation	SW	39.4±1.5	fabric age
P:10.	greenschist mylonite	mylonitic foliation	NE	32.3±1.25	fabric age
S:11.	greenschist mylonite[2]	porphyroclast	-	218.2±5.8	cooling age
		mylonitic foliation	ambiguous	92.9±2.7	fabric age

Table 5.1. Summary of kinematic analyses and $^{40}Ar/^{39}Ar$ laserprobe results of white mica generations from the Pelion Massif (P), Antihassia Mountains (A), Mavrovouni Massif (M) and Skiathos (S). Greenschists main constituents; quartz, albite, epidote, white mica, chlorite ± actinolite ± calcite; calc-mylonite; calcite, quartz, white mica ± chlorite; [1]) sample contains relic garnet, [2]) sample contains relic biotite, [3]) sample contains relic glaucophane, [4]) sample contains blue-green amhibole, [5]) fraction size below 63 μm.

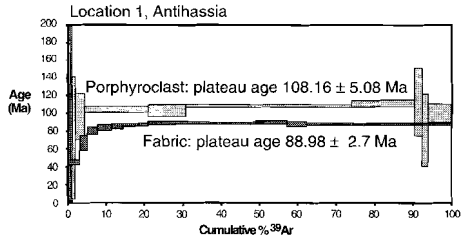
Location 1, Antihassia
Porphyroclast: plateau age 108.16 ± 5.08 Ma
Fabric: plateau age 88.98 ± 2.7 Ma
Age (Ma)
Cumulative %39Ar

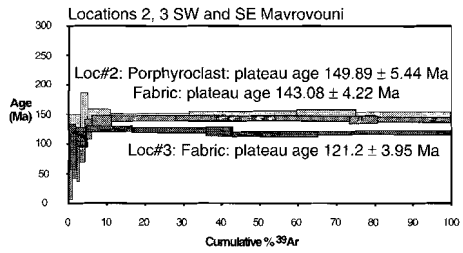
Locations 2, 3 SW and SE Mavrovouni
Loc#2: Porphyroclast: plateau age 149.89 ± 5.44 Ma
Fabric: plateau age 143.08 ± 4.22 Ma
Loc#3: Fabric: plateau age 121.2 ± 3.95 Ma
Age (Ma)
Cumulative %39Ar

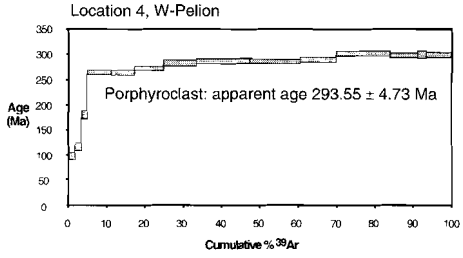
Location 4, W-Pelion
Porphyroclast: apparent age 293.55 ± 4.73 Ma
Age (Ma)
Cumulative %39Ar

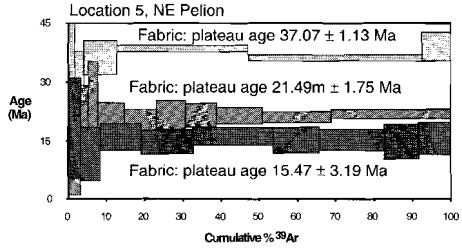
Location 5, NE Pelion
Fabric: plateau age 37.07 ± 1.13 Ma
Fabric: plateau age 21.49m ± 1.75 Ma
Fabric: plateau age 15.47 ± 3.19 Ma
Age (Ma)
Cumulative %39Ar

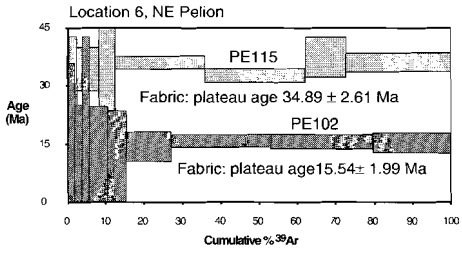
Location 6, NE Pelion
PE115
Fabric: plateau age 34.89 ± 2.61 Ma
PE102
Fabric: plateau age15.54± 1.99 Ma
Age (Ma)
Cumulative %39Ar

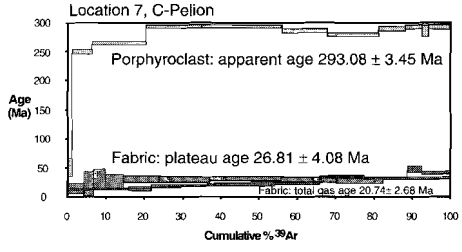
Location 7, C-Pelion
Porphyroclast: apparent age 293.08 ± 3.45 Ma
Fabric: plateau age 26.81 ± 4.08 Ma
Fabric: total gas age 20.74± 2.68 Ma
Age (Ma)
Cumulative %39Ar

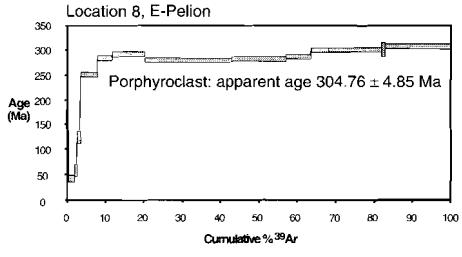
Location 8, E-Pelion
Porphyroclast: apparent age 304.76 ± 4.85 Ma
Age (Ma)
Cumulative %39Ar

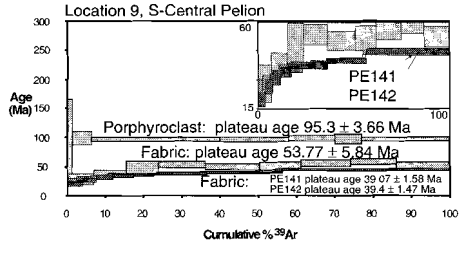
Location 9, S-Central Pelion
PE141
PE142
Porphyroclast: plateau age 95.3 ± 3.66 Ma
Fabric: plateau age 53.77 ± 5.84 Ma
Fabric:
PE141 plateau age 39.07 ± 1.58 Ma
PE142 plateau age 39.4 ± 1.47 Ma
Age (Ma)
Cumulative %39Ar

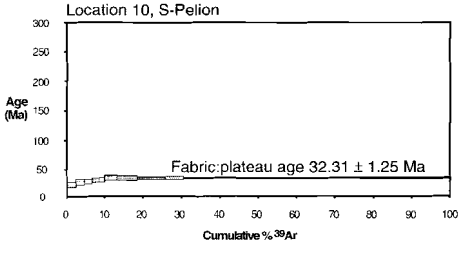
Location 10, S-Pelion
Fabric:plateau age 32.31 ± 1.25 Ma
Age (Ma)
Cumulative %39Ar

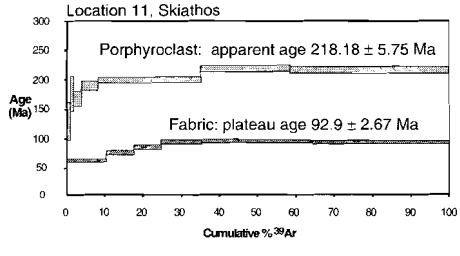
Location 11, Skiathos
Porphyroclast: apparent age 218.18 ± 5.75 Ma
Fabric: plateau age 92.9 ± 2.67 Ma
Age (Ma)
Cumulative %39Ar

Alpine cooling ages, which cluster around 280-300 Ma and 100-120 Ma, with the local occurrence of some intermediate ages. The regional preservation of a pre-Tertiary argon isotopic signature in the porphyroclasts indicates that subsequent metamorphic temperatures were low enough to preserve the $^{40}Ar/^{39}Ar$ isotopic signatures in white mica of the Alpine deformational fabrics. The preservation of these signatures permits the direct dating of the mylonite forming events by $^{40}Ar/^{39}Ar$ analyses of recrystallized white micas defining the mylonitic foliations, as long as the preservation of the argon isotopic signature in white mica is not obscured by excess argon (e.g. due to crystallization of white mica in an oversaturated Ar environment), and/or by argon loss (e.g. due to diffusion loss from the fabric micas with a, dominantly, slightly finer grainsize; chemical alteration, subsequent recrystallization etc.). The 143.1±4.2 Ma age from the mylonitic fabric of the Mavrovouni Massif (figure 5.2, location 2) is concluded to be a cooling age, as the result is not significantly younger than the age obtained from muscovite porphyroclasts of the same sample (149.9±5.4). Fabric ages from recrystallized micas from Antihassia (figure 5.2, location 1) and Skiathos (figure 5.2, location 11) both fall in the range around 90 Ma. All ages from the Pelion Massif were obtained from $^{40}Ar/^{39}Ar$ analyses of mylonitic foliations, which formed under greenschist facies conditions, following older HP metamorphism, and have ages ranging from 54 to 15 Ma (figure 5.2, table 5.1). The results tend to rule out the interpretation that the obtained fabric ages can be interpreted as cooling ages related to slightly lower temperatures (e.g. circa 350°C) than the closure temperatures for the muscovite porphyroclasts (e.g. circa 400°C). Such a scenario would have resulted, dominantly, in a homogeneous spread of data across the region, which is not reflected by the data, as several different fabric ages have been obtained from the same locations or nearby locations. It is shown in several spectra that some loss of argon has occurred in several mica populations (e.g. location 9, 10), which resulted in the produced lower ages in the first steps of the spectrum. This partial argon loss might be caused by diffusion of argon when the mica had been positioned for a long time interval at ambient temperatures, which still fall in the lower limits of the argon closure temperature range (e.g. 330°C). It is more likely however that some fabric micas have been affected by minor recrystallization or chemical alteration at younger times, which caused argon loss at the rims of the mica crystals.
In general, the consistency of the fabric age data suggest that a reliable dataset has been obtained, which can be used to further constrain the tectonothermal history of the Pelion

Figure 5.2. - Age spectra obtained by $^{40}Ar/^{39}Ar$ laserprobe incremental heating experiments. All analytical errors are in a 2σ interval. Location numbers as indicated in figure 5.1, significance of selected samples are outlined in table 5.1. Spectra which have been combined in one diagram, represent: i) analyses of two mica generations obtained from one single sample, i.e. porphyroclast cooling age versus mylonitic fabric age (e.g. location 1, location 2, location 11), ii) analyses of mylonitic fabric ages from different samples from the same sample area (e.g. location 5, location 6), iii) a combination of the porphyroclast cooling age versus mylonitic fabric age from one sample plus additional mylonitic fabric ages from samples of the same sample area (location 7; porphyroclast cooling age and 20.7 Ma total gas age from the same sample, 26.8 Ma fabric age from additional sample; location 9; porphyroclast cooling age and 53.7 Ma fabric age from the same sample, 39.1 and 39.4 Ma fabric ages from additional samples). Inset in age spectrum of location 9 presents close-up of the age spectra in the 15 to 60 Ma age interval over 0% to 100% of the cumulative ^{39}Ar fraction).

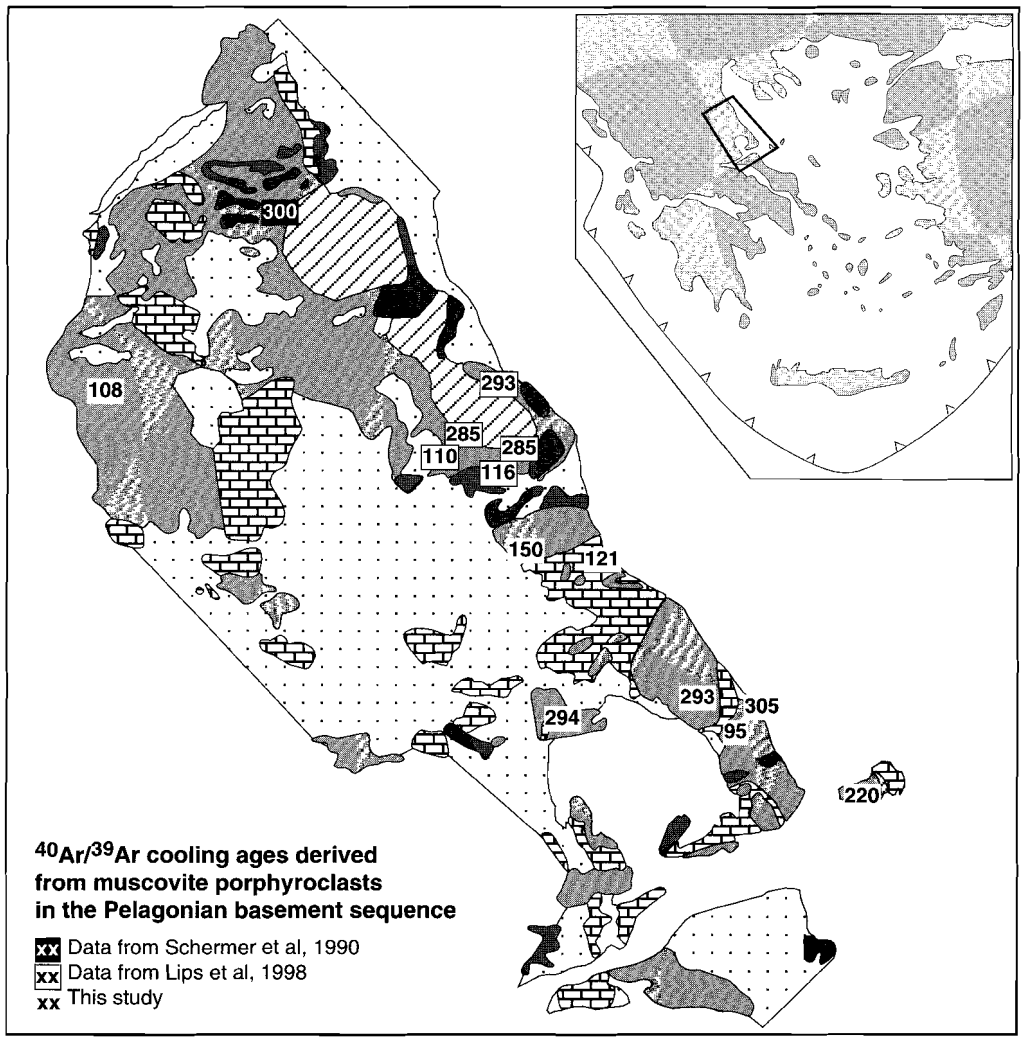

Figure 5.3. - Simplified geological map (modified after IGME, 1983) showing the spatial distribution of $^{40}Ar/^{39}Ar$ muscovite porphyroclast cooling ages.

Figure 5.4. - Summary of the thermotectonic events in the Pelagonian Zone. Data on the left side, Pelion data (this study), have been used in conjunction with data from the Olympos-Ossa area (right side) from Schermer et al (1990), and Lips et al (1998a; chapter 4). Sample frequency corresponds to ages obtained from individual samples. Thin vertical bars between age-axis and shaded horizontal bars (age domain), represent two sigma individual samples (data from this study, left side, and Lips et al, 1998a; chapter 4, right side). Light shaded age domains represent cooling ages, dark shaded age domains represent fabric ages. Tectonic transport directions obtained from individual samples (figure 5.1, this study, and Lips et al, 1998a; chapter 4) are presented; size of arrow represents number of samples with comparable kinematics.

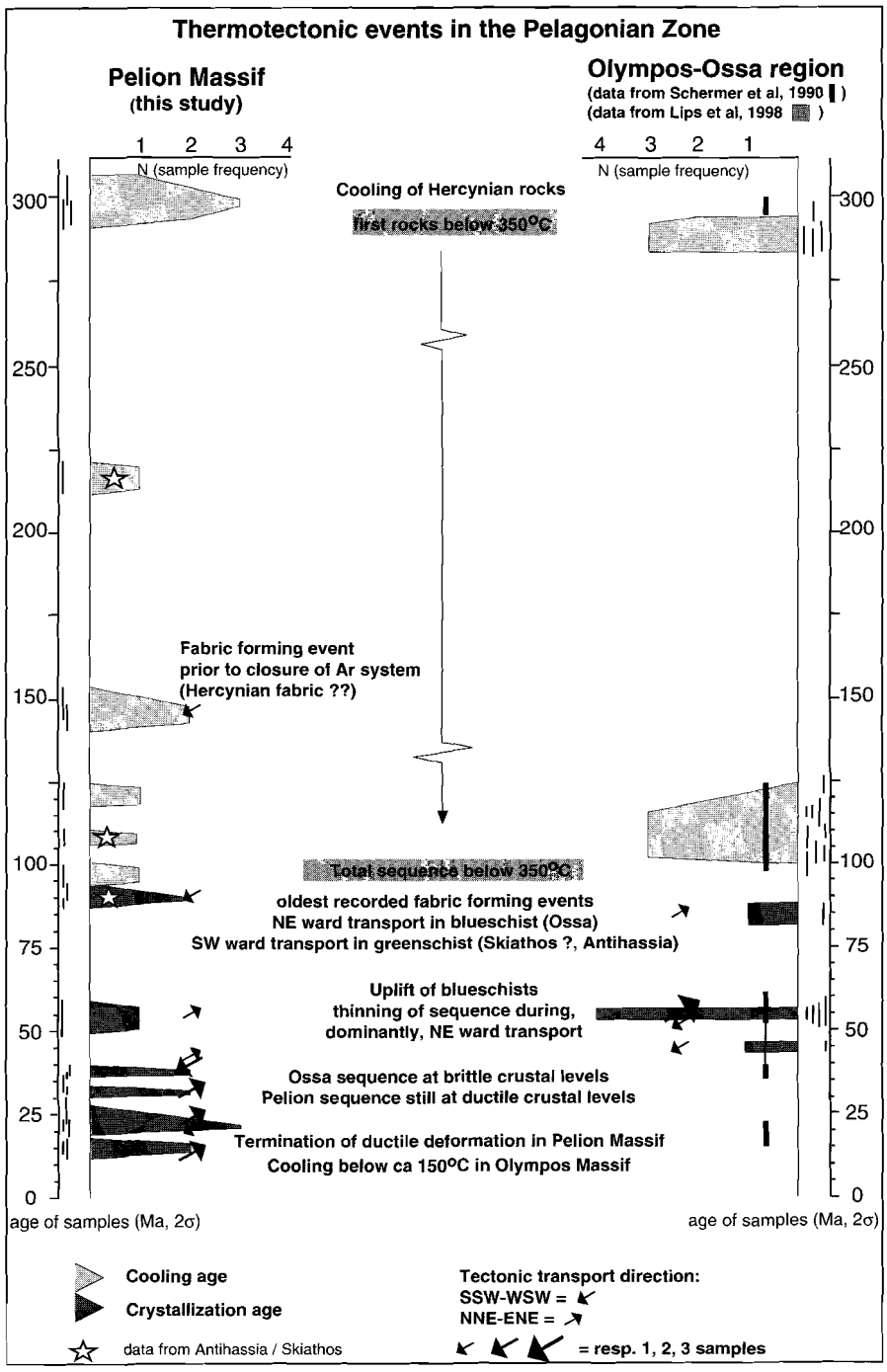
Thermotectonic events in the Pelagonian Zone
Pelion Massif
(this study)
Olympos-Ossa region
(data from Schermer et al, 1990)
(data from Lips et al, 1998)
1 2 3 4
N (sample frequency)
4 3 2 1
N (sample frequency)
Cooling of Hercynian rocks
first rocks below 350°C
Fabric forming event
prior to closure of Ar system
(Hercynian fabric ??)
Total sequence below 350°C
oldest recorded fabric forming events
NE ward transport in blueschist (Ossa)
SW ward transport in greenschist (Skiathos ?, Antihassia)
Uplift of blueschists
thinning of sequence during,
dominantly, NE ward transport
Ossa sequence at brittle crustal levels
Pelion sequence still at ductile crustal levels
Termination of ductile deformation in Pelion Massif
Cooling below ca 150°C in Olympos Massif
300
250
200
150
100
75
50
25
0
age of samples (Ma, 2σ)
age of samples (Ma, 2σ)
Cooling age
Crystallization age
data from Antihassia / Skiathos
Tectonic transport direction:
SSW-WSW =
NNE-ENE =
= resp. 1, 2, 3 samples

Massif. The greenschist mylonite fabric ages imply that blueschist facies metamorphism in the Pelion is older than 54 Ma. The mylonite ages have been combined with the established directions of tectonic transport to summarize the temporal distribution of the tectonic transport directions (figure 5.4, left panel). During the 54 Ma to 15 Ma interval existing mylonitic structures have been reactivated. This is best illustrated by the studied samples from location 9 (figure 5.2, table 5.1; near the village of Neohori) by the 39 Ma top-to-southwest directed mylonitic fabric which occurred in the same mylonitic interval as the 54 Ma top-to-northeast directed mylonitic fabric. In the field both mylonitic fabrics in the zone were interpreted to have formed as a result of a single phase of layer parallel stretching, but the $^{40}Ar/^{39}Ar$ laserprobe results show that they represent two separate events during which tectonic transport was reversed. The final stage of ductile deformation in the Pelion Massif is characterized by a protracted event, with layer parallel extension, from circa 40 Ma till 15 Ma (figure 5.4, left panel), producing a domal structure, after which it was crosscut by high angle brittle faults.

5.5 Thermotectonic evolution of the Pelagonian Zone

The results of the current study together with those of Schermer et al. (1990) and Lips et al. (1998a; chapter 4) provide an improved insight into the thermotectonic evolution of the Pelagonian Zone as a whole. The fabric forming events in the Pelion Massif and Olympos-Ossa Massifs are summarized in figure 5.4, and are discussed below in chronological order (from oldest to youngest). Figure 5.4 shows that the Pelagonian basement, which is currently exposed at the surface, had regionally cooled to circa 350±30°C by 100 Ma. The two dominant clusters of cooling ages, which occur in the Pelion Massif, had also been established in the Ossa Massif (Lips et al., 1998a; chapter 4; figure 5.4 right panel) and are related to the relative position of individual thrust sheets in the tectonostratigraphic sequence (figure 5.5). In the Ossa Massif, Hercynian porphyroclast cooling ages (~300 Ma) were derived from the basal thrust sheet of the allochthonous sequence and Cretaceous cooling ages (~110 Ma) were derived from a thrust sheet, which was in a relatively higher tectonostratigraphic position. In contrast to the proposed tectonostratigraphical distribution in the Olympos and Ossa Massifs, which has been related to a circa 110 Ma phase of basement imbrication, and was based on the distribution of clusters of Hercynian (lower structural levels) versus Cretaceous (higher structural levels) muscovite cooling ages, it is concluded that the formation of a mylonitic melange under post circa 54 Ma greenschist facies conditions has strongly affected the tectonostratigraphical order of the Pelion Massif, obliterating the potential regional correlation of these characteristic tectonostratigraphic intervals (figure 5.5).

The mylonite forming events, as recorded in the Pelagonian Zone, illustrate that the oldest Alpine fabric forming event, which is directly datable by the applied technique, occurred around 85-90 Ma. It has been recorded in greenschist facies mylonites (Antihassia and Skiathos) and blueschist facies mylonites (Ossa Massif). The tectonic significance of the conflicting tectonic transport directions, being regionally top-to-southwest for the Antihassian

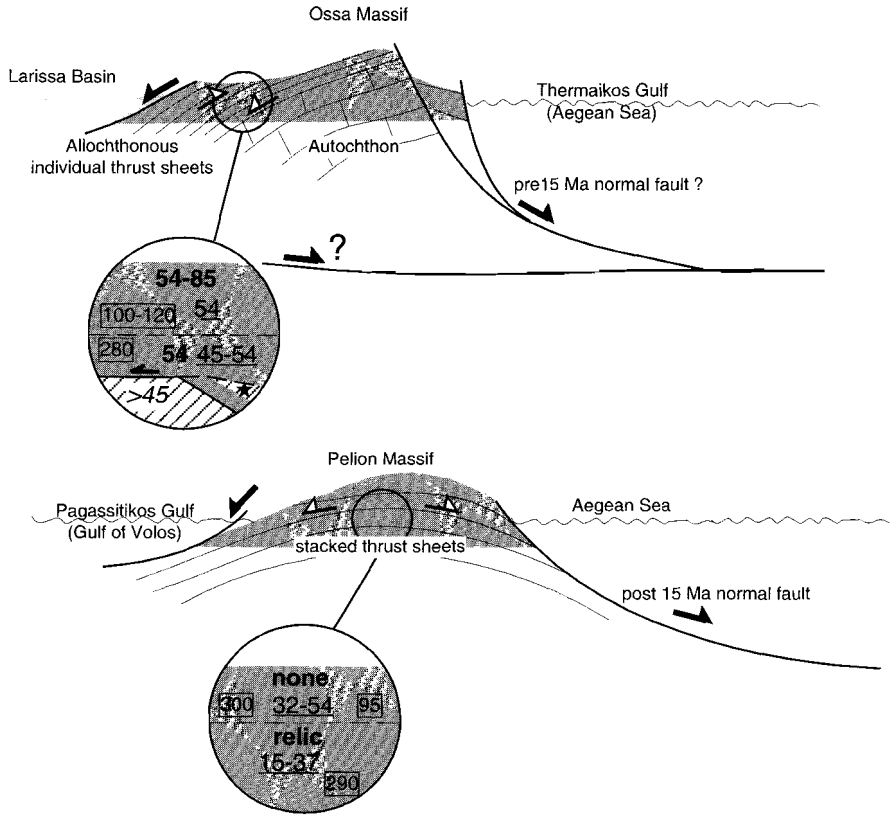

Figure 5.5. - Cartoon illustrating different tectonic scenario within the Ossa Massif compared to the Pelion Massif at Miocene times. In blow-ups; structural position of obtained chronological data (Ossa data, biostratigraphic age after Derycke & Godfriaux, 1978; $^{40}Ar/^{39}Ar$ ages after Lips et al, 1998a; chapter 4, this study: Pelion data; $^{40}Ar/^{39}Ar$ ages, this study); biostratigraphical age (italic); $^{40}Ar/^{39}Ar$ laserprobe white mica ages; porphyroclast cooling age (squares), blueschist fabrics (bold), greenschist fabrics (underlined). Star symbol in upper blow-up represents structural position of lawsonite bearing Tertairy flysch, after Derycke & Godfriaux (1978).

sample and locally top-to-northeast for the Ossa sample, would suggest that transport reversal at deeper structural levels might have taken place. The youngest blueschist facies mylonitic fabrics in the Pelagonian Zone were found in the Ossa-Olympos region and cluster around 54 Ma (Schermer et al., 1990; Lips et al., 1998a; chapter 4). The 54 Ma blueschist facies fabrics have formed during the same event as greenschist facies mylonitic fabrics which have been observed in the Ossa and Pelion Massifs. The observations are that HP metamorphism in the Pelagonian basement sequence had terminated by 54 Ma. The observation of lawsonite bearing Eocene (allochthonous) flysch intercalations in the Ossa Massif (Derycke & Godfriaux, 1978) indicates that parts of the flysch sequence experienced elevat-

ed pressures during southwestward transport of the basement sequence (which already was, or had been, affected by HP metamorphism) across the autochthonous Olympos-Ossa sequence, which resulted in the present-day observed tectonostratigraphical order by circa 40 Ma (figure 5.5).
After transport of the basement sequence across platform carbonates and phyllites in the Olympos-Ossa region by circa 45 Ma, relative uplift might have been accelerated by the rebound of the low density carbonates underlying the basement sequence. The result is the positioning of the currently exposed Olympos-Ossa sequence at (semi-)brittle crustal conditions by circa 36 Ma and, consequently, the absence of any ductile deformational events during Oligocene and Miocene times. The youngest recorded white mica ages in the Olympos region have been dated at 36-40 Ma (Schermer et al., 1990) and have been related by Schermer (1993) to a phase of top-to-southwest tectonic transport. In contrast to the termination of ductile deformation in the Ossa-Olympos region by circa 36-40 Ma, the basement sequence of the Pelion Massif experienced continued ductile deformation at greenschist facies conditions from circa 40 Ma till 15 Ma, with younger ductile fabrics located in the lower structural levels (figure 5.5). The continued greenschist facies deformation is reflected by the development of the mylonitic domal structure in the Pelion Massif and the contrasting morphology of the Olympos and Ossa domes (see figure 5.5 and Schermer et al., 1990).

5.6 Exhumation histories of Aegean high pressure sequences

The P-T-t evolution of the Pelion Massif (star symbols in figure 5.6a) went through four phases as outlined above. They are, in summary: 1) cooling of basement rocks below circa 350±30°C under greenschist facies conditions (pressures of circa 4-6 kbar) by circa 100 Ma, 2) peak HP conditions of 7-8 kbar and 320-360°C before circa 54 Ma; with continued greenschist facies metamorphism at shallower crustal levels (pressures of circa 3-5 kbar) at circa 90 Ma in Skiathos and Antihassia, 3) ductile deformation under, post HP, greenschist facies conditions (pressures of circa 3-6 kbar, temperatures below 350±30°C), during which older fabrics were continuously overprinted and reworked, between circa 54 Ma and circa 15 Ma, 4) brittle deformation from 15 Ma to Present, which is not recorded by $^{40}Ar/^{39}Ar$ white mica dating. The results from the Ossa Massif (dots in figure 5.6a after Lips et al., 1998a; chapter 4) further constrain the Early Alpine history by the recording of the onset of HP metamorphism in the Pelagonian region after 110 Ma, the 85 Ma HP mylonitic fabric and the 54 Ma deformational event which is related to the termination of blueschist facies metamorphism. The Oligocene-Early Miocene ductile deformation in the Pelion Massif (15 and 21 Ma see starred ages in figure 5.6a) shows the contrast to the recorded brittle deformation which affected the Olympos at the same time (see squared ages in figure 5.6a, Schermer et al., 1990), where Early Miocene brittle deformation is illustrated by 16-23 Ma K-feldspar cooling ages, which indicate that temperatures were below circa 200±50°C (left column in figure 5.6a indicates the closure temperature range in K-feldspar).

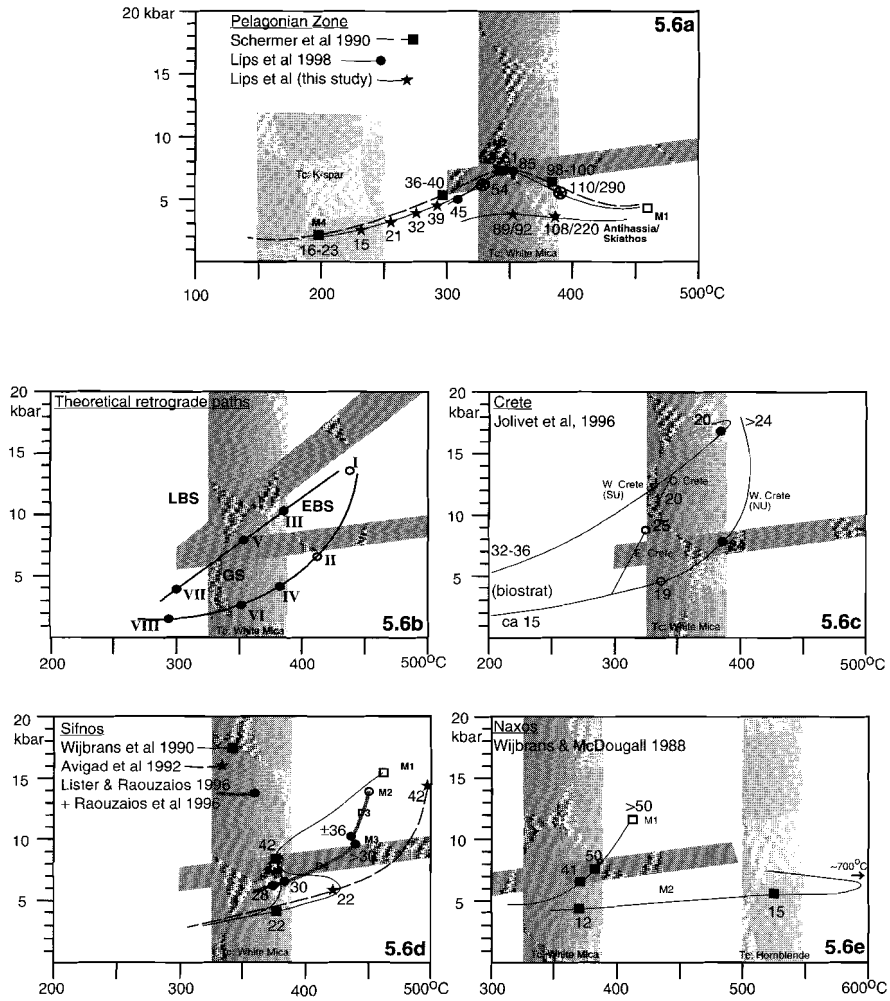

Figure 5.6. - Summary of retrograde P-T-t paths for basement rocks from different blueschist facies settings in the Aegean region. a) Pelagonian Zone (Schermer et al, 1990; Lips et al, 1998a; chapter 4; this study); b) theoretical retrograde paths of high pressure metamorphic sequence, positions I to VIII are discussed in text; c) Crete (Jolivet et al, 1996); d) Sifnos (Wijbrans et al, 1990; Avigad, 1992; Lister & Raouzaios, 1996; Raouzaios et al, 1996); e) Naxos (Wijbrans & McDougall, 1988). Open symbols indicate PT information, not constrained by $^{40}Ar/^{39}Ar$ dating results, filled symbols represent P-T-t information constrained by $^{40}Ar/^{39}Ar$ dating results (timing either obtained by correlation or direct analysis). Vertical columns represent average argon closure temperature ranges in white mica (Tc: white mica), hornblende (Tc: hornblende), and K-feldspar (Tc: K-spar) (average closure temperature ranges of white mica (figures 5.6a-e), hornblende (figure 5.6d), and K-feldspar (figure 5.6e) after Berger & York, 1981; Harrison, 1981; Harrison & McDougall, 1982; Sisson & Onstott, 1986; McDougall & Harrison, 1988; von Blanckenburg et al, 1989; Baldwin et al, 1990; Hanes, 1991; Hames & Hodges, 1993; Hodges et al, 1994). Dark shaded regions represent position of transition reactions of metamorphic stability fields; LBS = Lawsonite-Blueschist facies, EBS = Epidote-Blueschist facies; GS = Greenschist facies (after Evans, 1990).

The extended P-T-t history of the Pelagonian Zone allows comparison with existing P-T-t data from the Cycladic region (Sifnos and Naxos island) and from Crete to place the results in a wider regional perspective. Before comparison of the retrograde paths from Crete, Sifnos and Naxos with the Alpine P-T-t path from the Pelagonian Zone, two model P-T-t paths are presented (figure 5.6b) which will be discussed in detail. These model P-T-t paths will help to clarify the role of the argon closure temperature range for white mica in the blueschist-greenschist transition domain on the obtained P-T-t information.
The model retrograde paths (figure 5.6b) are presented for a HP metamorphic sequence which was affected by two hypothetical fabric forming events during the retrograde history (at temperatures around 350°C and 300°C respectively). The two model retrograde paths start at HP metamorphic conditions of circa 14 kbar and 450°C (figure 5.6b, point I). As the metamorphic temperature at peak HP conditions are too high to preserve the argon isotopic signature in white mica, the oldest recorded $^{40}Ar/^{39}Ar$ white mica age will be a cooling age (figure 5.6b, points III, IV), obtained when temperatures drop below circa 350±30°C. The PT conditions which are linked to the cooling ages might be actually located in the blueschist field (figure 5.6b, point III) or in the greenschist field (figure 5.6b, point IV), dependent on the cooling path followed. The ambient metamorphic conditions at the time of closure of the argon system in white mica are, in both cases, at pressures and temperatures much lower than indicated by the observed peak metamorphic assemblage of the selected sample. In addition to the lower cooling path, a blueschist to greenschist transition might be obtained from petrological investigations (figure 5.6b, point II), which also will not be recorded in the $^{40}Ar/^{39}Ar$ white mica ages. After closure of the argon isotopic system in white mica, newly formed metamorphic fabrics and/or deformational fabrics will be directly recorded in the argon signature of white mica. The two hypothetical deformational events might reflect either a fabric forming event at blueschist facies conditions (figure 5.6b, point V) overprinted by a greenschist facies deformational fabric (figure 5.6b, point VII) in the upper cooling path, or the recording of two separate fabric forming events at greenschist facies conditions (figure 5.6b, points VI, VIII) in the lower cooling path. In summary, the model retrograde P-T-t paths demonstrate that important differences in the thermotectonic significance of the observed $^{40}Ar/^{39}Ar$ white mica cooling ages and fabric development ages (i.e. cooling ages in the retrograde path after HP metamorphism or fabric forming ages under greenschist and/or blueschist facies conditions) are dependent upon subtle differences in the cooling path followed.

The investigation of the published P-T-t path from Crete (figure 5.6c) illustrates the relationships between retrograde metamorphic conditions and closure of the argon isotopic system. The path shows that the relevant chronological information is obtained in the temperature range below 350±30°C. As parts of the basement sequence of Crete have not experienced temperatures above 350±30°C during HP metamorphism, the age of near peak HP metamorphism of these parts is constrained at circa 20 Ma (figure 5.6c upper retrograde path, Western Crete, Southern Unit; after Jolivet et al. 1996). Other parts of the basement from Crete (figure 5.6c, lower retrograde path, Western Crete, Northern Unit; after Jolivet et al., 1996) have followed retrograde PT paths which are characterized by a phase of

isothermal decompression following HP metamorphism. Because ambient metamorphic temperatures might have been too high to preserve the argon isotopic signature in the white mica of the HP assemblage, the $^{40}Ar/^{39}Ar$ white mica ages at 24 Ma might constrain the cooling of this part of the sequence to circa 350±30°C. Biostratigraphical data from Crete confines the onset of HP metamorphism to be post 32 Ma (youngest ages of units involved in HP metamorphsim) and the last phase of exhumation to be circa 15 Ma (oldest age of non-metamorphosed units overlying the metamorphosed sequence).
The published retrograde paths from Sifnos in the central Cyclades (figure 5.6d) reflect conflicting P-T-t paths as the absolute ages that have been obtained (Raouzaios et al., 1996; Wijbrans et al., 1990) have been related to different metamorphic conditions (e.g. Wijbrans et al., 1990; Avigad et al., 1992). As peak metamorphic temperatures have been too high, $^{40}Ar/^{39}Ar$ white mica ages will reflect cooling to circa 350±30°C. The P-T-t information indicates that the recording of $^{40}Ar/^{39}Ar$ white mica ages of circa 42 Ma and younger occurred when the HP sequence of Sifnos had already been exhumed to crustal levels equivalent to pressures of circa 8-10 kbar. It also indicates that the initial retrograde metamorphic history (i.e. directly following peak HP metamorphism) with pressures decreasing from 14-16 kbar to 8-10 kbar is not constrained by $^{40}Ar/^{39}Ar$ white mica ages.
The P-T-t path from Naxos in the south-central Cyclades (figure 5.6e) is constrained by two dominant metamorphic events. The first event is a HP metamorphic event (figure 5.6e, M1) with temperature conditions which are, like Sifnos, too high to preserve the argon isotopic signature in white mica. Cooling of the HP sequence records circa 50 Ma $^{40}Ar/^{39}Ar$ white mica ages which are related to pressure and temperature conditions lower than the peak metamorphic conditions, indicating that the timing of peak HP metamorphism (figure 5.6e, M1) is older than the 50 Ma white mica cooling ages. The second event (figure 5.6e, M2) is related to the development of the Naxos migmatitic dome at Early Miocene times and is characterized by HT-LP metamorphism (see Andriessen et al., 1979). Depending upon the location of the retrogressed HP sequence with respect to the migmatite dome, $^{40}Ar/^{39}Ar$ white mica ages may have been reset and will record cooling of this Miocene thermal event (summarized in John & Howard, 1995). Initial cooling after the thermal event has been constrained by a circa 15 Ma $^{40}Ar/^{39}Ar$ hornblende cooling age which is also indicated in figure 5.6e (the right column indicates the closure temperature range in hornblende: 525±25°C) and continued untill circa 11 Ma (cooling ages on biotite, Wijbrans & McDougall, 1988; average closure temperature ~300°C).

In summary, the four P-T-t paths from the Aegean area presented in figure 5.6 show that the ages obtained from HP assemblages have different possible meanings. They reflect prograde, peak metamorphic, and retrograde episodes in the Pelagonian Zone and on Crete, and only retrograde metamorphic episodes in the Cycladic region. An estimate of timing of peak HP metamorphism in the Cyclades has been obtained by thermal modelling of the existing P-T-t data from Sifnos (Wijbrans et al., 1993) and resulted in a suggested minimum age of peak pressure metamorphism of around 60 Ma. However, as real rocks often show more complex histories than can be accommodated in numerical models, we contend that individual thrust sheets may have experienced locally different prograde HP paths. It is

shown that the first stage of exhumation in the Cyclades, with a corresponding pressure decrease of circa 6 kbar is hidden in the pre-Eocene tectonic history.

5.7 Summary and conclusions

The continental margin of Eurasia, as exposed in the Hellenides, shows evidence for subduction related HP metamorphism and subsequent ductile deformation under retrograde conditions. The regional preservation of relic Hercynian white mica ages reflects the lower maximum temperatures reached in the Pelagonian Zone in the north compared to the Cyclades and Crete in the south. These lower metamorphic temperatures allow direct dating of Alpine deformational fabrics in the Pelagonian Zone. Here the ductile deformation history can be traced back in time from the Miocene into the Cretaceous (figure 5.4).
The earliest, directly resolvable, fabric forming event (figure 5.4) at circa 90-85 Ma is characterized by southwestward directed transport under greenschist facies conditions from shallow parts of the Pelagonian basement (which are most likely equivalent to Pierien units and are now exposed on Skiathos and in the Antihassia mountains), while at deeper crustal levels blueschist facies mylonites developed during a northeastward direction of transport (Ambelakia and lower Pierien units; now exposed in the Ossa Massif). Whereas the oldest blueschist facies mylonitic fabric forming event is recorded at 85 Ma, the youngest recorded blueschist facies mylonitic fabrics are circa 54 Ma, seen in the Ossa Massif. This would imply that conditions favourable for HP metamorphism occurred over a timespan of at least 30 m.y. During the event at 54 Ma, the basement sequence of the Pelagonian was partially exhumed and was affected by subsequent ductile deformation at greenschist facies metamorphic conditions. Following the 54 Ma event, southwestward transport of the metamorphosed sequence to, and across, the autochthonous Olympos-Ossa sequence by circa 45 Ma caused elevated metamorphic pressures in parts of the Eocene flysch, which is related to the autochthonous sequence. This would indicate that the emplacement of a metamorphosed basement sequence, with a recorded HP episode of circa 85-54 Ma, would have caused an HP episode with slightly younger ages (as young as circa 45 Ma) at the present-day location. The greenschist facies deformation in the Pelagonian Zone had terminated by 40-36 Ma in the Ossa-Olympos region and continued till 15 Ma in the Pelion Massif.
In the Cyclades, to the south of the Pelagonian Zone, the phengite ages obtained from HP metamorphic assemblages consistently indicate the timing of cooling after HP metamorphism and cluster around 40 to 45 Ma, with local exceptions to slightly older ages (ca 50 Ma; Maluski et al., 1987; Wijbrans & McDougall, 1988). We suggest that the duration of the prograde and peak metamorphic episodes in the Cycladic blueschists might be similar in style to the observed history in the Pelagonian Zone, with peak HP ages in the Cyclades expected to be slightly younger than observed in the Pelagonian Zone. This hypothesis could potentially be tested by a systematic geochronological study on minerals with high isotopic closure temperatures (e.g. U-Pb zircon and monazite studies; Keay, 1998). The implications that the peak pressure conditions in the Cyclades might have been reached earlier than circa 45-50 Ma are of great importance when P-T-t paths for the region form the

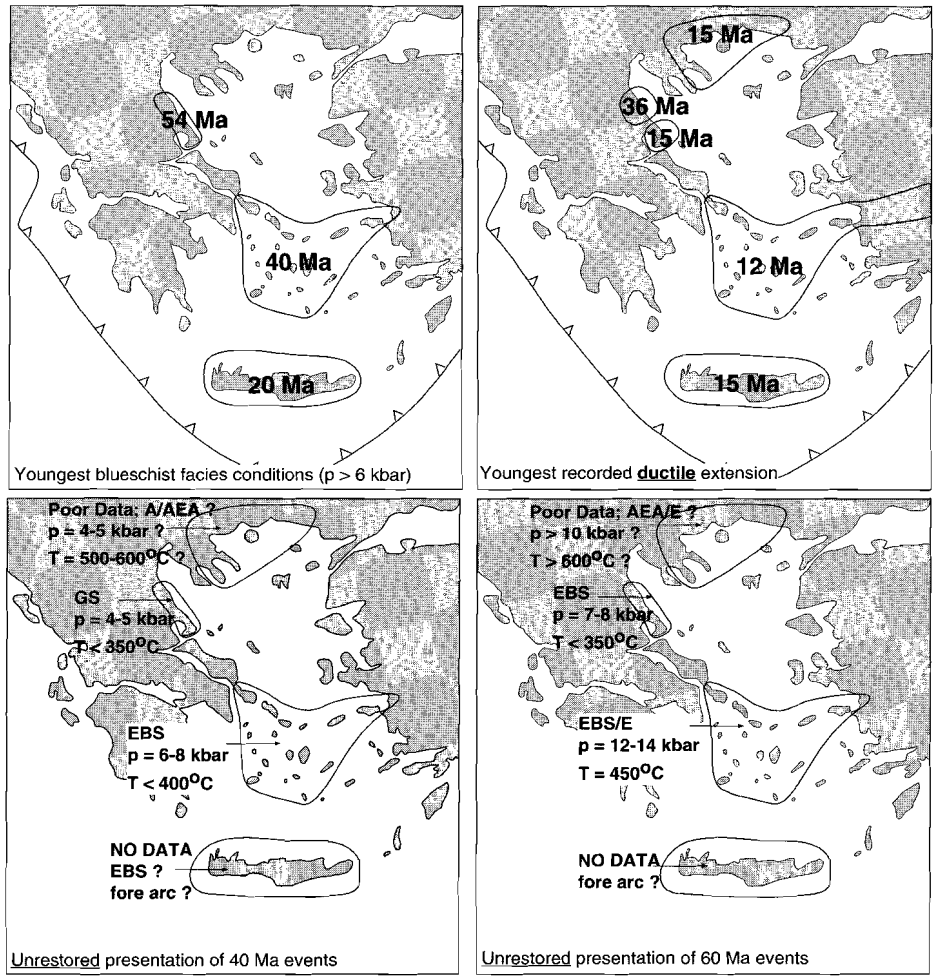

Figure 5.7. - Temporal and spatial distribution of metamorphic episodes and tectonic events in the Aegean. a) the timing of the termination of blueschist facies metamorphism, b) timing of youngest recorded ductile extension, c) and d) distribution of metamorphic events at 40 and 60 Ma, respectively (unrestored geographical distribution); P-T-t data of Rhodope region (northern region) extrapolated from data by Dinter et al (1995), Liati & Seidel (1994, 1996), Wawrzenitz & Mposkos (1997). Metamorphic stability fields; A = Amphibolite facies, AEA = Albite-Epidote-Amphibolite facies, E = Eclogite facies, EBS = Epidote-Blueschist facies; GS = Greenschist facies (after Evans, 1990).

basis of regional tectonic models (Wijbrans et al., 1993; Lister and Raouzaios, 1996). Comparison of retrograde metamorphic histories from HP localities in the Aegean shows a clear decrease in age at which blueschist facies metamorphism terminated, shifting progressively from circa 54 Ma in the Pelagonian Zone, to circa 40 Ma in the Cycladic region, and as young as circa 20 Ma on Crete. That is, younging is towards the active subduction zone (figure 5.7a). The age distribution related to recrystallization of white mica under post-

peak pressure metamorphic conditions suggests a diachronous exhumation of the high pressure rocks.

The ductile deformation had terminated in the Pelion Massif by circa 15 Ma, which is contemporaneous with the regionally recognized phase of Early Miocene extension, which also affected ductile crustal levels in the Cycladic region, Crete (figure 5.7b), the Rhodope Massif (Dinter & Royden, 1993; Dinter et al., 1995), the Menderes Massif in western Turkey (Hetzel et al., 1995), and may have extended further east into central Anatolia to the Nigde Massif (Whitney & Dilek, 1997). The 15 Ma phase of extension affected (semi-)brittle crustal levels in the Olympos Massif, where it has been identified, albeit less precisely, by Early Miocene $^{40}Ar/^{39}Ar$ K-feldspar cooling ages (figures 5.4 and 5.6a).

In contrast to the diachronous shift of termination of HP metamorphism in the Aegean towards the active subduction zone (figure 5.7a), the regionally observed phase of Early Miocene extension and subsequent termination of ductile deformation appears to be synchronous across the region (figure 5.7b). The shift from a diachronous uplift of HP sequences to a synchronous phase of ductile extension across the region at Early Miocene times suggests a change in dominant exhumation mechanism for the currently exposed Aegean basement rocks. In addition to the temporal distribution of the termination of HP metamorphism and ductile deformation in the region, a presentation of synchronous Alpine metamorphic episodes have been included to illustrate the spatial distribution of 40 and 60 Ma metamorphic conditions (figure 5.7c and 5.7d), albeit unrestored for the paleogeographical distribution. The 40 Ma and 60 Ma episodes illustrate the distribution of HT metamorphism and HP metamorphism in the prolonged history of the Aegean region and the Hellenic subduction complex.

Chapter 6

Kinematic investigations in circum-Aegean mid crustal basement

Section 6.4 submitted for publication in Terra Nova: Lips, A.L.W., D. Cassard, H. Sözbilir and H. Yilmaz: Multistage exhumation of basement rocks in western Anatolia; the Menderes Massif and Çine Submassif (Turkey).

6.1 Introduction

To investigate the regional significance of the deformational and kinematic events, which have been identified in the Pelagonian Zone west of the Aegean and extrapolated into the Cyclades and to Crete (chapter 5), additional research has been carried out in regions of outcropping mid-crustal basement in the north and east of the Aegean to give a circum Aegean coverage. Field based studies have been carried out in the Rhodope Zone of the Internal Hellenides in the northern Aegean and the Kazdag Massif of the Pontide Belt and the Menderes Massif and Çine Submassif of the Tauride Belt in the eastern Aegean (figure 2.1). After structural, kinematic and metamorphic characterization of these areas, $^{40}Ar/^{39}Ar$ laserprobe experiments have been applied to selected samples in order to obtain absolute age information in addition to the existing geochronological dataset (*Rhodope Zone*; Dinter et al., 1995; Wawrzenitz, 1997, *Kazdag Massif*; Okay et al., 1996, *Menderes Massif and Çine Submassif*; Satir & Friedrichsen, 1986; Hetzel et al. 1995b, Hetzel & Reischmann, 1996). In a regional tectonic framework, the Rhodope Zone is located at a more internal position of the Internal Hellenides than the Pelagonian Zone, the Kazdag Massif is interpreted to be located in an equivalent tectonic position to the Pelagonian Zone but in the Pontides, and the Menderes Massif and Çine Submassif are also in an equivalent tectonic position but are in the Taurides.

The three areas are characterized by the dominant presence of amphibolite facies and greenschist facies metamorphic rocks in their respective tectonostratigraphic sequences. Local enclaves of high pressure metamorphic assemblages have been reported in the Rhodope Zone and in the Menderes Massif (Liati & Seidel, 1996; Dora et al., 1997) and as part of an ophiolitic melange in the Kazdag Massif (Okay et al., 1991). In principle, the investigations in this study are concerned with the timing of the formation of these HP assemblages and their temporal relevance to the assembling of each tectonostratigraphic sequence. Additionally, the studies are also concerned with the investigation of the spatial and temporal characteristics of the Early Miocene extensional event which has been recognized across the Aegean region (see chapter 5).

The results of the studies, which will be presented in three subchapters, will facilitate a regional correlation of the results from the Pelagonian Zone (chapter 4 and 5) and the

extensive published dataset from other areas in the Aegean region in order to identify and differentiate local and regional deformational events. Ultimately, such a correlation should lead to the characterization the Tertiary kinematic history of the whole Aegean region and the tectonic evolution of the high pressure metamorphic assemblages in relation to this kinematic history.

6.2 Middle - Late Alpine thermotectonic evolution of the Rhodope Massif, Internal Hellenides, Greece

6.2.1 Introduction

The Rhodope Zone is the easternmost isopic zone of the Internal Hellenides in mainland Greece (see chapter 2). It can be traced from the east side of the Chalkidiki peninsula in the west, where it is bounded by the eastern boundary of the Serbo Macedonian Massif, into Bulgaria where it forms the southern boundary of the NNE-ward vergent Balkan mountain belt (figure 6.1). In this study, the Serbo Macedonian Massif and Rhodope Zone have been combined and broadly termed the "Rhodope Massif", as used recently by Jones et al. (1992) and Burg et al. (1996). Generally, the Rhodope Massif represents the total region in northeastern Greece and southern Bulgaria in which metamorphic basement sequences are currently exposed. This study will be concerned with the Greek part of the Rhodope Massif.

In map view, the Rhodope Massif is characterized by a large proportion of intrusives (figure 6.1) and in the past, several studies have focussed on their chemistry and their emplacement history (de Wet et al., 1989; Koukouvelas & Pe-Piper, 1991; Jones et al., 1992; Dinter et al., 1995; Frei, 1996). In summary, the intrusives are individual plutons, chiefly granitic to granodioritic in composition or they form suites of intrusives with varying (felsic to intermediate) chemistry (e.g. Vrondou Pluton, figure 6.1, as concluded by Jones et al., 1992). The granitoids have intruded in Tertiary times, with emplacement ages varying from circa 50 Ma (de Wet et al., 1989) to circa 22 Ma (Dinter et al., 1995). Locally, Early Alpine (syn- or pre-145 Ma) granites have been observed in the western Rhodope Massif (e.g. Arnea Pluton, figure 6.1, as analysed by de Wet et al., 1989). In their study, Jones et al. (1992) concluded on the basis of geochemical data for some of the calc-alkaline felsic to intermediate granitoids, that these granititoids have resulted from the anatexis of the lower parts of an overthickened continental crust, due to thermal breakdown of hydrous minerals which were present in the imbricated crustal units, and were emplaced in an extensional regime. Jones et al. (1992) suggested that the extensional regime could be related to the extensional collapse of the Rhodope Massif.

In a recent regional study in northeastern Greece and Bulgaria, Burg et al. (1996) have subdivided the total tectonostratigraphic sequence, which hosts the granitoids, into i) a "lower terrane", hosting a schist-carbonate-gneiss sequence, overlain by ii) "intermediate thrust sheets", which are, from bottom to top, a migmatite-orthogneiss sequence, an eclogite-metabasic-gneiss sequence, an undifferentiated gneiss sequence and a gneiss-marble sequence, which are, in turn, overlain by iii) an "upper terrane", hosting a meta-ophiolite-gneiss sequence. The above sequence is covered by low grade schists and Tertiary volcanics

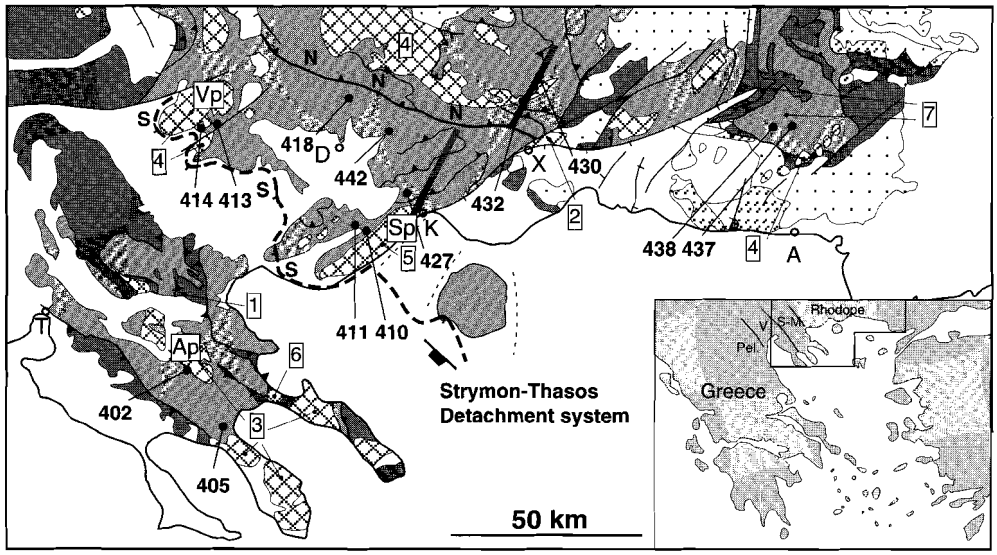

Granitoids
Tertiary volcanosedimentary cover
Low grade Mesozoic schists
Metaophiolite-gneiss (upper terrane)
Gneiss-marble-schist (lower terrane)

Nestos thrust
Strymon detachment

Section in figure 2

Ap Arnea Pluton
Vp Vrondou Pluton
Sp Symvolon Pluton

numbers in squares: previous geochronology:
1. Papadopoulos & Kilias, 1985, K-Ar
2. Liati, 1986, K-Ar
3. DeWet et al, 1989, 40Ar/39Ar
4. refs in Jones et al, 1992, K-Ar, Rb-Sr
5. Dinter et al, 1995, U-Pb, 40Ar/39Ar
6. Frey, 1996, U-Pb
7. Wawrzenitz & Mposkos, 1997, Sm-Nd, Rb-Sr

Locations mentioned in text:
T; Thessaloniki, D; Drama, K; Kavala
X; Xanthi, A; Alexandropolis

402-442 Sample locations discussed in text

Figure 6.1. - Simplified geological map of the Greek part of the Rhodope Massif (after Burg et al, 1996), presenting outcropping basement, position of the main tectonic structures (esp. Nestos Thrust and Strymon/Thasos Detachment), location of previous geochronological investigations and locations of samples used for $^{40}Ar/^{39}Ar$ laser-probe dating in this study.

and sediments. The major boundary between the lower terrane and the intermediate thrust sheets is formed by the Nestos Thrust (figure 6.1), which is interpreted to have been active in Early Eocene times, based on the youngest stratigraphic age of the Falakron marble series in its footwall (Dinter et al., 1995). Burg et al. (1996) observed a consistent direction of tectonic transport towards SSW in the lower and upper terranes, while during their study the opposite directions of tectonic transport (towards ENE and NNE) have been observed in some levels of the intermediate thrust sheets.

The tectonic evolution in the Rhodope Massif is characterized by a regional metamorphic episode which affected the basement sequences around circa 120-100 Ma (Papadopoulos & Kilias, 1985; Burg et al., 1990; Wawrzenitz & Mposkos, 1997). The metamorphic episode is

characterized by a regional amphibolite facies metamorphism and affected the intermediate and upper thrust sheets, with estimated pressures and temperatures of circa 8-11 kbar and 600-650°C respectively (Liati & Mposkos, 1990). Locally, higher metamorphic pressures and temperatures of circa 19 kbar and 700°C, overprinted by circa 15 kbar and over 800°C have been reported in parts of the intermediate thrust sheets near the village of Therme in the northern Central Rhodope (Liati & Mposkos, 1990; Liati & Seidel, 1994; 1996). The eclogite facies metamorphism is overprinted by the amphibolite facies metamorphism (Liati & Seidel, 1996; Wawrzenitz & Mposkos, 1997), although it might be a reflection of deeper crustal levels during the same metamorphic episode. Following amphibolite facies metamorphism, temperatures cooled to circa 350-400°C by Eocene times (Liati & Mposkos, 1990). Parts of the metamorphic sequence have been overlain by circa 30-35 Ma andesites (Eleftheriadis & Lippolt, 1984), evidencing that some parts of the basement had been exhumed to the surface by Early Oligocene times. Following SW-ward directed thrusting (Koukouvelas & Doutsos, 1990), local extensional collapse of the Rhodope Massif is interpreted to have begun in Middle Eocene times, synchronously with plate collision, and continued until circa Oligocene-Early Miocene times (Koukouvelas & Doutsos, 1990; Karfakis & Doutsos, 1995), after which the whole region underwent regional extension. The Early Miocene extension has been accommodated by a low angle normal fault system, which has been identified in the SW dipping Strymon and Thasos Detachment systems (Dinter et al., 1993; Sokoutis et al., 1993; Wawrzenitz, 1997). Prior to activity along the low angle normal fault system, exhumation has been reported to occur along a NW-ward dipping pre-Late Eocene ductile extensional fault zone, which is currently exposed as the Gabrov Dol Fault, just south of Sofia in Bulgaria (Bonev et al., 1995). The onset of activity along the Strymon Detachment system is confirmed by the intrusion and mylonitization of the 22 Ma Symvolon, or Kavala, granodiorite (Dinter et al., 1995). The detachment fault system affected the metamorphosed basement at ductile crustal levels and continued its activity till the basement sequences were positioned in brittle crustal levels around circa 12 Ma, after which activity along high angle normal faults facilitated further development of the supradetachment basins. Dinter & Royden (1993) argue that the transition from basement extension controlled by the low angle southwestward dipping Strymon Detachment to extension controlled by high angle northeastward dipping normal faults occurred after the development of the North Anatolian Fault zone, whose age of initiation is concluded to be Late Miocene (Dewey et al., 1986) to post-Miocene (Yilmaz et al., 1995).
In the next sections the results of the structural observations and $^{40}Ar/^{39}Ar$ laserprobe experiments will be presented in conjunction with published structural and geochronological data to characterize the Alpine thermotectonic evolution of the Greek Rhodope Massif.

6.2.2 Geological setting and structural characteristics

The main lithologies which are observed in the Rhodope Massif are presented in figure 6.1, based on the geological maps presented by Burg et al. (1996). The figure includes the main tectonic features in the Massif and the location of previous geochronological studies together with sample locations for the present study. As a field strategy, selected transects through the metamorphic sequence were studied in detail. In addition to the field observations, ori-

entated samples were collected for microstructural and petrological studies and mica characterization for $^{40}Ar/^{39}Ar$ laserprobe experiments. The samples for $^{40}Ar/^{39}Ar$ laserprobe experiments were selected to investigate the regional thermal conditions, namely the time at which metamorphic temperatures had decreased to and below the argon closure temperature range (ca 350±30°C) in white mica. After metamorphic temperatures have been at or below this temperature range thermally activated volume diffusion is known to be low enough to potentially record white mica fabric ages on subsequently recrystallized white mica fabrics (see chapter 3).

The summarizing lithotectonic relationships which are revealed by the transect, which is schematically presented in figure 6.2, links in previous studies concerning the recognition of HP-HT eclogites near Therme (Liati & Seidel, 1996) and published structural information (Koukouvelas & Doutsos, 1990). Regionally, the metamorphic sequence is characterized by NNE dipping thrusts, which place rocks of higher metamorphic grade at higher structural positions (figure 6.2). The sequence is intruded by sheet like granitoids and granitoid plutons, which have a dip which parallels the regional tectonic grain (figure 6.2, see also Koukouvelas & Pe-Piper, 1991; Jones et al., 1992). As mentioned previously the occurrence of sheet-like granitoid intrusions into NNE dipping structures has been explained by Jones et al. (1992) as the result of the granitoids intruding in an extensional setting, during which north dipping ductile Alpine thrusts provided conduits for the rising granitic magma. Granitoids which form batholithic shapes might reflect intrusion into cooler, thinner crust, or have formed because pre-existing thrusts were simply not present (Jones et al., 1992).

Directions of tectonic transport which were recognized in the field and in thin section confirm the conclusions of the extensive study by Burg et al. (1996). In addition to an overall SSW ward direction of tectonic transport, our observations indicate the existence of a subtle shift in the direction of tectonic transport during waning metamorphism (figure 6.3). It has been observed in outcrop that transport directions in amphibolite facies metamorphic structures are WSW to SSW directed and have been consistently overprinted by more SSW to S directed tectonic transport under retrograde and semi-brittle conditions. As a result the

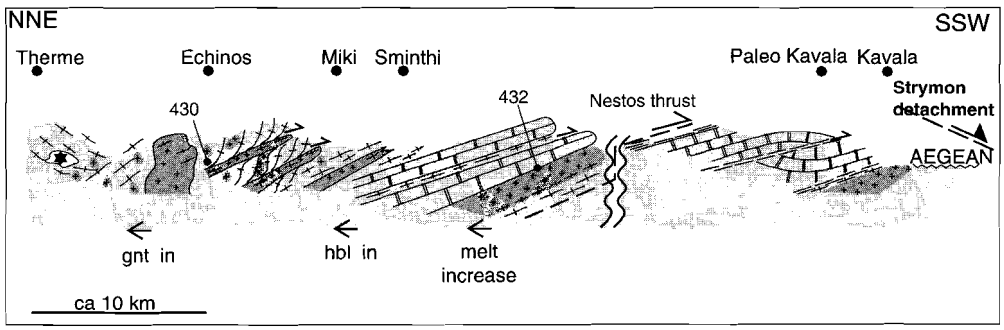

Figure 6.2. - Schematic cross section along the Therme-Kavala transect (exact location indicated in figure 6.1) showing the simplified lithotectonic relationships of the Rhodopian nappe sequence in the footwall of the Strymon / Thasos Detachment system. Star symbol; location described by Liati & Mposkos (1990) Liati & Seidel (1994, 1996), representing PT conditions of circa 19 kbar and 700°C.

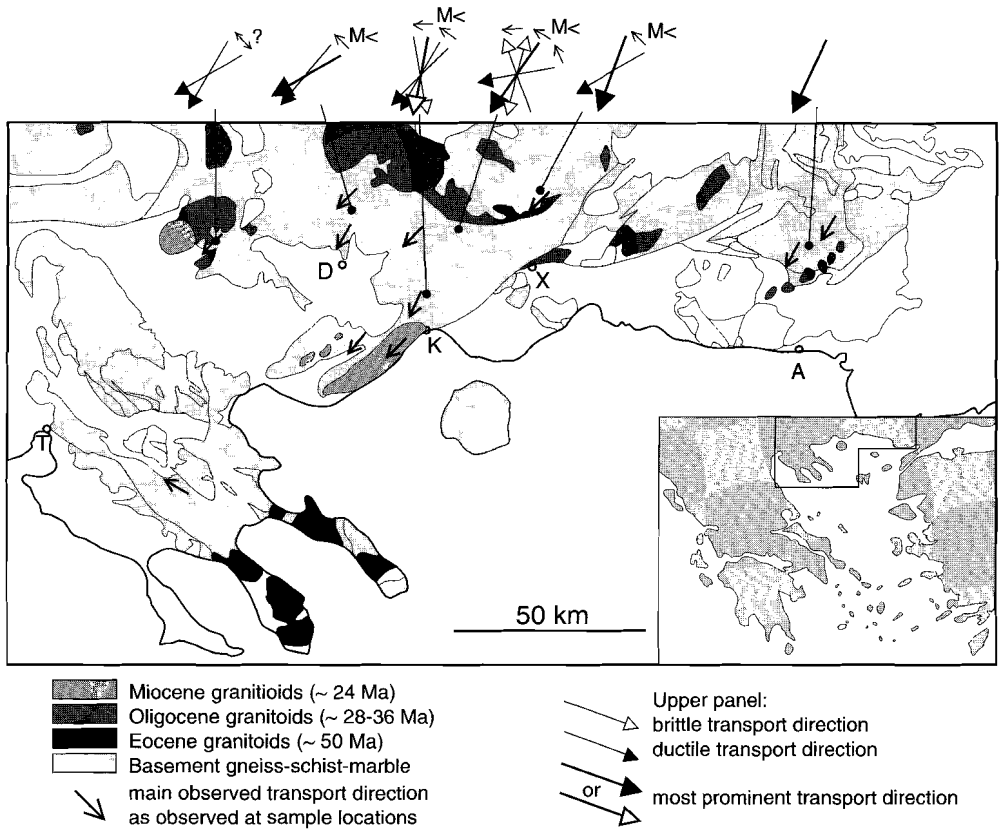

Figure 6.3. - Observed directions of tectonic transport and overprinting directions in the central Rhodope during decreasing metamorphic grade as observed at several locations in the Rhodope Zone. Upper panel: arrow and M< point to overprinting lineation. Map: Outcrop pattern of basement occurences (light grey) and of main Tertiary intrusions in combination with their emplacement age (see also figure 6.1).

gradual overprint during waning metamorphism, which has been presented in figure 6.3, shows an anticlockwise rotation of the overprinting directions of tectonic transport and allows to be linked in with the dating results (further discussed in section 6.2.4).

6.2.3 $^{40}Ar/^{39}Ar$ geochronology

6.2.3.1 Previous chronology

Several geochronological studies have been carried out in the Rhodope Zone. Some studies, which involved several dating techniques, concerned the timing of granitoid emplacement (e.g. de Wet et al., 1989; references in Jones et al., 1992; Dinter et al., 1995; and Frei, 1996; see figure 6.1 for the applied isotope systems) and show that most granitoids in the

Rhodope zone were emplaced at Tertiary times (Miocene to Eocene intrusion ages). Other studies have focussed on the dating of metamorphic assemblages (Papadopoulos & Kilias, 1985; Wawrzenitz & Mposkos, 1997) and resulted in Early Cretaceous K-Ar ages in the western Rhodope (ca 100-120 Ma, Papadopoulos & Kilias, 1985) and Early Cretaceous Sm-Nd garnet ages (ca 120 Ma) and Eocene Rb-Sr white mica ages (ca 37 Ma) in the eastern Rhodope (Wawrzenitz & Mposkos, 1997).

6.2.3.2 Laserprobe results

Mineral separation techniques were carried out in a similar way to that described in chapter 4 (and Lips et al., 1998a). Laserprobe incremental heating experiments and single fusion dating of duplicates were carried out on single crystals and small fractions (i.e. circa 0.2 mg) of white mica (table 6.1). The single fusion experiments were carried out to confirm ages for the incremental heating results and to obtain lower analytical errors. The results of the $^{40}Ar/^{39}Ar$ laserprobe experiments are presented in figure 6.4 and table 6.1, all with 2σ analytical errors. Metamorphic temperatures of mineral assemblages in which the analysed white mica had crystallized indicate that most micas have crystallized at temperatures above

#	description	analysed fractions	size + amount	total gas age (Ma) (IHE)	plateau age (Ma) (IHE)	%^{39}Ar (IHE)	Single Fusion age (Ma)	relevance
405	qtz-fsp mylonite	w.m. clast	1 ~500µm	270.6±11.0	275.3±7.5	92 %	280.5±5.5	cooling age
402	cc-qtz-fsp mylonite	w.m. clast	1 ~500µm	141.7±16.4	143.0±4.9	88 %	146.9±3.0	cooling age
414	btt-w.m. gneiss	w.m	1 ~500µm	15.9±7.8	15.2±2.3	63%	--	cooling age
		btt.	1 ~500µm	15.3±3.3	15.5±3.0	79%	--	cooling age
413	recryst. marble	w.m.	1 ~500µm	25.2±7.4	24.4±3.3	97%	22.0±1.0	cooling age
411	granite mylonite	w.m. clast	1 ~500µm	21.4±6.7	22.4±5.4	80%	--	cooling age
410	granite mylonite	w.m. clast	1 ~500µm	20.0±4.3	19.8±2.5	100%	19.1±0.8	cooling age
427	granite mylonite	w.m. clast	1 ~500µm	29.0±4.3	28.6±2.9	97%	29.8±1.5	cooling age
442	granite mylonite	w.m. clast	1 ~500µm	36.4±9.6	35.7±6.1	82%	35.5±1.0	cooling age
		w.m. fol.	4 ~250µm	35.3±8.3	35.3±6.3	100%	34.6±1.1	cooling age
418	w.m. gneiss	w.m.	1 ~500µm	36.3±7.7	36.1±5.0	82%	--	cooling age
432	cont.metam marble	w.m.	1 ~500µm	39.9±6.8	39.7±3.0	68%	37.1±2.4	cooling age
430	w.m. qtz vein	w.m.	1 ~1200µm	36.2±2.3	36.2±1.1	94%	36.1±0.5	cooling age
438	augengneiss	w.m. clast	1 ~500µm	43.0±4.0	42.4±2.3	82%	41.9±1.2	cooling age
		w.m. fol.	8 ~200µm	36.1±5.8	36.2±4.3	94%	36.0±0.7	cooling age
437	granite mylonite	w.m. clast	1 ~500µm	39.3±6.9	39.3±5.4	98%	37.6±1.9	cooling age
		w.m. fol.	10 ~160µm	35.9±6.7	35.3±4.4	85%	--	cooling age

Table 6.1. Summary of $^{40}Ar/^{39}Ar$ laserprobe experiments on samples from the Rhodope Zone (2σ analytical errors). Columns (from left to right): sample number; sample description (qtz; quartz, fsp; feldspar, cc; calcite, w.m.; white mica, btt; biotite); analysed mica generation (white mica porphyroclast, biotite and/or folaition forming white mica); number of crystals and fractionsize; total gas age (IHE; incremental heating experiment); plateau age; %^{39}Ar in plateau; results single fusion; relevance.

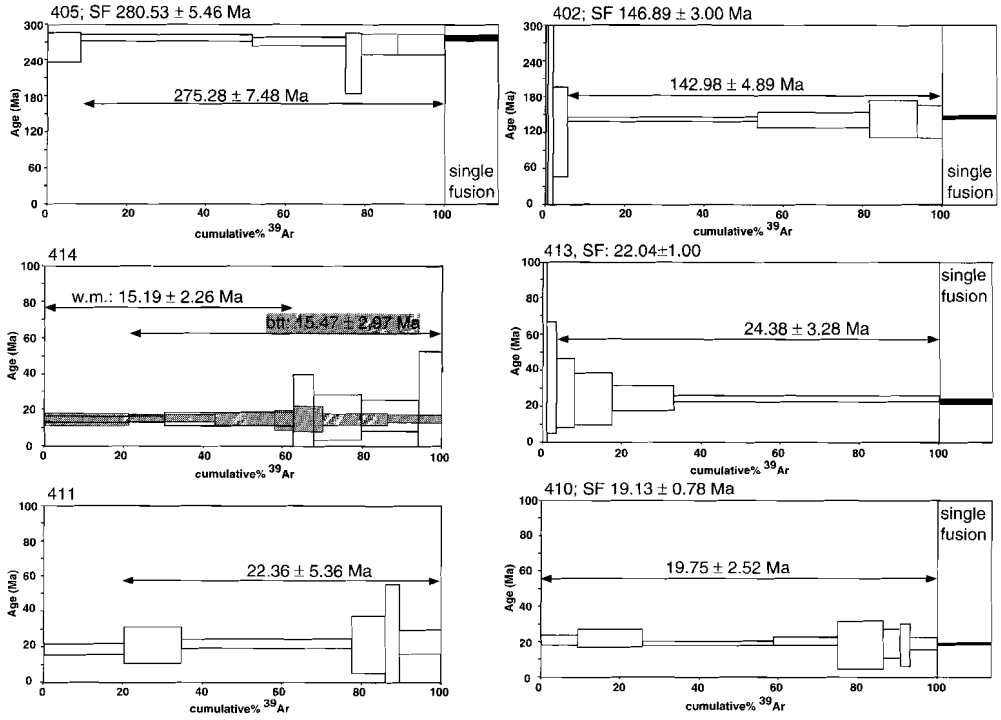

Figure 6.4. - $^{40}Ar/^{39}Ar$ age laserprobe results from samples of the Rhodope Zone (*6.4a*: western dataset (west of Drama-Kavala), *6.4b*: eastern dataset (east of Drama-Kavala)): the age spectra show the results of the incremental heating experiments; the right columns present the laserprobe fusion results. All age spectra are presented with a 2σ analytical error. Two spectra in one diagram represent muscovite and biotite analyses (sample 414) or analyses of coarse and fine white mica fractions (samples 442, 438, and 437). Consult figure 6.1 for sample locations.

their relevant argon closure temperature. Also identical ages have been obtained from muscovite porphyroclasts (expected to yield cooling ages, as the muscovites are related to primary igneous relics) and the enclosing mylonitic foliation from the same sample (e.g. sample 437, 438 and 442). This emphasizes that all ages obtained can be regarded as cooling ages. The results show Hercynian (ca 280 Ma) and Cretaceous (ca 145 Ma) cooling ages from the westernmost Rhodope and Eocene to Miocene (ca 42 to 15 Ma) cooling ages from the middle and eastern Rhodope. Amongst the cluster of Eocene to Miocene cooling ages it is seen that the cooling was relatively rapid in the central Rhodope and more gradual in the eastern Rhodope. This is illustrated by the overlap of white mica cooling ages, indicating cooling at circa 350±30°C, and biotite cooling ages, indicating cooling at circa 300±30°C, from sample 414. The rapid cooling in the central Rhodope is also illustrated by the overlap

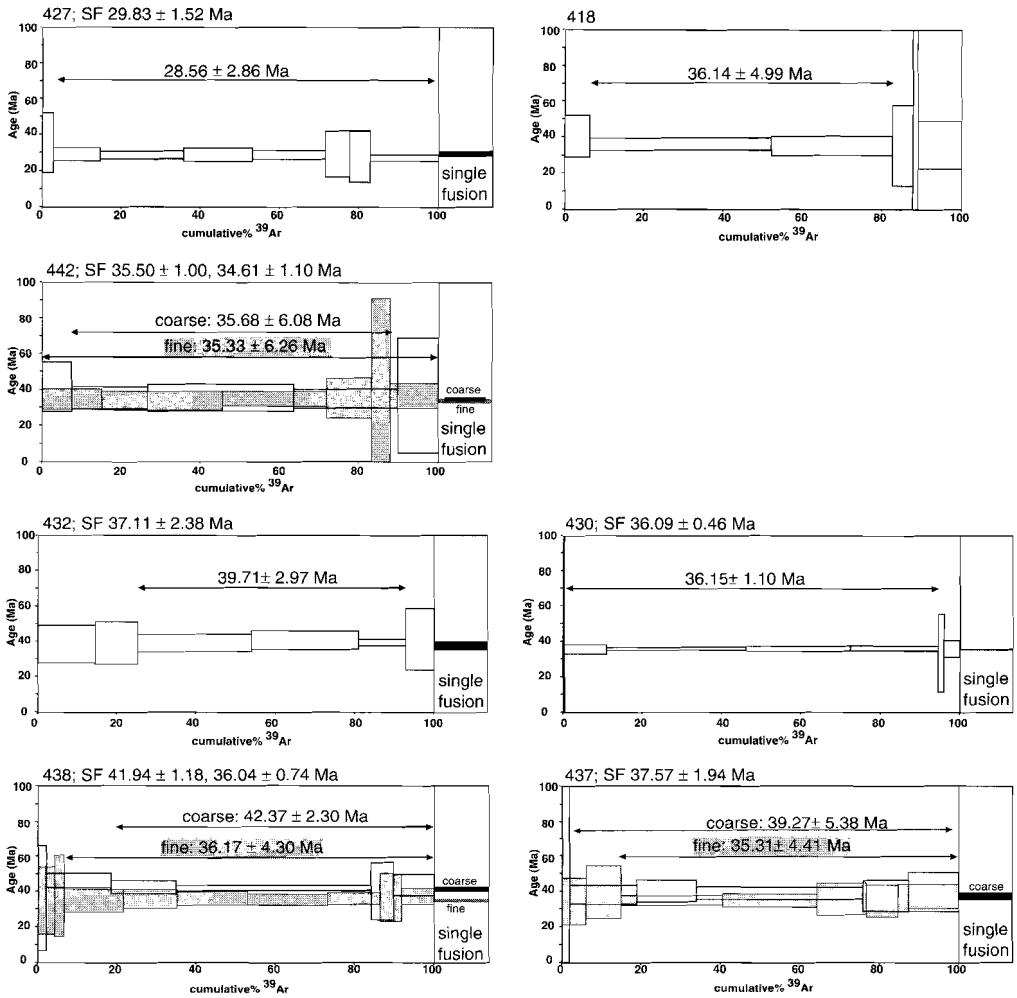

Figure 6.4. - cont'd

of cooling ages from fine grained white mica fractions (ca 250 μm) and coarse grained white mica fractions (ca 500 μm) from sample 442, in comparison to age differences in fine grained white mica fractions (ca 160-200 μm) and coarse grained white mica fractions (ca 500 μm) from samples 438 and 437. Smaller sized crystal fractions in theory have shorter pathways of effective diffusion, compared to larger sized crystal fractions. Cooling through the argon closure temperature window will theoretically result in older ages on large sized crystals and relatively younger ages on small sized crystals. Rapid cooling through the closure temperature range will cause cooling ages of crystals with different sizes to fall in the same range (see chapter 3 for further discussion).

6.2.4 Discussion

The $^{40}Ar/^{39}Ar$ laserprobe white mica cooling ages are summarized in figure 6.5 and have been combined with previously published absolute age information on granitoid emplacement (indicated by different greyscales of the granitoids in figure 6.5) and metamorphic assemblages (indicated by smaller fonts in figure 6.5). The results show a spatial distribution of $^{40}Ar/^{39}Ar$ white mica cooling ages and granitoid emplacement ages, both of which show oldest ages in the western Rhodope and youngest ages (Early Miocene) near the SW dipping Strymon Detachment and, then, with ages increasing (Oligocene-Late Eocene) gradually towards the east (see figure 6.6 which is further explained below).

In the western Rhodope, Hercynian (ca 280 Ma) and Earliest Cretaceous (ca 145 Ma) white mica cooling ages reflect conditions similar to the observations in the Pelagonian Zone (Lips et al., 1998a; b; chapters 4 and 5). The Miocene to Eocene cooling ages in the eastern Rhodope all post-date the amphibolite facies metamorphic episode. It is most likely that observed amphibolite facies sequences are related to an Early Cretaceous or even older metamorphic episode which is confirmed by the 145 Ma cooling age from similar assemblages in the western Rhodope and the reporting of 120 Ma Sm-Nd ages in the eastern Rhodope (Wawrzenitz & Mposkos, 1997). The 145 Ma cooling age might be related to the time of emplacement of granitoids (e.g. Arnea pluton) at Latest Jurassic time (de Wet et al.,

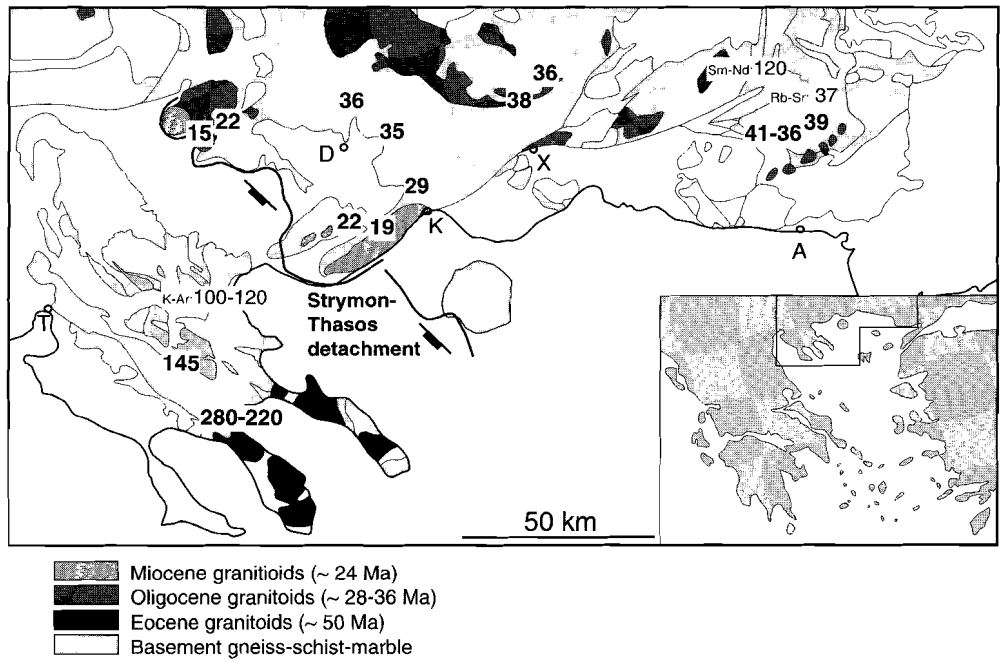

Figure 6.5. - Summary of published geochronology studies and results from $^{40}Ar/^{39}Ar$ laserprobe dating, showing the spatial distribution of both white mica cooling ages and emplacement ages of suites of granitoids of the Rhodope Massif. See figure 6.1 for locations and references.

1989). Granitoid emplacement and an associated thermal event in the Late Jurassic might explain the occurrence of Early Cretaceous (125-100 Ma) cooling ages (K-Ar ages by Papadopoulos & Kilias, 1985), which have also been found in the tectonostratigraphic sequence of the Pelagonian Zone (chapters 4 and 5). This time interval corresponds to the waning stages of the Kimmerian orogeny, which is related to the collision of Eurasia and the Kimmerian continental fragment and the associated closure of the Paleotethys. The Rhodope Massif has been generally interpreted to have formed the westernmost extension of the Kimmerian continental fragment (Sengör et al. 1980; Sengör 1984).

The spatial distribution of white mica cooling ages (ca 15 to 40 Ma) and emplacement ages in the footwall of the Strymon Detachment is further explained in figure 6.6. The figure shows the white mica cooling ages and their sample location relative to the distance from the Strymon Detachment (figure 6.6a). It illustrates that after most basement rocks had cooled below circa 350°C by 35 to 40 Ma further Late Oligocene-Early Miocene activity along the detachment caused rapid exhumation of basement in its near footwall sequence relative to the regional exhumation rate. Following further erosion to the present-day topography the spatial difference in white mica cooling ages and granitioid intrusion ages (figure 6.6b) in mapview is the result (figure 6.5). The onset of activity along the detachment is concluded to have occurred around circa 25-30 Ma, as sample 427 shows the oldest cooling age, which differs from the regional recognized cooling ages of circa 37 Ma. The different cooling ages are ascribed to the subsequent exhumation due to the activity along the Strymon Detachment. After initiation of activity along the detachment the metamorphic sequences in the footwall of this structure were gradually positioned at more shallow crustal levels. As a result of the exhumation of the footwall sequences and the gradual doming of this sequence there is the observed decrease in mica cooling ages towards the detachment, as the metamorphic sequence was gradually "closed" for argon isotope diffusion in white mica (figure 6.6b). Also granitoids, which appear to have preferentially intruded in the footwall near or into the detachment structure, show a gradual decrease in emplacement ages towards the detachment (figure 6.6b). The preferred granitoid emplacement near or into the detachment structure is interpreted to be related to the more shallow positioning of relatively hot lithospheric and/or astenospheric material and related melting of lower crustal levels below the detachment structure (see also section 2.5.2 for discussion on concepts on detachment faulting).

The gradual overprint in tectonic transport direction, as shown in figure 6.3, is characterized by an anticlockwise rotation of transport directions with waning metamorpic conditions, has been schematically summarized in figure 6.7. The schematic diagram illustrates the observed gradual change in directions of tectonic transport, over time, from ductile, amphibolite grade, to ductile greenschist grade, to brittle, from WSW to SSW. In addition to the relation in direction of tectonic transport and the metamorphic characteristics of the mylonitic assemblage and the brittle or ductile nature of the analysed deformational fabric, the garnet stability field and some absolute age information has been included. The garnet-in isograd has been positioned in the figure, as tectonic transport directions to SSW have been derived from mylonitic assemblages in which garnet has been observed. Additionally the minimum age of 100 Ma, derived from Sm-Nd garnet dating (Wawrzenitz, 1997) has

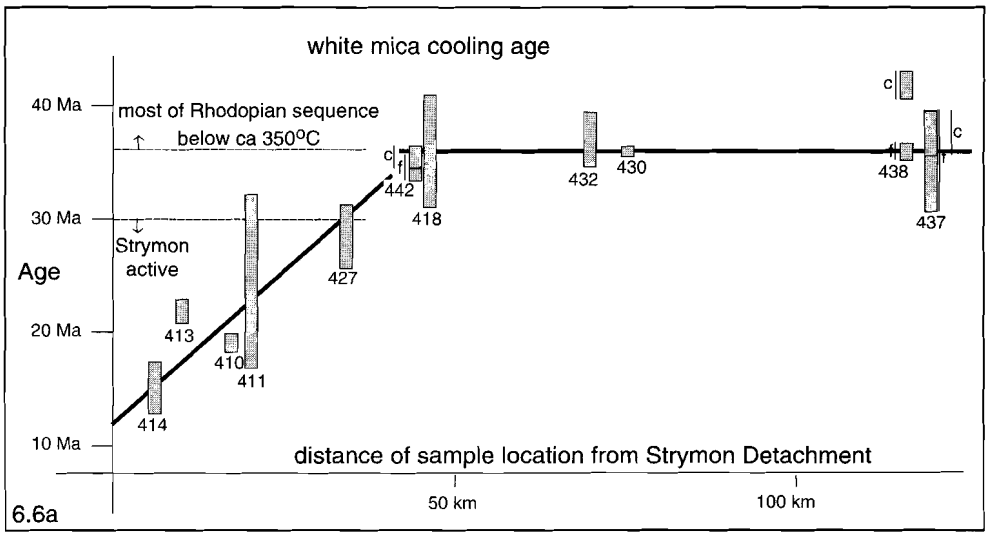
white mica cooling age
40 Ma
most of Rhodopian sequence
↑ below ca 350°C
30 Ma
Strymon
active
Age
20 Ma
10 Ma
413
410
411
414
427
442
418
432
430
438
437
distance of sample location from Strymon Detachment
50 km
100 km
6.6a

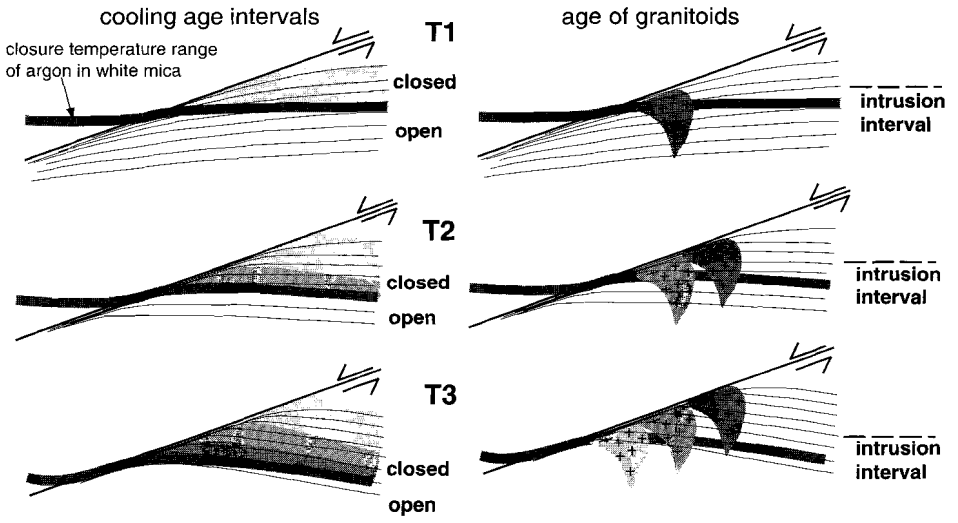
cooling age intervals
closure temperature range
of argon in white mica
T1
closed
open
age of granitoids
intrusion
interval
T2
closed
open
intrusion
interval
T3
closed
open
intrusion
interval

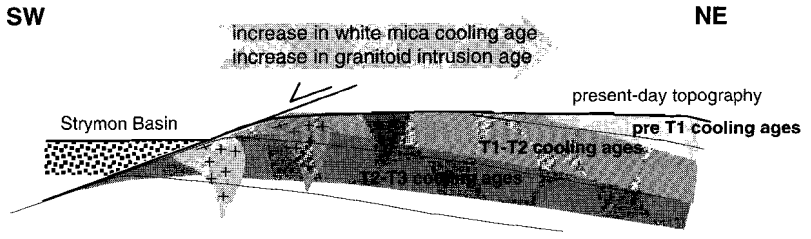
SW
NE
increase in white mica cooling age
increase in granitoid intrusion age
present-day topography
Strymon Basin
pre T1 cooling ages
T1-T2 cooling ages
T2-T3 cooling ages

Figure 6.6. - *6.6a.* Distribution of white mica cooling ages relative to the distance of the sample location from the Strymon Detachment. *6.6b.* Schematic presentation illustrating the development of the spatial distribution of white mica cooling ages and granitoid intrusion ages as a result of detachment faulting as observed in the footwall sequence of the Strymon Detachment.

been extrapolated to the observed direction of tectonic transport (see figure 3.5 for temperature limits of Sm-Nd dating). More age information on the overprinting relationships has been derived from the mica cooling ages in this study and is represented by the argon closure temperature window (upper box in ductile field of figure 6.7), which summarizes the range of closure temperatures (ca 15 to 40 Ma) and extrapolates the argon closure temperature systematics which predict that white mica cooling ages and fabric ages are derived from the topmost part of the ductile crust (see chapter 3 and 4, and Dunlap, 1997; Baldwin & Lister, 1998; for discussion).

On average, the observed change in direction of tectonic transport to WSW and SSW might be related to one single kinematic system, which continued to operate from Cretaceous (pre-100 Ma) amphibolite facies metamorphic structures, dominantly thrusts, to

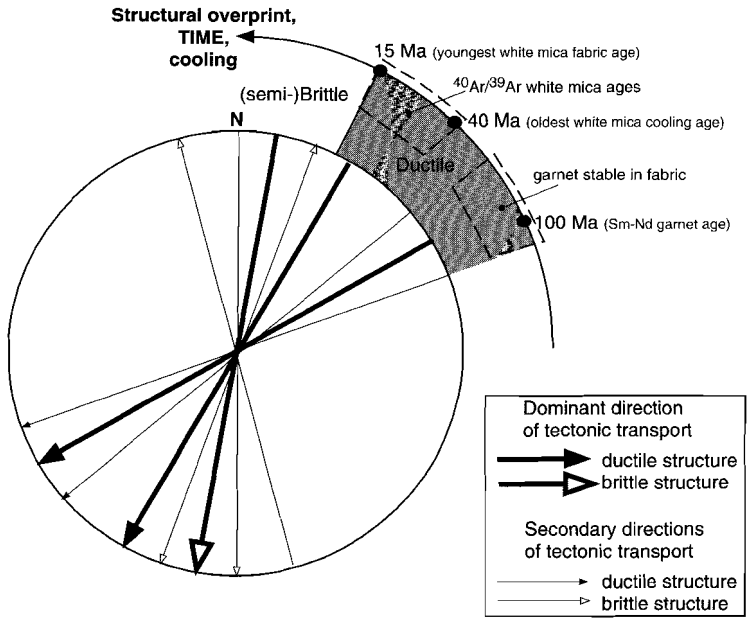

Figure 6.7. - Schematic overview of observed overprinting directions of tectonic transport directions during decreasing metamorphic temperatures. The age of formation of the different overprinting fabrics and directions of tectonic transport has been obtained by the presence or absence of white mica and/or garnet in the observed fabric and and the extrapolation of the white mica cooling ages (taken as upper age limit of ductile deformation) and of the Sm-Nd garnet age (taken as age of formation of garnet bearing assemblages; Sm-Nd data from Wawrzenitz & Mposkos, 1997).

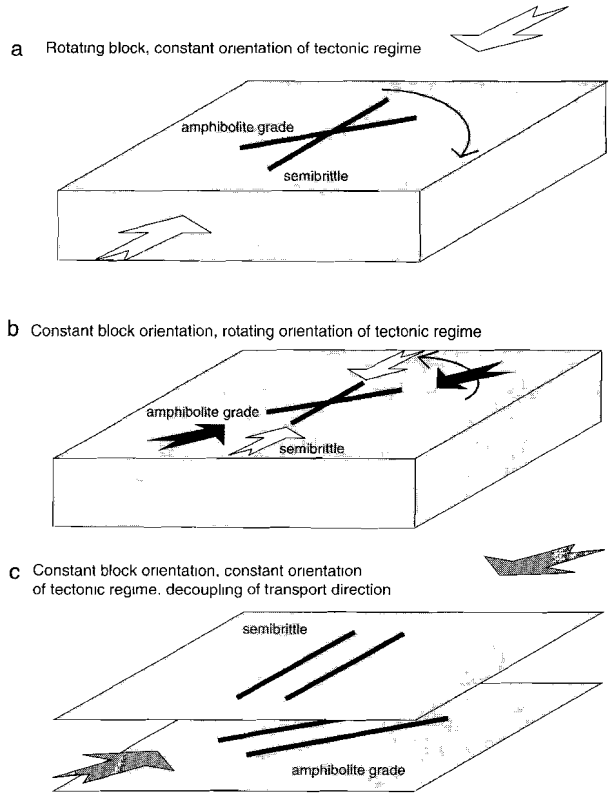

Figure 6.8. - Cartoons illustrating the possible explanations for the observed WSW-ward directed amphibolite grade tectonic transport and consequently becomes overprinted by a more SSW-ward directed tectonic transport during greenschist facies ductile to semi-brittle conditions. a) clockwise rotation with external forces controlling the tectonic transport, e.g. due to clockwise blockrotation with a continuous SSW-NNE tectonic transport , b) anticlockwise rotation of internal forces controlling tectonic transport, e.g. due to anticlockwise rotation of the driving mechanism for tectonic transport or c) subtle difference in dominant direction of tectonic transport at different crustal levels, i.e. in lower crustal and upper crustal levels.

Miocene (post-15 Ma) semibrittle and brittle structures, dominantly extensional structures. In detail, the possible causes of the gradual change in directions of tectonic transport, over time, from ductile, amphibolite facies, WSW to brittle SSW, can be explained by three general scenarios (figure 6.8): first, a clockwise rotation might have affected the Rhodope Block over time, during which *external* forces controlled the observed tectonic transport (figure 6.8a); second, an anticlockwise rotation of *internal* forces which control the observed tectonic transport might have occurred (figure 6.8b); and third, over time, a decoupling of different crustal levels and associated differences in ductile versus brittle movement directions (Bourne et al., 1998) might have affected the Rhodope region (figure 6.8c). Considering the general paleogeographic history of the Aegean region (see figure 2.3 and paragraph 2.3) it is shown that the Rhodope Massif has been interpreted to form part of the Eurasian margin at which the Pelagonian continental fragment accreted in the Early Tertiary, during which the Pelagonian rotated counterclockwise. After accretion, the whole system (Pindos, Pelagonain and Rhodope Zones) rotated clockwise in the Oligocene and Miocene. If the paleogeographic history is correct, the post Eocene rotation and associated overprint in tectonic transport directions favors the scenario in figure 6.8a. This implies that the forces which dominated during the post-Eocene history and which controlled the exhumation history and associated detachment faulting in the Rhodope Massif also operated outside the

Rhodope crustal block. In other words, the extensional collapse of the Rhodopian basement was driven by a process which formed part of a larger scale tectonic setting and was not driven by an instability in the Rhodopian wedge alone.

6.2.5 Summary and conclusions

$^{40}Ar/^{39}Ar$ laserprobe experiments on white mica porphyroclasts and white mica from deformational fabrics from the Rhodope Massif have all resulted in cooling ages. The resulting cooling ages are not only suggested by the relevant metamorphic temperature of formation of the assemblage (upper greenschist to amphibolite facies) in which the fabric forming white micas had crystallized, but has also been concluded by the observation that white mica porphyroclasts yielded cooling ages which were similar as the ages derived from white micas derived from the mylonitic fabric, enclosing the porphyroclasts. The distribution of ages shows the preservation of Hercynian (ca 280 Ma) to Lower Cretaceous (ca 145 Ma) white mica cooling ages in the western Rhodope and Late Eocene to Early Miocene white mica cooling ages (40-15 Ma) in the central and eastern Rhodope. The Late Eocene cooling ages in the central and eastern Rhodope illustrate that most basement rocks, which are currently exposed at the surface, cooled below circa 350°C by circa 40 Ma. Consequently, the observed SW-ward vergent thrusts which are related to the assembling of the tectonostratigraphic sequence under upper greenschist to amphibolite facies conditions have all been formed prior to the 40 Ma cooling age. It has been concluded from other studies that the observed amphibolite facies sequences are most likely related to an Early Cretaceous, or perhaps even older, metamorphic episode (Papadopoulos & Kilias, 1985; Wawrzenitz, 1997). The metamorphic episode might be related to the waning stages of the Kimmerian Orogeny (Sengör et al., 1984a) which appears to be confirmed by the 145 Ma white mica cooling age from amphibolite facies metamorphic assemblages in the western Rhodope (Papadopoulos & Kilias, 1985) and the reporting of 120 Ma Sm-Nd garnet ages in the eastern Rhodope (Wawrzenitz & Mposkos, 1997).

Activity along the southwestdipping Strymon Detachment system was initiated at circa 30 Ma and subsequently exhumed the metamorphic sequences in its footwall. As a result of the activity along the detachment and doming of the footwall sequence, white mica cooling ages and granitioid emplacement ages in the footwall of the detachment system gradually show Early Miocene ages closest to the detachment system and a range of Oligocene ages (ca 28-38 Ma) away from the system. The 30 Ma onset of activity along the Strymon Detachment contrasts with an onset of activity at 24 Ma, as reported by Dinter et al. (1995), which was related to the emplacement of the Symvolon pluton into the detachment system, and indicates that the detachment system might have developed prior to the emplacement of the syn-tectonic intrusions.

Although characterized by an overall SW-ward direction of tectonic transport over a timespan which might range from pre-100 Ma until post-15 Ma, it has been shown that, over time, the dominant direction of tectonic transport changed from a WSW-ward orientation in amphibolite facies mylonites to a SSW-ward orientation in semi-brittle fault zones. The subtle change in the dominant direction of tectonic transport can be explained by; a clockwise rotation of the Rhodopian crust in an overall SSW-NNE striking tectonic regime,

which was controlled by *external* forces (i.e. away from / outside the Rhodopian system), or an anticlockwise rotation of the driving mechanism, which would be controlled by *internal* forces (i.e. within the Rhodopian system), and has characterized the Late Alpine tectonics in the Rhodope. Alternatively decoupling of different crustal levels and slightly different directions of tectonic transport might have affected lower crustal and upper crustal levels. The paleogeographic reconstructions of the Aegean region suggest that the Rhodopian crust underwent a clockwise rotation since circa 40 Ma. If this is correct, the post-40 Ma tectonic regime, and thus also the extensional collapse of the Rhodopian basement, has been controlled by forces which operated on a larger scale than just in the Rhodopian system.

Before the discussion on the Tertiary tectonic setting in the northern Aegean is continued, this chapter will continue with two other studies in the region, which also concerned the thermotectonic characteristics of the exhumation of metamorphosed basement occurrences and which, therefore, provide a regional overview. The two remaining studies have been carried out in the Kazdag and Menderes Massifs of western Turkey in the eastern Mediterranean. The Kazdag Massif, which will be discussed in the next sections, is situated circa 200 km SE from the eastern limits of the Rhodope Massif.

6.3 Thermotectonic study of the Kazdag Massif, Biga Peninsula, Turkey

6.3.1 Introduction

The Kazdag Massif is situated on the Biga Peninsula in northwestern Turkey (figure 6.9a). It forms part of the Sakarya Zone which is situated in the Pontides between the Izmir Ankara Suture, north of the Anatolide-Tauride block, and Intra Pontide Suture zone, south of the Istanbul block (Okay et al., 1996). Before completion of the collision of the different blocks, which is suggested to have occurred around Middle Eocene times (Okay et al., 1996), opening of the western Black Sea influenced the development of the Sakarya Zone from Late Cretaceous times onwards (Okay et al., 1994). Southward thrusting of peridotite massifs and volcanosedimentary complexes is suggested to be associated with the closure of the Intra Pontide Suture at Late Cretaceous to Paleocene time. The present-day correlation of basement rocks is influenced by Miocene extensional tectonics and graben formation and post Miocene strike slip tectonics, namely the development of the North Anatolian Fault Zone (Seyitoglu & Scott, 1996). A major splay of the North Anatolian Fault runs SW-NE across the Biga Peninsula and continues E-W in the Gulf of Edremit (Zanchi & Angelier, 1993).

In the western Kazdag Massif, the volcanosedimentary complex is positioned on top of amphibolite facies metamorphic gneisses of the Kazdag series (figure 6.9b). A greenschist facies mylonite zone occurs at the interface of the two units and contains limestone and serpentinite lenses. It has been suggested that the greenschist facies mylonite forms the carapace of an inferred Eocene extensional core complex (figure 6.10a, after Okay et al., 1996). The Eocene age of the extensional mylonite zone however contrasts with the proposed

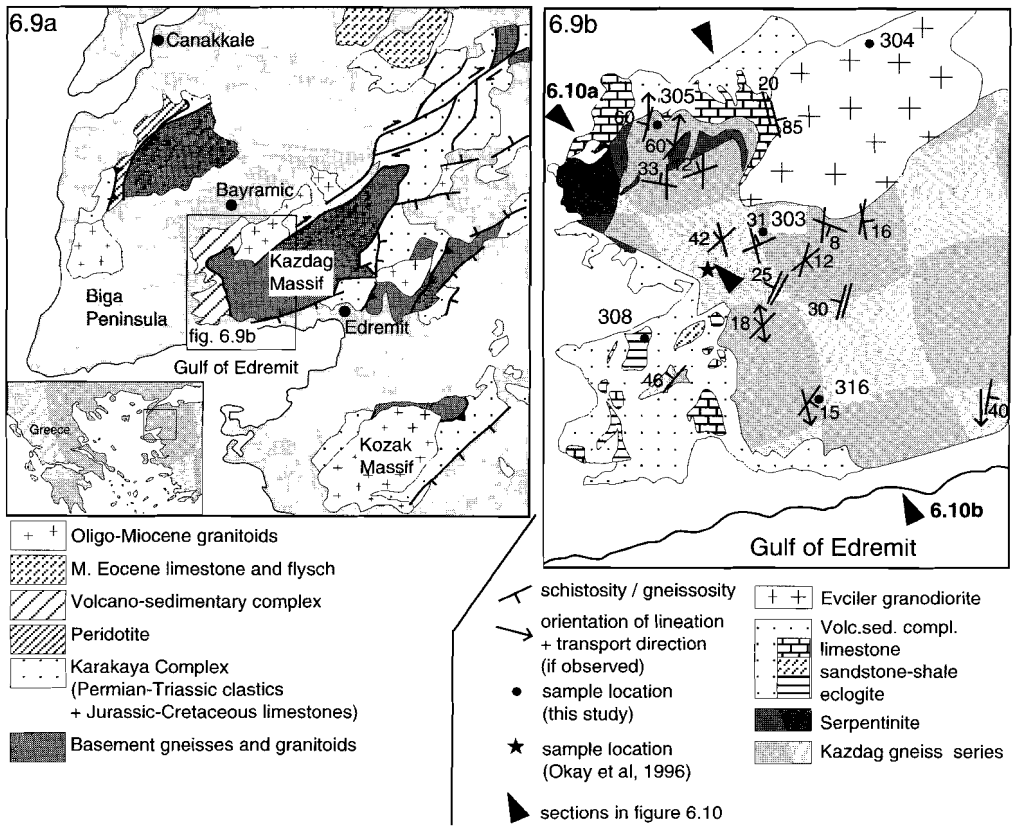

Figure 6.9. - Regional geological setting of the Kazdag Massif and the Biga peninsula after Okay et al (1991; 1996) (see also figure 2.1, for the location of the Kazdag Massif in the Aegean region). 6.9a. Outcrop patterns of main lithologies in the Biga Peninsula and the location of the Kazdag Massif. 6.9b. Summary of the geology of the western Kazdag Massif including the general trend of the structural observations, the sample locations and the locations of the schematic cross-section presented in figure 6.10.

Pliocene age of the core complex by Okay et al. in 1991. Because of the regional occurrence of the low grade to non-metamorphosed ophiolite and accretionary complex related rocks, several studies have discussed the Alpine paleogeographical configuration of this part of the Aegean (Okay et al., 1996; Pickett & Robertson, 1996).

The present study has been undertaken in order to temporally constrain the kinematics in the greenschist facies mylonite zone and to investigate the thermotectonic development of the Kazdag Massif. As deformational fabrics in the greenschist facies mylonite might contain white mica which recrystallized below the argon closure temperature range, the structure has the potential to be directly dated by $^{40}Ar/^{39}Ar$ white mica dating.

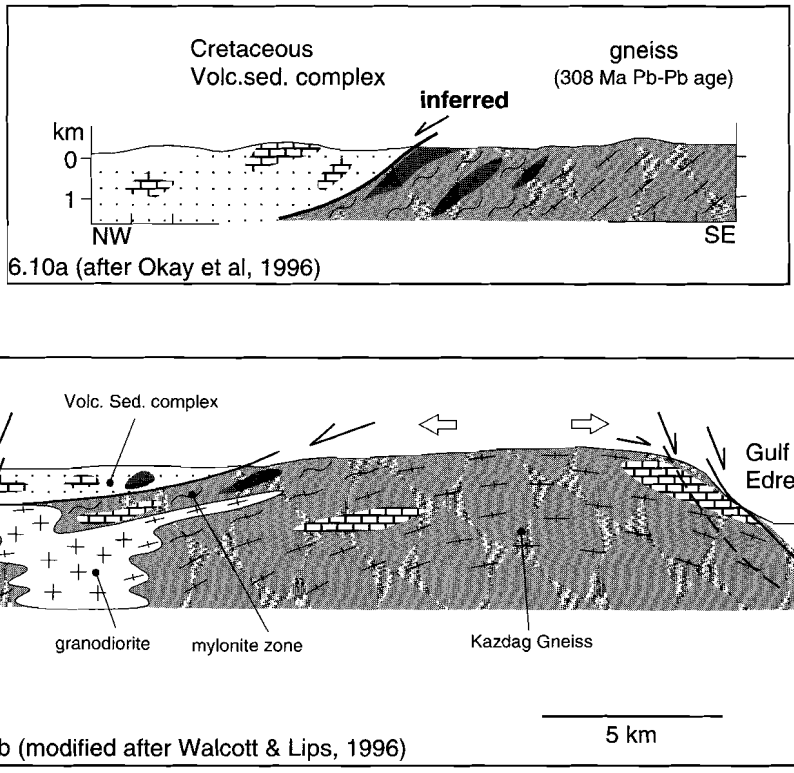

Figure 6.10. - 6.10a. Simplified cross-section through northflank of Kazdag Massif (from Okay et al, 1996) showing the structural position of the Kazdag gneisses and overlying volcano-sedimentary complex and the inferred direction of tectonic transport in the low angle mylonite zone which separates the two main units. *6.10b.* Schematic cross section across the Kazdag Massif (schematic vertical scale) summarizing the overall tectonic configuration of the massif (modified after Walcott & Lips, 1996). Fill patterns similar to legend in figure 6.9b.

6.3.2 Geological setting and structural characteristics

The Kazdag gneisses, which occur at the base of the tectonostratigraphic sequence (see figure 6.10) have been metamorphosed to amphibolite facies conditions and are topped by the above mentioned greenschist facies mylonitic schist zone with carbonate and serpentinite lenses. The schist zone is only present on the northwestern margin of the Kazdag gneiss series and the contact zones between the gneisses and schists is transitional (see figure 6.10). The schist and gneisses of the Kazdag series are overlain with a sharp contact by the volcanosedimentary complex (the Çetmi ophiolitic melange of Okay et al., 1991). The complex includes exotic blocks of limestone, eclogite, sandstones, and volcanic rocks. The limestones are Late Triassic, Late Jurassic-Early Cretaceous and Late Cretaceous in age (Okay et al., 1991). The tectonostratigraphic sequence is intruded by the Evçiler granodiorite (figure 6.9b). The contact between the granodiorite and adjacent rocks is defined either by a sharp

brittle fault, as seen at the contact of the granodiorite and the limestone on the western margin of the intrusion, or by a ductile shear zone, which is transitional from undeformed granodiorite to the Kazdag gneisses. In both cases contact metamorphic features are missing. The above tectonostratigraphic sequence is covered by a sequence of volcanics which range in age from Oligocene to Pliocene. The occurrence of Oligocene andesites in the cover sequence might be related to the emplacement of the granodiorite, as seen elsewhere in the circum-Aegean region (e.g. Rhodope Massif, section 6.2, and Menderes Massif, section 6.4) and indicates that parts of the basement was exhumed to surface levels by Oligocene times. The present day morphology is suggested to be a reflection of circa 2000 metres of uplift from the Pliocene onwards (Okay et al., 1991).

The structural characteristics of the Kazdag series reveal that the basement has been intensely deformed under ductile conditions during which it was stretched in a N-S direction (figure 6.9b, and Walcott & Lips, 1996; Walcott, 1998). Overprinting mineral lineations demonstrate that stretching was contemporaneous with retrogression of the basement sequence, which is most likely related to the exhumation of these structural levels and associated doming of the Kazdag Massif (figure 6.10b, after Walcott & Lips, 1996). Earliest lineations are defined by hornblende, which are overgrown by extended biotite rods, locally followed by chlorite (Walcott, 1998). Ductile shear sense indicators are lacking in the central parts of the massif, which strongly suggests the overall pure shear regime at mid-crustal levels. On the northern and southern flank of the massif, respectively, a top-to-NNW and top-to-S direction of tectonic transport has been deduced from ductile to semiductile shear sense indicators, chiefly shear band foliations. Slickenline orientations on the northwestern margin of the Kazdag Massif indicate that direction of tectonic transport remained parallel under further brittle conditions (Walcott & Lips, 1996). The low angle extensional structures which occur at the margins of the Kazdag gneisses are cross-cut by high angle normal faults (figure 6.10b), which are interpreted to be related to the SW-NE splay and the major E-W trending branch of the North Anatolian Fault Zone, which run across the Biga Peninsula and through the Gulf of Edremit respectively (figure 6.9 and see also Zanchi & Angelier, 1993).

In addition to the proposed tectonic development of the Kazdag Massif of Walcott & Lips (1996), samples were collected for further microstructural studies and $^{40}Ar/^{39}Ar$ laserprobe experiments. The samples for $^{40}Ar/^{39}Ar$ dating were taken from; i) the Kazdag gneiss series (sample 303) to investigate their timing of closure of the argon isotopic system and the effect of the granodiorite intrusion on thermally activated argon loss in the gneiss series; ii) the Evçiler granodiorite (sample 304) to establish the emplacement age of the intrusion; iii) the main mylonite zone on the northern flank of the Kazdag Massif (sample 305) in order to obtain a white mica fabric age and temporally constrain the kinematics on this mylonite zone; iv) a mylonite zone on the southern flank of the Kazdag Massif (sample 316) in order to obtain a white mica fabric age and temporally constrain the kinematics on this mylonite zone; and from v) an exotic eclogite block in the volcanosedimentary complex (sample 308) to constrain the episode of eclogite facies metamorphism and the maximum age of formation of the volcanosedimentary complex.

6.3.3 *$^{40}Ar/^{39}Ar$ geochronology*

6.3.3.1 Previous chronology

Some paleontological age determinations for the carbonate sequences are available, but few isotopic determinations have been carried out in the region. In the Kazdag Massif, Rb-Sr and K-Ar studies have been undertaken by Bingöl (1971). The study resulted in circa 23 to 27 Ma K-Ar mineral ages and circa 29 to 253 Ma Rb-Sr mineral and whole rock ages. The results suggest that before the Oligocene, the Kazdag gneiss series were positioned at crustal levels with corresponding temperatures which were too high to preserve the argon isotopic signature (i.e. above circa 350±30°C), but low enough to preserve the Rb-Sr signature (i.e. below circa 500°C; see figure 3.5 for temperature windows of isotopic dating systems). Alternatively, the Oligocene-Miocene magmatism might have elevated the temperatures in the Kazdag series and might have reset the K-Ar system. Most recently, Okay et al. (1996) have carried out some single zircon Pb evaporation experiments on samples in the Kazdag Massif, which resulted in a zircon population age of circa 308 Ma in the western Kazdag Massif (star symbol in figure 6.9b) and a zircon population age of circa 400 Ma from a basement sample east of Edremit. Additionally Okay et al. (1996) have applied $^{40}Ar/^{39}Ar$ age dating experiments to basal structures of the peridotite massifs in the region and obtained 110-120 Ma plateau ages on hornblende and plagioclase separates. Further to the east of the Kazdag Massif (south of Bursa), Harris et al. (1994) and Okay & Kelley (1994) carried out several laserspot analyses on white mica, biotite, glaucophane and hornblende from blueschist facies assemblages and granodiorites in the Tavsanli region (figure 2.1). Although no complete crystals were analysed, the results indicate circa 48 to 53 Ma intrusion ages for the granodiorites and an 88 Ma white mica age and 108 Ma glaucophane age associated with blueschist facies metamorphism.

#	description	analysed fractions	size + amount	total gas age (Ma) (IHE)	plateau age (Ma) (IHE)	$\%^{39}Ar$ (IHE)	Single Fusion age (Ma)	relevance
303	qtz-fsp-w.m.-btt gneiss	w.m.	1 ~500µm	22.5±9.4	21.9±4.8	95 %	21.5±2.4	cooling age
		btt.	1 ~500µm	21.6±12.2	19.1±4.7	91 %	20.3±1.6	cooling age
304	Evçiler granodiorite	w.m.	1 ~500µm	mixed	mixed	--	22.9±2.4	cooling age
		biotite	1 ~500µm	23.5±11.2	22.1±6.8	93 %	22.9±2.1	cooling age
305	cc mylonite	w.m	6 ~200µm	52.4±36.4	49.5±13.5	71 %	55.0±6.2	fabric age ?
308	eclogite schist	w.m.	1 ~500µm	101.5±27.3	100.7±16.3	99%	99.3±2.3	cooling age
316	calcite mylonite	w.m. clast	10 ~150µm	35.7±70.0	28.0±32.9	91%	26.7±2.8	fabric age ?

Table 6.2. Summary of $^{40}Ar/^{39}Ar$ laserprobe experiments on samples from the Kazdag Massif (2σ analytical errors). Columns (from left to right): sample number; sample description (qtz; quartz, fsp; feldspar, cc; calcite, w.m.; white mica, btt; biotite); analysed mica generation (white mica porphyroclast, biotite and/or foliation forming white mica); number of crystals and fractionsize; total gas age (IHE; incremental heating experiment); plateau age; $\%^{39}Ar$ in plateau; results single fusion; relevance.

6.3.3.2 Laserprobe results

Mineral separation procedures and laserprobe techniques used on these samples are similar to those discussed by Lips et al. (1998a; 1998b; chapters 4 and 5). The results of the laserprobe incremental heating and single fusion experiments are presented in figure 6.11 and summarized in table 6.2. A combination of factors, such as the selection of extremely small mineral fractions (e.g. less than 0.2 mg), unforeseen young ages of the samples, and short irradiation times, have resulted in the analyses of unexpectedly low gas fractions per incremental heating step and corresponding high analytical errors. In addition to the incremental heating experiments (spectra shown in figure 6.11), single fusion experiments (shown in figure 6.11) were carried out on duplicates of the selected mica fractions. The single fusion experiments have resulted in similar ages, as obtained by the incremental heating experiments, and lower corresponding analytical errors. The $^{40}Ar/^{39}Ar$ analyses put some temporal constraints on the tectonothermal evolution of the Kazdag Massif, albeit that the large analytical errors limit further correlation or extrapolation of the observed constraints.

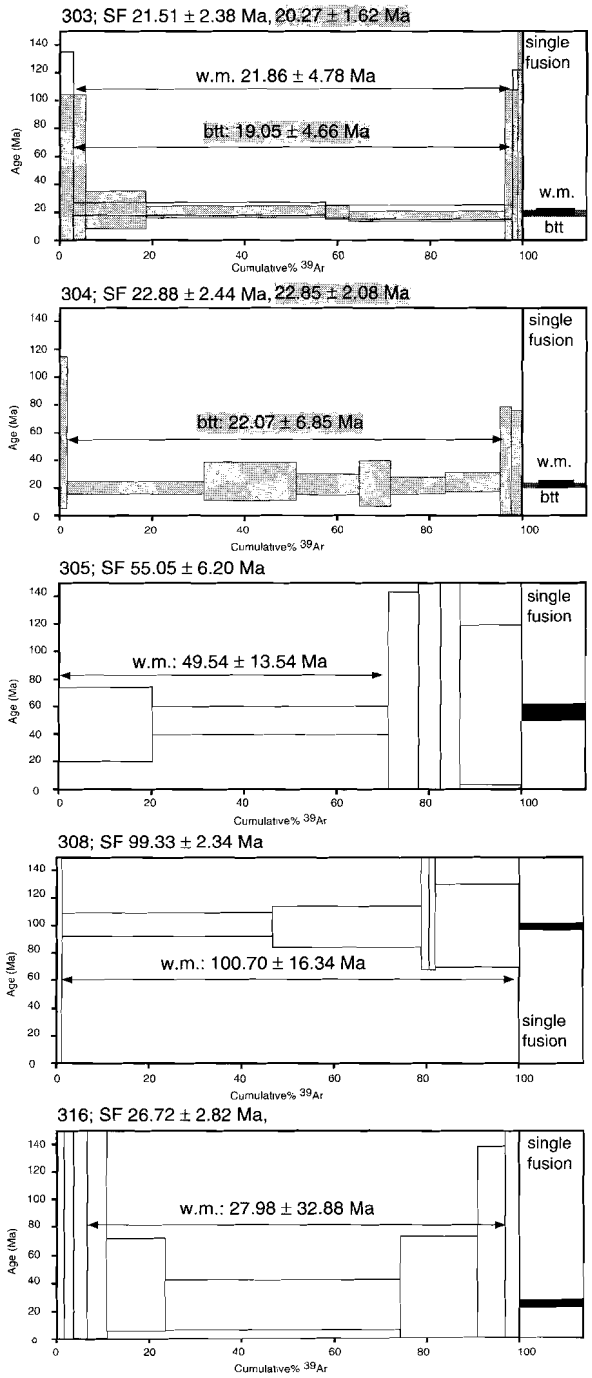

Figure 6.11. - Results of $^{40}Ar/^{39}Ar$ laserprobe experiments. Age spectra; incremental heating experiments on white mica (colorless spectra) or biotite (grey spectra). Single fusion experiments on white mica (black bars) or biotite (grey bars). All errors are presented in 2σ intervals. Summary of geochronological results are presented in table 6.2.

The experiments on most samples (samples 303, 304, 316) have yielded circa 20-25 Ma white mica ages and biotite cooling ages (i.e. cooling below 300±30°C). The 20-25 Ma ages are cooling ages (samples 303 and 304) and are related to exhumation and/or cooling after granodiorite emplacement. The 25-30 Ma white mica from sample 316 of the southern flank of the massif might be related to a similar cooling or to the formation of the mylonitic fabric. As the white mica was separated from a mylonitic marble, the metamorphic assemblage has been too limited to establish temperature constraints on the formation of the white mica. In a similar way, the circa 50-55 Ma white mica age from the carbonate mylonite from the northern flank of the massif (sample 305), might be related to a fabric age or could be related to cooling of this level of the tectonostratigraphic sequence to circa 350±30°C by 50-55 Ma.
Experiments on white mica from an eclogitic schist (sample 308) have resulted in a circa 100 Ma white mica age. The age is related to either the formation of the white mica fabric (fabric age), when the assemblage recrystallized at temperatures at or below circa 350±30°C, or to the cooling of the sample below 350±30°C *after* recrystallization of the assemblage (cooling age). As the sample contains a white mica + garnet bearing assemblage it has been interpreted that this assemblage most likely formed at temperatures above circa 400°C. Consequently, the 100 Ma white mica age is a cooling age, which post-dates the episode of eclogite facies metamorphism.

6.3.4 Discussion and conclusions

The structural observations and $^{40}Ar/^{39}Ar$ laserprobe experiments on selected samples of the Kazdag sequence have resulted in the recognition of a ductile dome which is characterized by N-S ductile stretching along low angle structures and additional thinning of the tectonostratigraphic sequence (figure 6.12). The timing of the onset of ductile stretching in the Kazdag sequence is poorly constrained by the large analytical errors on the $^{40}Ar/^{39}Ar$ dataset, but appears to have initiated before or during the development of the 50 to 55 Ma enveloping greenschist facies mylonite zone. The emplacement of the Evçiler granodiorite at Latest Oligocene time has reset the argon isotopic signature in white mica and biotite in the nearby basement. Away from the intrusion, 100 Ma white mica cooling ages have been preserved in the samples from the eclogite facies exotic blocks in the volcanosedimentary complex. Consequently the eclogite facies metamorphism is concluded to be predating the 100 Ma white mica cooling age as the eclogite mineral assemblage strongly suggests that eclogite facies metamorphic temperatures (ca 400-450°C) have been above the white mica closure temperature range (ca 350±30°C). The 100 Ma white mica cooling age also indicates that the volcanosedimentary complex has formed post-100 Ma, as the non-metamorphosed matrix contains the exotic eclogite blocks. A similar age for the formation of the volcanosedimentary complex has also been suggested by the presence of limestone blocks, as young as Late Cretaceous - Early Paleocene in age, in the complex (Okay et al., 1991). The deposition of Middle Eocene flysch and limestones over the volcanosedimentray complex confines the formation and deposition of the melange to a circa 15 m.y. interval between circa 65 and 50 Ma. Prior to the formation of the complex, eclogite facies assemblages, with cooling ages of circa 100 Ma must have been further exhumed to surface levels,

to become part of the unmetamorphosed melange matrix. A poorly confined white mica age of circa 50-55 Ma of the greenschist facies mylonite between the unmetamorphosed volcanosedimentary complex and underlying amphibolite facies Kazdag (gneiss) series indicate formation of this structure around 50-55 Ma, or, alternatively, cooling by 55-50 Ma after formation of the mylonitic fabric. The mylonite age of pre- to syn- 55-50 Ma and the youngest stratigraphic age of 50 Ma of the volcanosedimentary complex in the hangingwall suggests that formation of the mylonite has most likely occurred near circa 50 Ma.
The deformed nature of the margins of the Evçiler granodiorite suggests that ductile stretching of the massif continued to Early Miocene times, during which the dominant direction of stretching might have been rotated to a slightly more NNE-SSW orientation. The brittle, and most recent, part of the history is characterized by high angle normal faulting along the southern margin of the massif, which has been caused by the above mentioned SW- to W-ward propagation of the North Anatolian Fault Zone and resulted in the development of the Gulf of Edremit (Zanchi & Angelier, 1993).

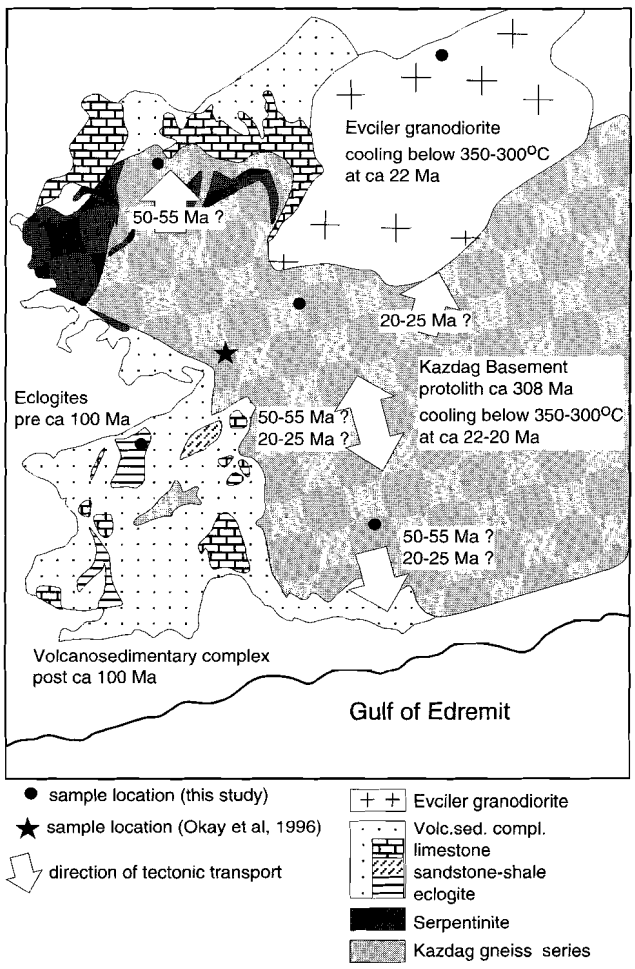

Figure 6.12. - Summary of structural observations and geochronological results projected to sample locations in the Kazdag Massif. White arrows represent concluded directions of tectonic transport (topblock transport).

To summarize, the study in the Kazdag Massif has identified the Early Miocene stage of ductile extension and contemporaneous granodiorite emplacement, and the latest ductile extension, followed by high-angle normal faulting, equivalent to other locations in the Aegean region. The study has also shown that exhumation of the amphibolite facies metamorphic basement might have initiated at circa 50 Ma. The exhumation clearly initiated in pre-Miocene times, as basement occurrences appeared at the surface from Oligocene times onwards.

Large analytical errors however do not allow extensive correlation of the $^{40}Ar/^{39}Ar$ dataset of this study and limits further discussion on the regional implications of the identified events.
The above thermotectonic study of the Kazdag Massif, and the previously discussed Tertiary history of the Rhodope Massif will be compared with the last study of this chapter, which will also concern the thermotectonic characteristics of the exhumation of metamorphosed basement occurrences. The remaining study has been carried out in the Menderes Massif and the Çine Submassif of western Turkey in the eastern Mediterranean. The Menderes Massif, which will be discussed in the next section, is situated circa 200 km south of the Kazdag Massif and forms part of the Tauride Belt at the southern side of the Izmir Ankara Suture zone.

6.4 Multistage exhumation of basement rocks in western Anatolia; the Menderes Massif and Çine Submassif (Turkey).

Submitted for publication in Terra Nova as Lips, A.L.W., D. Cassard, H. Sözbilir and H. Yilmaz: Multistage exhumation of basement rocks in western Anatolia; the Menderes Massif and Çine Submassif (Turkey).

6.4.1 Introduction

In the past decade, several studies in the Eastern Mediterranean have recognized low angle extensional structures that accommodated the exhumation of mid to deep crustal rocks (e.g. Lister et al., 1984; Gautier & Brun, 1994; Jolivet et al., 1994b; Avigad et al., 1992; Dinter et al., 1995; Hetzel et al., 1995b; Whitney & Dilek 1997). As these extensional structures operated at ductile crustal conditions and continued their activity at brittle crustal conditions, they have witnessed a substantial part of the Late Alpine to post-Alpine tectonic history. The large scale extensional structures, which often were accompanied by ductile doming of the footwall sequence, are found in basement complexes around the present day Aegean sea (inset in figure 6.13) and are known to have experienced a dominant phase of activity at Early Miocene times, which has been resolved by $^{40}Ar/^{39}Ar$ isotopic dating (Wijbrans & McDougall, 1988; Hetzel et al., 1995b) and combined $^{40}Ar/^{39}Ar$ and U-Pb isotopic dating (Dinter et al., 1995) of magmatic minerals from syntectonic intrusions. As the dating of syntectonic intrusions might reflect only a small time interval of activity along the extensional structures, direct isotopic dating of the deformational structures in the extensional fault zones might refine the Late Alpine tectonic history. A careful investigation of the deformational structures and the characterization of mica bearing assemblages which formed in these structures, combined with the characteristic high sensitivity, low blank, $^{40}Ar/^{39}Ar$ laserprobe age dating on individual mica populations has proved to be an excellent way to resolve the timing of deformation in tectonic structures with a complex deformation history (Lips et al., 1998a; 1998b, chapters 4 and 5).
In this study, detailed structural investigations were carried out along selected transects across the Menderes Massif and the southern Çine Submassif in southwestern Turkey (fig-

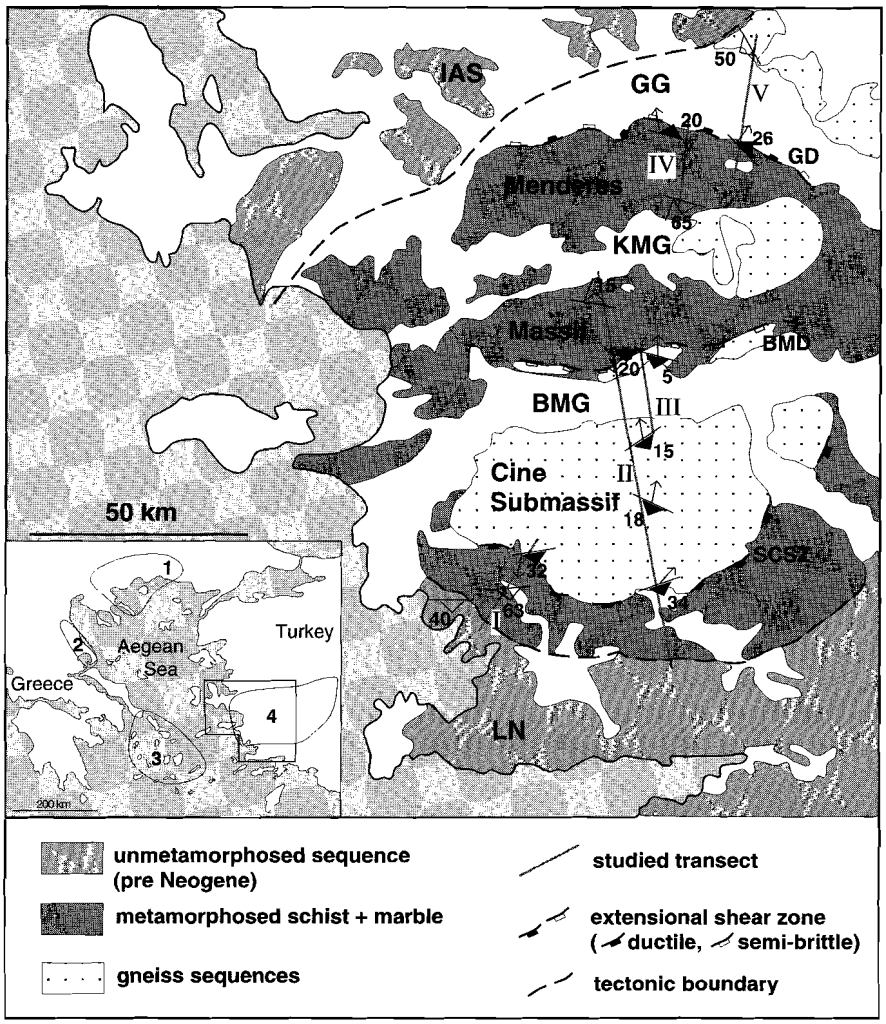

Figure 6.13. - Simplified geological map showing location of dominant structural units and tectonic boundaries in southwestern Turkey and the location of the selected transects across the Menderes Massif and Cine Submassif (presented in figure 6.14). Open structural symbols summarize dominant foliation orientation (plus mineral lineation orientation, if observed), filled symbols represent mylonitic foliation orientations, arrows give direction of tectonic transport (top-block). Abbreviations (from north to south): IAS = Izmir Ankara Suture zone, GG = Gediz Graben, GD = Gediz Detachment, KMG = Kücük Menderes Graben, BMD = Büyük Menderes Detachment, BMG = Büyük Menderes Graben, SCSZ = South Cine Shear Zone, LN = Lycian Nappes. Inset: Location of reported Miocene domes in the Aegean region; 1. the Rhodope Zone (this study, section 6.2, and Dinter & Royden, 1993; Dinter et al, 1995); 2. the Olympos-Ossa-Pelion region (this study, chapters 4 and 5, and Schermer 1993); 3. the Cyclades archipelago (Buick, 1991; Gautier & Brun, 1994; John & Howard, 1995; Jolivet et al, 1994; Lee & Lister, 1992; Lister et al, 1984; Vandenberg & Lister, 1996); and, 4. the Menderes Massif (Emre & Sözbilir, 1997; Hetzel et al, 1995a; 1995b).

ure 6.13). As the area is known to have undergone extension along low angle structures (Bozkurt & Park, 1994; Hetzel et al., 1995a; Hetzel & Reischmann, 1996) the study has been undertaken to characterize the temporal development of the structures and to investigate their overall role in the tectonic development of the region.

6.4.2 Geological setting

The Menderes Massif and Çine Submassif are crosscut by three east-west trending graben systems (see figure 6.13), which are (from north to south); the Gediz, or Alasehir, Graben (GG), the Küçük Menderes Graben (KMG) and the Büyük Menderes Graben (BMG), and are bordered by unmetamorphosed sequences of the Lycian Nappes (LN) in the south and of the Izmir Ankara Suture Zone (IAS) in the north. The selection of the transects has been based on recently published structural, petrological, stratigraphical and geochronological information to establish an up-to-date regional tectonic interpretation of western Turkey. In contrast to the large amount of work carried out in the region, a detailed synthetic cross-section is still missing. Our study presents a detailed cross-section across the Menderes Massif and Çine Submassif, which might serve as input for future research in the region (figure 6.14).

The sequence in the Çine Submassif consists of a gneissic composite basement, characterized by amphibolite to granulite facies metasediments which locally underwent partial melting, by meta-igneous rocks, and by younger intrusions which crosscut existing fabrics. Incremental evaporation experiments on single zircons from the sequence in the southern Çine Submassif resulted in Pan African (ca 546 Ma) ^{207}Pb–^{206}Pb ages (Hetzel & Reischmann, 1996), which already had been suggested, albeit less precisely, by Rb-Sr

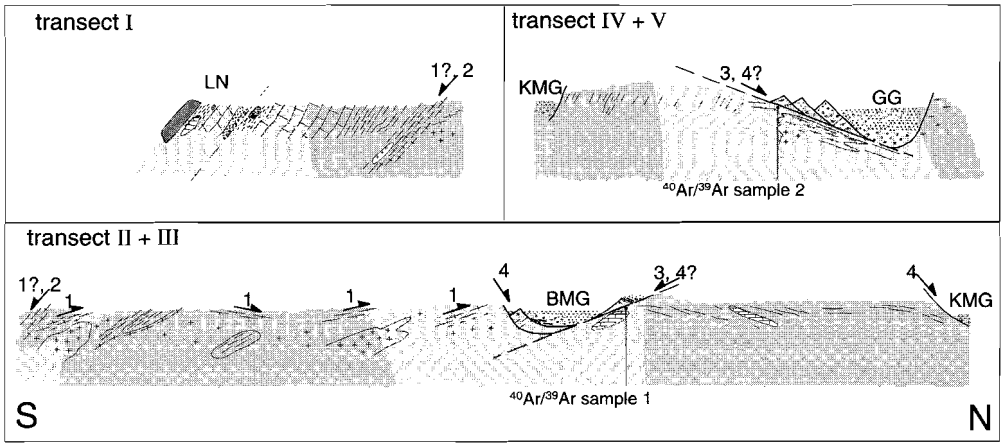

Figure 6.14. - 6.14a. Simplified cross-sections of selected transects across Menderes Massif and Cine Submassifs (location of transects in figure 6.13) and locations of $^{40}Ar/^{39}Ar$ samples (results of analyses in figure 6.14). Observed tectonic transport directions are indicated; numbers refer to relative age relationships (1=oldest, 4=youngest). Abbreviations as in figure 6.13. *6.14b* (right page). Schematic cross-section which summarizes published work in the region in conjunction with the structural and geochronological investigations of this study.

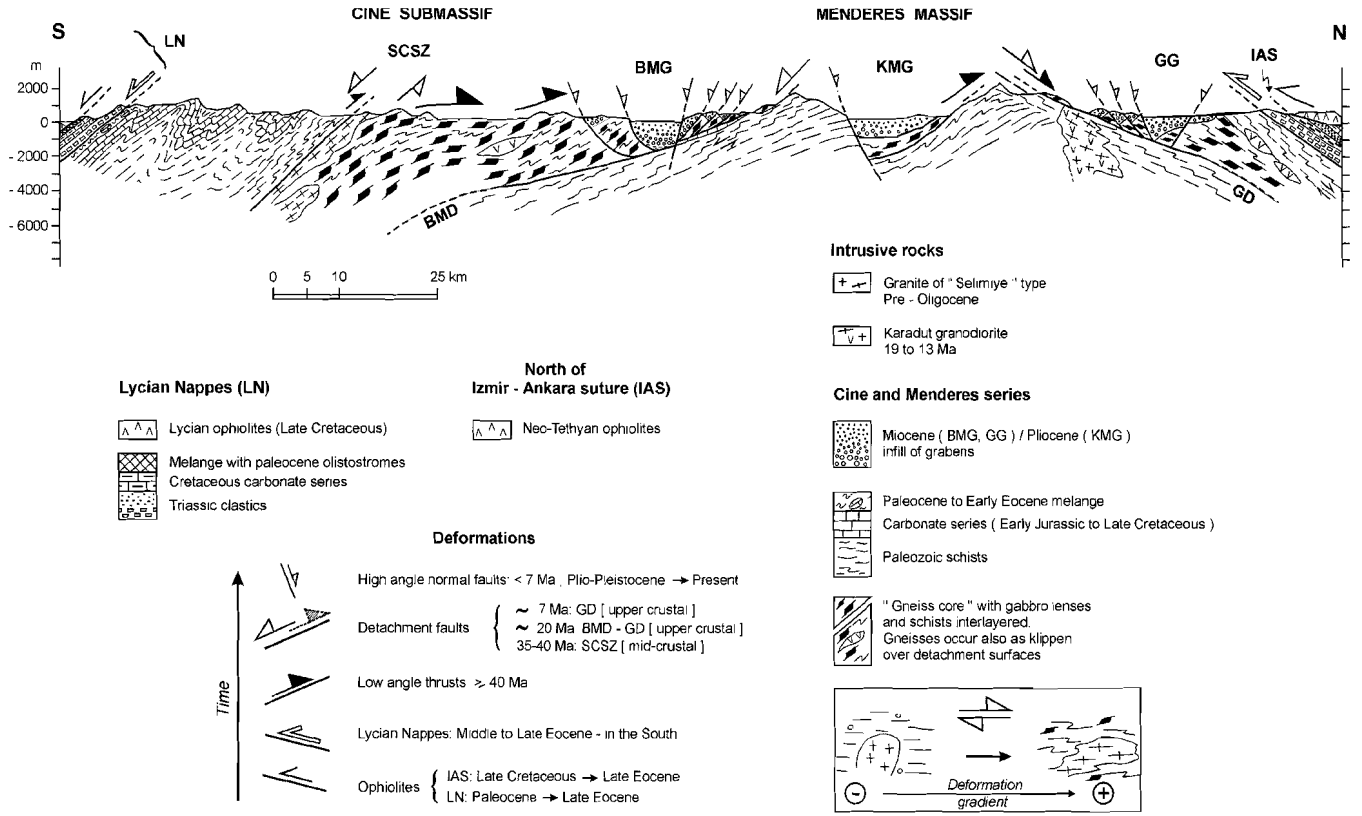
CINE SUBMASSIF
MENDERES MASSIF
S
N
LN
SCSZ
BMG
KMG
GG
IAS
GD
BMD
m
2000
0
- 2000
- 4000
- 6000
0 5 10 25 km
Intrusive rocks
Granite of " Selimiye " type
Pre - Oligocene
Karadut granodiorite
19 to 13 Ma
Lycian Nappes (LN)
North of
Izmir - Ankara suture (IAS)
Lycian ophiolites (Late Cretaceous)
Neo-Tethyan ophiolites
Melange with paleocene olistostromes
Cretaceous carbonate series
Triassic clastics
Cine and Menderes series
Miocene (BMG, GG) / Pliocene (KMG)
infill of grabens
Paleocene to Early Eocene melange
Carbonate series (Early Jurassic to Late Cretaceous)
Paleozoic schists
" Gneiss core " with gabbro lenses
and schists interlayered.
Gneisses occur also as klippen
over detachment surfaces
Deformations
Time
High angle normal faults: < 7 Ma , Plio-Pleistocene → Present
Detachment faults
~ 7 Ma: GD [upper crustal]
~ 20 Ma BMD - GD [upper crustal]
35-40 Ma: SCSZ [mid-crustal]
Low angle thrusts ≥ 40 Ma
Lycian Nappes: Middle to Late Eocene - in the South
Ophiolites
IAS: Late Cretaceous → Late Eocene
LN: Paleocene → Late Eocene
Deformation
gradient

whole rock ages at 502 to 472 Ma ± 10 Ma (Satir & Friedrichsen, 1986). The southern margin of the gneiss sequence in the Çine Submassif is characterized by a well-documented low-angle extensional shear zone (Bozkurt & Park, 1994; 1997; Bozkurt et al., 1995; Bozkurt, 1996; Hetzel & Reischmann, 1996), which in this study is termed "the South Çine Shear Zone (SCSZ)". The activity along this south dipping structure, which separates felsic gneisses in the footwall from metamorphosed schists and marbles in the hangingwall, has been inferred to be Eocene in age (i.e. between circa 43 and 37 Ma; Satir & Friedrichsen, 1986; Hetzel & Reischmann, 1996).
The gneissic basement, exposed in the Çine Submassif, is regarded as the "core" of the Menderes sequence (Sengör et al., 1984; Dora et al., 1997; Oberhänsli et al., 1997) following first postulations by Schuiling (1962). However, klippen of the gneiss sequence have been recorded north of the Çine Submassif on top of lower grade metamorphosed sediments in the Menderes Massif (Candan et al., 1992; Hetzel et al., 1995b; Sözbilir & Emre, 1996; Emre & Sözbilir, 1997; Oberhänsli et al., 1997), which clearly illustrates that the gneisses are not in the lowest structural positions of the tectonostratigraphic pile.

In contrast to the amphibolite to granulite facies metamorphic rocks and intrusions of the Çine Submassif, the Menderes Massif is characterized by greenschist facies metamorphic schists and marbles. As mentioned in the above section, the sequence in the Menderes Massif is the deepest exposed structural unit of the tectonostratigraphic sequence of western Turkey, as gneisses of the Çine Submassif are found, tectonically emplaced, on top of the Menderes sequence. Sözbilir & Emre (1996) and Emre & Sözbilir (1997) already postulated that the basal structure of the gneiss klippen had formed as a result of Eocene-Oligocene compressional tectonism in western Anatolia which had been reactivated as a detachment fault system in the Miocene.
Recent studies have concluded that the Menderes sequence was exhumed by the development of a bivergent detachment fault system (Hetzel et al., 1995a), of which the north dipping structure occurs along the southern margin of the Gediz Graben (Hetzel et al., 1995a; 1995b; Emre & Sözbilir, 1997) and the south dipping low angle structure occurs along the northern margin of the Büyük Menderes Graben (observed by Emre & Sözbilir, 1997). The north dipping and south dipping structure are termed in this study the Gediz Detachment and Büyük Menderes Detachment, respectively (figure 6.13). It has been concluded that the activity along both structures has played a very important role on the tectonic denudation of the Menderes Massif at Miocene times (Sözbilir & Emre, 1996). Conventional $^{40}Ar/^{39}Ar$ experiments on mineral separates of syntectonic intrusions indicate a dominant phase of activity along the Gediz Detachment at Lower Miocene times (Hetzel et al., 1995b). A comparable age has been obtained from palynological investigations on coal lenses which were deposited at the base of the sedimentary infill of the Büyük Menderes supradetachment basin system (Seyitoglu et al., 1992; Cohen et al., 1995; Sözbilir & Emre, 1996; Emre & Sözbilir, 1997). The detachment faults and sedimentary infill are crosscut by high-angle faults which caused a relative uplift of the margins of the Miocene grabens and appear to control the development of the Küçük Menderes Graben in the central parts of the Menderes Massif (Akcay et al., 1996).

6.4.3 $^{40}Ar/^{39}Ar$ laserprobe experiments

In this study, several $^{40}Ar/^{39}Ar$ laserprobe experiments have been carried out on two samples from the Menderes Massif. The samples were selected to investigate the presence of tectonic events older, or younger, than the well reported Lower Miocene extensional event related to the basin formation and granodiorite intrusions in western Turkey (Seyitoglu et al., 1992; Hetzel et al. 1995b). After a detailed structural investigation in the field, the samples were selected and subjected to further microstructural analyses, followed by careful characterization of the white mica population, and mineral separation, following similar techniques described by Lips et al. (1998a; 1998b, chapters 4 and 5). After final handpicking of the white mica population, the samples were split into four fractions. In the experiments it was preferred to analyse minimal sample fractions to minimise contamination of the selected mica population with relic populations which also might exist in the deformational structures. The analysis of extremely small samples (i.e. less than 0.2 mg) and related small gas fractions, gives rise to the large analytical errors (figure 6.15), but allows dating of dis-

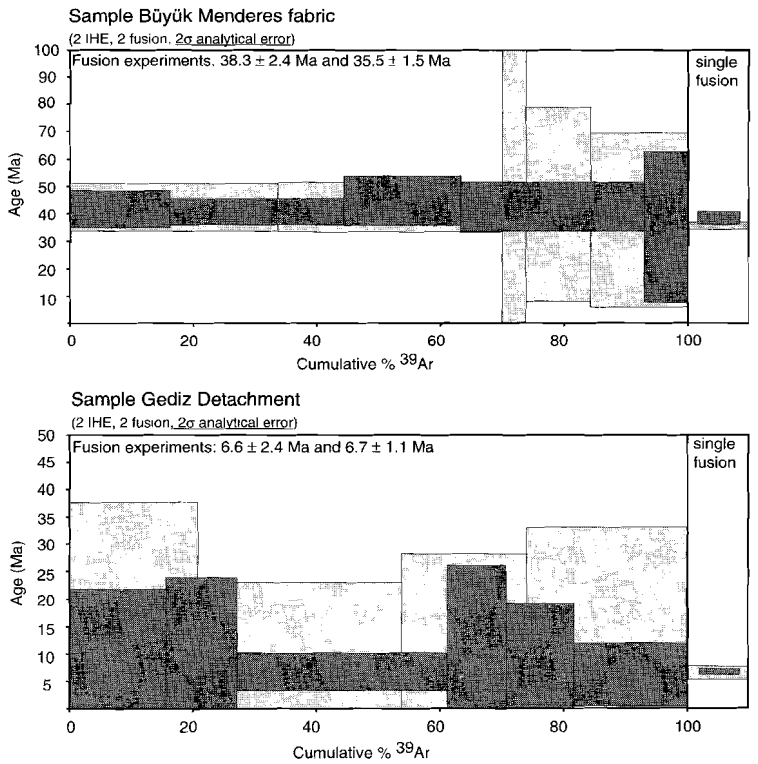

Figure 6.15. - Results of $^{40}Ar/^{39}Ar$ laserprobe experiments of samples from the Büyük Menderes (figure 6.15a) and Gediz (figure 6.15b) Detachments. Locations of samples are indicated in figure 6.14. All IHE and fusion results are presented with 2σ analytical errors.

crete deformational events. Two fractions of the samples were analysed applying an incremental heating experiment (IHE), to investigate the possible presence of a contaminating (relic) white mica population. After confirmation of the existence of an uncontaminated mica population, the other two fractions were outgassed by a single fusion experiment, in order to analyse the total gas fraction, which is expected to be identical in composition as the total gas fraction of the IHE. Analytical procedures of the experiments and data processing were carried out in a similar way as discussed by Lips et al. (1998a, chapter 4). It is emphasized that all data are presented with a 2σ analytical error. Superposition of the results of the two analyses by IHE's, with large analytical errors, and the results of the two fusion experiments, with small analytical errors, leads to the recording of a fabric forming event, with a statistically meaningfull 2σ age interval of approximately 1.0 to 1.5 Ma (figure 6.15).

6.4.4 Results

A summary of the field observations along the selected transects is presented in three schematic cross sections (figure 6.14). The cross sections show the relative age relationships of the observed directions of tectonic transport and the location of the $^{40}Ar/^{39}Ar$ samples.

Our structural observations in the gneiss sequence across the Çine Submassif and Menderes Massif show the existence of a consistent internal fabric which is related to a northward directed tectonic transport (figure 6.14; transect II+III). The northward directed tectonic transport is observed in asymmetric structures which occur in highly ductily deformed mylonitic augen gneisses and ultramylonites (see also White et al., 1980; Lister & Snoke, 1984; Passchier & Trouw, 1996; for discussion). The mylonite zones (1 to 100 meters wide) crosscut the gneissic composite basement and are found throughout the gneiss sequence. The northward directed tectonic transport is overprinted in the south by the observed, and documented, southward directed tectonic transport of the SCSZ (figure 6.14; transects I and II+III).

In the Menderes Massif, the bivergent detachment fault system has been observed and studied in detail (figure 6.14; transects IV+V and II+III). The Gediz Detachment shows a well developed ductile mylonite zone with decreasing metamorphic grade of the mylonitic foliation towards the top of the structure, which is defined by a cataclastic zone. The Büyük Menderes Detachment is characterized by a semi-ductile to brittle extensional fault system only. Structural investigations of the gneiss klippen indicated the preservation of a highly ductile northward directed tectonic transport, which predates the development of the extensional structures and which is interpreted to be related to the tectonic emplacement of the Çine Sequence on top of the low grade metamorphic sediments of the Menderes Sequence.

The results of the $^{40}Ar/^{39}Ar$ laserprobe experiments on a sample from the Büyük Menderes Detachment, below a gneiss klippe on the southern flank of the Menderes Massif (figure 6.14; sample 1), reveal an age around 37 Ma (figure 6.15a). This age is interpreted to be related to the tectonic emplacement of the Çine gneiss sequence over the Menderes sequence. $^{40}Ar/^{39}Ar$ laserprobe experiments on micas from the second sample which was derived from the Gediz Detachment and was taken from the mylonite zone, directly below the cataclastic zone (figure 6.14; sample 2), results in an fabric age of 6-7 Ma (figure 6.15b).

This age is related to the reactivation of the Gediz Detachment by circa 7 Ma and illustrates that the detachment system continued to be active subsequent to its initial development in the Early Miocene.

6.4.5 Conclusions

In this study, an up-to-date detailed synthetic cross-section through the southwest of Anatolia is presented, which is based on existing studies in the region and additional structural and geochronological investigations. The cross section is a key contribution to a better understanding of the tectonic evolution of the Menderes Massif, Çine Submassif and adjacent areas. In contrast to previous regional tectonic interpretations (Sengör et al., 1984; Erdogan & Güngör, 1992; Dora et al., 1992; 1997), which all regard the gneiss sequence of the Çine Submassif as the lowermost structural unit of the tectonostratigraphic sequence in the region, we have re-emphasized that the amphibolite facies gneiss sequence (Çine sequence), has been tectonically emplaced on schist and marbles of lower metamorphic grade (Menderes sequence) in Late Eocene times. During and after tectonic emplacement of the composite basement, the region has been affected by an episodic collapse, which resulted in a multistage exhumation of the basement series, as indicated by the sets of isotopic data from the region. Rather than a single Early Miocene phase of extensional collapse as has been documented so far (Seyitoglu & Scott, 1996), the main exhumation events associated with the extensional collapse occurred at circa 40-35, 20-18 and 7-6 Ma and are schematically presented in figure 6.16. The 40-35 Ma event has been constrained by a

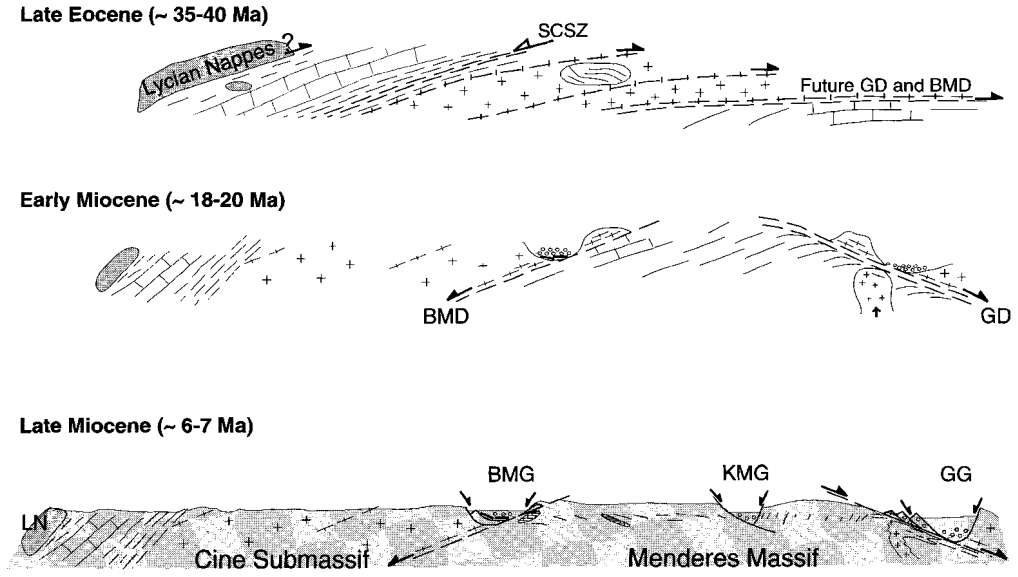

Figure 6.16. - Cartoon illustrating the Late and Post Alpine tectonic evolution of the Menderes Massif and Cine Submassif for the Late Eocene, Early Miocene and Late Miocene. Active structures are indicated with arrows. Abbreviations as in figure 6.13.

$^{40}Ar/^{39}Ar$ fabric age in the present-day Büyük Menderes Detachment (this study) and by mica cooling ages in the Çine Submasif, near the South Çine Shear Zone, derived from Rb-Sr and $^{40}Ar/^{39}Ar$ studies, by Satir & Friedrichsen (1986) and Hetzel & Reischmann (1996) respectively. The 20-18 Ma is constrained by $^{40}Ar/^{39}Ar$ hornblende cooling ages from syntectonic granodiorites in the Gediz Detachment (Hetzel et al., 1995b), and by stratigraphic information of the supradetachment basins (Seyitoglu et al., 1992). The 7-6 Ma event is constrained by a $^{40}Ar/^{39}Ar$ fabric age from the Gediz Detachment (this study). The first stage of exhumation around 40-35 Ma was induced by imbrication of the composite basement and northward directed thrusting, which was accompanied, or shortly followed, by extensional ductile faulting along the current southern margin of the Çine Submasif. The Latest Eocene phase of regional extension conflicts with the conclusion of Bozkurt & Park (1997), who claimed a Late Oligocene age of activity along the South Çine Shear Zone, which is disputed by the isotopic data and by stratigraphical information on sediments which overly the South Çine Shear Zone. A similar style of extension, coeval and subsequent to piling up of the tectonic sequence has also been documented in nearby regions (e.g. Rhodope Zone, Burg et al. 1996; section 6.2). The Early Miocene phase of the late-orogenic extensional collapse was characterized by the development of the Gediz Detachment, which started to operate at ductile crustal conditions, was intruded by granodiorites and continued its activity under semi-ductile conditions. Synchronously, at semi-ductile to brittle crustal levels, the antithetic Büyük Menderes Detachment developed, which allowed doming of the Menderes Massif and accelerated the exhumation of the footwall of the detachment systems. The development of the detachment fault was accompanied by the formation of two large sized half graben systems as supradetachment basins, the Gediz Graben and Büyük Menderes Graben. The last stage of semi-ductile tectonic activity along the Gediz Detachment terminated around 6-7 Ma when high-angle normal faults had developed, which, most likely, crosscut the low angle structures and caused relative uplift of the graben margins plus further exhumation of the detachment structures and their footwalls.

6.5 Summary and conclusions

Structural observations have been combined with $^{40}Ar/^{39}Ar$ laserprobe experiments on selected samples from the Rhodope Massif in the Internal Hellenides of the northeastern Greek mainland, the Kazdag Massif of the Pontides belt in northwestern Turkey and the Menderes Massif and Çine Submassif of the Taurides belt in southwestern Turkey. The three massifs show amphibolite facies and eclogite facies metamorphic rocks. The investigations in the massifs characterize the dominant operating exhumation mechanisms and place temporal constraints on the metamorphic episodes and exhumation kinematics of the mid-crustal rocks (figure 6.17). The results of these investigations when linked in with the results from the Pelagonian Zone (chapters 4 and 5) and with the published data of the Aegean region provide temporal constraints on the regional tectonic development of the Aegean region.

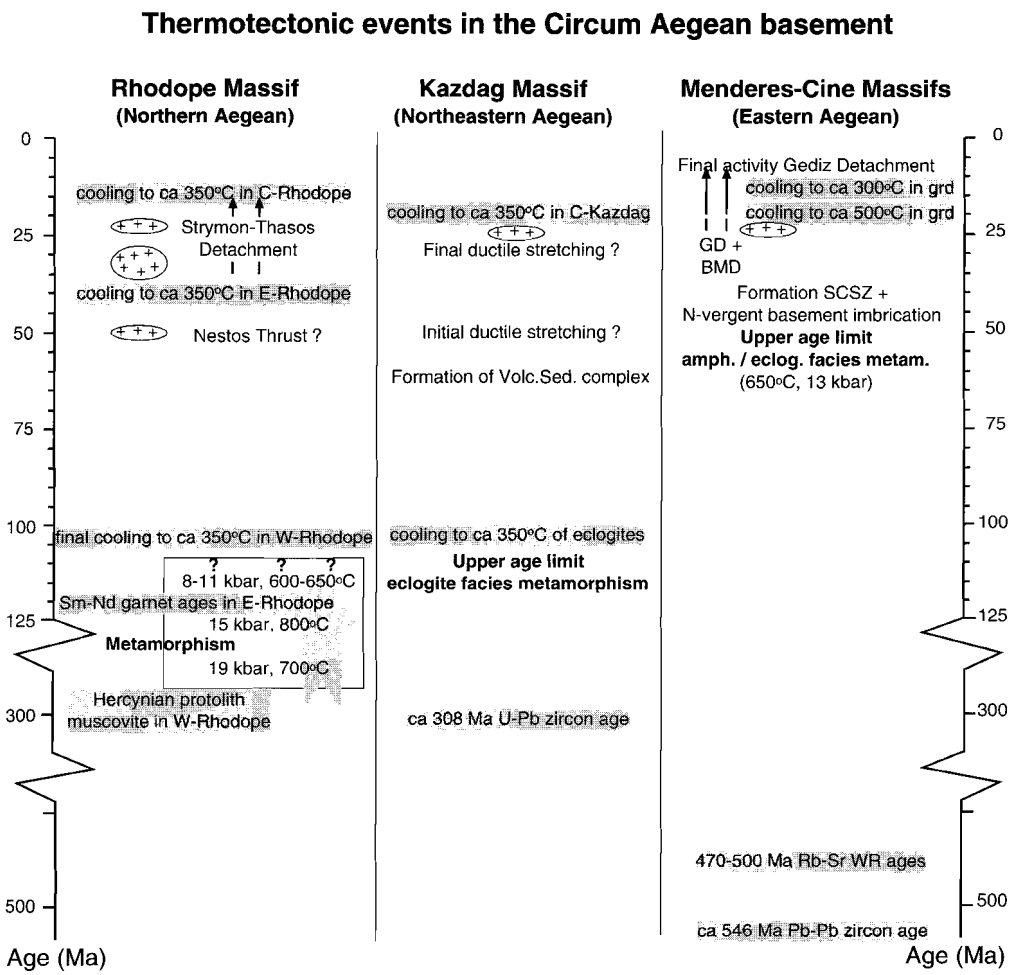

Figure 6.17. - Diagram which summarizes the main thermotectonic events in the basement of the Rhodope, Kazdag and Menderes Massifs. The summary illustrates i) the pre-100 Ma (Rhodope and Kazdag Massifs) and pre circa 50 Ma age of eclogite facies metamorphism (Menderes Massif) in the northern and eastern Aegean region, ii) the pre 25 Ma initiation of regional extnesion in all three massifs, and iii) the regional occurrence of circa 25-20 Ma granodiorites.

In the Rhodope Massif, $^{40}Ar/^{39}Ar$ laserprobe incremental heating and single fusion experiments on white mica porphyroclasts and white mica from deformational fabrics have all resulted in cooling ages. The obtained white mica ages show the preservation of Hercynian (ca 280 Ma) to Early Cretaceous (ca 145 Ma) cooling ages in the westernmost Rhodope and Late Eocene to Early Miocene cooling ages (40-15 Ma) in the central and eastern Rhodope. The Late Eocene white mica cooling ages in the central and eastern Rhodope indicate that

most basement rocks, which are currently exposed in this area, cooled below circa 350°C by circa 40 Ma. Consequently the observed mylonitic structures (thrusts) and metamorphic assemblages (upper greenschist facies to amphibolite facies metamorphic assemblages) within the basement sequence have formed prior to circa 40 Ma. Exhumation of the basement sequence occurred since circa 30 Ma along the shallow SW-dipping Strymon Detachment, which crosscuts the upper greenschist facies to amphibolite facies structures and separates the western Rhodope with 145 and 280 Ma white mica cooling ages in its hangingwall from the central and eastern Rhodope with 40 to 15 Ma white mica cooling ages in its footwall. Activity along the Strymon Detachment has positioned the sequence from ductile crustal conditions to brittle crustal conditions after which final exhumation occurred along a system of high angle normal faults. Although characterized by an overall direction of tectonic transport to the SW, it has been shown that a subtle change in dominant direction of tectonic transport occurred during exhumation of the sequence. This observed change in direction of tectonic transport is most likely caused by a clockwise rotation of the Rhodopian crust in an overall SSW-NNE striking extensional regime, related to the regional extensional collapse of the Aegean.

In the Kazdag Massif in northwestern Turkey, amphibolite facies rocks (Kazdag gneiss series) are tectonically overlain by a greenschist facies mylonite zone and an unmetamorphosed volcanosedimentary complex in which exotic blocks of eclogite facies rocks occur. The investigations reveal that the Kazdag Massif is a ductile dome which is characterized by N-S ductile stretching and additional thinning of the tectonostratigraphic sequence. Granodiorite emplacement at Latest Oligocene time (the Evçiler granodiorite) has reset the argon isotopic signature in nearby basement white mica and biotite. Away from the intrusion, older white mica ages have been preserved and show a circa 100 Ma cooling age after eclogite facies metamorphism and, consequently, post 100 Ma formation of the volcanosedimentary complex. Additionally, a poorly confined white mica age of circa 50-55 Ma of the greenschist facies mylonite between the unmetamorphosed volcanosedimentary complex and underlying Kazdag gneiss series indicate formation of this structure around 50-55 Ma, or, alternatively, cooling by 55-50 Ma after formation of the mylonitic fabric. The deformed nature of the margins of the Evçiler granodiorite suggests that ductile stretching of the massif continued until Miocene times. The brittle, and most recent, part of the history is characterized by high angle normal faulting along the southern margin of the massif, which has been caused by the SW to W ward propagation of the North Anatolian Fault Zone.

The research in the Menderes Massif and Çine Submassif have resulted in a detailed synthetic cross-section through southwest Anatolia and indicates that the onset of Late Alpine extension directly followed tectonic emplacement of mid crustal continental basement by Late Eocene times (ca 40 Ma). Further exhumation of basement rocks occurred by a two-phase collapse which initiated the development of Neogene supradetachment basins at circa 20 Ma and 7 Ma respectively. During the Miocene stage of the extensional collapse, the north dipping Gediz Detachment system developed under ductile conditions by the reactivation of thrust planes which are associated with the Late Eocene phase of basement emplacement. Subsequent reactivation of the old thrusts resulted in the development of the

antithetic semibrittle Büyük Menderes Detachment system, which, together with the Gediz Detachment, accommodated the doming of the Menderes Massif and controlled the architecture of the Gediz and Büyük Menderes supradetachment basins.

On a regional scale, the investigations in the Rhodope, Kazdag and Menderes Massifs reveal evidence for the involvement of pre-Alpine basement with Hercynian (Kazdag Massif) or Pan-African affinities (Menderes Massif) in Alpine extensional and compressional tectonics (figure 6.17). The Hercynian protolith ages (Kazdag Massif) hint to an Eurasian affinity, whereas the Pan-African cooling ages (Menderes Massif) hint to an Gondwanan affinity. The difference suggests that the sources of these protoliths have originated from the northern side (Kazdag) and southern side (Menderes) of the Paleotethys, respectively.
The presence of Early Cretaceous eclogite facies metamorphic assemblages as enclaves in the Rhodope Massif and as exotic blocks in a volcanosedimentary complex in the Kazdag Massif indicates an Early-Alpine or pre-Alpine episode of HP metamorphism (figure 6.17). The exact timing of the eclogite facies metamorphic episode remains, however, unclear. It is also unclear if the pre- Late Eocene eclogite occurrences in the Menderes Massif are related to the similar episode or to a younger Alpine episode of HP metamorphism.
Thrusting and development of the tectonostratigraphic successions in the massifs had completed before 40 Ma, after which the complexes were progressively exhumed (figure 6.17). The onset of thrusting has not been temporally constrained, but together with the final phase of recorded ductile compression in the metamorphic sequences which occurred in the Eocene (ca 40 Ma in the Menderes Massif), ductile extensional fault zones had developed, which have been recognized on the southern margin of the Çine Submassif (section 6.4, and Bozkurt & Park, 1994; Hetzel & Reischmann, 1996) and the northern margins of the Kazdag Massif (section 6.3) and the Rhodope Massif (Bonev et al., 1995). It has been shown by the study of the Menderes Massif that older thrust surfaces might focus well developed extensional structures at later times in the tectonic history.
The three studies all summarize that the onset of exhumation related to regional extension had initiated by circa 35 Ma. This indicates that the widely recognized phase of Early Miocene extension and related emplacement of syn-tectonic intrusions is not the solely episode during which the Aegean region was affected by extension. The Oligocene to Recent regional tectonic history is dominated by the development of metamorphic domes and associated detachment fault zones in the Late Oligocene - Early Miocene (ca 25-20 Ma), and high angle normal faulting in the Late Miocene - Pliocene (post 7 Ma). Related to the detachment faulting and high angle normal faulting is the development of the main sedimentary basins which are still further developing in the present Aegean configuration.

Chapter 7

Geodynamic synthesis

7.1 Introduction

This study has illustrated the successful application of $^{40}Ar/^{39}Ar$ laserprobe analysis of white mica bearing deformational fabrics to directly date the formation of such fabrics. The results are used to constrain in time the deformational and kinematic events and to quantify a tectonothermal evolution path. In order to be able to do this succesfully, the white mica in the analysed sample should have formed below its closure temperature range for the Ar isotope system. In summary, on the crystal scale, the setting or resetting of the argon isotopic system in white mica is determined by the rate of diffusion of argon in the crystal lattice. Since argon is an inert gas, the diffusion rate is controlled by thermally activated volume diffusion and the presence or absence of preferred diffusion pathways which might become available during or after chemical alteration or deformation of the selected white mica. It is emphasized that thermally activated volume diffusion can reset the argon isotopic system without producing evidence for an observable retrogression of the bulk mineral assemblage. Suspected resetting of the argon isotopic system by chemical alteration and/or deformation of the selected white mica population can be detected by optical microscopy and/or SEM studies (see chapter 3 for discussion). Partial recrystallization by chemical reactions and/or deformation often results in the development of a recognizable multiple generation white mica population in deformed and metamorphosed basement rocks. As these multiple generations may contain valuable information with respect to the tectonothermal evolution of the host rock, they should be separated into individual generations before $^{40}Ar/^{39}Ar$ analysis is undertaken. Careful evaluation of the proposed experiment is the key starting point to the dating of the tectonothermal events recorded by the micas of the metamorphosed and deformed samples. Although this appears to be very trivial, the literature demonstrates that this starting point has sometimes been overlooked. In general, when the formation of the white mica has occurred well above its relevant argon closure temperature (ca 350±30°C), a white mica ***cooling age*** will be obtained, which postdates the observed (re-) crystallization event of the mica. This is the case, when the white mica has crystallized from a melt or may have formed in a metamorphic assemblage or deformation fabric above 350±30°C. Alternatively, a white mica cooling age will also be obtained if the mineral assemblage, after its formation, has been reheated at temperatures in excess of circa 350±30°C for a sufficient period of time to allow total argon loss. A white mica ***fabric age***, directly related to the formation of white mica by deformational or metamorphic/chemical recrystallization, can only be preserved when the formation of the white mica fabric occurred at temperatures below circa 350±30°C. The white mica fabric age may be preserved if the analysed white mica generation has not been affected by younger, partial, recrystallization or by the subsequent reheating.

As has been summarized in chapters 3 and 4, relevant white mica ages will only be obtained

after regional thermal conditions are well constrained. The regional thermal conditions must be established so that the effects of any exposure of the white mica to later thermal perturbations can be considered. After careful characterization of the metamorphic assemblage and deformational fabric, the analysed white mica can be uniquely related to a particular fabric forming event and/or a particular metamorphic assemblage. In other words: before analysis, a given phase of mica generation must be uniquely identified in a sample with respect to a multiple phase generation history displayed by the overal mica population.

Research on basement rocks from the Aegean region, reported in this thesis, has shown that low temperature greenschist and blueschist facies metamorphic assemblages, as found in the Pelagonian Zone, have proved to be suitable for the direct dating of different fabric forming events, by applying the $^{40}Ar/^{39}Ar$ laserprobe technique to white mica (chapters 4 and 5). The characterized events of the Pelagonian Zone can be integrated with further data obtained from the Rhodope Zone of NE Greece, from the Kazdag and Menderes Massifs of W-Turkey (chapter 6) and with the published data from Circum-Aegean areas (i.e. from Crete, Cyclades, Rhodope Zone, Kazdag Massif, Tavsanli and Menderes Massif, see figure caption of figure 7.1 for references) to provide an overview of the tectonic development of the Aegean region as a whole.
When constructing a regional synthesis based on the $^{40}Ar/^{39}Ar$ analyses, two important points should be borne in mind. Firstly, any proposed regional tectonic synthesis which is obtained for the internal parts of the Aegean region should be compatible with basin formation and/or sedimentation in the external and more frontal parts of the region, with respect to the present-day subduction zone. Secondly, it is important to realize that regional tectonic and kinematic events might have affected the currently exposed rocks at different crustal levels within different paleogeographic configurations to those seen today and especially with respect to each other.

7.2 Tectonothermal evolution of the Aegean region: metamorphic episodes versus deformational events

The tectonic events which have been described in this study (chapters 4, 5 and 6) in combination with published data from the region (see figure 2.1) have been used to construct a tectonothermal evolution of the Aegean region, as presented in figure 7.1. Figure 7.1 also illustrates the long time periods (minimal circa 20 m.y.) over which a given set of PT conditions (episode) prevailed in contrast to relatively short time periods (ca 2 to 5 m.y.) during which deformation occurred (event). The diagram reconfirms a potential pitfall of

Figure 7.1. - Summary of the recognized metamorphic episodes and deformational events in the exposed basement rocks of the Aegean region along with the timing of carbonate sedimentation and flysch/clastics deposition in pre- and/or non-metamorphosed parts of the Hellenic orogen. The summary is presented from most internal position (Eurasia) to most external position (closest to present-day active subduction zone) in the ***present-day configuration*** along a regional N-S transect across the circum-Aegean region (figure 7.1a; Rhodope Zone to Crete) and in

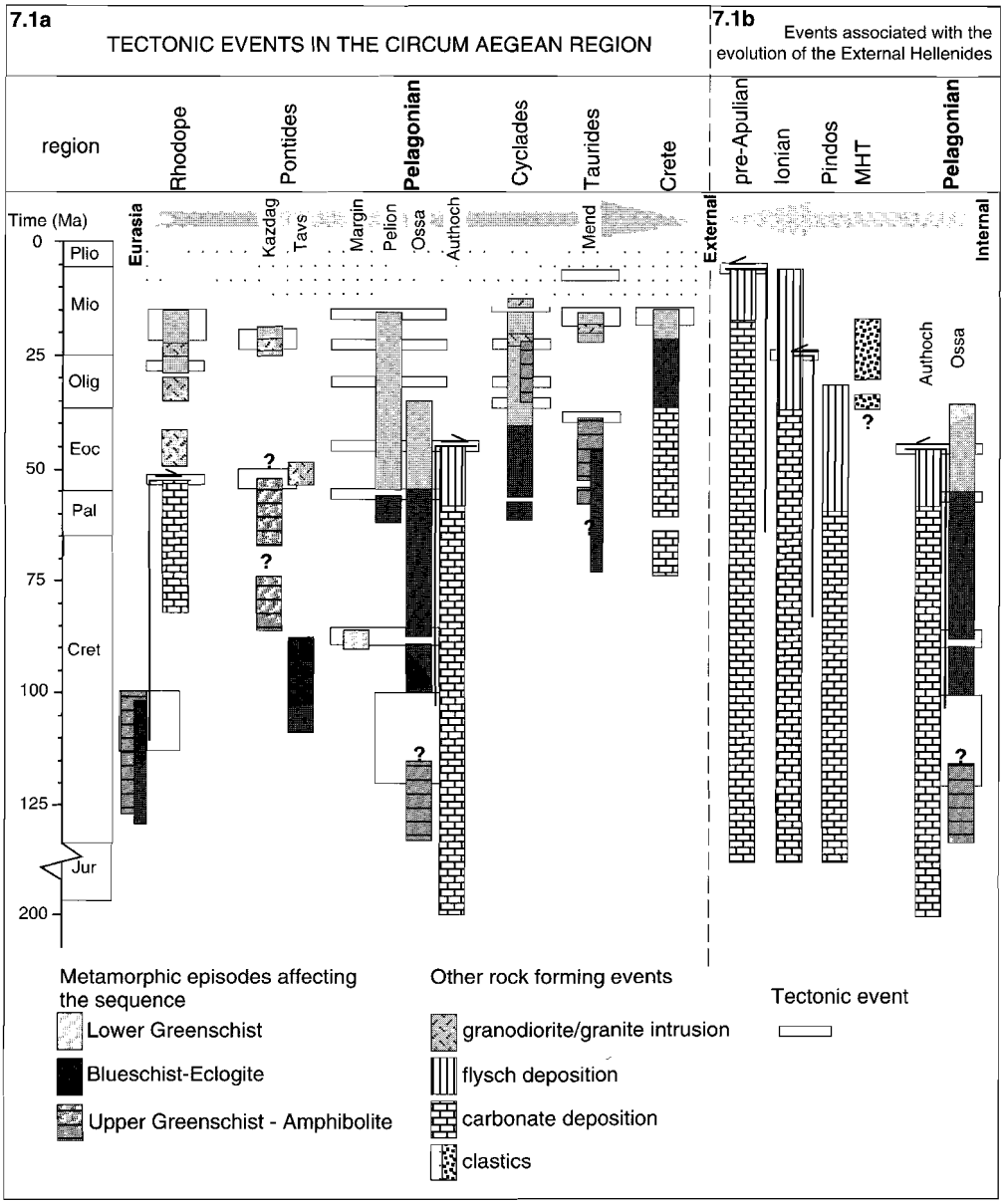

detail along a local ENE-WSW transect across the Hellenic orogen on mainland Greece from the Pelagonian Zone to the pre-Apulian Zone (figure 7.1b). Abbreviations; Tavs, Tavsanli region; Autoch, autochthonous units; Mend, Menderes and Cine Massifs; MHT, Meso Hellenic Trench. Data from this study and from Wijbrans & McDougall, 1988; de Wet et al, 1989; Wijbrans et al, 1990; Harris et al, 1994; Dinter et al, 1995; Hetzel et al, 1995b; Hetzel et al, 1996; Jolivet et al, 1996; Okay & Kelley, 1994; Okay et al, 1996; Raouzaios et al, 1996; Wawrzenitz, 1997, Thomson et al, 1998, External Hellenides data primarily after Aubouin et al, 1963; Underhill, 1989; Jones & Robertson, 1991).

geochronology studies which concern the dating of "metamorphic events"; *age information obtained for white mica from a characteristic assemblage might have been recovered from a single protracted metamorphic episode during which several deformational events, and thus several fabric forming events, could have occurred.* If the analysed white mica is related to an incorrectly interpreted metamorphic assemblage or an inappropriate deformational structure, the regional tectonic significance of the determined isotopic age becomes obscured. It is likely that regional tectonic events have been operative at different crustal levels at any given time, and will therefore produce co-temporal deformational fabrics with different associated metamorphic assemblages. As a consequence, analysed white mica from the different metamorphic assemblages which formed during the same deformational event but at different crustal levels may not be recognized, microstructurally, as being related to the same event.

The distribution of three high pressure metamorphic belts as recorded in the Aegean region (see figure 2.8) has been critically evaluated and it is concluded that the HP metamorphism in the Aegean region cannot be characterized in terms of distinct episodes. This study has emphasized that the termination of high pressure metamorphism in the Aegean, on a regional scale, should be regarded as a single and diachronous process across the region (see chapter 5 for discussion). Because the process was diachronous the earliest exhumation of HP sequences is circa 54 Ma in the more internal parts of the Aegean region (Pelagonian Zone) and becomes younger as the present-day subduction zone is approached, chiefly, circa 40 Ma in the Cyclades region and circa 20 Ma on Crete.

To indicate the interrelationship of tectonic events and metamorphic episodes, the main tectonic events and related metamorphic conditions of the Pelagonian Zone are summarized below (see chapters 4 and 5 for more details on the Pelagonian tectonothermal history). The main compressional and extensional events that affected different crustal levels and which resulted in a complex distribution of $^{40}Ar/^{39}Ar$ white mica ages in the final tectonostratigraphic sequence in the Pelagonian Zone are presented in figure 7.2. The main events, which affected the Pelagonian Zone, commence with a phase of basement imbrication from circa 120 Ma to circa 100 Ma, which occurred at mid-crustal levels in the relic Hercynian basement. The imbrication of relic basement might have initiated HP metamorphism in deeper levels of the Pelagonian basement, while at shallower levels greenschist facies conditions continued to prevail. Evidence for this scenario is seen in mylonite fabrics which formed by circa 85-90 Ma under blueschist facies conditions at low structural levels of the Pelagonian basement (now exposed in the Ossa Massif) but under greenschist facies conditions at relatively high structural levels of the Pelagonian basement (now exposed in the western margin of the Pelagonian Zone). Termination of HP metamorphism in the Pelagonian Zone occurred as a response to an extensional event at circa 54 Ma which involved overall thinning of the basement sequence during bivergent tectonic transport under blueschist and greenschist facies metamorphic conditions. After 54 Ma, the currently exposed Pelagonian basement was brought into shallow crustal levels where it was affected by lower greenschist facies metamorphism and was thrusted over the autochthonous carbonate sequences and flysch deposits by circa 45-40 Ma. During the 45-40 Ma thrusting event, the basement units had been partly imbricated with slices of the carbonate and flysch

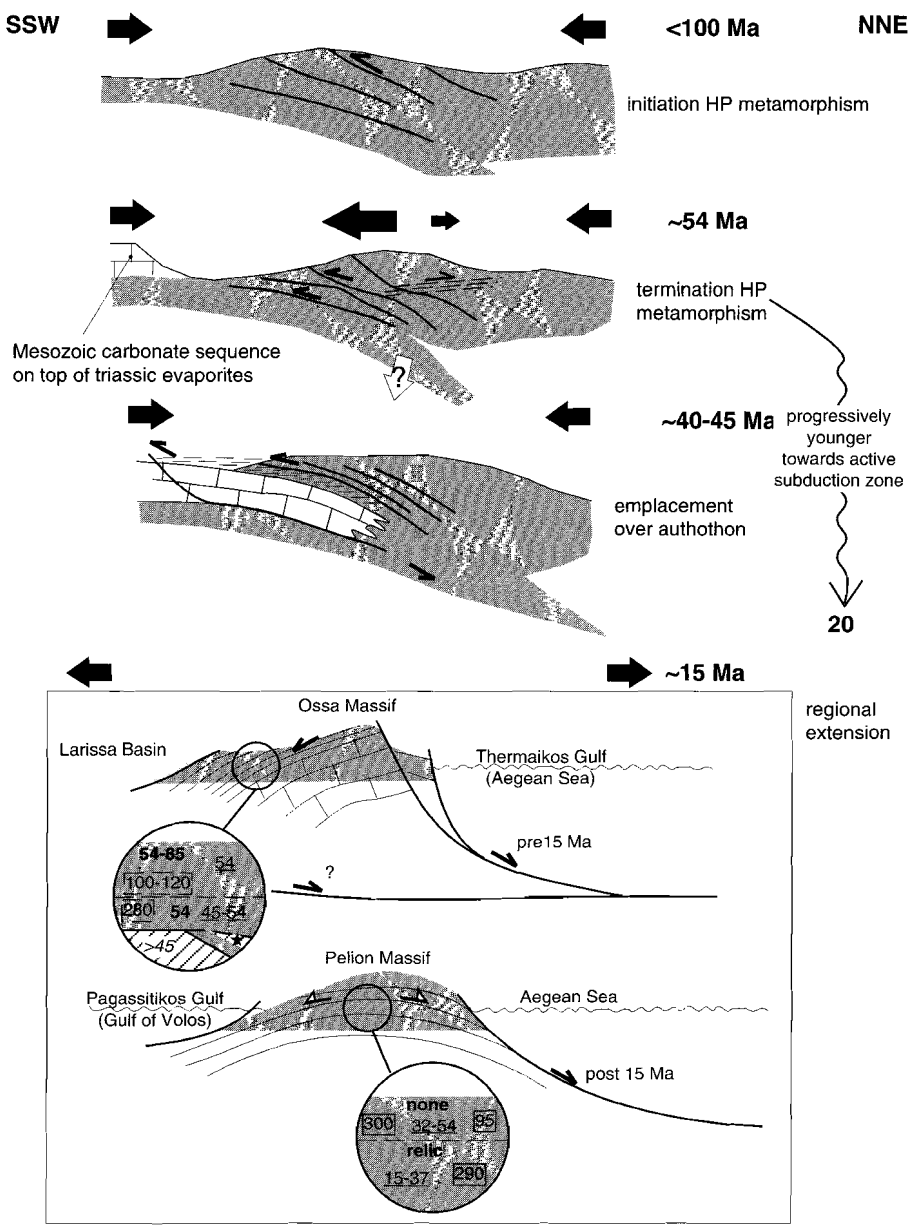

Figure 7.2. - Schematic presentation of the tectonic evolution of the Pelagonian Zone in cross-section. The main tectonic events, which affeceted the Pelagonian Zone have been presented in combination with the expected regional distribution of compression and extension. The bottom diagram shows the complexity in structural position and distribution of $^{40}Ar/^{39}Ar$ laserprobe results in the Ossa and Pelion Massifs (see also chapter 5, especially figure 5.5) in the Late Miocene to Recent configuration (muscovite cooling ages in squares, blueschist mylonitic mica ages in bold, greenschist mylonitic mica ages underlined, stratigraphic information italic).

which had been derived from depths with pressure equivalents of over circa 3 kbar, as lawsonite porphyroblast bearing flysch slices occur in the basal structure of the allochthonous basement sequence. Continued uplift and erosion, as well as activity along low angle and high angle normal faults caused further exhumation of the Pelagonian basement and of the underlying carbonates and flysch. By circa 36 to 40 Ma the basement near the present-day Ossa-Olympos region had been brought into brittle crustal levels, while greenschist facies ductile deformation continued to affect and to rework the metamorphosed sequence in the present-day Pelion region until circa 15 Ma. The tectonic evolution of the Pelagonian Zone is schematically summarized in figure 7.2 and shows the operation of four main tectonic events; characterized by compression at circa 100 Ma and at circa 45 Ma and by extension at circa 54 Ma and at circa 20 to 15 Ma. The main tectonic events operated at blueschist facies, greenschist facies and/or brittle crustal conditions and have resulted in a complex spatial distribution of $^{40}Ar/^{39}Ar$ white mica ages. The $^{40}Ar/^{39}Ar$ ages are presented in the bottom parts of the diagrams in figure 7.2 (see also chapter 5, figure 5.5) and have been derived from the muscovite porphyroclasts from the mylonite zones (in squares), phengitic white micas from blueschist mylonites (bold) and from greenschist mylonites (underlined), respectively (see chapter 4 and 5 for discussion).

7.3 Aegean tectonics: an interplay of diachronous and synchronous processes

The main tectonic events which have been recognized in this study and which have been integrated with data from the literature (figure 7.1) are schematically presented in figure 7.3. In contrast to the regionally correlated synchronous compressional and extensional events which continued to affect the whole Aegean during its Alpine tectonic history, it is again emphasized, that the termination of the HP metamorphism is a diachronous process across the Aegean region, with younger ages being recorded towards the present day active subduction zone (see figures 7.2 and 7.3 and chapter 5 for discussion). The recognition of specific synchronous events alternating with diachronous processes in the present study is to be expected theoretically in any orogen (e.g. development of a fold-and-thrust belt, or an accretionary wedge evolution) and has recently been proposed for the Himalayas (Ruddiman, 1998). The dominant mechanisms which control the established tectonic events should be compatible with the observed regional correlation of these synchronous and diachronous events. The balance between synchronous compressional and extensional events and the diachronous termination of the HP metamorphism and of the related partial exhumation result in the identification of different sequences of tectonic events across the region. In figure 7.2 and 7.3 it can be seen that the Alpine tectonic history in the Pelagonian Zone is characterized by compression (ca 120 to 100 Ma), extension (ca 54 Ma), compression (ca 45-40 Ma) and extension (ca 22 to 16 Ma). In contrast, the sequence of tectonic events in the Cycladic and Cretan region is characterized by a recognized episode of compression followed by a recognized long period of extension. The interaction of the circa 45-40 Ma regional compressional event and a contemporaneous local extensional

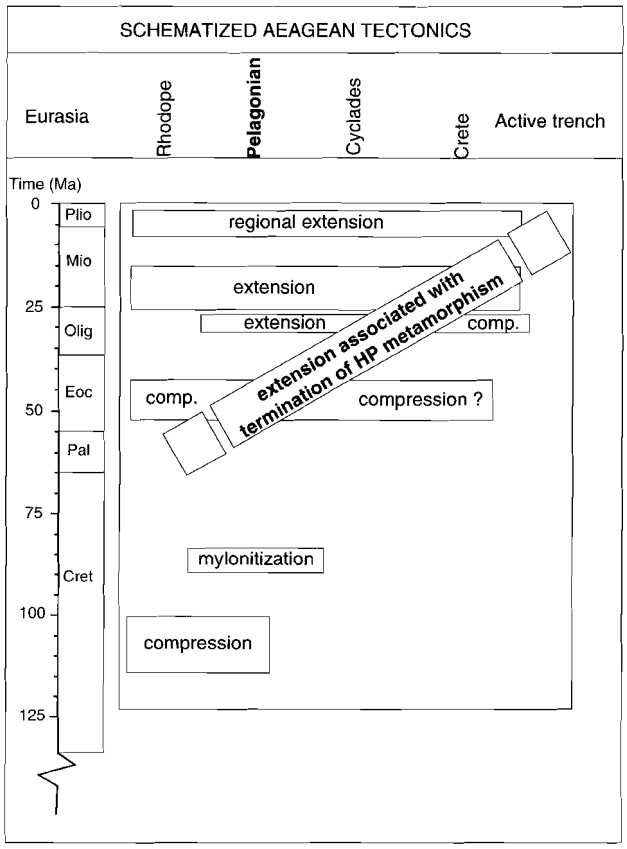

Figure 7.3. - Schematized diagram of Aegean tectonics illustrating the interplay of a diachronous extensional event, related to the termiantion of HP metamorphism and progressive shift towards the active trench) and synchronous events extensional, compressional and (undifferentiated) mylonitic events, affecting the different parts of the Aegean.

event in the Cyclades will handicap their recognition as two individual events. As a consequence, the interplay between these two events will create a complex local tectonic setting and complex overprinting deformational fabrics during the termination of the HP metamorphism. Additionally, the 45-40 Ma compressional event might have contributed to the formation of HP assemblages on Crete, while the interaction between circa 20 Ma local extension overprinted by regional extension will be hard to identify separately on Crete and might be an explanation for the accelerated exhumation of the Cretan HP assemblages, as has been summarized by Thomson et al. (1998). In a way similar to that illustrated for the Pelagonian Zone, Cyclades area and Crete, a sequence of events can be erected for other parts of the Aegean region, e.g. the Rhodope Zone, western Turkey and the external Hellenides, albeit less well constrained because of the limited number of geochronological data. On a regional scale it is illustrated that external locations with respect to the present-day subduction zone have experienced several phases of compression before they were affected by extension in the Miocene and/or later periods (e.g. Crete, External Hellenides, Lycian Nappes). Locations within the internal parts of the Aegean region (Rhodope and Pelagonian Zones) have experienced a distinguishable alternation of compressional and extensional events (see chapters 4, 5 and 6), which may also have occurred in the Kazdag Massif (see chapter 6). Intermediate locations (e.g. Menderes Massif, Cyclades) experienced a complex tectonic history in the Eocene and Oligocene due to the interplay of local extension during on-going regional convergence (see chapter 6).

7.4 Exhumation of Aegean basement; possible causes and consequences.

7.4.1 Introduction

As already discussed in chapter 2, it has been proposed by several workers that exhumation of the circum Aegean HP sequences has been dominantly controlled by detachment fault systems which operated across the Aegean at Early Miocene times (Lister et al., 1984; Gautier & Brun, 1994; Jolivet et al., 1994b; Hetzel et al., 1995a). Other workers proposed an additional Oligocene extensional event to initiate exhumation of HP sequences (Avigad et al., 1997). In this study, it is concluded that Early Miocene detachment faults have contributed to the final exhumation of ductile rocks in the Aegean region. It has also been concluded that the Early Miocene extensional setting succeeded an older tectonic setting which initiated exhumation of metamorphosed basement (see chapter 5 and 6 for discussion). In the Cyclades and the Pelagonian Zone of the Aegean region, ambient metamorphic pressures had already been reduced to maximum 4-6 kbar by Early Miocene times. Aegean HP metamorphism ceased to affect the Cycladic sequences by circa 40 Ma when PT conditions had dropped below circa 6 kbar and 350-400°C (the lower boundary of the epidote blueschist facies field). This followed peak pressure conditions of circa 14 to 16 kbar and indicates that the earliest exhumation of HP assemblages from >45 km to <20 km, and the associated pressure decrease of circa 8 kbar, is hidden in the pre 40 Ma tectonic history (see chapter 5 for discussion). Additionally, the occurrence of HP enclaves in amphibolite facies metamorphic mid-crustal rocks in the Menderes Massif is restricted to the hangingwall of the Early Miocene detachment fault system (chapter 6), which also shows that the Early Miocene detachment faults are clearly not the single mechanism, by which these HP rocks were exhumed.

7.4.2 The timing of extensional events and the dominant tectonic processes

The balance between synchronous regional extension and the diachronous termination of the HP metamorphism and partial exhumation of HP metamorphic assemblages is an integral part of convergent mountain belts and regional accretionary wedge settings. It involves a dynamic system which is balanced by convergence, subduction, accretion and the exhumation of material. The associated accommodating mechanisms are well studied in both the present-day and past accretionary wedge settings. Some studies have recognized that exhumation of HP assemblages occurred during on-going convergence (see Platt, 1993, for a summary). If the exhumation of the HP assemblages is related to a compressional event, uplift and erosion are the controlling factors to position these rocks closer to the surface (Stüwe & Barr, 1998). Alternatively, if the exhumation is related to extension during overall convergence other mechanisms may be involved. The dominant tectonic processes which have been proposed to control syn-convergence extension involve gravity gliding, critical taper formation (Davis et al., 1983; Dahlen, 1990), underplating (Houseman & England, 1993), convective removal of thickened lithosphere (Platt & England, 1993; Vissers et al., 1995), roll-back of the subducted slab (Royden, 1993a; 1993b), corner flow in an accretionary wedge (Platt, 1993; Merle, 1994; Allemand & Lardeaux, 1997) or a combi-

nation of these mechanisms which influence the gradients in the gravitional potential energy across the orogenic belt or wedge. The diachronous termination of HP metamorphism suggests a scenario which is characterized by local extension during overall regional convergence. The regional controlling process of the extension should be compatible with the observed progressive shift in the termination of HP metamorphism towards the present day active subduction zone. The process should allow a net outward flow of material in the overriding plate towards the active subduction zone and promote local extension in back arc regions. The theoretical crustal response to the proposed tectonic processes, which accommodate syn-convergence extension, only allows limited differentiation between these processes. Several of the processes can be distinguished in mantle tomographic studies, such as underplating, removal of thickened lithosphere, and/or roll-back of a subducted slab (see e.g. Wortel & Spakman, 1992). The tomographic studies are only applicable to the investigation of tectonic processes which operate near the base of the lithosphere in active or young tectonic settings. This implies that the dominant process causing the syn-convergence extension in ancient tectonic settings can only be speculated upon. The following sections will present the characteristics of the extensional setting and of the exhumation processes which affected the Aegean region in the Neogene (paragraph 7.4.3) and the Paleogene (paragraph 7.4.4). The characterization of the Neogene and Paleogene settings is

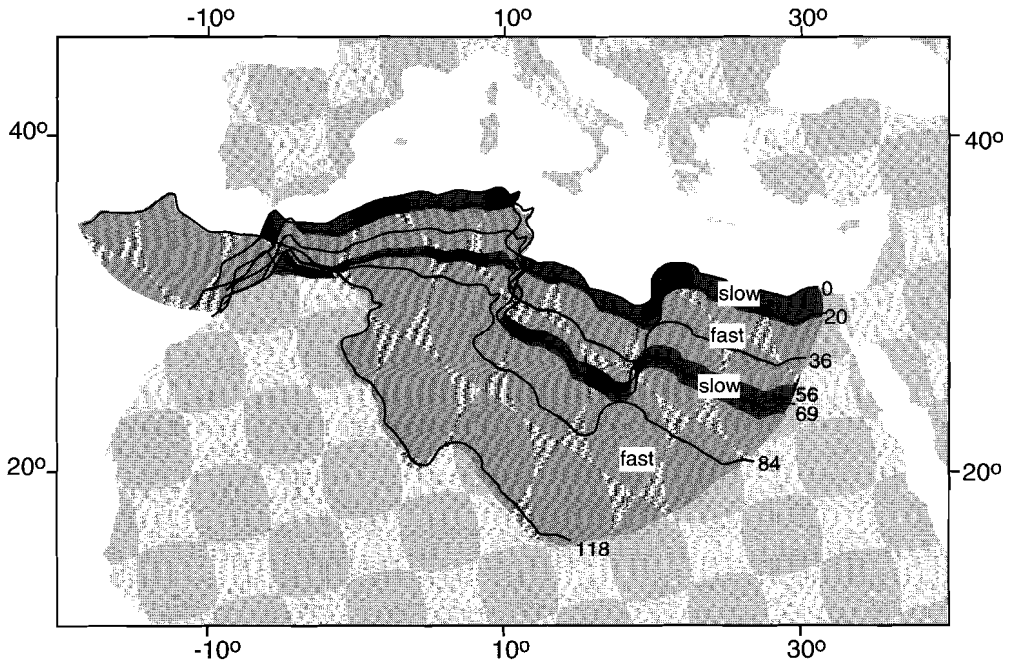

Figure 7.4. - Summary of overall convergence rates of African and Eurasian plates (data extrapolated from Müller & Roest, 1992), indicating alternation of "fast" convergence (pre circa 75-70 Ma and circa 55-50 to 25-20 Ma; above 15-20 km/m.y.) and "slow" convergence (ca 75-70 to 55-50 Ma and circa 25-20 Ma to Recent; circa 6-8 km/m.y.).

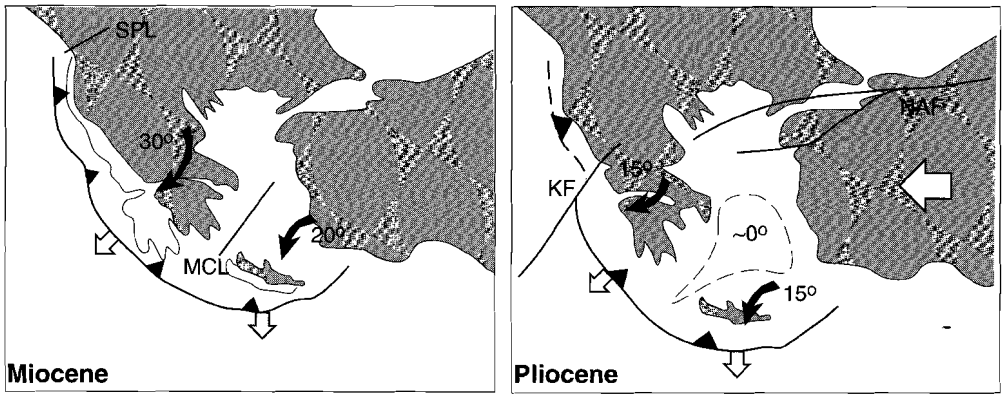

Figure 7.5. - Schematized *crustal response* to Miocene to Recent extension in the Aegean region and associated block rotations (modified after Walcott (1998). Consult figure 2.6 for proposed controlling dynamics. Abbreviations; SPL, Scutari Pec Line; MCL, Mid Cycladic Lineament; KF, Kefalonia Fault zone; NAF, North Anatolian Fault zone.

followed by a tentative model for the dominant mechanisms, which have accounted for the observed periods of syn-convergent extension in the Aegean region (paragraph 7.4.5 and section 7.5).

7.4.3 Neogene exhumation in the Aegean region

The regional extension which affected the Aegean in Miocene times has been related to a global decrease in spreading and/or convergence rates of the main plates (see figure 7.4, and Müller & Roest, 1992). Figure 7.4 is a modification of figure 2.8 (after data from Müller & Roest, 1992) and shows that for the past circa 100 Ma, convergence between the African and Eurasian plates is characterized by slow convergence rates, which show an alternation of periods of very slow (i.e. 6-8 km/m.y.) and relatively faster (i.e. above 15-20 km/m.y.) convergence rates. Two periods of extremely slow convergence rates are identified, of which the 20 Ma to Recent period has been best identified in the Mediterranean region. A similar, circa 20 m.y., period of very slow convergence rates has also occurred in the latest Cretaceous and through the Paleocene (circa 75 to 55 Ma), the tectonic implications of

Figure 7.6. - Summary of orientation of kinematics in Early Miocene low angle extensional structures and of emplacement ages of syn-tectonic intrusives, after re-examination of the data from this study, and from Wijbrans & McDougall, 1988; Urai et al, 1990; Lee & Lister, 1992; Dinter & Royden, 1993; Gautier & Brun, 1994; Dinter et al, 1995; Hetzel et al, 1995b; Jolivet et al, 1996; Vandenberg & Lister, 1996; Wawrzenitz, 1997 Whitney & Dilek, 1997). *7.6a.* Location of main Early Miocene metamorphic domes and North Anatolian Fault Zone (NAF) and Mid Cycladic Lineament (MCL) reported in the circum Aegean region. The Early Miocene domes have been presented in combination with their present-day ductile stretching lineation orientation: 1. Pelion Massif, 2. Strymon-Thasos detachment, 3. Cyclades (west Aegean block), 4. Cyclades (east Aegean block), 5. Crete, 6. Kazdag Massif, 7. Menderes Massif, and 8. Nigde Massif. *7.6b.* Orientation of reconstructed detachment kinematics, restored for the Early Miocene configuration (restored after proposed configuration of Walcott, 1998). The observed kinematics have been differentiated in the dominant transport direction in main detachment of the metamorphic dome (black arrow) and the secondary transport direction in the antithetic detachment (white arrow). *7.6c.* Summary of crystallization ages of syn-tectonic granodiorites which have been emplaced into detachment zones.

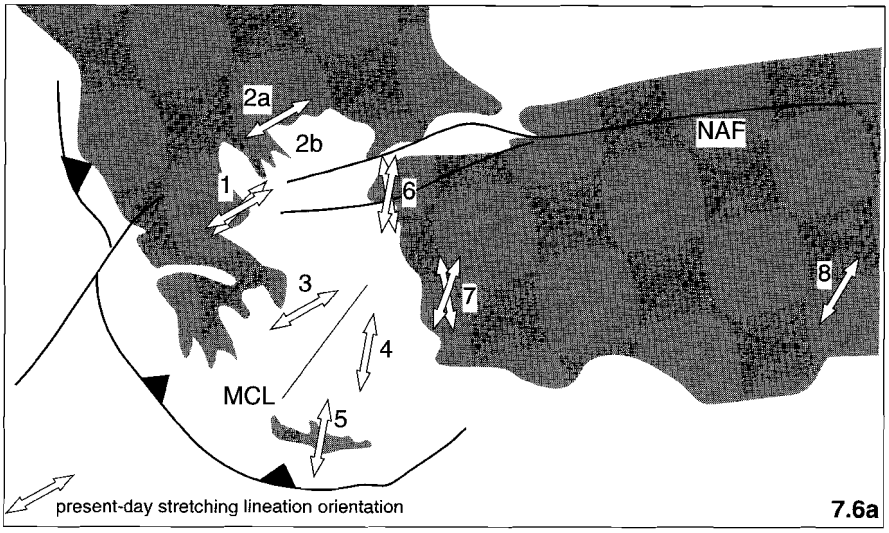
2a
2b
1
6
NAF
3
7
8
4
MCL
5
present-day stretching lineation orientation

7.6a

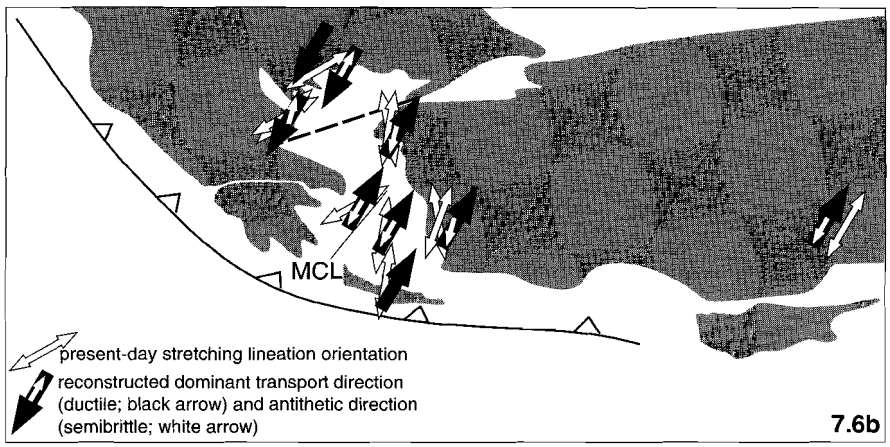
MCL
present-day stretching lineation orientation
reconstructed dominant transport direction
(ductile; black arrow) and antithetic direction
(semibrittle; white arrow)

7.6b

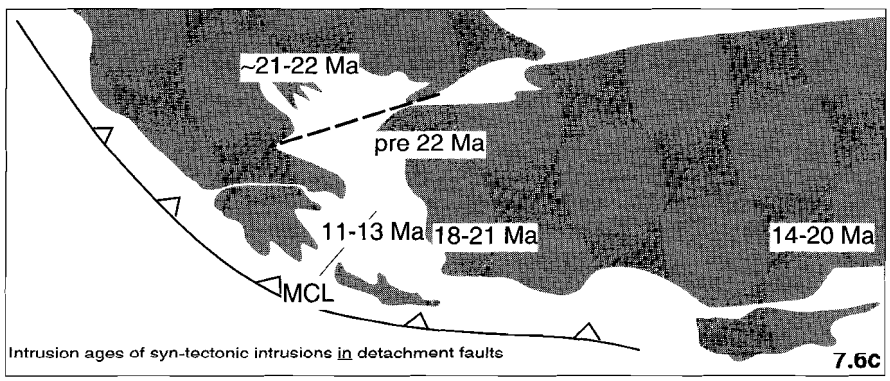
~21-22 Ma
pre 22 Ma
11-13 Ma
18-21 Ma
14-20 Ma
MCL
Intrusion ages of syn-tectonic intrusions in detachment faults

7.6c

which will be further discussed.
The general decrease in convergence rates will cause the retreat of the subducting slab (roll-back) by the gravitational instability of the subducted lithosphere (see also figure 2.4). The roll-back will cause upwelling of asthenospheric material in the back-arc region and will enhance the associated back-arc extension (Royden, 1993a; 1993b). Additionally, the pronounced roll-back of a long-lived subduction zone and its associated subducted old and dense lithosphere might even promote detachment of the subducting slab (Spakman et al., 1988; Wortel & Spakman, 1992). The combination of slab roll-back and slab detachment has been proposed to be the dominant dynamic model for the Miocene to Recent extension in the Aegean region (Meijer & Wortel, 1997; Walcott, 1998). By the end of the Miocene, the westward expulsion of Turkey is likely to interfere with the established

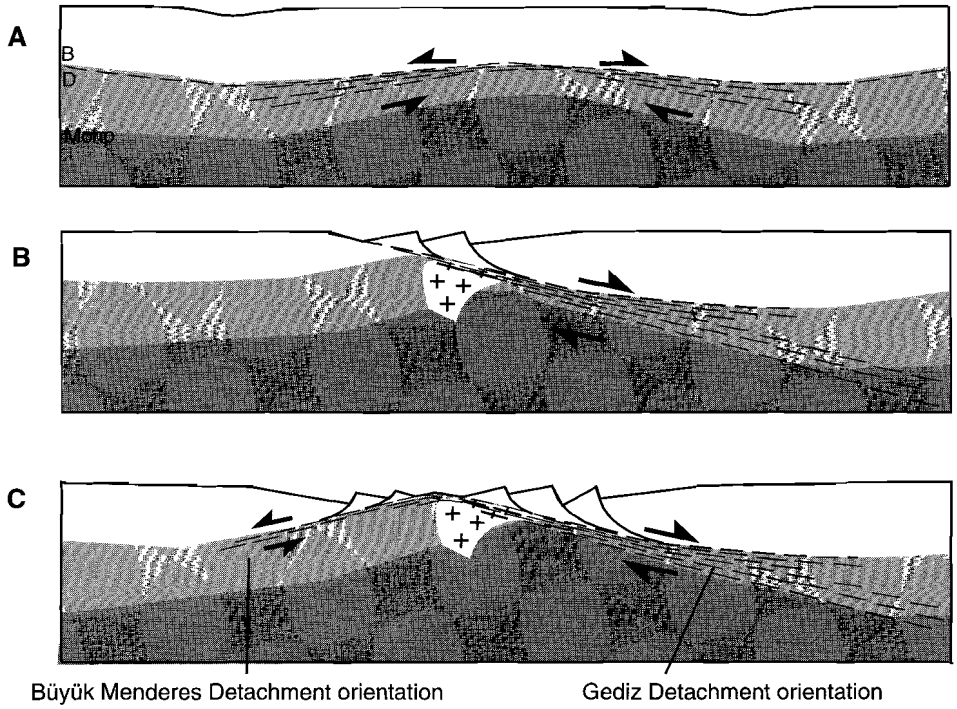

Figure 7.7. - Schematic development of Miocene metamorphic domes in the Aegean. *7.7a.* Proposed initial stretching of ductile crust and mantle lithosphere and associated decoupling of ductile and brittle crust, which is the precursor of detachment fault formation. The initial development of the future detachment date might be an explanation of the time lag between the age of formation of the detachment mylonite and the age of formation of the supradetachment (half-)grabens. *7.7b.* Detachment fault formation and supradetachment basin formation associated with the development of an initial asymmetric extensional structure after further stretching of the ductile crust and mantle lithosphere (relative to the scenario in figure 7.7a) and the associated break up of the brittle crust. *7.7c.* Antithetic detachment fault formation and development of a final bivergent extensional system which accomodates further doming of the ductile crust and lithosphere in the footwall of the detachment structures (following on the scenario as presented in 7.7b).

extensional setting in the present-day Aegean region (see figure 7.5, after Le Pichon et al., 1995; Meijer & Wortel, 1997; Walcott, 1998). The westward expulsion of Turkey has been related to the final collision between the Arabian microplate and Eurasia and which has been accommodated by movement along the North Anatolian and East Anatolian Fault Zones (c.f. figure 2.1).

The Early Miocene phase of regional extension was accomodated by detachment fault systems, which have been recognized across all of the Aegean region and as far east as central Anatolia, that is, from the Pelion Massif till the Nigde Massif (figure 7.6a). Detachment faulting has often been accompanied by emplacement of syn-tectonic granodiorites, which have been recognized in the Rhodope Massif, Cyclades, Kazdag Massif, Menderes Massif and Nigde Massif (figure 7.6c), but are not found in outcrop in the Pelion Massif, Thassos Island (south of the Rhodope Massif) and Crete. The granodiorites have been emplaced at very shallow crustal levels, as derived from PT conditions in the contact aureole (indicating intrusion depths of less than 10 km in the Nigde Massif, following Whitney & Dilek, 1997 and Cyclades; e.g. Naxos, following Jansen, 1977), and as indicated by their close relationship with hypabyssal and volcanic andesitic dacites (suggesting circa 5 km depth of intrusion for the Salihli granodiorite in the Menderes detachment, chapter 6). The difference in pressure estimates of the mylonitized footwall metamorphic assemblage (ca 4 to 6 kbar), which corresponds to a depth of circa 15 km and the emplacement depth of the granodiorite intrusions (5 to 10 km), indicate that the granodiorite intrusion post-dates the onset of detachment faulting and occurred after circa 5 to 10 km of unroofing. As a result, the *onset* of the formation of the metamorphic core complex, or metamorphic dome, predates the emplacement of the intrusions and therefore cannot be directly derived from age information of the syn-tectonic intrusions. The onset of the formation of the core complex might have occurred at pre-Miocene times or, alternatively, the initial exhumation must have been rapid and was directly followed by emplacement of the intrusions.
Research in the Menderes Massif and Çine Submassif in western Turkey (section 6.4) has recognized a close harmony between the formation of the Menderes dome and the formation of Early-Mid Miocene coal deposits in the main supra-detachment basins. This observation indicates either that the initial 8-10 km of unroofing of footwall rocks has been confined to a narrow time interval, between circa 24 and 20 Ma for the Menderes Massif if basin formation is directly related to the *initiation* of detachment faulting. Alternatively, basin formation might post-date detachment fault formation as a result of the decoupling of middle crustal and upper crustal levels and related doming of the ductile mid-crust prior to the deformation of the upper crustal levels (figure 7.7a). Considering the temporal evolution of the Menderes Massif (figure 6.16), it is suggested that the Miocene dome formed as a result of the development of a north dipping main detachment fault system (the Gediz Detachment) at ductile crustal levels and an antithetic low angle normal fault system (the Büyük Menderes Detachment), which appears to postdate the initial development of the main detachment fault system and formed at semi-ductile crustal levels (schematized in figures 7.7b and 7.7c). The final bivergent system has led to the postulation that the initial extension was also accommodated by a bivergent system (Hetzel et al., 1995a), but this is

not indicated by the sequential structural development as outlined above and by the time lag between the two extensional fault systems.

Detailed investigations show that the Miocene domes in the Aegean are often characterized by a semi-bivergent extensional system (data from the Pelion Massif, this study; Thasos, Wawrzenitz, 1997; the Kazdag Massif, this study; the west Aegean block, Ios, Vandenberg & Lister, 1996; the east Aegean block, Naxos, John & Howard, 1995; the Menderes Massif, this study; and the Nigde Massif, Whitney & Dilek, 1997). The semi-bivergent system is often related to a temporal difference in the development of the two major normal fault systems that control the formation of the dome. The result of the temporal difference is the development of an asymmetric dome formed by one dominant ductile fault zone, which also is the locus of the syn-tectonic granodiorites, and a second antithetic semi-ductile fault zone (figures 7.7b and 7.7c) in a similar fashion to that observed in the Menderes Massif (see section 6.4). Restoration of the orientations of the main detachment faults and the antithetic faults to an Early Miocene configuration (figure 7.6b), shows that the main detachments are SSW dipping in the northern Aegean region and NNE dipping in the central to southern Aegean and Turkish regions. It is shown that the region of NNE dipping main detachments is not limited to the southern side of the Mid Cycladic Lineament (figures 7.6 and 7.8, see also Walcott, 1998), a structure which Walcott (1998) concluded to have played an important role in the Neogene tectonic history of the Aegean region (figures 7.5 and 2.3). This indicates that formation of the detachment faults occurred prior to the important role of the MCL in Miocene tectonics. Additionally, the transition from NNE to SSW dipping detachments suggests the occurrence of a transfer fault in the ductile and brittle parts of the crust in the northern Aegean Sea (dashed line in figures 7.6 and 7.8), separating the two domains and accommodating the difference in asymmetric extension, before it was followed by development of the antithetic detachments and regional bivergent extension (figure 7.8). The location and orientation of such a transfer fault might be inherited during formation of a younger tectonic structure such as the North Anatolian Fault Zone (figure 7.6). That is, it is possible that it became the focus for the westward propagation of the North Anatolian Fault Zone.

7.4.4 Paleogene exhumation in the Aegean region

The Miocene to Recent tectonic scenario for the Aegean is relatively well understood, as the end-product is the observable in present-day geology of the Aegean region. In contrast, less is known about the pre-Neogene tectonic processes which affected the region. In theory, the Paleogene history has often been summarized as the period of Alpine compression predating the period of post-orogenic extensional collapse (Dewey, 1988). However, it is clear from recent work that the Paleogene dynamics are not solely characterized by regional compression, but also by local and/or regional extension (see chapters 4, 5 and 6). The Paleogene dynamics will be discussed in detail below. The regional compression is expressed by the well developed fold-and-thrust belt and related Eocene to Miocene flysch deposition in the flexurally controlled basins of the External Hellenides on mainland Greece and of the Lycian Nappes in southwestern Turkey. The exact timing of the development of the fold-and-thrust belt in the External Hellenides is well constrained by stratigraphic data

for the flysch deposits in the main isopic zones (figure 7.1, right column) and suggests that the activity of the main thrusts progressively shifted from earliest Oligocene (Pindos Zone over Gavrovo-Tripolitza Zone), to latest Oligocene (Pindos Zone over Ionian Zone) and, finally, to latest Miocene (Ionian Zone over pre-Apulian Zone) (Underhill, 1989; Jones &

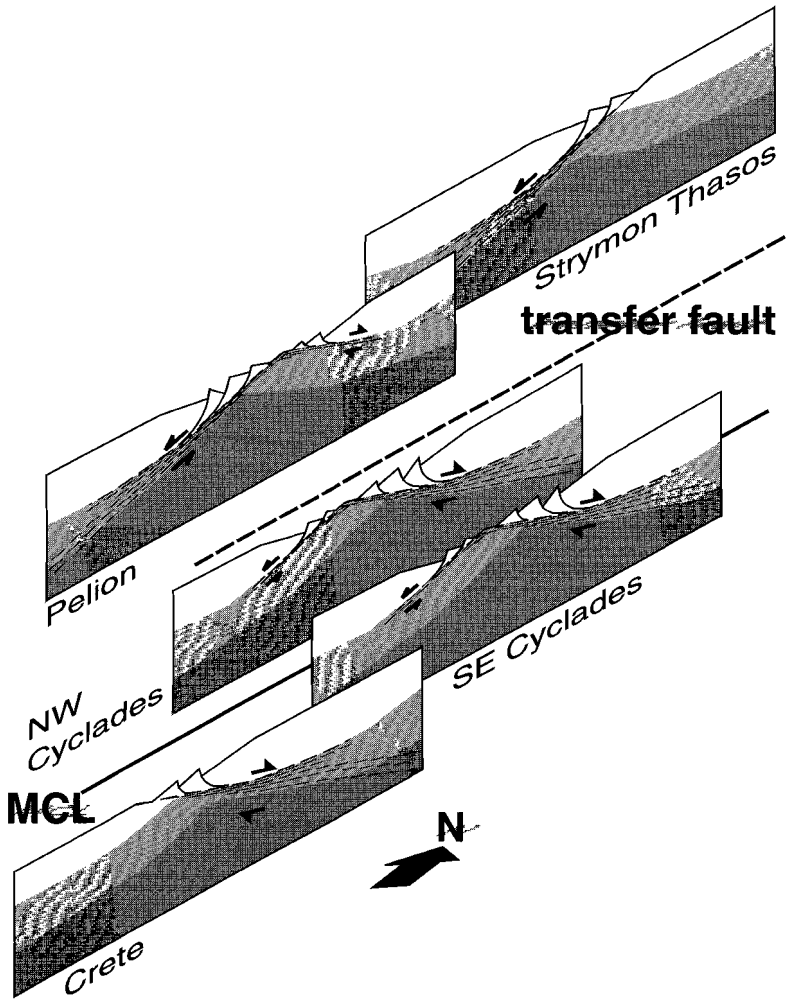

Figure 7.8. - Proposed geometry of the detachment fault systems in the Aegean in their Early Miocene configuration. The position and orientation of the dominant detachment faults and antithetic detachment faults have been presented with respect to the Mid Cycladic Lineament (MCL), and indicate the inferred location of a circa Late Oligocene transfer fault (dashed line) which would accomodate the different detachment fault geometries on either side. The suspected transfer fault would be located north of the Cyclades Archipelago and south of the Pelion Peninsula and could correspond to the western extension of the North Anatolian Fault zone.

Robertson, 1991). In contrast to the well preserved thrust sequence in the External Hellenides, the Lycian Nappes in southwestern Turkey (figure 2.1) are highly dismembered and dispersed. An idealized time sequence for the Lycian thrusting has been proposed by Collins & Robertson (1997). They propose the Paleocene reactivation of a Maastrichtian structure, and subsequent development of Late Eocene, early Oligocene and Middle Miocene thrusts.

Contemporaneous with the development of the fold-and-thrust belts in the external parts of the Aegean region, the extensional structures started to operate in nearby internal regions. In southwestern Turkey, the South Çine Shear Zone (chapter 6), a ductile southdipping low-angle normal fault, had developed in the Late Eocene and separates the Çine gneiss series in the footwall from schist and marbles overthrusted by the Lycian Nappes in the hangingwall (figure 7.9a). On mainland Greece, the Meso Hellenic Trench started to develop in Eocene-Oligocene times while thrusting was still affecting external parts of the Hellenic Orogen (figure 7.9b). The onset of extension related to the exhumation of the HP sequences is known to have occurred in the Pelagonian Zone from Late Paleocene time onwards and progressively shifted to Miocene ages on Crete. The circa 70 Ma to circa 45 Ma period is characterized not only by a regional reduction in ambient metamorphic pressures in the Pelagonian and Cycladic HP sequences (from 8 to 4 kbar and 14 to 8 kbar respectively, see chapter 5 for discussion), but also by the record of detrital HP minerals in flysch deposits of the External Hellenides (Faupl et al., 1996), indicating that parts of the HP metamorphic sequence had been exposed to the surface and were eroded. Also, Oligocene volcanics which directly overly metamorphosed sequences in the Rhodope and Kazdag Massifs (sections 6.2 and 6.3) indicate that exhumation operated prior to the Neogene phase of extension.

To summarize, local extension during the Paleogene is indicated by; i) Paleocene-Eocene exhumation of HP sequences in the Pelagonian Zone (chapters 4 and 5), ii) Eocene and Oligocene exhumation of ductile basement (chapters 4, 5 and 6), iii) Eocene-Oligocene formation of the Meso Hellenic Trench (Caputo & Pavlides, 1993), and iv) Eocene-Oligocene formation of a ductile normal fault systems, such as the South Çine Shear Zone, in southwestern Turkey (see section 6.4).

The geodynamic processes which controlled the observed Paleogene extension and exhumation are subject to speculation. It is observed that some localized extension initiated during the circa 75 to 55 Ma period of very slow convergence, whilst other periods of extension occurred during the circa 55 to 20 Ma period which corresponds to relatively faster convergence rates between the African and Eurasian plates (figure 7.4). Consequently, the temporal and spatial characteristics of the tectonic processes responsible for the observed extensional phenomena during periods of both slow and rapid convergence require a compatibility with such a tectonic scenario (see also section 7.4.2). Partial exhumation of the HP sequences in the Paleocene can be related to a phase of minimal convergence of the African and Eurasian plates, which initiated at circa 75 Ma and culminated at circa 55 Ma (figure 7.4). As mentioned in the previous section, such a phase of extremely low convergence rates would initiate accelerated roll-back of the subducting slab and associated back-arc spreading. Further exhumation of HP sequences in the Eocene and Oligocene can be tenta-

tively related to a process involving uplift and erosion by compression during overall convergence. The development of the extensional South Çine Shear Zone in south western Turkey by circa 40-38 Ma and the Meso Hellenic Trench by circa 35 Ma indicate that local extension also operated during the period of fast convergence in the Eocene and Oligocene. These observations, plus the observed kinematics in the basement sequences, suggest that

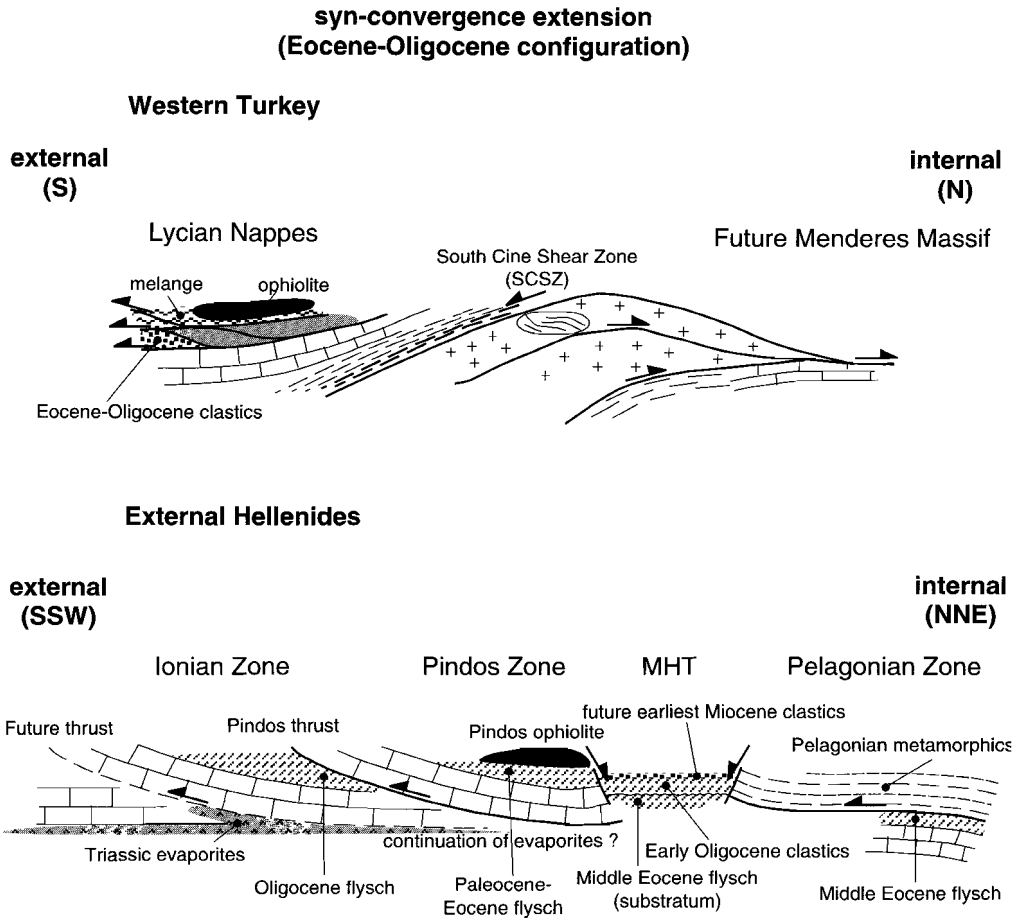

Figure 7.9. - Schematic cross sections (not to scale) through southwestern Turkey (N-S section) and mainland Greece (NNE-SSW section), in an Eocene-Oligocene configuration, showing the location of the extensional structures (South Cine Shear Zone, SCSZ, and Meso Hellenic Trench, MHT) which operated contemporaneous with the development of the fold-and thrust belts in the external parts of the orogen (Lycian Nappes of Taurides, and External Hellenides, respectively). The development of the extensional structures initiated shortly after Eocene emplacement of basement rocks in the Cine Submassif (N-ward thrusting of amphibolite facies metamorphic rocks over the future Menderes greenschist facies schists) and in the Pelagonian Zone (SSW-ward thrusting of retrograde blueschist facies metamorphic rocks over weakly metamorphosed autochthonous carbonate and flysch sequence).

syn-convergence extension did contribute to the progressive exhumation of basement in the Eocene and Oligocene.

7.4.5 Destabilization and restoration of the Hellenic orogenic wedge at Eocene times

The control of extension in the developing fold-and-thrust belt during relatively faster rates of convergence (from circa 55 to 20 Ma), may be related to the development of a critical wedge geometry. The geometry of an orogenic wedge evolves during its development to an optimum, the critical wedge, or critical taper, configuration (Davis et al., 1983; Dahlen, 1990). In the critical wedge configuration, extension in the rear of the developing wedge may be caused by a preferred outward flow of material towards the active site of accretion (i.e. the subduction zone) because of the occurrence of a preferred hinterland dipping backstop in the rear of the wedge (e.g. an inherited hinterland dipping thrust; Dahlen, 1990). The driving force for the preferred outward flow of material can be related to lithospheric processes, which create a preferred gradient in gravitational potential energy (e.g. Platt & England, 1993; Houseman & England, 1993) or to corner flow of accreted material in the regional accretionary wedge (see figure 2.10b, and Platt, 1993; Merle 1994). As mentioned previously (see section 7.4.2), the exact cause is hard to unravel, as only the crustal response to the possible operating processes is preserved in the present-day geology.

It is known that the critical height-width geometry of the critical wedge is dependent on the friction of the basal decollement to the wedge (figure 7.10, after Davis et al., 1983; Dahlen, 1990). The presence of Triassic evaporites in the Hellenic orogen and their known role in thrust zone localization (Underhill, 1989) leads to the probability that they played a role in the Paleogene development of the Hellenic orogenic wedge. The evaporites, in the current structural configuration, occur at a depth of circa 5 km and outcrop as smears along, or diapirs in or arising from the main thrust faults of the External Hellenides (figure 7.9; see also Underhill, 1989). The evaporites underly the pelagic and platform carbonate sequences of the External Hellenides and have been brought to the surface in the pre-Apulian and Ionian Zone. They are also likely to extend beneath the Pindos Zone, albeit that they have not been observed in outcrop along the Pindos Thrust or more internal positions (see figure 7.9b). As the Mesozoic and Early Tertiary carbonate sequence of the Hellenides is covered by flysch sequences of Paleocene-Eocene and younger ages it can be concluded that the carbonate sequence was involved in the development of the Hellenic orogenic wedge during most of the Tertiary. The investigation of the theoretical change in wedge geometries before and after decollement formation (figure 7.10) indicates that the wedge will destabilise after decollements form along evaporite horizons and/or they become smeared with evaporites and they will re-organise to a wider and flatter wedge geometry. The geometrical concepts are presented in figure 7.10 (after Davis et al., 1983; and Dahlen, 1990). A schematic geometrical configuration of the orogenic wedge as would be observed along a ENE-WSW section across mainland Greece is presented in figure 7.11. This figure proposes a speculative sequence of geometries for the orogenic wedge starting with its initial geometry before formation of the evaporitic decollement (figure 7.11a; dashed outline indicates the wedge geometry before formation of the evaporite decollement), through the initial phase of formation of the evaporitic decollement (figure 7.11b), to the final phase of the

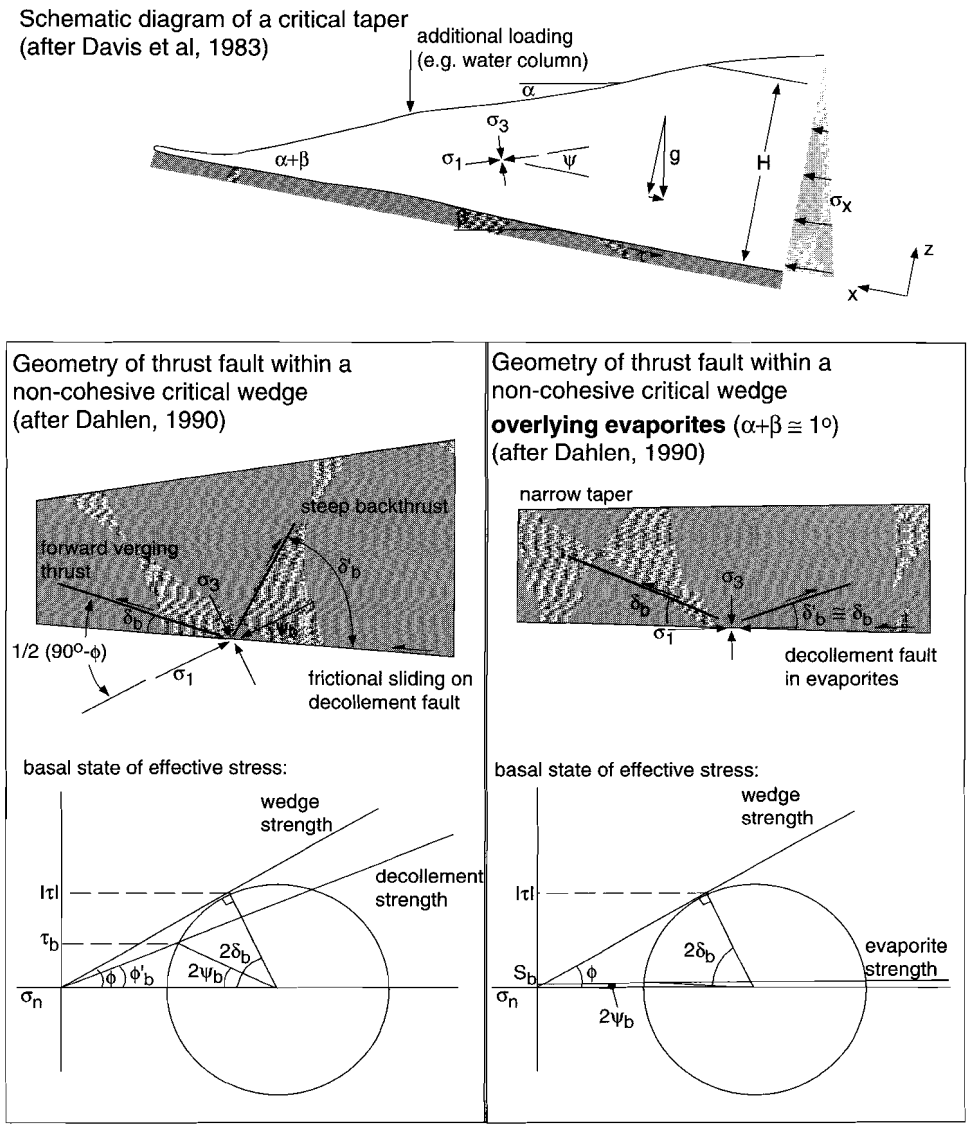

Figure 7.10. - Schematic diagrams showing the critical taper or critical wedge concept (top diagram after Davis et al, 1983) and its geometries in a non-cohesive wedge with and without frictional sliding on a basal fault (lower diagrams after Dahlen, 1990). The two bottom diagrams illustrate the difference in critical wedge geometry when the basal decollement experiences high friction (narrow and high wedge) or experiences no friction, e.g. due to evaporite decollement formation (wide and flat wedge). The Mohr diagrams illustrate the basal state of effective stress for critical wedges experiencing a high basal friction (left) and no basal friction (right). In right Mohr diagram; S_b = plastic strength of salt. The dynamic consequences are further explained in the text (section 7.4.5) and projected on a schematic geometrical configuration of the Hellenides on mainland Greece (figure 7.11).

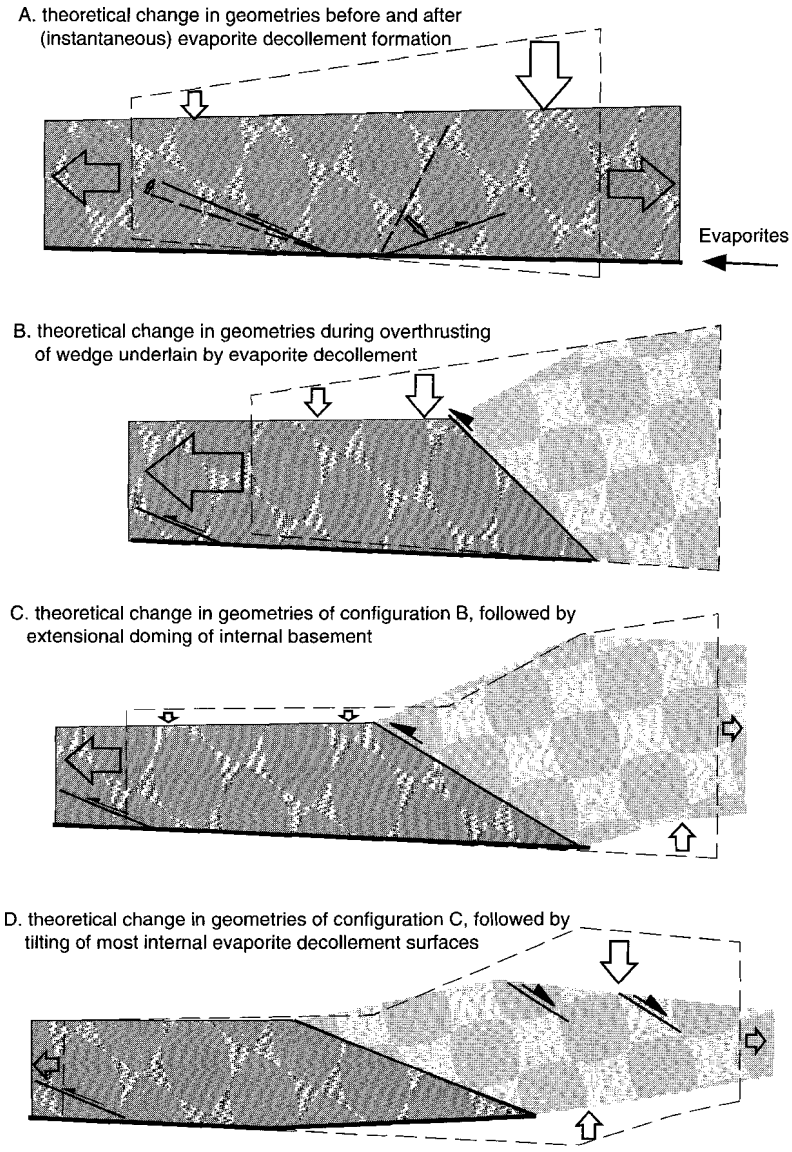

Figure 7.11. - Schematic representation of the development of an accretionary wedge after initiation of a decollement fault in evaporites, projected to the schematic geometrical configuration of the Hellenides on mainland Greece. See also figure 7.10 for geometrical constraints. *7.11a.* restoration of the wedge geometry after the development of a decollement along evaporites. *7.11b.* restoration of the wedge geometry after accretion of material overlying an evaporite decollement. *7.11c.* restoration of the wedge geometry shown in figure 7.11b after internal doming of overthrusted material. *7.11d.* restoration of the wedge geometry shown in figure 7.11c after continued doming and associated tilting of the decollement horizon, which will initiate further gravitational sliding along the decollement.

extensional collapse of the internal parts of the wedge (figure 7.11c and d). The main difference in the internal structures of the wedge restoration after the formation of the evaporitic decollement involves the development of less steep back-thrusts after the friction along the hinterland dipping basal decollement has been reduced to almost zero, as shown by Mohr constructions in figure 7.10. Considering the evolution of the Hellenic orogenic wedge it is shown that the carbonate sequence is partly overthrust by an imbricate of metamorphosed units (the Internal Hellenides) which promotes an outward escape of material; opposite to the initial movement of the carbonate sequence after evaporite decollement formation (figure 7.11b). The destabilization and re-organization of the external parts of the orogenic wedge are expected to be accompanied by a repositioning of the main subduction zone to more external parts of the orogen, after which the carbonate sequence can be regarded as being accreted to the orogenic wedge. A further contribution to the re-organization of the orogenic wedge can occur after the extensional collapse of the internal parts of the orogen. The outward directed gradient of excess potential energy can cause further, extension driven, movement of the internal parts of the orogen over the carbonate sequence, which will be further "squeezed out" above the evaporite decollement (figure 7.11c). Further extensional doming of the internal parts of the orogen and related shallowing of the Moho, as observed in the present day Aegean region (see figure 2,7 for regional Moho depths), will cause a tilt of the evaporite decollement surface. The tilting would result in a foreland dipping decollement and would further drive outward directed gravitational sliding along the decollement (figure 7.11d) and associated continued extension of the orogen.

The above Paleogene scenario leads to the question; *what were the controlling processes of the late-orogenic extension.* The classical view indicates that the extensional collapse of the Hellenic orogen was driven by roll-back of the subducted slab since the Early Miocene, in co-operation with westward expulsion of Turkey and/or further detachment of the subducted slab (Le Pichon et al., 1995; Meijer & Wortel, 1997; Walcott, 1998). An alternative tentative interpretation is proposed in this study which concludes that the destabilization of the Aegean orogenic wedge has been caused by several processes which first affected the orogenic wedge in the Early Tertiary and then continued to the present. This will be further discussed below. However before doing this the question concerning the position of the Pelagonian Zone with respect to Eurasian and/or Gondwana will be addressed.

7.5 The Pelagonian Zone; a fragment of Eurasia or Gondwana ?

Most paleogeographic reconstructions regard the Pelagonian Zone as former part of the Gondwanan margin, i.e. at the southern side of the Tethys Ocean (see chapter 2 and figure 2.3). In conflict to the reconstructions, the geochronological results in this study indicate that the allochthonous metamorphosed sequence in the Pelagonian Zone exhibits a Hercynian affinity and suggest that the sequence has been derived from the Eurasian margin. The kinematic observations confirm a northeastern origin of the metamorphosed sequence.

It is speculated that on a regional scale, covering the complete southern margin of the Eurasian plate, the Aegean region can be regarded as a single accretionary and/or orogenic wedge related to the subduction of the African plate beneath the Eurasian plate. At the northeastern side of the present-day Vardar Zone, the imbricated Eurasian margin is found in the Rhodope Zone. The metamorphosed rocks which have been found south of the Rhodope Zone are all in an allochthonous position and have composed the accretionary wedge of the Aegean subduction zone and consist of imbricated fragments of the Eurasian continental basement which were involved in the subduction process together with accreted sediments, carbonate sequences and ophiolitic material. The fragments of continental basement in the Pelagonian Zone, Cyclades, Peloponese, Crete, and Kazdag Massif, all have Hercynian affinities. That is, their protolith ages are around circa 300 Ma. In contrast, the protolith ages in the Çine Submassif yield a Pan-African affinity (see chapter 6), i.e. their protolith ages are around 500 to 550 Ma and lack an Hercynian overprint.
The occurrence of a large amount of allochthonous metamorphosed sequences handicaps the identification of the Tethys suture zone. It is concluded that the best candidate of this suture zone is located at the present-day subduction zone. It separates subducting (thinned) African lithosphere in the south, from an overriding region with carbonate sequences, sediments (flysch), and ophiolitic material intermixed with continental fragments with dominantly Hercynian protolith ages in the north. Further north, in the Rhodope Zone, the metamorphosed basement with Hercynian affinity is at a, dominantly, autochthonous position, and marks the, relatively, stable Eurasian margin. Hercynian rocks have been identified in the northwestern African margin (Morocco, Algeria, Tunisia) but have not been recognized further to the east (Hsü, 1995; Smith. 1996). The northeastern African margin is characterized by rocks with a Pan-African affinity and might have been the locus of a rifted continental fragment which became part of the Eurasian accreted margin and is currently identified in the Çine Submassif.
In the proposed speculation the tectonostratigraphic sequence of the Pelagonian Zone is characterized by metamorphosed sequences with an Hercynian affinity (the allochthonous sequence), which overly platform carbonates and flysch (the autochthonous sequences) that *might be* positioned on a substratum with Pan-African affinity. Consequently, the Vardar Zone cannot be regarded as the main suture of the Tethys Ocean.

7.6 Development of the Aegean subduction complex during the Tertiary

Following on from the proposed geodynamic mechanisms which have operated in the Aegean region and which affected the Aegean orogenic wedge during the Tertiary, a tentative model for the evolution of the Aegean orogenic wedge is proposed below. The proposed evolution is further illustrated schematically in cross-section and in map view (figures 7.12a and 7.12b) and highlights the suggested processes which operated to destabilize the Aegean orogenic wedge, during and after its development.
The different geodynamic mechanisms which might have operated, and the way in which

they combined during the development of the Aegean region in the Tertiary will be further discussed in chronological order, from oldest to youngest.

pre 70 Ma: Build-up of the orogenic wedge initiated in (pre-)Cretaceous times. Obduction of the ophiolite sequences occurred from circa 180-170 Ma in the Hellenides and Dinarides to circa 90 Ma in the Taurides. The compressional regime during a period of high convergence rates caused imbrication of mid-crustal basement at circa 120-100 Ma, which resulted in the recognized imbricated basement and associated distribution of Hercynian and Early Cretaceous muscovite cooling ages in the Pelagonian Zone, and the range of 120 to 100 Ma ages established by application of various isotopic systems in the Rhodope Zone.

70-55 Ma: Earliest destabilization affected the Aegean wedge in the Paleocene when overall convergence rates of the main African and Eurasian plates had decreased to low rates, similar to or even lower than the convergence rates of the recognized phase of Miocene to Recent convergence (figure 7.4). The slow rate of convergence has induced the roll-back of the, possibly still young, subducted slab and the associated back-arc extension before the Aegean orogenic wedge had reached a final, stable, geometrical configuration. The wedge remained immature and the back-arc extension caused a partial exhumation of the Aegean basement.

50-40 Ma: After acceleration of the overall convergence rates in the Eocene (see figure 7.4, after data from Müller & Roest, 1992) the already partially destabilized Aegean wedge was further rebuilt but did not reach the idealized geometry.

circa 45-0 Ma: The accretionary wedge was again destabilized after final accretion of a carbonate platform in the Eocene. Evaporites, which formed part of the deeper levels of the accreted carbonate sequence, caused a loss of friction of the basal decollement of the wedge after the formation of a major decollement within, or containing, evaporites. The reduced friction along the basal decollement forced the Aegean wedge to restore its critical wedge geometry. Associated with the restoration of the critical wedge geometry, an outward flow of material was initiated, opposite to the initial direction of movement of the carbonate sequence, due to the hinterland dipping backstop provided by the overriding internal parts of the orogen (e.g. Pelagonian and Rhodope Zones; see figure 7.12b). Continued outward flow of material, overriding the subduction zone, and continued outward migration of the

Figure 7.12. - Schematic presentation of the development of the Aegean subduction complex and the effect of the two periods of roll-back and the evaporite decollement formation on the stability of the Aegean orogenic wedge in cross-section (7.12a) and plan view (7.12b). The different stages illustrate wedge formation (ca 120-55 Ma), Paleocene roll-back and associated back arc extension resulting in the initial destabilization of the orgenic wedge (ca 70-55 Ma), rebuilding of the destabilized wedge (post circa 55 Ma), trench shift and protracted restoration of wedge geometry after low friction basal decollement formation (post circa 45 Ma), final collapse and fragmentation of the orogen by the co-operation of Miocene roll-back and additional slab detachment and westward Anatolian expulsion (post circa 20 Ma). In figure 7.12a the black arrows indicate the overall movement of material (the arrow size is indicative of the relative amount of movement). In figure 7.12b the areas of compressional (dark grey areas) and extensional tectonics (light grey areas) during the different tectonic stages are indicated and evidence the exhumation of wedge material in the interal parts of the accretionary wedge and continuous outward migration of wedge material, including basement slices (white blocks in present-day configuration; positions of: Rh, Rhodope; Pe, Pelagonian; Pp, Peloponese; Cr, Crete; Cy, Cyclades; Me, Menderes; Kd, Kazdag; Tv, Tavsanli).

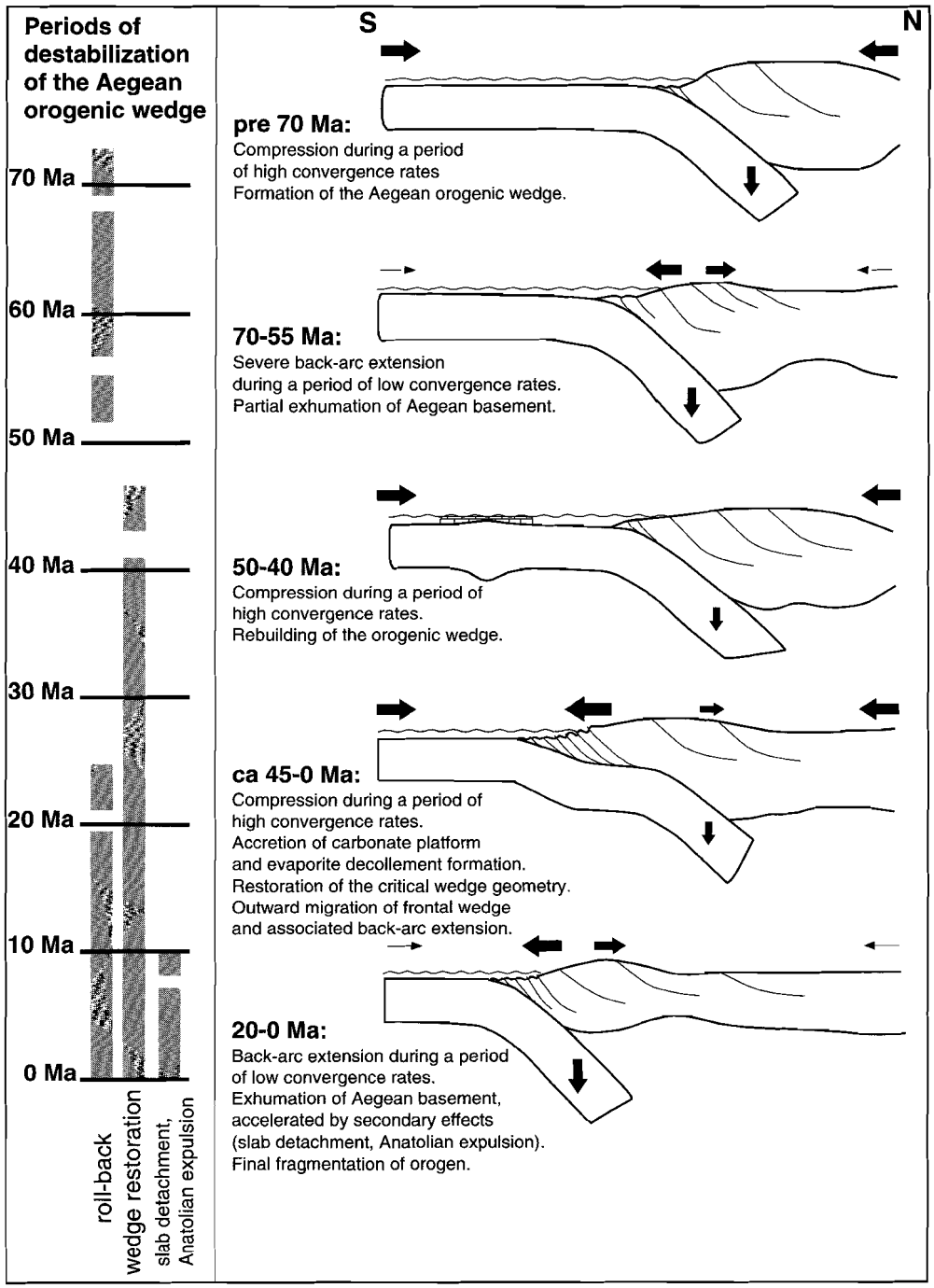
Periods of destabilization of the Aegean orogenic wedge
70 Ma
60 Ma
50 Ma
40 Ma
30 Ma
20 Ma
10 Ma
0 Ma
roll-back wedge restoration
slab detachment, Anatolian expulsion
S
N
pre 70 Ma:
Compression during a period of high convergence rates
Formation of the Aegean orogenic wedge.
70-55 Ma:
Severe back-arc extension during a period of low convergence rates.
Partial exhumation of Aegean basement.
50-40 Ma:
Compression during a period of high convergence rates.
Rebuilding of the orogenic wedge.
ca 45-0 Ma:
Compression during a period of high convergence rates.
Accretion of carbonate platform and evaporite decollement formation.
Restoration of the critical wedge geometry.
Outward migration of frontal wedge and associated back-arc extension.
20-0 Ma:
Back-arc extension during a period of low convergence rates.
Exhumation of Aegean basement, accelerated by secondary effects (slab detachment, Anatolian expulsion).
Final fragmentation of orogen.

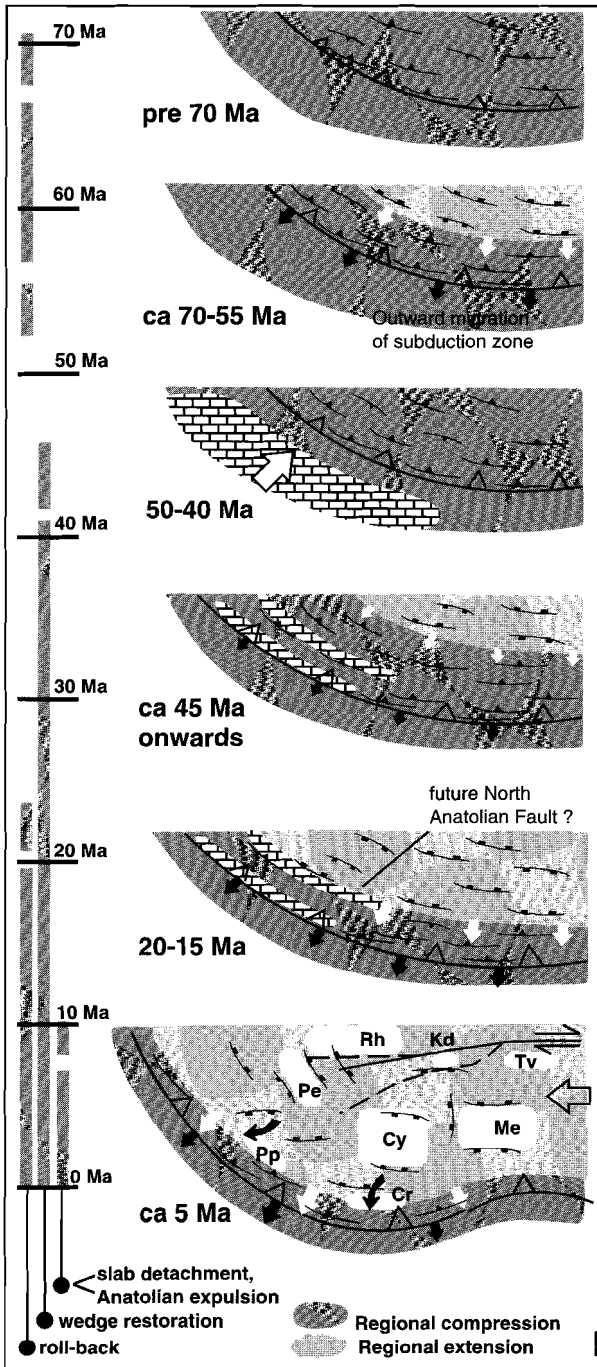

Compression during a period of high convergence rates. **Wedge formation** with imbricated slices of Eurasian basement, ophiolite sequences and accreted sediments.

Initial destabilization of the orogenic wedge. Roll-back of subducted slab during a period of low convergence rates. Related back-arc extension and partial exhumation of basement rocks in internal parts of the wedge.

Compression during a period of high convergence rates. **Rebuilding** of the orogenic wedge.

Accretion of carbonate sequences at the base of the wedge. Outward migration of subduction related compressional front during a period of high convergence rates. **Wedge restoration** after evaporite decollement formation. Pronounced extension and related exhumation in back-arc regions.

Acellerated outward migration of subduction related compressional front, due to **collapse** of the internal orogen by pronounced roll-back of the subducting slab superimposed on restoration of wedge configuration.

Continued outward migration of subduction related compressional front. Final **fragmentation** of back-arc region after termination of activity along Mid Cycladic Lineament during westward expulsion of Turkey and associated formation of North Anatolian Fault zone. Continued rotation of individual blocks and pronounced extension and basin formation along high angle normal faults parallel and perpendicular to orogenic grain.

main subduction zone, due to the drive to restore the critical wedge geometry, accelerated the exhumation of material in the internal parts of the wedge (e.g. HP assemblages).
20-0 Ma: Miocene to Recent roll-back further accelerated the outward migration of material and accommodated back-arc extension along low angle normal fault zones. As a result of the roll-back and the superimposed detachment of the subducting slab and westward expulsion of Anatolia (see Le Pichon et al., 1995) a final fragmentation affected the total orogen, of which individual blocks of the brittle crust, separated by high angle normal faults, accommodated further movement of material by rigid body rotation and translation (see also Walcott, 1998).

In summary, the Tertiary development of the Aegean orogenic wedge is characterized by a continuous outward migration of the subduction related compressional front, which was initiated in the Late Cretaceous - Early Tertiary by roll-back of the subducted slab and associated back-arc extension during a period of slow convergence rates. Following initial roll-back of the subducted slab in the Paleogene and partial subduction of the carbonate sequence overlying evaporites in the Eocene, the orogenic wedge was further destabilized by evaporite decollement formation and the subsequent loss of friction at the base of the wedge. The re-organization of the critical wedge geometry and related outward flow of material might have enhanced further destabilization which would lead to continuous extension in the Miocene and final fragmentation of the total wedge. Parts of the accretionary wedge which were spatially positioned in the transition zone between the back-arc extensional and the frontal compressional region were subject to a complex interplay of local compressional and extensional tectonics. The outward migration of the compressional front accelerated exhumation of HP sequences in the internal parts of the wedge and caused an associated shift of the compressional front towards the active subduction zone. As a result, some HP assemblages might have remained in the frontal part of the wedge and were further separated from their original position of formation. During their outward migration, parts of these assemblages might have been recycled in the frontal part of the wedge and repositioned at HP metamorphic conditions together with subsequently accreted material.

Chapter 8

Conclusions of this thesis and recommendations for future research

8.1 Conclusions of this thesis

The research of this study has led to the following conclusions:

1. Direct dating of deformational and kinematic events by $^{40}Ar/^{39}Ar$ laserprobe dating techniques is possible when; i) regional thermal conditions are well constrained and it has been concluded that the analysed fabric had formed below its relevant argon closure temperature range, ii) the analysed minerals have been related to the correct metamorphic assemblage and to the correct deformational and kinematic fabric, and iii) the mineral separation follows careful characterization of the selected material, as incomplete recrystallization might have resulted in a multigeneration population of the selected material in a single sample.

2. The applied direct dating provides the temporal constraints on the individual deformational events and metamorphic episodes that produced a multiple generation white mica population in a single sample. The technique allows differentiation of overprinting fabric forming events, which are characterized by different kinematics. As an example of the potential resolution of this approach, samples from this study have confirmed a muscovite cooling age and the age of formation of two overprinting mylonitic fabrics within a single sample. Examples are provided which are characterized by i) a blueschist facies mylonitic foliation with an ENE direction of tectonic transport with an overprinting, 40 m.y. younger, greenschist facies mylonitic foliation with a WSW direction of tectonic transport (sample 4, Ossa Massif), and by ii) a greenschist facies mylonitic foliation with a ENE direction of tectonic transport and an overprinting, 15 m.y. younger, shear band foliation indicating a WSW direction of tectonic transport (sample 141, Pelion Massif).

3. The intersection of the older mylonitic foliation and the shear band foliation, in the example in conclusion 2(ii), is normal to the stretching lineation. In microstructural analysis this is interpreted to indicate that both foliations formed during the same event of mylonitic deformation (after Passchier & Trouw, 1996). The recognition of the above 15 m.y. time lag between formation of the top-to-NE mylonitic foliation and associated microstructures and the top-to-SW shear band foliation within a single mylonitic interval illustrates that these structures do not necessarely develop during a single kinematic event. The research shows that the geometrical relationship in orientations between the

stretching lineation and the shear band foliation does not automatically imply that they share a time relation. If a temporal difference exists in the development of the stretching lineation and the shear band foliation, the latter might have formed in a kinematic setting with a different orientation. Also, if the temporal independence of the two structures is not recognized, a possible rotation in the orientation of the kinematic setting, which might be crucial to the understanding of the regional kinematic history, will remain overlooked.

4. Application of the integrated microstructural, petrological and geochronological research research has resulted in a detailed recording of deformational and kinematic events in the high pressure, low temperature, metamorphic assemblage of the Pelagonian Zone. The record of deformational and kinematic events covers the Middle Cretaceous to Recent tectonic history and is characterized by an alternation of compressional and extensional events, which affected the Pelagonian basement at 120-100 Ma and 45-40 Ma (compressional) and 54 Ma and circa 30, 22 and 15 Ma (extensional), respectively. The geodynamic controls on this sequence of events might be local, i.e. Aegean wide, and, therefore, unique for the tectonic setting in the Aegean region. Alternatively, if the geodynamic controls on this sequence of events are in part dictated by more far field forces, such as the direction and rate of convergence of the Eurasian and African plates, one might expect a similar sequence of events more widespread along the Eurasian plate margin.

5. Additional investigations in adjacent areas, which cover similar orogenic settings (Rhodope Zone, northern Greece, Kazdag and Menderes Massifs, western Turkey), and correlation of the results of these studies with published data (chiefly, the Cyclades and Crete) have resulted in the recognition of a complex tectonic history which is characterized by an interplay between synchronous and diachronous tectonic events. The main diachronous event is characterized by extension and the related termination of HP metamorphism. The diachronous event becomes progressively younger towards the present-day active subduction zone and is superimposed on regional compressional events at circa 120-100 Ma and 45-40 Ma and a regional extensional event from circa 20 Ma to Recent.

6. The balance between the synchronous and diachronous tectonic processes in the Aegean region requires specific controlling geodynamic processes. The geodynamic scenario of the Aegean region is characterized by the overall convergence of the African and Eurasian plates. Further stagnation of the convergence rates between the two main plates at circa 70-55 Ma and 20-0 Ma has enhanced roll-back of the subducted lithosphere and caused the associated acceleration of back-arc spreading in the overriding plate. The effect of increased roll-back of the subducting plate in the Paleogene, plus the restoration of the orogenic wedge to regain a critical wedge geometry after evaporite decollement formation in accreted carbonate sequences in Early Eocene times, has caused a destabilization of the orogenic wedge from Paleocene - Early Eocene onwards.

The destabilization of the orogenic wedge was continued during the final extensional collapse of the orogen at Miocene times which resulted in a total fragmentation of the orogen, with different fragments being subjected to individual block rotations and movements.

7. Exhumation of high pressure metamorphic sequences in the Aegean region is associated with the recognized phases of syn- to post-orogenic regional extension and occurred in the Eocene and Oligocene prior to the widely recognized phase of Neogene extension. During overall convergence, outward migration of the subduction related compressional front facilitated pronounced localized extension in the internal parts of the accretionary wedge. This gradually exhumed high pressure metamorphic sequences in the internal parts of the wedge, while, in the external parts of the wedge the metamorphic sequences were continuously repositioned closer to the active subduction zone and reworked with younger accreted material. As a result, the age of the termination of high pressure metamorphism progressively becomes younger towards the active subduction zone. Detachment fault systems developed during post-orogenic extension and caused the final fragmentation of the orogen. The detachment fault systems developed in asymmetric extensional domes, which were controlled by NNE dipping faults in the central and southern Aegean region and Turkey and by SSW dipping faults in the northern Aegean region. Following formation of the main detachment fault zone at ductile crustal levels, an antithetic fault zone developed at semi-ductile levels and initiated bivergent extension, which continued by formation of high angle normal faults across the whole Aegean region.

8.2 Future work and recommendations

The contribution of this thesis to the understanding of the Alpine geodynamic scenario in the Aegean region and to the refining of the applied $^{40}Ar/^{39}Ar$ absolute age dating technique on multiply deformed and metamorphosed rocks has identified several areas which need to be addressed further. The remaining questions and new fields to study include the following topics:

1. The success of $^{40}Ar/^{39}Ar$ absolute age dating on multiply deformed rocks is heavily dependent on the understanding and quantification of argon diffusion rates and formation of diffusion pathways. The present research study has only qualitatively touched this problem. Not only is the estimation of the argon diffusion rate in white mica still much dependent on an old dataset, as prime investigations have been carried out by Robbins (1972), but also a better understanding is required in the role of chemical alteration and deformation on the Ar and K distribution in the main K-bearing minerals, in order to address the individual contribution of the dominant diffusion controlling mechanisms which operated during the lifecycle of the analysed material.

2. This study has shown that samples selected for $^{40}Ar/^{39}Ar$ absolute age dating, which are derived from multiply deformed rocks are likely to contain a multiple generation mica population. The presence of a complex mica population might result in misinterpretation of resultant $^{40}Ar/^{39}Ar$ dates. As a result, an erroneous and conflicting dataset will handicap geodynamic studies and can lead to under- or overestimation of the timing and rates of kinematic processes. Critical examination and characterization prior to careful mineral separation is an absolute necessity for isotopic age dating. In future dating studies, it is recommended that the handpicked mineral separates are further characterized by high resolution SEM back-scattered studies, after which image analysis methods can be used to quantify the purity of the separate. A quantification of the purity of the handpicked mineral separate may be essential in order to give an objective interpretation of the $^{40}Ar/^{39}Ar$ age spectra and to avoid any discussion on the outgassing of a possibly mixed sample.

3. The role of Early Tertiary destabilization of the Aegean orogenic wedge, caused by the restoration of the critical wedge geometry after evaporite decollement formation in the accreted carbonate sequence of the External Hellenides might serve as a prime input to a numerical model. The numerical simulation can investigate the tentative Tertiary evolution of the Aegean orogenic wedge, as proposed in the above chapter. The model can test i) the role of evaporite decollement formation in the destabilization of an orogenic wedge and ii) the long-term contribution of initial wedge destabilization to the final collapse of the orogen.

4. The kinematic role of evaporites in focussing decollement surfaces in an orogen is well understood. In contrast, the geodynamic implications of evaporite decollement formation in an orogenic wedge with an original high friction related critical geometry has received limited investigation. This should be incorporated in the geodynamic analyses of orogens which are partly positioned on evaporite bearing strata, such as the European Alps and Pyrenees, as the tectonic evolution of a fold-and-thrust belt could be influenced by initiation of evaporite decollement formation.

5. The Rhodope area provides the key to the understanding of the role of the internal parts of the Aegean orogenic wedge in its Alpine evolution. Although this thesis shows that its role started in the Cretaceous, its subsequent role could not be investigated by white mica analyses with the $^{40}Ar/^{39}Ar$ laserprobe. This reflects the relatively high metamorphic temperatures reached in the Rhodope Zone. Consequently it is recommended that other techniques such as $^{40}Ar/^{39}Ar$ hornblende dating, Rb-Sr, Sm-Nd and U-Pb dating, are applied to resolve this problem to reveal the nature of the lower crust in the development of the Aegean ororgenic wedge.

References:

Akcay M., Ozkan H.M., Moon C.J. and B.C. Scott, 1996. Secondary dispersion from gold deposits in west Turkey. *J. Geochem. Expl.*, 56: 197-218.

Akkök R., 1981. Metamorphic conditions of gneisses and schists in the Menderes Massif, Alasehir-Manisa. *Bull. Geol. Soc. Turkey*, 24: 11-20.

Aldrich L.T. and A.O. Nier, 1948. Argon 40 in potassium minerals. *Phys. Rev.*, 74: 876-877.

Allemand P. and J-M Lardeaux, 1997. Strain partitioning an metamorphism in a deformable orogenic wedge: Application to the Alpine belt. *Tectonophysics*, 280: 157-169.

Altherr R., M. Schliestedt, M. Okrusch, E. Seidel, H. Kreuzer, W. Harre, H. Lenz, I. Wendt and G.A. Wagner, 1979. Geochronology of high-pressure rocks on Sifnos (Cyclades, Greece). *Contrib. Mineral. Petrol.*, 70: 245-255.

Altherr R., H. Kreuzer, I., Wendt, H. Lenz, G.A. Wagner, J. Keller, W. Harre and A. Höhndorf, 1982. A Late Oligocene/Early Miocene high temperature belt in the Attic-Cycladic crystalline complex (SE Pelagonian, Greece). *Geol. Jb.*, 23: 97-164.

Andriessen P.A.M., N.A.I.M. Boelrijk, E.H. Hebeda, H.N.A. Priem, E.A.Th. Verdurmen and R.H. Verschure, 1979. Dating the events of metamorphism and granitic magmatism in the Alpine orogen of Naxos (Cyclades, Greece). *Contrib. Mineral. Petrol.*, 69: 215-255.

Armstrong R.L., E. Jager and P. Eberhardt, 1966. A comparison of K-Ar and Rb-Sr ages on Alpine biotites. *Earth Planet. Sci. Lett.*, 1: 13-19.

Aubouin J., J.H. Brunn, P. Celet, J. Dercourt, I. Godfriaux and J. Mercier, 1963. Esquisse de la geologie de la Grèce. *Mem. h. ser. Soc. géol. Fr.*, II: 583-610.

Avigad D., A. Matthews, B.W. Evans and Z. Garfunkel, 1992. Cooling during the exhumation of a blueschist terrane: Sifnos (Cyclades), Greece. *Eur. J. Mineral.*, 4: 619-634.

Avigad D., 1993. Tectonic juxtaposition of blueschists and greenschists in Sifnos Island (Aegean Sea)- Implications for the structure of the Cycladic blueschist belt. *J. Struc. Geol.*, 15: 1459-1469.

Avigad D., Z. Garfunkel, L. Jolivet and J.M. Azanon, 1997. Back arc extension and denudation of Mediterranean eclogites. *Tectonics*, 16: 924-941.

Baldwin S.L. and T.M. Harrison, 1989. Geochronology of blueschists from West-Central Baja California and the timing of uplift in subduction complexes. *J. Geol.*, 97: 149-163.

Baldwin S.L., T.M. Harrison and J.D. Fitz Gerald, 1990. Diffusion of ^{40}Ar in metamorphic hornblende. *Contrib. Mineral. Petrol.*, 105: 691-703.

Baldwin S.L. and G.S. Lister, 1998. Thermochronology of the South Cyclades Shear Zone, Ios, Greece: Effects of ductile shear in the argon partial retention zone. *J. Geoph. Res.*, 103: 7315-7336.

Barton C.M., 1976. The tectonic vector and emplacement age of an allochthonous basement slice in the Olympos area, N.E. Greece. *Bull. Soc. géol. France*, 18(2): 253-258.

Beckinsale, R.D. and N.H. Gale, 1969. A re-appraisal of the decay constants and branching ratio of ^{40}K. *Earth Planet. Sci. Lett.*, 6: 289-294

Behrmann J.H., 1984. A study of white mica microstructure and microchemistry in a low grade mylonite. *J. Struc. Geol.*, 6: 283-292.

Berger G.W. and D. York, 1981. Geothermometry from $^{40}Ar/^{39}Ar$ dating experiments. *Geoch. Cosmoch. Act.*, 45: 795-811.

Bingöl E., 1971. Fiziksel yas tayini metodlarini siniflama denemesi ve Rb-Sr ve K-Ar metodlarinin Kazdag'da bir uygulamasi. *Türk. Jeol. Kur. Bült*, 14: 1-16.

Blake M.C., M. Bonneau, J. Geyssant, J.R. Kienast, C. Lepvrier, H. Maluski and D. Papanikolaou, 1981. A geologic reconaissance of the Cycladic blueschist belt, Greece. *Geol. Soc. Am. Bull.* 92: 247-254.

v. Blanckenburg F., I.M. Villa, H. Baur, G. Morteani and R.H. Steiger, 1989. Time calibration of a PT-path from the Western Tauern Window, Eastern Alps: the problem of closure temperatures. *Contrib. Mineral. Petrol.*, 101: 1-11.

Bonev K., Z. Ivanov and L-E. Ricou, 1995. Denudation tectonique au toit du noyau metamorphique rhodopien-macedonien: la faille normale ductile de Gabrov Dol (Bulgarie). *Bull. Soc. géol. France*, 166: 49-58.

Bonneau M. and J.R. Kienast, 1982. Subduction, collision et schistes bleus: l'exemple de l'Egee (greece). *Bull. Soc. geol. France*, 7: 785-792.

Bonneau M. 1984. Correlation of the Hellenic nappes in the south-east Aegean and their tectonic reconstruction. In A.H.F. Robertson & J.E. Dixon (Eds.), the geological evolution of the eastern Mediterranean. *Geol. Soc. Special publ* 17: 517-527.

Boundy T.M., E.J. Essene, C.M. Hall, H. Austrheim and A.N. Halliday, 1996. Rapid exhumation of lower crust during continent-continent collision and late extension: Evidence from $^{40}Ar/^{39}Ar$ incremental heating of hornblendes and muscovites, Caledonian orogen, western Norway. *GSA Bulletin*, 108: 1425-1437.

Bourne S.J., P.C. England and B. Parsons, 1998. The motion of crustal blocks driven by flow of the lower lithosphere and implications for slip rates of continental strike-slip faults. *Nature*, 391: 655-659.

Bozkurt E., J.A. Winchester and R.G. Park, 1995. Geochemistry and tectonic significance of augen gneisses from the southern Menderes Massif (West Turkey). *Geol. Mag.*, 132: 287-301.

Bozkurt E., 1996. Metamorphism of Palaeozoic schists in the Southern Menderes Massif: Field, petrographic, textural and microstructural evidence. Tr. *J. of Earth. Sci.*, 5: 105-121.

Bozkurt E. and R.G. Park, 1994. Southern Menderes Massif: an incipient metamorphic core complex in western Anatolia, Turkey. *J. Geol. Soc. London*, 151: 213-216.

Bozkurt E. and R.G. Park, 1997. Evolution of a mid-Tertiary extensional shear zone in the southern Menderes Massif, western Turkey. *Bull. Soc. géol. France*, 168: 3-14.

Bröcker M., 1990. Blueschist-to-greenschist transition in metabasites from Tinos Island, Cyclades, Greece: Compositional control or fluid infiltration ? *Lithos*, 25: 25-39.

Bröcker M., H. Kreuzer, A. Matthews and M. Okrusch, 1993. $^{40}Ar/^{39}Ar$ and oxygen isotope studies of polymetamorphism from Tinos Island, Cycladic blueschist belt, Greece. *J. Metam. Geol.*, 11: 223-240.

Bröcker M. and H.W. Day, 1995. Low-grade blueschist facies metamorphism of metagreywackes, Franciscan Complex, northern California. *J. Metam. Geol.*, 13: 61-78.

Buick I.S. and T.J.B. Holland, 1989. The P-T-t path associated with crustal extension, Naxos, Cyclades, Greece. In J.S. Daly, R.A. Cliff & B.W.D. Yardley (Eds.), Evolution of metamorphic belts Blackwell: 365-369.

Buick I. S., 1991. Mylonitic fabric development on Naxos, Greece. *J. Struc. Geol.*, 13: 643-655.

Burchfiel B.C., 1980. Eastern European Alpine system and the Carpathian orocline as an example of collision tectonics. *Tectonophysics*, 63: 31-61.

Burg J-P., Z. Ivanov, L-E. Ricou, D. Dimor and L. Klain, 1990. Implications of shear-sense criteria for the tectonic evolution of the Central Rhodope massif, southern Bulgaria. *Geology*, 18: 451-454.

Burg J-P., L-E. Ricou, I. Godfriaux, D. Dimov and L. Klain, 1996. Syn-metamorphic nappe complex in the Rhodope Massif. Structure and kinematics. *Terra Nova*, 8: 6-15.

Candan O., O-Ö Dora, N. Kun, C. Akal and E. Koralay, 1992. Aydin Daglari (Menderes Masifi) Giney Kesimindeki Allokton Metamorfik Birimler (Allochtonous metamorphic units at the southern part of the Aydin Mountains; Menderes Massif). *Bull. TPJD*, 4: 93-110.

Caputo, M., G.F. Panza and D. Postpischl, 1970. Deep structure of the Mediterranean basin. *J. Geoph. Res.*, 75: 4919-4923.

Caputo, R. and S. Pavlides, 1993. Late Cainozoic geodynamic evolution of Thessaly and surroundings (central-northern Greece). *Tectonophysics*, 223: 339-362.

Cliff R.A., 1985. Isotopic dating in metamorphic belts. *J. Geol. Soc. London*, 142: 97-110.

Cloos M., 1985. Thermal evolution of convergent plate margins: Thermal modeling and reevaluation of isotopic Ar-ages for blueschists in the Franciscan Complex of California. *Tectonics*, 5: 421-433.

Cloos M., 1993. Lithospheric buoyancy and collisional orogenesis: subduction of oceanic plateaus, continental margins, island arcs, spreading ridges, and seamounts. *Geol. Soc. Am. Bull.*, 105: 715-737.

Cohen H.A., Dart C.J., Akyuz H.S. and Barka A., 1995. Syn-rift sedimentation and structural development of the Gediz and Büyük Menderes graben, western Turkey. *J. Geol. Soc. London*, 152: 629-638.

Coleman M. and K. Hodges, 1995. Evidence for Tibetan plateau uplift before 14 Myr ago from a new minimum age for east-west extension. *Nature*, 374: 49-52.

Collins A.S. and A.H.F. Robertson, 1997. Lycian melange, southwestern Turkey: An emplaced Late Cretaceous accretionary complex. *Geology*, 25: 255-258.

Costa S. and H. Maluski, 1988. Use of the $^{40}Ar/^{39}Ar$ stepwise heating method for dating mylonite zones: an example from the St. Barthélémy Massif (Northern Pyrenees, France). *Chem. Geol.*, 72: 127-144.

Dahl P.S., 1996. The crystal-chemical basis for Ar retention in micas: inferences from interlayer partitioning and implications for geochronology. *Contrib. Mineral. Petrol.*, 123: 22-39.

Dahlen F.A., 1990. Critical taper models of fold-and-thrust belts and accretionary wedges. *Annu. Rev. Earth Planet. Sci.*, 18: 55-99.

Dallmeyer R.D., A. Takasu and K Yamaguchi, 1995. Mesozoic tectonothermal development of the Sambagawa, Mikabu and Chichibu belts, south-west Japan: evidence from $^{40}Ar/^{39}Ar$ whole-rock phyllite ages. *J. Metamorphic Geol.*, 13: 271-286.

Dalrymple G.B. and M.A. Lanphere, 1969. Potassium-argon dating. Freeman, San Francisco: 258 p.

Dalrymple G.B. and M.A. Lanphere, 1971. $^{40}Ar/^{39}Ar$ technique of K-Ar dating: a comparison with the conventional technique. *Earth Planet. Sci. Lett.*, 12: 300-308.

Davis D., J. Suppe and F.A. Dahlen, 1983. Mechanics of fold-and-thrust belts and accretionary wedges. *J.Geoph.Res.*, 88: 1153-1172.

Davis G.H., 1983. Shear-zone model for the origin of metamorphic core complexes. *Geology*, 11: 342-347.

Dercourt J., L.P. Zonenshain, L-E. Ricou, V.G. Kazmin, X. Le Pichon, A.L. Knipper, C. Grandjacquet, I.M. Sbortshikov, J. Geyssant, C. Lepvrier, D.H. Pechersky, J. Boulin, J-C. Sibuet, L.A. Savostin, O. Sorokhtin, M. Westphal, M.L. Bazhenov, J.P. Lauer and B. Biju-Duval, 1986. Geological evolution of the Tethys belt from the Atlantic to the Pamirs since the Lias. *Tectonophysics*, 123: 241-315.

Derycke F. and I. Godfriaux, 1976. Metamorphismes <schistes bleus et schistes verts> dans l'Ossa et le Bas-Olympe (Thessalie-Grèce). *Bull. Soc. géol. France*, 2: 252.

Derycke F. and I. Godfriaux, 1978. Découverte de microfaunes paléogenes dans le flysch métamorphique de Spilia (Ossa, Grèce). *C.R. Acad. Sc. Paris*, 286: 555-558.

Dewey J.F., W.C. Pitman III, W.B.F. Ryan and J. Bonnin, 1973. Plate tectonics and the evolution of the Alpine system. *Geol. Soc. Am. Bull.*, 84: 3137-3180.

Dewey J.F., M.R. Hempton, W.S.F. Kidd, F. Saroglu and A.M.C. Sengör, 1986. Shortening of continental lithosphere: the neotectonics of Eastern Anatolia - a young collision zone. In M.P. Coward & A.C. Ries (Eds.), Collision tectonics Blackwell: 3-36.

Dewey J.F., 1988. Extensional collapse of orogens. *Tectonics*, 7: 1123-1139.

Dilek Y. and D.L. Whitney, 1997. Counterclockwise P-T-t trajectory from the metamorphic sole of a Neo-Tethyan ophiolite (Turkey). *Tectonophysics*, 280: 295-310.

Dinter D.A. and L. Royden, 1993. Late Cenozoic extension in northeastern Greece. *Geology*, 21: 45-48.

Dinter D.A., A. Macfarlane, W. Hames, C. Isachsen, S. Bowring and L. Royden, 1995. U-Pb and $^{40}Ar/^{39}Ar$ geochronology of the Symvolon granodiorite: Implications for the thermal and structural evolution of the Rhodope metamorphic core complex, northeastern Greece. *Tectonics*, 14: 886-908.

Dodson M.H., 1973. Closure temperature in cooling geochronological and petrological systems. *Contrib. Mineral. Petrol.*, 40: 259-274.

Dora O.O., Kun N. and Candan O., 1992. Geotectonic position and metamorphic history of the Menderes Massif. *Geol. Bull. of Turkey*, 35: 1-14.

Dora O.O., O. Candan, S. Dürr and R. Oberhansli, 1997. New evidence on the geotectonic evolution of the Menderes Massif. *IESCA 1995 proceedings*, 1: 53-72.

Draper G. and R. Bone, 1981. Denudation rates, thermal evolution, and preservation of blueschist terrains. *J. Geol.*, 89: 601-613.

Duermeijer C.E., W. Krijgsman, C.G. Langereis and J.H. Ten Veen, 1998. Post early Messinian counter-clockwise rotations on Crete: implications for late Miocene to Recent kinematics of the southern Hellenic Arc. *Tectonophysics*, accepted.

Dunlap W.J., C. Teyssier, I. McDougall and S.L. Baldwin, 1991. Ages of deformation from K/Ar and $^{40}Ar/^{39}Ar$ dating of white micas.

Geology, 19: 1213-1216.

Dunlap W.J. and C. Teyssier, 1995. Paleozoic deformation and isotopic disturbance in the southeastern Arunta Block, central Australia. *Prec. Res.*, 71: 229-250.

Dunlap W.J., 1997. Neocrystallization or cooling? $^{40}Ar/^{39}Ar$ ages of white micas from low-grade mylonites. *Chemical Geology*, 143: 181-203.

Dunlap, W.J., 1998. The tectonic significance of a porphyroblastic blueschist facies overprint during Alpine orogenesis: Sifnos, Aegean Sea, Greece: Discussion. *J. Struc. Geol.*, 20: 819-821.

Edel J.B., D. Kondopoulou, S. Pavlides and M. Westphal, 1992. Paleomagnetic evidence for a large counterclockwise rotation of northern Greece prior to the Tertiary clockwise rotation. *Geodyn. Acta.*, 5: 245-259.

Eide E.A., M.O. McWilliams and J.G. Liou, 1994. $^{40}Ar/^{39}Ar$ geochronology an exhumation of high-pressure to ultrahigh-pressure metamorphic rocks in east-central China. *Geology*, 22: 601-604.

Eleftheriadis G. and H.J. Lippolt, 1984. Altersbestimungen zum oligozänen vulkanismus der Süd Rhodopen/Nord Griechenland. *Neues Jahrb. Geol. Paläontol. Monatsh.*, 3: 179-191.

Emre T. and Sözbilir H., 1997. Field evidence for metamorphic core complex, detachment faulting and accommodation faults in the Gediz and Büyük Menderes Grabens, Western Anatolia. *IESCA 1995 proceedings*, 1: 73-94.

Ernst W.G., 1963. Significance of phengitic micas from low-grade schists. *Am. Mineral.*, 48: 1357-1373.

Ernst W.G., 1973. Blueschist metamorphism and P-T regimes in active subduction zones. *Tectonoph.*, 17: 255-272.

Ernst W.G., 1975. Systematics of large-scale tectonics and age progressions in alpine and circum-pacific blueschist belts. *Tectonophysics*, 26: 229-246.

Ernst W.G., 1988. Tectonic history of subduction zones inferred from retrograde blueschist P-T paths. *Geology*, 16: 1081-1084.

Erdogan B. and Güngör T., 1992. Stratigraphy and tectonic evolution of the Northern Margin of Menderes Massif. *TAPG Bulletin*, 4: 9-34.

Evans, B.W., 1990. Phase relations of epidote blueschists. *Lithos*, 25: 3-23.

Evirgen M.M. and Ataman G., 1982. A study of metamorphism in the Central zone of the Menderes massif isograde, pressures and temperature. *Bull. Soc. géol. France*, 24: 309-319.

Fassoulas C., A. Kilias and D. Mountrakis, 1994. Postnappe stacking extension and exhumation of high-pressure/low-temperature rocks in the island of Crete, Greece. *Tectonics*, 13: 127-138.

Faupl P., A. Pavlopoulos, M. Wagreich and G. Migiros, 1996. Pre-Tertiary blueschist terrains in the Hellenides: evidence from detrital minerals of flysch successions. *Terra Nova*, 8: 186-190.

Faure G., 1986. Principles of isotope geology. John Wiley & Sons. New York: 590 p.

Ferriere J., 1976. Etude preliminaire d'un secteur des massifs cristallins internes (<zone pélagonienne>): la région de Volos, Grèce continentale-orientale. *Bull. Soc. geol. France*, 2: 265-272.

Ferriere J., I. Godfriaux and A. Schmitt, 1988. Les series metamorphiques infrapieriennes et pagasitiques; bordure orientale de la zone (isopique) Pélagonienne (Thessalie, Grèce) ? *Deltio tes Ellenikes Geologikes Etaireias*, 20: 193-206.

Foster D.A., T.M. Harrison, P. Copeland and M.T. Heizler, 1990. Effects of excess argon within large diffusion domains on K-feldspar age spectra. *Geoch. Cosmoch. Act.*, 54: 1699-1708.

Franz L., and M. Okrusch, 1992. Aragonite-bearing blueschists on Arki island, Dodecanese, Greece. *Eur. J. Mineral.*, 4: 527-537.

Frei R., 1996. The extent of inter-mineral isotope equilibrium: a systematic bulk U-Pb and Pb step leaching (PbSL) isotope study of individual minerals from the Tertiary granite of Jerissos (northern Greece). *Eur. J. Mineral.*, 8: 1175-1189.

Frey M., C. De Capitani and J.G. Liou, 1991. A new petrogenetic grid for low-grade metabasites. *J. Metam. Geol.*, 9: 497-509.

Fytikas M., F. Innocenti, P. Manetti, R. Mazzuoli, A. Peccerillo and L. Villari, 1984. Tertiary to Quaternary evolution of volcanism in the Aegean region. In A.H.F. Robertson & J.E. Dixon (Eds.), the geological evolution of the eastern Mediterranean, *Geol. Soc. Special publ* 17: 687-699.

Garner E.L., T.J. Murphy, J.W. Paulsen and I.L. Barnes, 1975. Absolute isotopic abundance ratios and the atomic weight of a reference sample of potassium. *J. Res. Natl. Bureau Stand.*, 79a: 713-725.

Gautier P. and J-P Brun, 1994. Ductile crust exhumation and extensional detachments in the Central Aegean (Cyclades and Evvia Islands). *Geodin. Act.*, 2: 57-85.

Ghent E.D., P. Erdmer, D.A. Archibald and M.Z. Stout, 1996. Pressure-temperature and tectonic evolution of Triassic lawsonite-aragonite blueschists from Pinchi Lake, British Columbia. *Can. J. Earth. Sci.*, 33: 800-810.

Godfriaux I., 1968. Etude géologique de la region de l'Olympe (Grèce). *Annls. Geol. Pays Hell.*, 19: 1-271.

Godfriaux I., J. Ferriere and A. Schmitt, 1988. Le dévelopment en context continental d'un métamorphisme HP/BT; les "schistes bleus" tertiaires Thessaliens. *Deltio tes Ellenikes Geologikes Etaireias*, 20: 175-192.

Hames W.E. and K.V. Hodges, 1993. Laser $^{40}Ar/^{39}Ar$ evaluation of slow cooling and episodic loss of ^{40}Ar from a sample of polymetamorphic muscovite. *Science*, 261: 1721-1724.

Hames W.E. and S.A. Bowring, 1994. An empirical evaluation of the argon diffusion geometry in muscovite. *Earth Planet. Sci. Lett.*, 124: 161-167.

Hanes J.A., D. York and C.M. Hall, 1985. An $^{40}Ar/^{39}Ar$ geochronological and electron microprobe investigation of an Archean pyroxenite and its bearing on ancient atmospheric compositions. *Can. J. Earth Sci.*, 22: 947-958.

Hanes J.A., 1991. K-Ar and $^{40}Ar/^{39}Ar$ geochronology: Methods and Applications. In L. Heaman & J.N. Ludden (Eds.), Short course handbook on applications of radiogenic isotope systems to problems in geology. Mineralogical association of Canada, Toronto: 27-57.

Harris N.B.W., S. Kelley and A.I. Okay, 1994. Post-collision magmatism and tectonics in northwest Anatolia. *Contrib. Mineral. Petrol.*, 117: 241-252.

Harrison T.M. and I. McDougall, 1980. Investigations of an intrusive contact, northwest Nelson, New Zealand- I Thermal, chronological and isotopic constraints. *Geoch. Cosmoch. Act.*, 44: 1985-2003.

Harrison T.M., 1981. Diffusion of ^{40}Ar in Hornblende. *Contrib. Mineral. Petrol.*, 78: 324-331.

Harrison, T.M. and I. McDougall, 1981. Excess ^{40}Ar in metamorphic

rocks from Broken Hill, New South Wales: Implications of $^{40}Ar/^{39}Ar$ age spectra and the thermal history of the region. *Earth Planet. Sci. Lett.*, 55: 123-149.

Harrison T.M. and I. McDougall, 1982. The thermal significance of potassium feldspar K-Ar ages inferred from $^{40}Ar/^{39}Ar$ age spectrum results. *Geoch. Cosmoch. Act.*, 46: 1811-1820.

Harrison T.M., I. Duncan and I. McDougall, 1985. Diffusion of ^{40}Ar in biotite: Temperature, pressure and compositional effects. *Geoch. Cosmoch. Act.*, 49: 2461-2468.

Harrison T.M., O.M. Lovera and M.T. Heizler, 1991. $^{40}Ar/^{39}Ar$ results for alkali feldspars containing diffusion domains with differing activation energy. *Geoch. Cosmoch. Act.*, 55: 1435-1448.

Hatzfeld D., 1994. On the shape of the subducting slab beneath the Peloponnese, Greece. *Geoph. Res. Lett.*, 21: 173-176.

Heizler M.T. and T.M. Harrison, 1988. Multiple trapped argon isotope components revealed by $^{40}Ar/^{39}Ar$ isochron analysis. *Geoch. Cosmoch. Act.*, 52: 1295-1303.

Hetzel R., C.W. Passchier, U. Ring and O.O. Dora, 1995a. Bivergent extension in orogenic belts: The Menderes massif (southwestern Turkey). *Geology*, 23: 455-458.

Hetzel R., U. Ring, C. Akal and M. Troesch, 1995b. Miocene NNE-directed extensional unroofing in the Menderes Massif, southwestern Turkey. *J. Geol. Soc. London*, 152: 639-654.

Hetzel R. and T. Reischmann, 1996. Intrusion age of Pan-African augen gneisses in the southern Menderes Massif and the age of cooling after Alpine ductile extensional deformation. *Geol. Mag.*, 133: 565-572.

Hill E.J. and S.L. Baldwin, 1993. Exhumation of high-pressure metamorphic rocks during crustal extension in the D'Entrecasteaux region, Papua New Guinea. *J. metamorphic Geol.*, 11: 261-277.

Hodges K.V., W.E. Hames and S.A. Bowring, 1994. $^{40}Ar/^{39}Ar$ age gradients in micas from a high-temperature-low-pressure metamorphic terrain: Evidence for very slow cooling and implications for the interpretation of age spectra. *Geology*, 22: 55-58.

Holm D.K., T.B. Holst and D.R. Lux, 1993. Postcollisional cooling of the Penokean orogen in east-central Minnesota. *Can. J. Earth Sci.*, 30: 913-917.

Holm D.K. and D.R. Lux, 1996. Core complex model proposed for gneiss dome development during collapse of the Paleoproterozoic Penokean orogen, Minnesota. *Geology*, 24: 343-346.

Houseman G. and P. England, 1993. Crustal thickening versus lateral expulsion in the Indian-Asian continental collision. *J. Geoph. Res.*, 98: 12233-12249.

Hsü K.J., 1995. The geology of Switzerland - An introduction to tectonic facies. Princeton University Press, New Jersey: 250 p.

Hunziker J.C., J. Desmons and A.J. Hurford, 1992. Thirty-two years of geochronological work in the Central and Western Alps: a review on seven maps. *Mémoires de Géologie (Lausanne)*, 13: 1-59.

Hynes A.J., E.G. Nisbett, A.G. Smith, M.J. Welland and D.C. Rex, 1972. Spreading and emplacement ages of some ophiolites in the Othris region (eastern central Greece). *Z. dt geol. Ges.*, 123: 455-468.

IGME, 1983. Geological map of Greece, scale 1:500,000. second edition (directed by: K. Papavassiliou).

Jackson J., 1994. Active tectonics of the Aegean region. *Annu. Rev. Earth Planet. Sci.*, 22: 239-271.

Jacobshagen V. and E. Wallbrecher, 1984. Pre-Neogene nappe structure and metamorphism of the North Sporades and the southern Pelion peninsula. In A.H.F. Robertson & J.E. Dixon (Eds.), the geological evolution of the eastern Mediterranean, *Geol. Soc. Special publ* 17: 591-602.

Jäger E., 1973. Rb-Sr and K-Ar geochronology of alpine metamrophic rocks. *Fortschr.Miner.*, 50: Bh 3, 3.

Jansen J.B.H., 1977. The geology of Naxos. *Geol. Geol. Met.*, 19: 100 pp.

John B.E. and K.A. Howard, 1995. Rapid extension recorded by cooling-age patterns and brittle deformation, Naxos, Greece. *J. Geoph. Res.*, 100, B7: 9969-9979.

Jolivet L., J.M. Daniel, C. Truffert and B. Goffe, 1994. Exhumation of deep crustal metamorphic rocks and crustal extension in arc and back-arc regions. *Lithos*, 33: 3-30.

Jolivet L., J-P. Brun, P. Gautier, S. Lallemant and M. Patriat, 1994b. 3D-kinematics of extension in the Aegean region from the early miocene to the Present, insights from the ductile crust. *Bull. Soc. géol. France*, 165: 195-209.

Jolivet L., B. Goffé, P. Monié, C. Truffert-Luxey, M. Patriat and M. Bonneau, 1996. Miocene detachment in Crete and exhumation P-T-t paths of high-pressure metamorphic rocks. *Tectonics*, 15: 1129-1153.

Jolivet L., C. Faccenna, B. Goffe, M. Mattei, F. Rossetti, C. Brunet, F. Storti, R. Funiciello, J-P Cadet, N. d'Agostino and T. Parra, 1998. Midcrustal shear zones in post-orogenic extension: Example from the northern Tyrrhenian Sea. *J. Geoph. Res.*, 103: 12123-12160.

Jones G. and A.H.F. Robertson, 1991. Tectono-stratigraphy and evolution of the Mesozoic Pindos ophiolite and related units, northwestern Greece. *J. Geol. Soc.*, 148: 267-288.

Jones C.E., J. Tarney, J.H. Baker and F. Gerouki, 1992. Tertiary granitoids of Rhodope, northern Greece: magmatism related to extensional collapse of the Hellenic Orogen ? *Tectonophysics*, 210: 295-314.

Karfakis I. and T. Doutsos, 1995. Late orogenic evolution of the Circum-Rhodope Belt, Greece. *N. Jb. Geol. Paläont. Mh.*, H5: 305-319.

Keay S.M., 1998. The geological evolution of the Cyclades, Greece: Constraints from SHRIMP U-Pb geochronology. *PhD thesis, ANU Canberra*: 341 p.

Kelley S., 1995. Ar-Ar dating by laser microprobe. In J.F.W. Bowles, P.J. Potts, S.J.B. Reed, M.R. Cave (Eds.), Microprobe techniques in the Earth Sciences. Chapman & Hall, London: 327-358

Kirschner D.L., M.A. Cosca, H. Masson and J.C. Hunziker, 1996. Staircase $^{40}Ar/^{39}Ar$ spectra of fine-grained white mica: Timing and duration of deformational and empirical constraints on argon diffusion. *Geology*, 24: 747-750.

Kissel C. and C. Laj, 1988. The Tertiary geodynamical evolution of the Aegean arc: a paleomagnetic reconstruction. *Tectonophysics*, 146: 183-201.

Kohn M.J., F.S. Spear, T.M. Harrison and I.W.D. Dalziel, 1995. $^{40}Ar/^{39}Ar$ geochronology and P-T-t paths from the Cordillera Darwin metamorphic complex, Tierra del Fuego, Chile. *J. metamorphic Geol.*, 13: 251-270.

Konak N., Akdeniz N. and Ozturk E.M., 1987. Geology of the south of Menderes Massif. *IGCP project no 5, correlation of Variscan and pre-Variscan events of the Alpine-Mediterranean mountain belt*: 42-53.

Koppers A.A.P., 1998. $^{40}Ar/^{39}Ar$ geochronology and isotope geochemistry of the west Pacific seamount province: Implications for absolute Pacific plate motions and the motions of hotspots.

PhD thesis, Vrije Universiteit Amsterdam: 260 p.

Koukouvelas I. and T. Doutsos, 1990. Tectonic stages along a traverse cross cutting the Rhodopian zone (Greece). *Geol. Rundsch.*, 79/3: 753-776.

Koukouvelas I. and G. Pe-Piper, 1991. The Oligocene Xanthi pluton, northern Greece: a granodiorite emplaced during regional extension. *J. Geol. Soc. London*, 148: 749-758.

Layer P.W., C.M. Hall and D. York, 1987. The derivation of $^{40}Ar/^{39}Ar$ age spectra of single grains of hornblende and biotite by laser step-heating. *Geophys. Res. Lett.*, 14: 757-760.

Le Pichon X. and J. Angelier, 1979. The Hellenic arc and trench system: a key to the neotectonic evolution of the eastern Mediterranean area. *Tectonophysics*, 60: 1-42.

Le Pichon X., N. Chamot Rooke, S. Lallement, R. Noomen and G. Veis, 1995. Geodetic determination of the kinematics of central Greece with respect to Europe: implications for eastern Mediterranean tectonics. *J. Geoph. Res.*, 100: 12675-12690.

Lee J.K.W., T.C. Onstott and J.A. Hanes, 1990. An $^{40}Ar/^{39}Ar$ investigation of the contact effects of a dyke intrusion, Kapuskasing Structural Zone, Ontario. *Contrib. Mineral. Petrol.*, 105: 87-105.

Lee J. and G.S. Lister, 1992. Late Miocene ductile extension and detachment faulting, Mykonos, Greece. *Geology*, 20: 121-124.

Liati A. and E. Mposkos, 1990. Evolution of the eclogites in the Rhodope Zone of northern Greece. *Lithos*, 25: 89-99.

Liati A. and E. Seidel, 1994. Sapphirine and högbomite in overprinted kyanite-eclogites of central Rhodope, N. Greece: first evidence of granulite-facies metamorphism. *Eur. J. Mineral.*, 6: 733-738.

Liati A. and E. Seidel, 1996. Metamorphic evolution and geochemistry of kyanite eclogites in central Rhodope, northern Greece. *Contrib. Mineral. Petrol.*, 123: 293-307.

Lips A.L.W., White S.H. and Wijbrans J.R., 1998a. $^{40}Ar/^{39}Ar$ laser-probe direct dating of discrete deformational events: a continuous record of Early Alpine tectonics in the Pelagonian Zone, NW Aegean area, Greece. *Tectonophysics spec. issue* (A.H.F. Robertson Ed.): accepted, Chapter 4 of this thesis.

Lips A.L.W., J.R. Wijbrans and S.H. White, 1998b. New insights from $^{40}Ar/^{39}Ar$ laserprobe dating of white mica fabrics from the Pelion Massif, Pelagonian Zone, Internal Hellenides, Greece: Implications for the timing of metamorphic episodes and tectonic events in the Aegean region. *Geol.Soc.London spec.* volume (L. Jolivet Ed.): accepted, Chapter 5 of this thesis.

Lister G.S., G. Banga and A. Feenstra, 1984. Metamorphic core complexes of Cordilleran type in the Cyclades, Aegean Sea, Greece. *Geology*, 12: 221-225.

Lister G.S. and Snoke A.W., 1984. S-C Mylonites. *J. Struc. Geol.*, 6: 617-638.

Lister G.S., M.A. Etheridge and P.A. Symonds, 1986. Detachment faulting and evolution of passive continental margins. *Geology*, 14: 246-250.

Lister G.S. and G.A. Davis, 1989. The origin of metamorphic core complexes and detachment faults formed during Tertiary continental extension in the northern Colorado River region. *J. Struc. Geol.*, 11: 65-94.

Lister G.S. and S.L. Baldwin, 1993. Plutonism and the origin of metamorphic core complexes. *Geology*, 21: 607-610.

Lister G.S. and A. Raouzaios, 1996. The tectonic significance of a porphyroblastic blueschist facies overprint during Alpine orogenesis: Sifnos, Agean Sea, Greece. *J. Struc. Geol.*, 18: 1417-1435.

Lister, G.S., 1998. The tectonic significance of a porphyroblastic blueschist facies overprint during Alpine orogenesis: Sifnos, Aegean Sea, Greece: Reply. *J. Struc. Geol.*, 20: 823-825.

Lovera O.M., 1992. Computer programs to model $^{40}Ar/^{39}Ar$ diffusion data from multidomain samples. *Comp. Geosc.*, 18: 789-813.

v.d.Maar P.A. and J.H.B. Jansen, 1983. The geology of the polymetamorphic complex of Ios, Cyclades, Greece, and its significance in the Cycladic Massif. *Geol. Rundsch.*, 72: 283-299.

Makropoulos K.C. and P.W. Burton, 1984. Greek tectonics and seismicity. *Tectonophysics*, 106: 275-304.

Malavieille J., 1993. Late orogenic extension in mountain belts: insights from the Basin and Range and the Late Paleozoic Variscan Belt. *Tectonics*, 12: 1115-1130.

Maluski H., P. Vergely, D. Bavay, P. Bavay and G. Katsikatsos, 1981. $^{40}Ar/^{39}Ar$ dating of glaucophanes and phengites in Southern Euboa (Greece) geodynamic implications. *Bull. Soc. geol. France*, 23: 469-476.

Maluski H., M. Bonneau and J.R. Kienast, 1987. Dating the metamorphic events in the Cycladic area: $^{40}Ar/^{39}Ar$ data from metamorphic rocks of the island of Syros (Greece). *Bull. Soc. Geol. France*, 3: 833-842.

Mares V.M. and A.K. Kronenberg, 1993. Experimental deformation of muscovite. *J. Struc. Geol.*, 15: 1061-1075.

McDougall I. and T.M. Harrison (1988). Geochronology and Thermochronolgy by the $^{40}Ar/^{39}Ar$ Method Oxford University Press, New York: 212 p.

McKenzie D., 1970. The plate tectonics of the Mediterranean region. *Nature*, 226: 239-243.

McKenzie D., 1978. Active tectonics of the Alpine-Himalayan Belt, the Aegean sea and surrounding regions. *Geoph. J. R. Astr. Soc.*, 55: 217-254.

Megrue G.H., 1967. Isotopic analysis of rare gases with a laser microprobe. *Science*, 76: 4956-4968.

Merrihue C. and G. Turner, 1966. Potassium-argon dating by activation with fast neutrons. *J. Geoph. Res.*, 71: 2852-2857.

Meijer P.T., 1995. Dynamics of active continental margins: the Andes and the Aegean region. PhD thesis, Utrecht University; *Geologica Ultraiectina*, 130: 220 p.

Meijer P.T. and M.J.R. Wortel, 1997. Present-day dynamics of the Aegean region: a model analysis of the horizontal pattern of stress and deformation. *Tectonics*, 16: 879-895.

Mercier J., 1973. Contributions à l'étude du métamorphism et de l'évolution magmatique des zones internes des Hellenides. *Annls Geol. Pays Hell.*, 20: 597-792.

Merle O., 1994. Syn-convergence exhumation of the Central Alps. *Geodinamica Acta*, 7: 129-138.

Monié P., 1990. Preservation of Hercynian $^{40}Ar/^{39}Ar$ ages through high-pressure low-temperature Alpine metamorphism in the Western Alps. *Eur. J. Mineral.*, 2: 343-361.

Monié P., J. Galindo-Zaldivar, F. Gonzales Lodeiro, B. Goffé and A. Jalaboy, 1991. $^{40}Ar/^{39}Ar$ geochronology of Alpine tectonism in the Betic Cordilleras (southern Spain). *J. Geol. Soc. London*, 148: 289-297.

Montigny R., 1989. The conventional Potassium-Argon method. In E. Roth and B. Poty (Eds.), Nuclear methods of dating, CEA, Paris: 295-324.

Müller R.D. and W.K. Roest, 1992. Fracture zones from combined

Geosat and Seasat data. *J. Geoph. Res.*, 97: 3337-3350.

Nance D., 1981. Tectonic history of a segment of the Pelagonian zone, northeastern Greece. *Can.J.Earth Sci.*, 18: 1111-1126.

Oberhänsli R., O. Candan, O.Ö. Dora and St.H. Dürr, 1997. Eclogites within the Menderes Massif / western Turkey. *Lithos*, 41: 135-150.

Okay A.I., 1984. Distribution and characteristics of the north-west Turkish blueschists. In A.H.F. Robertson & J.E. Dixon (Eds.), the geological evolution of the eastern Mediterranean, *Geol. Soc. Special publ* 17: 455-466.

Okay A.I., M. Siyako and K.A. Bürkan, 1991. Geology and tectonic evolution of the Biga Peninsula, northwest Turkey. *Bull. Tech. Univ. Istanbul*, 44: 191-256.

Okay A.I., A.M.C. Sengör and N. Görür, 1994. Kinematic history of the opening of the Black Sea and its effect on the surrounding regions. *Geology*, 22: 267-270.

Okay A.I. and S.P. Kelley, 1994. Tectonic setting, petrology and geochronology of jadeite+glaucophane and chloritoid+glaucophane schists from north-west Turkey. *J. metamorphic Geol.*, 12: 455-466.

Okay A.I., M. Satir, H. Maluski, M. Siyako, P. Monié, R. Metzger and S. Akyüz 1996. Paleo- and Neo-Tethyan events in northwestern Turkey: geologic and geochronologic constraints. In A. Yin &. T.M. Harrison (Eds.), The tectonic evolution of Asia, Cambridge University Press: 420-441.

Okrusch M., P. Richter and G. Katsikatsos. 1984. High-pressure rocks of Samos, Greece. In A.H.F. Robertson & J.E. Dixon (Eds.), the geological evolution of the eastern Mediterranean, Geol. Soc. Special publ 17: 529-536.

Okrusch M. and M. Brocker, 1990. Eclogites associated with high-grade blueschists in the Cycladic archipelago, Greece: a review. *Eur. J. Mineral.*, 2: 451-478.

Onstott T.C., C.M. Hall and D. York, 1989. $^{40}Ar/^{39}Ar$ thermochronometry of the Imataca Complex, Venezuela. *Precambrian. Res.*, 42: 255-291.

Papadopoulos C. and A. Kilias, 1985. Altersbeziehungen zwischen Metamorfose und Deformation im Zentralen Teil des Serbomazedonischen Massivs (Vertiskos Gebirge, Nord-Griechenland). *Geol. Rundsch.*, 74: 77-85.

Papanikolaou D.J., 1984. The three metamorphic belts of the Hellenides: a review and a kinematic interpretation. In A.H.F. Robertson & J.E. Dixon (Eds.). the geological evolution of the eastern Mediterranean, *Geol. Soc. Special publ* 17: 551-561

Passchier C.W. and R.A.J. Trouw, 1996. Microtectonics. Springer, Berlin Heidelberg: 289p.

Pe-Piper G. and D.J.W. Piper, 1989. Spatial and temporal variation in Late Cenozoic back-arc volcanic rocks, Aegean Sea region. *Tectonoph.*, 169: 113-134.

Phillips D. and T.C. Onstott, 1986. Application of $^{36}Ar/^{40}Ar$ versus $^{36}Ar/^{39}Ar$ correlation diagrams to the $^{40}Ar/^{39}Ar$ spectra of phlogopites from Southern African kimberlites. *Geoph. Res. Lett.*, 13: 689-692.

Phillips D. and, T.C. Onstott, 1988. Argon isotopic zoning in mantle phlogopite. *Geology*, 16: 542-546.

Pickett E.A. and A.H.F. Robertson, 1996. Formation of the Lat Palaeozoic-Early Mesozoic Karakaya Complex and related ophiolites in NW Turkey by Palaeotethyan subduction-accretion. *J. Geol. Soc.*, 153: 995-1009.

Pirajno F., 1995. Volcanic-hosted epithermal systems in northwest Turkey. *S. Afr. J. Geol.*, 98: 13-24.

Platt J.P., 1986. Dynamics of orogenic wedges and the uplift of high-pressure metamorphic rocks. *Geol. Soc. Am. Bull.*, 97: 1037-1053.

Platt J.P. and R.L.M. Vissers, 1989. Extensional collapse of thickened continental lithosphere: A working hypothesis for the Alboran Sea and Gibraltar arc. *Geology*, 17: 540-543.

Platt J.P., 1993. Exhumation of high-pressure rocks: a review of concepts and processes. *Terra Nova*, 5: 119-133.

Platt J.P. and P.C. England, 1993. Convective removal of lithosphere beneath mountain belts: Thermal and mechanical consequences. *Am. J. Sci.*, 294: 307-336.

Plieninger T. and O.A. Schaeffer, 1976. Laser probe ^{39}Ar-^{40}Ar ages of indivdual mineral grains in Lunar basalt 15607 and Lunar breccia 15465. *Proc. 7th Lunar Sci. Conf.*: 2055-2066.

Purdy J.W. and E. Jäger, 1976. K-Ar ages on rock-forming minerals from the Central Alps. *Mem. Inst. Geol. Min. Univ. Padova*, 30: 31 pp.

Raouzaios A., G.S. Lister and D. Foster, 1996. Oligocene exhumation and metamorphism of eclogite-blueschists from the island of Sifnos, Cyclades, Greece. *Geol. Soc. Australia, Abstracts of 13th AGC*, 141: 358.

Reddy S.M., S.P. Kelley and J. Wheeler, 1996. A $^{40}Ar/^{39}Ar$ laser probe study of micas from the Sesia Zone, Italian Alps: implications for metamorphic and deformation histories. *J. metamorphic Geol.*, 14: 493-508.

Renne P.R., C.C. Swisher, A.L. Deino, D.B. Karner, T.L. Owens and D.J. DePaolo. 1998. Intercalibration of standards, absolute ages and uncertainties in $^{40}Ar/^{39}Ar$ dating. *Chem. Geol.*, 145: 117-152.

Ricou L-E., 1994. Tethys reconstructed: plates, continental fragments and their boundaries since 260 Ma from Central America to South-eastern Asia. *Geodinamica Acta*, 7: 169-218.

Ridley J., 1984. Evidence of a temperature-dependent 'blueschist' to 'eclogite' transformation in high-pressure metamorphism of metabasic rocks. *J. Petr.*, 25: 852-870.

Robbins G.A., 1972. Radiogenic argon diffusion in muscovite under hydrothermal conditions. *M.Sc. thesis, Brown University, Providence (U.S.).*

Robertson A.H.F. and J.E. Dixon, 1984. Introduction: aspects of the geological evolution of the Eastern Mediterranean. In A.H.F. Robertson & J.E. Dixon (Eds.), the geological evolution of the eastern Mediterranean, *Geol. Soc. Special publ* 17: 1-74.

Robertson A.H.F., 1994. Role of the tectonic facies concept in orogenic analysis and its application to Tethys in the Eastern Mediterranean region. *Earth Sci. Rev.*, 37: 139-213.

Roddick J.C., R.A. Cliff and D.C. Rex, 1980. The evolution of excess argon in alpine biotites. A 40Ar-39Ar analysis. *Earth Planet. Sci. Lett.*, 48: 185-208.

Royden L.H., 1993a. Evolution of retreating subduction boundaries formed during continental collision. *Tectonics*, 12: 629-638.

Royden L.H., 1993b. The tectonic expression slab pull at continental convergent boundaries. *Tectonics*, 12: 303-325.

Royden L.H., 1993c. The steady state thermal structure of eroding orogenic belts and accretionary prisms. *J. Geoph. Res.*, 98: 4487-4507.

Ruddiman W., 1998. Early uplift in Tibet ? *Nature*, 394: 723-725.

Satir M. and H. Friedrichsen, 1986. The origin and evolution of the Menderes Massif, W-Turkey: A rubidium/strontium and oxygen isotope study. *Geol. Rundsch.*, 75: 703-714.

Scaillet S., G. Feraud, Y. Lagabrielle, M. Ballevre and G. Ruffet, 1990. $^{40}Ar/^{39}Ar$ laser-probe dating by step heating and spot fusion of phengites from the Dora Maira nappe of the western Alps, Italy. *Geology*, 18: 741-744.

Scaillet S., G. Feraud, M. Ballevre and M. Amouric, 1992. Mg/Fe and [(Mg,Fe)Si-Al2] compositional control on argon behaviour in high-pressure white micas: A $^{40}Ar/^{39}Ar$ continuous laser-probe study from the Dora-Maira nappe of the internal western Alps, Italy. *Geoch. Cosmoch. Acta*, 56: 2851-2872.

Schermer E.R., 1990. Mechanisms of blueschist creation and preservation in an A-type subduction zone, Mount Olympos region, Greece. *Geology*, 18: 1130-1133.

Schermer E.R., D.R. Lux and B.C. Burchfield, 1990. Temperature-time history of subducted continental crust, Mount Olympos region, Greece. *Tectonics*, 9: 1165-1195.

Schermer E.R., 1993. Geometry and kinematics of continental basement deformation during the Alpine orogeny, Mt. Olympos region, Greece. *J. Struc. Geol.*, 15: 571-591.

Schliestedt M. and A. Matthews, 1987. Transformation of blueschists to greenschist facies rocks as a consequence of fluid infiltration, Sifnos (Cyclades), Greece. *Contrib. Mineral. Petrol.*, 97: 237-250.

Schmitt A., 1983. Nouvelles contributions a l'étude géologique des Pieria, de l'Olympe, et de l'Ossa (Grèce du Nord). *Thesis at Faculté Polytechnique de Mons, Belgium*: 215.

Schuiling R.D., 1962. On petrology, age and structure of the Menderes migmatite complex (SW-Turkey). *Bull. Mineral. Res Explor. Inst. Turkey*, 58: 71-84.

Seidel E., H. Kreuzer and W. Harre, 1982. A Late Oligocene/Early Miocene high pressure belt in the External Hellenides. *Geol. Jb.*, E23: 165-206.

Sengör A.M.C., Y. Yilmaz and I. Ketin, 1980. Remnants of a pre-Late Jurassic ocean in northern Turkey: Fragments of Permian-Triassic Paleo-Tethys ? *Geol. Soc. Am. Bull.*, 91: 599-609.

Sengör A.M.C., 1984. The Cimmeride orogenic system and the tectonics of Eurasia. *Geol. Soc. Am. Spec. Paper*, 195: 1-82.

Sengör A.M.C., Y. Yilmaz and O. Sungurlu, 1984a. Tectonics of the Mediterranean Cimmerides: nature and evolution of the western termination of Palaeo-Tethys. In A.H.F. Robertson & J.E. Dixon (Eds.), the geological evolution of the eastern Mediterranean, *Geol Soc. Special publ* 17: 77-112.

Sengör A.M.C., M. Satir and R. Akkök, 1984b. Timing of tectonic events in the Menderes Massif, Western Turkey: implications for tectonic evolution and evidence for Pan-African basement in Turkey. *Tectonics*, 3: 693-707.

Sengör, A.M.C., N. Görür and F. Saroglu, 1985. Strike-slip faulting and related basin formation in zones of tectonic escape: Turkey as a case study. Strike slipe deformation, basin formation and sedimentation, *Spc. of Ec. Pal. and Min., Tulsa*: 227-264.

Seyitoglu G., B.C. Scott and C.C. Rundle, 1992. Timing of Cenozoic extensional tectonics in west Turkey. *J. Geol. Soc. London*, 149: 533-538.

Seyitoglu G. and B.C. Scott, 1996. The cause of N-S extensional tectonics in western Turkey: tectonic escape vs back-arc spreading vs orogenic collapse. *J. Geodynamics*, 22: 145-153.

Sigurgeirsson T. (1962). Age dating of young basalts with the potassium argon method *No. Physics Laboratory, University of Iceland.*

Sisson V.B. and T.C. Onstott, 1986. Dating blueschist metamorphism: A combined $^{40}Ar/^{39}Ar$ and electron microprobe approach. *Geochim. Cosmochim. Act.*, 50: 2111-2117.

Skarpelis N., 1989. Metamorphosed ultramafic rocks in the blueschist (arna unit) of the external metamorphic belt of the Hellenides (Peloponnesos and Kythira Island, Greece). *Bull. Geol. Soc. Greece*, XXIII: 345-358.

Smith A.G. and N.H. Woodcock, 1982. Tectonic syntheses of the Alpine-Mediterranean region: a review. In H. Berkheimer and K. J. Hsü (Eds.). Alpine and Mediterranean Geodynamics: 15-38.

Smith A.G., 1996. Some aspects of the Phanerozoic paleogeographic evolution of Europe. *Z. dt. geol. Ges.*, 147: 147-168.

Sokoutis D., J.P. Brun, J. van den Driessche and S. Pavlides, 1993. A major Oligo-Miocene detachment in southern Rhodope controlling north Aegean extension. *J. geol. Soc. London*, 150: 243-246.

Sözbilir H. and T. Emre, 1996. Menderes Masifi'nin neotektonik evriminde olusan supradetachment havzalar ve rift havzalari (Supradetachment basin and rift basin developed during the neotectonic evolution of the Menderes Massif). *Abstracts of the 49th Geological Congress of Turkey*: 30-31.

Spakman W., M.J.R. Wortel and N.J. Vlaar, 1988. The Hellenic Subduction Zone: A tomographic image and its geodynamic implications. *Geoph. Res. Lett.*, 15: 60-63.

Spear F.S., 1993. Metamorphic phase equilibria and pressure-temperature-time paths. Washington D.C.: 799 p.

Spray J.G. and J.C. Roddick, 1980. Petrology and $^{40}Ar/^{39}Ar$ geochronology of some hellenic sub-ophiolite metamorphic rocks. *Contrib. Mineral. Petrol.*, 72: 43-55.

Spray J.G., J. Bébien, D.C. Rex and J.C. Roddick, 1984. Age constraints on the igneous and metamorphic evolution of the Hellenic-Dinaric ophiolites. In A.H.F. Robertson & J.E. Dixon (Eds.), the geological evolution of the eastern Mediterranean, *Geol. Soc. Special publ* 17: 619-629.

Steiger R.H. and E. Jäger, 1977. Subcommission on geochronology: convention on the use of decay constants in geo- and cosmochronology. *Earth Planet. Sci. Lett.*, 36: 359-362.

Stüwe K. and T.D. Barr, 1998. On uplift and exhumation during convergence. *Tectonics*, 17: 80-88.

Theye T., E. Seidel and O. Vidal, 1992. Carpholite, sudoite and chloritoid in low-grade high-pressure metapelites from Crete and the Peloponnese, Greece. *Eur. J. Mineral.*, 4: 487-507.

Thomson S.N., B. Stöckhert and M.R. Brix, 1998. Thermochronology of the high-pressure metamorphic rocks of Crete, Greece: Implications for the speed of tectonic processes. *Geology*, 26: 259-262.

Till A.B. and L.W. Snee, 1995. $^{40}Ar/^{39}Ar$ evidence that formation of blueschists in continental crust was synchronous with foreland fold and thrust belt deformation, western Brooks Range, Alaska. *J. metamorphic Geol.*, 13: 41-60.

Triboulet C. and Y. Bassias, 1988. Geothermo-barometry on zoned amphiboles and progressive metamorphism in glaucophane-bearing metabasites from the Parnon massif (external Hellenides, Peloponnesus, Greece). *C.R. Acad. Sci. Paris*, 306: 991-996.

Tsokas G.N. and R.O. Hansen, 1997. Study of the crustal thickness and the subducting lithosphere in Greece from gravity data. *J.Geoph.Res.*, 102: 20585-20597

Turcotte D.L. and E.R. Oxburgh, 1972. Mantle convection and the

new global tectonics. *Ann. Rev. fluid Mech.*, 4: 33-68.

Turner G., J.A. Miller and R.L. Grasty, 1966. The thermal history of Bruderheim meteorite. *Earth Pla. Sci. Lett.*, 1: 155-157.

Underhill J.R., 1989. Late Cenozoic deformation of the Hellenide foreland, western Greece. *Geol. Soc. Am. Bull.*, 101: 613-634.

Urai J.L., R.D. Schuiling and J.B.H. Jansen, 1990. Alpine deformation on Naxos (Greece). *J. Geol. Soc. London*, 54: 509-522.

Vandenberg L.C. and G.S. Lister, 1996. Structural analysis of basement tectonites from the Aegean metamorphic core complex of Ios, Cyclades, Greece. *J. Struc. Geol.*, 18: 1437-1454.

Vissers R.L.M., J.P. Platt and D. van der Wal, 1995. Late orogenic extension of the Betic Cordillera and the Alboran Domain: A lithospheric view. *Tectonics*, 14: 786-803.

Walcott, C.R. and A.L.W. Lips, 1996. A structural history of NW Turkish Basement. *unpublished preliminary report to La Source SAS and Eurogold*: 4 p.

Walcott C.R. and S.H. White, 1998. Constraints on the kinematics of post-orogenic extension imposed by stretching lineations in the Aegean region. Tectonophysics spec. issue (A.H.F. Robertson Ed.): accepted.

Walcott C.R., 1998. The Alpine evolution of Thessaly (NW Greece) and late Tertiary Aegean kinematics. PhD thesis, Utrecht University; Geologica Ultraiectina, 162: 176 p.

Wang C-Y. and Y-L Shi, 1984. On the thermal structure of subduction complexes. a preliminary study. *J. Geoph. Res.*, 89: 7709-7718.

Wawrzenitz N. and E. Mposkos, 1997. First evidence for Lower Cretaceous HP/HT-metamorphism in the Eastern Rhodope, North Aegean region, North-East Greece. *Eur. J. Mineral.*, 9: 659-664.

Wawrzenitz N., 1997. Mikrostrukturell unterstützte Datierung von Deformationsinkrementen in Myloniten: Dauer der Exhumierung und Aufdomung des metamorphen Kernkomplexes der Insel Thasos (Süd-Rhodope, Nordgriechenland). *PhD thesis, University of Nürnberg*: 198 p.

Wernicke B., 1985. Uniform sense normal simple shear of the continental lithosphere. *Can. J. Earth Sci.*, 22: 108-125.

West D.P. and D.R. Lux, 1993. Dating mylonite deformation by the $^{40}Ar/^{39}Ar$ method: an example from the Norumbega Fault Zone, Maine. *Earth Plan. Sci. Lett.*, 120: 221-237.

de Wet A.P., J.A. Miller, M.J. Bickle and J. Chapman, 1989. Geology and geochronology of the Arnea, Sithonia and Ouranopolis intrusions, Chalkidiki Peninsula, northern Greece. *Tectonophysics*, 161: 65-79.

White S.H., Burrows S.E., Carreras J., Shaw N.D. and Humphreys F.J., 1980. On mylonites in ductile shear zones. *J. Struc. Geol.*, 2: 175-187.

Whitney D.L. and Y. Dilek, 1997. Core complex development in central Anatolia, Turkey. *Geology*, 25: 1023-1026.

Wijbrans J.R., 1985. Geochronology of metamorphic terrains by the 40Ar/39Ar age spectrum method. *PhD thesis, ANU Canberra*: 267 p.

Wijbrans J.R. and I McDougall, 1986. $^{40}Ar/^{39}Ar$ dating of white micas from an Alpine high-pressure metamorphic belt on Naxos (Greece); the resetting of the argon isotopic system. *Contrib. Mineral. Petrol.*, 93: 187-194.

Wijbrans J.R. and I McDougall, 1988. Metamorphic evolution of the Attic Cycladic metamorphic belt on Naxos (Cyclades, Greece) utilizing $^{40}Ar/^{39}Ar$ age spectrum measurements. *J. Metam. Geol.*, 6: 571-594.

Wijbrans J.R., M. Schliestedt and D. York, 1990. Single grain argon laser probe dating of phengites from the blueschist to greenschist transition on Sifnos (Cyclades, Greece). *Contrib. Mineral. Petrol.*, 104: 582-593.

Wijbrans J.R., J.D. van Wees, R.A. Stephenson and S.A.P.L. Cloetingh, 1993. Pressure-temperature-time evolution of the high-pressure metamorphic complex of Sifnos, Greece. *Geology*, 21: 443-446.

Wijbrans J.R., M.S. Pringle, A.A.P. Koppers and R. Scheveers, 1995. Argon geochronology of small samples using the Vulkaan argon laserprobe. *Proc. Kon. Ned. Akad. v. Wetensch.*, 98: 185-218.

Wilson C.J.L. and I.A. Bell, 1979. Deformation of biotite and muscovite: optical microstructure. *Tectonophysics*, 58: 179-200.

Wortel M.J.R. and W. Spakman, 1992. Structure and dynamics of subducted lithosphere in the Mediterranean region. *Proc. Kon. Ned. Akad. v. Wetensch.*, 95: 325-347.

Yarwood G.A. and M. Aftalion, 1976. Field relations and U-Pb geochronology of a granite from the Pelagonian zone of the Hellenides (High Pieria, Greece). *Bull. Soc. geol. Fr.*, 18: 259-264.

Yarwood G.A. and J.E. Dixon, 1977. Lower Cretaceous and younger thrusting in the Pelagonian rocks of High Pieria, Greece. *Sixth Colloq. Aegean Region, Athens*: 269-280.

Yilmaz Y., S.C. Genc, E. Yigitbas, M. Bozcu and K. Yilmaz, 1995. Geological evolution of the late Mesozoic continental margin of Northwestern Anatolia. *Tectonophysics*, 243: 155-171.

York D., C.M. Hall, Y. Yanase, J.A. Hanes and W.J. Kenyon, 1981. $^{40}Ar/^{39}Ar$ dating of terrestrial minerals with a continuous laser. *Geoph. Res. Lett.*, 8: 1136-1138.

Zanchi A. and J. Angelier, 1993. Seismotectonics of western Anatolia: regional stress orientation from geophysical and geological data. *Tectonophysics*, 222: 259-274.

Zeitler P.K., 1989. The geochronology of metamorphic processes. In J.S. Daly, R.A. Cliff & B.W.D. Yardley (Eds.), Evolution of metamorphic belts Blackwell: 131-147.

Zimmerman J. Jr. and J.V. Ross, 1976. Structural evolution of the Vardar root zone, northern Greece: Discussion and reply. *Bull. geo. Soc. Am.*, 90: 126-128.

Appendix 1

Basic principles of $^{40}Ar/^{39}Ar$ laserprobe geochronology

A1.1 The natural decay of ^{40}K

The first quantitative measurement of ^{40}Ar, produced by decay of ^{40}K has been presented by Aldrich & Nier (1948). The decay constants at present used for calculating ages are those recommended by Steiger & Jäger (1977). The theory behind the K-Ar technique, and thus the $^{40}Ar/^{39}Ar$ technique, has been extensively discussed (see Dalrymple & Lanphere, 1969, 1971; Faure, 1986; McDougall & Harrison, 1988), and will be described briefly in the next sections.

The principle of the K-Ar method is fairly simple. There are three naturally-occurring isotopes of potassium (abundances after Garner et al, 1976); ^{39}K (ca 93.2581%), ^{40}K (ca 0.01167%), and ^{41}K (ca 6.7302 %). One of these potassium isotopes, ^{40}K, is radioactive and decays to two daughter isotopes (figure 3.1), namely to ^{40}Ca through a β^- process, what is favoured by 88.8 % of the atoms and to ^{40}Ar in the other 11.2 % of the cases. As ^{40}Ca is the most abundant of all Ca isotopes and ^{40}K is the least abundant of all K isotopes, it implies that the isotopic variations of Ca produced by decay of ^{40}K are, in most cases, negligible. This explains why the decay of ^{40}K to ^{40}Ca is not widely used in geochronology studies. The parent isotope ^{40}K decays to the daughter isotope ^{40}Ar with an half-life time of 1.72×10^{10} years (Steiger & Jäger, 1977). The decay to ^{40}Ar occurs in three different ways; i) an electron of the K-shell is captured by the nucleus and a neutron is created at the expense of a proton. The argon atom is in an excited state and rapidly decays to the ground state by emitting gamma photons; ii) an almost similar process consists of an electronic capture gamma ray emission. This process occurs in 0.16 % of all cases and causes a slight rise of the error in the measurement of decay constants of ^{40}K, which are determined by gamma or beta counting; iii) the third mechanism results from the emission of a positron, β^+, which changes a proton into a neutron, and which occurs in 0.001% of the cases. As is the case with other radioactive decay systems, an age can be calculated when the quantities of daughter and parent isotope are precisely known. The decay of the parent isotope ^{40}K and production of daughter isotopes ^{40}Ca and ^{40}Ar in a closed system is given by the equation:

$$^{40}Ar^{\star} + {}^{40}Ca^{\star} = {}^{40}K\,(e^{\lambda t} - 1) \qquad (1)$$

$^{40}Ar^{\star}$ and $^{40}Ca^{\star}$ are the amounts of ^{40}Ar and ^{40}Ca produced by the in situ decay of ^{40}K.
λ is the total decay constant of ^{40}K (i.e. 5.543×10^{-10} yrs^{-1}).
t is the duration of decay.

The total decay constant, λ, can be separated into two partial decay constants, one for the decay of ^{40}K to ^{40}Ca (4.962×10^{-10}/yr) and the other for the decay of ^{40}K to ^{40}Ar (0.581×10^{-10}/yr):

$$\lambda = \lambda_{Ar} + \lambda_{Ca} \qquad (2)$$

λ_{Ar} refers to the decay of ^{40}K to ^{40}Ar (i.e. 0.581×10^{-10} yrs^{-1})
λ_{Ca} refers to the decay of ^{40}K to ^{40}Ca (i.e. 4.962×10^{-10} yrs^{-1})

Rewriting the two equations results in the following equation for the age of the sample, which forms the basis for the K-Ar and $^{40}Ar/^{39}Ar$ dating method:

$$t = 1/\lambda \ln \{^{40}Ar^*/^{40}K (\lambda/ \lambda_{Ar}) + 1\} \qquad (3)$$

In the conventional K-Ar method, the ^{40}Ar and ^{40}K contents are measured on separate aliquots of the sample to be dated. The K content is measured as total K on one aliquot by flame photometry, atomic absorption, or X-ray fluorescence analysis, or as ^{40}K by isotope dilution. The ^{40}Ar content is measured on the other aliquot in a noble gas mass spectrometer in static mode by the isotope dilution technique. Because of the need to measure absolute contents of K and Ar from two separate aliquots, it is important that the sample is as homogeneous as possible. The $^{40}Ar/^{39}Ar$ technique has significant advantages over the K-Ar method. The sample does not need to be split into two aliquots, so problems of sample heterogeneity can be avoided. The date is determined by the mass-spectrometric measurement of the ratio of the argon isotopes, which is more precise than measuring absolute concentrations of ^{40}K and ^{40}Ar.

A1.2 Irradiation and correction factors

The $^{40}Ar/^{39}Ar$ technique was first conceived by Sigurgeirsson (1962), with the first detailed experiments reported by Merrihue & Turner (1966). The $^{40}Ar/^{39}Ar$ method is based on the measurement of the ^{40}K in the sample by a neutron activation procedure involving the conversion of a fraction of ^{39}K, the main naturally occurring K isotope (which occurs in a constant ratio to ^{40}K), to ^{39}Ar by irradition of the sample with fast neutrons in a nuclear reactor. ^{39}Ar is itself radioactive but its half life of 265 years is sufficiently long for any error in a mass spectrometry measurement to be (usually) very small. Following this irradiation, the sample is fused in an ultra high vacuum system (UHV) and the purified Ar gas is measured isotopically by noble gas mass spectrometry. After the mass intensities have been corrected for atmospheric argon and mass interference, due to production of additional Ar isotopes derived from irradiated K, Ca and Cl in the analysed material, the $^{40}Ar/^{39}Ar$ ratio can be obtained (see also appendix 1.2 for the correction procedures). The effect of the production of an Ar isotopic ratio in the sample not only allows the determination of this ratio with a higher analytical precision than the analysis of two separate aliquots, but also allows stepwise extraction and analysis of the argon isotopes from the sample (incremental heating experiment) to investigate the presence of an heterogeneous or homogeneous Ar distribution in the sample. A single spectrometric analysis is sufficient to determine the K/Ar ratio which is a parameter of the age equation, because the quantity of ^{39}Ar is a function of the quantity of

total K, and thus ^{40}K. A sample with known K-Ar ratio (called a *standard* or *monitor*) is required to establish a precise knowledge of the ^{39}Ar production during irradiation. The standard is irradiated simultaneously with the unknown samples and analysed to obtain its $^{40}Ar^*/^{39}Ar$ ratio. An irradiation parameter, J, is defined that is appropriate for both the standard and the unknown samples:

$$J = (e^{\lambda t} - 1) / (^{40}Ar^* / {}^{39}Ar_K) \quad (4)$$

t is age of standard

$^{39}Ar_K$ is the amount of ^{39}Ar derived from irradiation of ^{39}K

The variation in neutron fluence is mapped out to establish the exact irradiation parameter per sample. Once J is known, ages can be calculated:

$$t = 1/\lambda \ln\{J (^{40}Ar^* / {}^{39}Ar_K)+1\} \quad (5)$$

The uncertainty in the calculated age includes uncertainties in; i) the determination of J, ii) the system blanks, iii) the regression of intensities of individual isotopes, iv) the correction factors, and v) the discrimination correction.

As with the conventional K-Ar method, correction for atmospheric argon based on the measurement of ^{36}Ar ($^{40}Ar/^{36}Ar_{atm} = 295.5$) is necessary. The irradiation also causes formation of additional argon isotopes, following the main reactions; $^{40}Ca(n,na)\ ^{36}Ar$, $^{42}Ca(n,a)\ ^{39}Ar$ and $^{40}K(n,p)\ ^{40}Ar$. Correction at masses 36 and 39 is obtained through a further circa reaction; $^{40}Ca(n,a)\ ^{37}Ar$, after irradiation of a pure calcium glass/salt and analysis of the $^{39}Ar/^{37}Ar$ and $^{36}Ar/^{37}Ar$ isotopic ratios after fusion of the glass/salt (^{37}Ar decays with a half life of 35.1 days, a factor that should be incorporated in the corrections). The ^{40}Ar production is measured by irradiating a zero-age pure K-compound. Finally, mass intensities corrected for interference and atmospheric argon can be expressed by the following simple equations:

$$^{40}Ar^* = {}^{40}Ar_m - (^{40}Ar_{atm} + {}^{40}Ar_K) \quad (6)$$

$$^{39}Ar_K = {}^{39}Ar_m - {}^{39}Ar_{Ca} \quad (7)$$

$$^{36}Ar_{atm} = {}^{36}Ar_m - {}^{36}Ar_{Ca} \quad (8)$$

(m=measured, *=radiogenic, atm=atmospheric)

In the analysed white mica in this study, mass interference due to additional Ar istope production during irradiation is limited. The white micas contain little or no Ca, which results in very few to no production of calcium derived ^{36}Ar, ^{37}Ar, and ^{39}Ar. The production of ^{40}Ar from ^{40}K introduces a small but important bias that can be corrected for.

To summarize, the main factors which contribute to the final analytical uncertainty of the

established absolute age concern the measurement of; i) the relative quantities of the three naturally occurring isotopes of potassium (as it is assumed that ^{39}K occurs in a constant ratio to ^{40}K, after Garner et al, 1975), ii) the decay constant of ^{40}K decay to ^{40}Ar, recommended by Steiger & Jäger (1977), resulting from recalculated values of Beckinsale & Gale (1969) with the data presented by Garner et al (1975), iii) the irradiation parameter J (which is controlled by the error on the K-Ar age of the used flux monitor, by the error on the $^{40}Ar/^{39}Ar$ analysis of the flux monitor and by the error estimate of the variation in neutron fluence in the tray of samples; see also Renne et al, 1998, for further details), iv) the uncertainty on the mass spectrometric analysis of the Ar intensities (including the error on the blanks), v) the mass interferences of radiogenic Ar with atmospheric Ar and potassium, calcium and chlorine derived Ar, and, additionally, vi) the error on the weighted mean of the individual steps which contribute to the plateau age, established from an age spectrum after completion of an incremental heating experiment. Dalrymple & Lanphere (1971) obtained the following expression for the final error in the calculated age:

$$\sigma^2 = (J^2\sigma^2_R + R^2\sigma^2_J)/(\lambda^2(1 + RJ)^2) \qquad (9)$$

J is the irradiation parameter
R is the $^{40}Ar^*/^{39}Ar_K$ ratio

The variance of the $^{40}Ar^*/^{39}Ar_K$ ratio is expressed in the following formula by Dalrymple & Lanphere (1971):

$$\sigma^2_R = \sigma^2_M + A^2\sigma^2_N + (C_1M - AC_1N + AC_2)^2\,\sigma^2_P \qquad (10)$$

M is the measured $^{40}Ar/^{39}Ar$ ratio
A is the ratio in atmospheric Ar; $(^{40}Ar/^{36}Ar)_A = 295.5$
N is the measured $^{36}Ar/^{39}Ar$ ratio
C_1 is the ratio in Ca derived $^{39}Ar/^{37}Ar$
C_2 is the ratio in Ca derived $^{36}Ar/^{37}Ar$
P is the measured $^{37}Ar/^{39}Ar$ ratio

A1.3 Laserinstrumentation and VULKAAN laserprobe characteristics

The use of lasers in isotope studies was introduced by Megrue in 1967 with the analysis of He and Ne in meteorites. Further refinement of the technique resulted in the application of a laser system for dating lunar samples (Plieninger & Schaeffer, 1976) and subsequent terrestrial rock samples by the $^{40}Ar/^{39}Ar$ technique (York et al, 1981). The instrumentation used for the age determination of minerals in this study is the VULKAAN argon laserprobe at the Faculty of Earth Sciences of the Vrije Universiteit in Amsterdam. The VULKAAN laserprobe consists of a 24W argon ion laser, beam optics, a low volume UHV gas inlet system, and a MAP 215-50 noble gas mass spectrometer. The inlet system consists of a central

water-cooled getter cross fitted with two Fe-V-Zr (SAES St172©) internally heated alloy getter elements operated at about 250°C. A Pyrex cold finger and a filament heated Zr-Al cartridge (SAES GP10-St101©) can be included in the sample house segment. The getter cross is pumped with a Balzers TPU062 hybrid turbo/drag pump, backed-up by a triode ionpump, to vacuum levels of $\leq 5x10^{-9}$ mbar. The foreline vacuum is pumped to levels lower than 2 mbar with a Vacuubrand MD4 diaphragm pump. The total volume of the inlet line is around 100 ml. Because the mass spectrometer volume is circa 1500 ml, expansion of the gas ensures transfer of more than 90% of the gas into the mass spectrometer for isotopic measurements. The mass spectrometer is fitted with a Nier type electron bombardment source, that is operated at a 75 eV electron energy, 200mA trap current and 3 kV acceleration voltage. The source housing is pumped for reactive gases with a SAES NP50 getter pump fitted with a Zr-Al alloy cartridge at room temperature. The isotopic composition of the argon gas was measured using a double focussing noble gas mass spectrometer (MAP215-50) in static mode. Beam intensities were measured on a secondary electron multiplier detector (gain 60,000) and switchable preamplifier resistor settings (10, 100 and 1000 MOhm) by peak jumping at half mass intervals down from mass 40 to 35.5.
Further description of the operating characteristics can be found in Wijbrans et al (1995). The VULKAAN argon laserprobe is characterized by a laser with typical wavelengths of 488 and 514.5 nm, which fall in the visible light range (blue(-green) and green light, respectively). The currently used visible light laser is a versatile compromise that combines adequate focussing (spot fusion) with the available laserpower (incremental heating). With the current developments in laser optics an infrared laser appears to be best suited for single grain incremental heating experiments, and a pulsed UV, a quadruple mode Nd-YAG or an Excimer laser appears to be more suited for spot fusion experiments. Application of spot fusion dating with the argon laser is limited as the laserbeam with the defined wavelengths might generate substantial heat in the analysed material. The generated heat will activate thermal diffusion of argon from a domain which is larger in diameter than the applied spot size. As a consequence individual laser shots need to be of short duration.

A1.4 Degassing procedures, age spectra and isochron plots

The $^{40}Ar/^{39}Ar$ laserprobe incremental heating experiments (IHE) are most effective for samples that might have a heterogeneous distribution of ^{40}Ar. In the IHE a sample is heated by a defocussed laserbeam and the argon that is released by degassing of the sample is collected. After cleaning of the released gas, the argon isotopes are measured, the corrections are applied and an age is calculated using the equations 1 to 8. The laserpower is then increased and the process is repeated. The final result is an argon release spectrum (*age spectrum*).
If it is assumed that gas is evolved from the sample during IHE by thermally activated volume diffusion, then the successively higher-temperature steps are sampling gas from progressively deeper in the crystals (e.g. already suggested by Turner et al, 1966). In the case of a rapidly cooled mineral that has not lost Ar since it passed through its closure temperature or a mineral that ≤has crystallized rapidly below its relevant closure temperature range, there

should be a uniform distribution of Ar throughout the crystal given that the crystal has not been affected by other factors which might control argon loss (e.g. recrystallization, chemical alteration, etc.). Theoretically, then, all ages obtained in a IHE of such a sample will be within uncertainty and the age spectrum will be flat. Such a flat spectrum (*plateau age*) is taken to indicate that the sample has remained a closed system to argon (loss or gain), and that the date represents an age of geological significance. However, when argon from grain edges and grain centres evolves at the same time during step-heating, a meaningless plateau date can be the result. Therefore, a plateau spectrum is generally a necessary, but not sufficient indication, that a mineral has not partially lost argon since it last passed through its closure temperature.

In the age spectrum a contaminating argon component with a non-atmospheric $^{40}Ar/^{36}Ar$ ratio might be present (i.e. *excess, extraneous, inherited argon*, cf. Dalrymple & Lanphere, 1969). The excess argon in such a sample is dominantly derived from diffusion of argon from an oversaturated argon environment. In general, argon preferably partitions into the fluid phase and subsequently partitions into biotite over white mica. The shape of a $^{40}Ar/^{39}Ar$ age spectrum can often signal the presence of excess argon, since it is commonly distributed inhomogeneously throughout the mineral (e.g. saddle shaped spectra of Broken Hill hornblendes, Harrison & McDougall, 1981). The result will be a disturbed age spectrum that is sometimes quite complex. If the excess argon is concentrated in grain-boundary sites, its presence may be reflected by high dates in the initial gas steps, followed by a meaningfull plateau age in the remaining steps. Lee et al (1990) showed that laser spot dating may help map out the distribution of such excess-argon contamination in a mineral grain. The nature of non-radiogenic, trapped argon can, in some cases, be determined by the isochron approach, a technique that is analogous to the Rb-Sr isochron method. With the $^{40}Ar/^{39}Ar$ step-heating approach an isochron plot can be constructed from a single sample, using all the steps as data points on a plot of $^{40}Ar/^{36}Ar$ against $^{39}Ar/^{36}Ar$. In this case, any straight line reflects mixing of two reservoirs of gas, one being the radiogenic ^{40}Ar and the other being the non radiogenic argon component, which may consist of atmospheric argon, excess argon and sometimes hydrocarbon or HCl contaminants. An alternate, and more common, way to analyse the data is to plot $^{36}Ar/^{40}Ar$ against $^{39}Ar/^{40}Ar$ (inverse isochron or correlation plot), in which the age is given by the intercept on the $^{39}Ar/^{40}Ar$ axis, and the composition of the trapped argon is given by the intercept on the $^{36}Ar/^{40}Ar$ axis (see also Roddick et al, 1980; Phillips & Onstott, 1986; Heizler & Harrison, 1988).

Appendix 2

Geochronology samples: locations & descriptions

Locationcode

OS = Ossa Massif
MV = Mavrovouni Massif
PE = Pelion Massif
NA = west Volos (Nea Angialos)
AG = Antihassia Mountains
SK = Skiathos Island
Rh = Rhodope Zone
KD = Kazdag Massif
MD = Menderes Massif
[...] = GPS coordinates (UTM, or 00°00.000')

Structural abbreviations

S = main foliation (undiff)
L = main lineation (undiff)
Lmin = mineral lineation
Lex = extension lineation
crenS = crenulation foliation
crenL = crenulation lineation
Fp = fold plunge

Mineral abbreviations

qtz = quartz
alb = albite
chl = chlorite
msv = muscovite
phn = phengite
w.m. = white mica (undiff.)
glc = glaucophane (blue amphibole undiff.)
cc = calcite
apt = apatite
sph = sphene
ept = epidote
px = pyroxene
Ksp = K-feldspar
law = lawsonite

BSF = blueschist facies
GSF = greenschist facies

Fieldwork October 1994, Pelagonian (1)

OS001. (24/10/94) Greenschist Unit close to Phyllite contact, 3 km along road from Spilia to Anatoli. Greenschist containing qtz, alb, phn, msv, cc, apt. Greenschist mylonite, WSW transport (top to 256). Main S 093S57, veins 122S88, crenS-1 148N53, crenS-2 098S78.

OS003. (24/10/94) Greenschist Unit, road Spilia to Sikourio, greenschistmylonite, undiff transport (WSW ?), with glaucophane fragments, containing act, qtz, phn, sph, chl, alb, apt, ept.

OS004. (24/10/94) Blueschist Unit, road Spilia to Sikourio, glaucophaneschist with glaucophane lineation (later kinked), blueschist mylonite, NE transport (060), containing alb, phn, apt, qtz, glc, ept, cc, sph, relic btt.

OS005. (24/10/94) Basement, road Spilia to Sikourio, two mica granite gneiss near blueschist contact, containing qtz, btt, msv, phn, Ksp, alb, incipient glc. White mica (coarse and fine), biotite (coarse with white mica rims), microcline. The white micas that rim the primary biotite are fine grained and stable with crossite.

NA007. (26/10/94) Granite Gneiss, road Volos to Nea Angialos, granite gneiss, containing msv, phn, ept, alb, qtz. Transport dominantly to 240, but ambiguous, associated 060 stretching lineation overprints 280 rodding/sheathing

PE009. (27/10/94) Phyllite Unit, msv porphyroclasts in phyllite in quarry near Kalamaki, transport to NE along 040 extension lineation.

PE013. (28/10/94) Granite Gneiss near Greenschist Unit, granitic schist (mylonite) along road Milies-Kalamaki, two schistosities visible in handspecimen, transport to 060. Mineralogy; msv, phn, qtz, alb.

PE015a. (28/10/94) Greenschist at Mylies railroad, greenschist, relic glc, containing ept, edt, qtz, mgt, apt, phn, cc, chl. Transport to 240

OS024. (31/10/94) Blueschist Unit, E-side of Ossa, blueschist/greenschist facies granite gneiss

OS026. (31/10/94) Blueschist Unit, E-side Ossa,blueschist, containing alb, rcht, phn, msv, apt, glc.

OS029. (2/11/94) Basement Gneiss, btt-msv basement gneiss along road Sikourio-Spilia, alternating felsic-basic layers, S 060SE50, Faxis 040NE06, Lmin 150SE46.

OS030. (2/11/94) Basement Gneiss, Sikourio-Spilia road, second fabric in btt-msv basement gneiss, suggested transport to NW (330), general S 060SE50, secondary fabric almost horizontal.

Fieldwork June-July 1995, Pelagonian (2)

PE102 (22/6/95), unmarked, Makrirachi in riverbed. Main S=010NW70, Lex= 020S20 transport to N. Chlorite schist (ept, chlt, cc) with marble bands.

OS106. (23/6/95), unmarked, road from Anatoli. Crenulated w.m. btt in basement (evidence for BSF, GSF ?).

OS109 (23/6/95), unmarked, road from Anatoli next to OS108. New segregation with w.mc.

PE111 (24/6/95), north of Pouri. Lineated gneiss / greenschist mylonite. Chlt, w. mc, qtz.

PE113 (24/6/95), north of Pouri, greenschist mylonite, transport to NE (025)?

PE114 (24/6/95), PouriBeach. Well developed mylonite. S=020E40, Lex to 025. Ductile shears indicating NE transport, overprint by semi-brittle SW transport. Old cren fabric, Fp//Lex, veins//S +refolded. Chlt, w.mc.

PE115 (24/6/95), road Zagora-Volos, circa 8 km out of Zagora. ex-gabbro, sulphides/copper/btt? chlt or w.m., greenschist mylonite, transport to NE.

MV117 (25/6/95), road Kalamaki-Elafos. Shear in basement unit S=070SE28, Lex to 218, transport to SW. Boudin in shear; gnt, chlt, w.mc, (amph).

MV118 (25/6/95), next to MV117. Main mylonite; chlt, w.mc, abt, epdt. Lex to 218

MV121 (25/6/95), Sklithro-Keramidi 4 km out of Sklithro. Basement schist under limestone unit. Gnt, w.mc, btt.

OS138 (3/7/95), lineation 30 degrees to 210, N of Pournari,. S=340W35, Lex 030S//blue-green amphibole, Tg 300E40, NNE movement. Epdt laminated rock. Lith variation in basement-retrograde BSF contact shear.

PE139 (4/7/95), Platania. S=348W34, Lex=030, semiductile shearbands to SW, ductile shear bands to NE.

PE140 (4/7/95), Neochori. NE transport in granite gneiss (similar characteristics as Milies granite mylonite, PE013). Chlt, w.m., abt, qtz.

PE141 (4/7/95), Neochori. Well developed shears in granite gneiss, SW transport.

PE142 (4/7/95), Neochori. SW shears, 2 w.mc generations?

OS146 (6/7/95), road to Spilia. NE (055) transport in basement unit, greenschist mylonite with relic glaucophane.

OS149 (7/7/95), road to Spilia. NE (045) transport in blueschist mylonite. S=310SW42, Lex + Lmin = 046

OS151 (8/7/95), road to Spilia, crenulated blueschist, S = 328SW60, crenulated glc lin + new lin.

OS152 (8/7/95), road to Spilia. discrete shear in blueschist mylonite, main S=310SW58, 2nd shear s=290E84, glc lin 064, both transport to SW (244).

SK154 (11/7/95), between Koukounaries and Troulos. Foliated granite gneiss, microcline, ambiguous shear sense.

AG156 (15/7/95), near Longa. Granite gneiss GSF, Lex 040NE12, transport to 220, NE dipping shearzone, boundary shear from Pelagonian ?

OS159 (sampled by S.H. White), Ossa near central limestone, greenschist mylonite transport to SW (235).

Fieldwork October 1996, Kazdag Massif, Menderes Massif (1)

KD303 Kazdag gneiss, btt msv, qtz, feldspar, lineation circa 030,

KD304 Evçiler granodiorite Quarry [0475424, 4404923] massive undeformed hbl, btt, (msv) granodiorite

KD305 [0463499, 4399094] marble mylonite, L = 023N44 in nearby schists S = 015W60, L = 015, NNE transport.

KD315 Elliayak Hill [0463826, 4388928] eclogite of melange sequence, felsic eclogite w.m. gnt schist.

KD316 Narli [0472464, 4384482] marble mylonite, S = 035SE15, L = 344, SE transport.

MD318 (3/10/96) [0595326, 4254599] near Allahdiyen, greenschist mylonite below cataclasite, anastamosing foliation, S = 270N48, L = 356, new mica growth

MD319 (4/10/96), N of Incirliova, near [0565617, 4201027], Buyuk Menderes Detachment, gneiss klippe. In footwall structure, new mica in low grade schists (ductile N transport overprint by semi-brittle S transport, S = 274S20, Lex=357

Fieldwork November, 1996, Rhodope region

Rh402 (Arnea) [40°27.420', 23°31.285'] foliated marble; S = 310S76 L=300E65 transport to 300; unorr.

Rh405 (Agios Nikolaos) [40°17.212', 23°40.997'] schists

Rh410 (Symvolon) [40°53.864', 24°15.438'] lineated augengneiss, L=050; S=025NW20

Rh411 (Kipia) mylonite quarry L=040NE08, S=346SW12, movement to 040

Rh413 (Ano Vrondou), near Rh414, flaggy marbles S=053SE28

Rh414 (Ano Vrondou) [41°13.081', 23°39.392'] btt-w.m. gneiss, S=072SE32, weakly foliated sheet granites.

Rh418 (Livadero) [41°17.292', 24°12.768'] marble with schist intercalations S=335E50

Rh427 (Livadero) [41°00.256', 24°23.948'] schist in marble L=014, thrust movement to 194.

Rh430 (Echinos) between [41°19.597', 24°57.525'] and [41°15.894', 24°56.752'] musc. veins in btt granodiorite (Rh431); unorr.

Rh432 (Sminthi) [41°14.245', 24°53.111'] contactmetamorphic marble near granite; calc-silicates, unorr.

Rh437 (Megalo Derio) [41°12.573', 25°59.404'] felsic mylonite / augengneiss, coarse mica, K-spar; S=290N05, L=010, transport to 190

Rh438 (Sapka Pass) [41°07.575', 25°53.134'] augengneiss;S = 260S24, L=015 transport to 195

Rh442 (Polyneri) between Drama and [41°14.362', 24°26.870'] 050 mylonite; S=330NE32

Appendix 3

$^{40}Ar/^{39}Ar$ laserprobe analyses.

The following appendix lists the data of the $^{40}Ar/^{39}Ar$ laserprobe analyses, used in this study (chapters 3, 4, 5 and 6). The outgassing procedure and data reduction has been described briefly in section 4.8.4. The raw data has been processed with a reduction program in MS-Excel, which has been developed inhouse by A.A.P. Koppers and provides spreadsheets with $^{40}Ar/^{39}Ar$ laserprobe data as age spectra and isochron plots. For further details on the raw data reduction and spreadsheet characteristics consult; Koppers, 1998.

The appendix presents the processed $^{40}Ar/^{39}Ar$ laserprobe data by chapter.
General corrections factors include (see also appendix 1, and Koppers, 1998):

40/39(K)	0.00086
36/37(Ca)	0.00026
39/37(Ca)	0.00067
40/36(atm)	295.5
$1/\lambda$	1804.077
K/Ca	0.49

CHAPTER 3, all data

Sample Number = **Spot Fusion VU17-NA007** Irradiation Number = VU17
Material = white mica (porphyroclast, foliation) Location = W-Volos

Datafile	fabric	$^{36}Ar(a)$	^{37}Ar	^{38}Ar	$^{39}Ar(K)$	$^{40}Ar(a+r)$	Age ± 2σ	$^{40}Ar(r)$	K/Ca
97M0348B	clast	0,00053	0,00000	-0,00012	0,31049	11,03933	227,83 ± 2,48	98,59%	No Ca
97M0348C	fol	0,00002	0,16906	0,00001	0,00183	0,04734	148,25 ± 181,4	86,06%	0,005
97M0348D	clast	0,00026	0,00018	0,00014	0,02702	0,62583	135,28 ± 15,48	87,56%	74,784
97M0348E	clast	0,00034	0,00018	0,00010	0,11307	3,89856	218,94 ± 4,00	97,45%	312,773
97M0348G	clast	0,00040	0,00018	-0,00009	0,16130	7,45632	290,41 ± 3,74	98,39%	445,665
97M0348H	fol	0,00008	0,00018	-0,00011	0,00763	0,07982	50,36 ± 50,79	70,44%	21,067
97M0348I	clast	0,00010	0,00018	-0,00012	0,02792	1,15829	260,41 ± 17,11	97,48%	77,077
97M0348J	clast	0,00005	0,00018	0,00004	0,02147	0,32152	95,98 ± 18,85	95,02%	59,251
97M0348L	fol	0,00017	0,00018	0,00005	0,00180	0,06767	61,35 ± 218,1	23,90%	4,951
97M0348N	clast	0,00010	0,37460	-0,00004	0,14981	6,25773	267,18 ± 3,44	99,51%	0,196
97M0348O	clast	0,00005	0,28829	-0,00016	0,09380	4,31086	292,21 ± 4,37	99,63%	0,159
97M0348P	fol	0,00006	0,30484	0,00004	0,04261	0,43144	66,21 ± 10,21	96,15%	0,068
97M0348R	fol	0,00013	0,34685	-0,00005	0,00858	0,13635	76,62 ± 40,32	71,10%	0,012
97M0348S	clast	0,00003	0,27337	-0,00009	0,00664	0,12738	120,91 ± 51,68	94,03%	0,012
97M0348U	fol	0,00030	0,00020	0,00010	0,02282	0,35332	78,84 ± 25,07	75,13%	55,061
97M0348V	clast	0,00005	0,17329	-0,00001	0,02019	0,41990	133,63 ± 24,67	96,28%	0,057
97M0348W	clast	0,00000	0,04555	0,00002	0,01546	0,16844	73,93 ± 35,21	99,99%	0,166
97M0348Y	clast	0,00000	0,00020	-0,00012	0,02126	0,43116	135,31 ± 25,88	99,99%	51,201
97M0348Z	clast	0,00000	0,25765	0,00006	0,06085	2,19581	234,12 ± 8,23	100,00%	0,116
97M0348!	clast	0,00002	0,19780	0,00002	0,06760	3,04616	287,31 ± 8,52	99,76%	0,167
97M0348@	clast	0,00005	0,00020	0,00008	0,03053	1,55685	319,86 ± 17,22	99,06%	73,335
97M0348$	clast	0,00000	0,05910	0,00004	0,02342	1,16680	315,76 ± 23,89	100,00%	0,194
97M0348%	clast	0,00000	0,26941	0,00004	0,10070	4,94736	311,78 ± 6,14	100,00%	0,183
97M0348^	clast	0,00003	0,30678	0,00007	0,03861	2,09594	340,20 ± 13,85	99,56%	0,062
97M0348&	clast	0,00000	0,37929	0,00017	0,11906	4,19616	228,99 ± 5,10	100,00%	0,154
97M0348)	clast	0,00000	0,58036	0,00018	0,09333	1,32563	95,81 ± 5,44	99,99%	0,079
97M0348{	clast	0,00000	0,41036	-0,00008	0,07121	2,92695	264,41 ± 9,03	100,00%	0,085

Irradiation values

J	0,003840
sd-J(1s)	0,000019

Sample Number = **Spot Fusion VU17-OS004** Irradiation Number = VU17
Material = white mica (single crystal, aggregates) Location = Ossa

Datafile	fabric	$^{36}Ar(a)$	^{37}Ar	^{38}Ar	$^{39}Ar(K)$	$^{40}Ar(a+r)$	Age ± 2σ	$^{40}Ar(r)$	K/Ca
97M0022B	clast	0,00143	0,00000	0,00017	0,66894	11,16950	103,36 ± 1,24	96,22%	NoCa
97M0022C	clast	0,00039	0,00000	-0,00002	0,31368	5,36948	107,61 ± 1,6	97,83%	36293,1
97M0022E	retro-BS	0,00017	0,00931	-0,00027	0,21418	2,33740	69,40 ± 2,02	97,90%	11,3
97M0022F	retro-BS	0,00051	0,03245	0,00007	0,52393	5,33390	64,33 ± 1,02	97,16%	7,9
97M0022G	BS	0,00067	0,00382	0,00016	0,52147	6,81002	82,07 ± 1,18	97,10%	67,0
97M0022I	GS	0,99953	0,01620	0,00016	0,54637	4,38947	50,59 ± 0,92	96,45%	16,5
97M0022J	GS	0,00057	0,02020	0,00013	0,45075	3,46940	47,87 ± 0,98	95,17%	10,9
97M0022K	GS	0,00119	0,00549	0,00013	0,65914	4,93576	45,46 ± 1,24	92,85%	58,8
97M0022L	GS	0,00078	0,01945	-0,00005	0,69319	4,83152	43,43 ± 0,7	95,24%	17,5
97M0022N	retro-BS	0,00111	0,00894	0,00014	0,89334	7,71143	53,92 ± 0,78	95,75%	49,0
97M0022O	retro-BS	0,00049	0,03893	0,00006	0,81024	6,76623	53,31 ± 0,76	97,84%	10,2
97M0022P	BS	0,00038	0,02088	0,00011	0,58423	8,19416	89,35 ± 1,30	98,63%	13,7
97M0022Q	BS	0,00072	0,01933	0,00024	0,50526	6,92145	85,82 ± 1,30	96,90%	12,8
97M0022S	retro-BS	0,00066	0,04174	-0,00003	0,78364	7,43103	60,12 ± 0,80	97,36%	9,2

Irradiation values

J	0,003670
sd-J(1s)	0,000018

Sample Number = **Spot Fusion VU17-PE141** Irradiation Number = VU17
Material = white mica aggregates Location = Pelion

Datafile	fabric	$^{36}Ar(a)$	^{37}Ar	^{38}Ar	$^{39}Ar(K)$	$^{40}Ar(a+r)$	Age ± 2σ	$^{40}Ar(r)$	K/Ca
97M0020B	s1-2	0,00067	0,00000	0,00077	1,59615	9,56024	41,12 ± 0,58	97,93%	NoCa
97M0020C	s2	0,00032	0,00800	-0,00037	0,15730	0,75287	29,41 ± 2,18	87,35%	9,6
97M0020E	s2	0,00036	0,00000	0,00033	0,20072	1,36926	44,10 ± 2,24	92,28%	24622,6
97M0020F	s1	0,00021	0,00668	0,00001	0,14998	1,18678	52,35 ± 2,84	94,67%	11,0
97M0020G	s2	0,00020	0,00234	-0,00015	0,09571	0,54790	35,86 ± 3,68	89,23%	20,0
97M0020I	s1	0,00010	0,00101	0,00032	0,15661	1,02669	44,61 ± 2,74	97,17%	76,3
97M0020J	s1	0,00017	0,00328	0,00013	0,06710	0,52405	49,52 ± 4,78	90,65%	10,0
97M0020K	s2	0,00041	0,00273	0,00039	0,52313	3,15776	40,68 ± 0,92	96,13%	93,9
97M0020L	s2	0,00027	0,01144	0,00012	0,14941	0,66415	27,59 ± 2,50	88,20%	6,4
97M0020N	s2	0,00047	0,00000	0,00025	0,14287	0,73538	29,44 ± 2,86	81,31%	17467,2
97M0020O	s1	0,00057	0,00000	0,00009	0,34056	2,87818	55,57 ± 1,06	94,17%	41618,5
97M0020P	s1	0,00012	0,00000	0,00011	0,25685	1,30157	34,60 ± 1,70	97,20%	31376,0
97M0020Q	s2	0,00048	0,02249	0,00000	0,24236	1,54908	40,75 ± 1,60	90,93%	5,3
97M0023B	s1	0,00006	0,00000	0,00008	0,32336	2,67024	53,51 ± 1,24	99,32%	NoCa
97M0023C	s1-2	0,00051	0,00000	0,00015	0,30996	2,49218	49,34 ± 1,06	93,95%	35151,2
97M0023D	s1-2	0,00031	0,00000	0,00015	0,18201	1,11137	36,74 ± 2,56	91,79%	20630,1
97M0023E	s2	0,00035	0,00000	-0,00010	0,27573	1,58235	35,21 ± 1,34	93,55%	31231,2

Irradiation values

J(0020)	0,003930	J(0023)	0,003670
sd-J(1s)	0,000020	sd-J(1s)	0,000018

Sample Number = **Spot Fusion VU17-OS151** Irradiation Number = VU17
Material = white mica (aggregate) Location = W-Ossa

Datafile	fabric	$^{36}Ar(a)$	^{37}Ar	^{38}Ar	$^{39}Ar(K)$	$^{40}Ar(a+r)$	Age ± 2σ	$^{40}Ar(r)$	K/Ca
97M0350B	S1	0,00019	0,00000	0,00005	0,05363	0,58541	60,27 ± 5,78	90,46%	NoCa
97M0350C	S1	0,00000	0,00023	-0,00005	0,02568	0,27888	66,16 ± 15,02	99,99%	53,91
97M0350D	S1	0,00002	0,00023	-0,00006	0,00461	0,04821	58,02 ± 81,56	90,78%	9,67
97M0350F	S1	0,00000	0,00023	-0,00007	0,01042	0,09464	55,29 ± 39,94	99,61%	21,84
97M0350G	S1	0,00005	0,05553	-0,00006	0,00490	0,05260	45,63 ± 58,25	69,35%	0,04
97M0350H	S1	0,00000	0,00023	-0,00002	0,01389	0,15140	66,42 ± 19,99	99,98%	29,06
97M0350I	S1	0,00000	0,14073	0,00010	0,02848	0,24670	52,97 ± 13,23	99,99%	0,10
97M0350K	S1	0,00010	0,00023	0,00007	0,00572	0,08549	61,04 ± 51,10	66,93%	11,95
97M0350L	clast	0,00009	0,00023	0,00003	0,02279	0,67921	169,37 ± 15,26	95,98%	47,60
97M0350M	S1	0,00003	0,00023	0,00005	0,03609	0,33458	55,23 ± 9,10	97,49%	75,37
97M0350N	S1	0,00010	0,00023	0,00003	0,02584	0,31714	68,10 ± 12,04	91,10%	53,93
97M0350Q	S2	0,00001	0,17302	0,00004	0,15045	1,27903	51,91 ± 2,40	99,81%	0,43
97M0350R	S2	0,00000	0,03430	-0,00005	0,02741	0,29914	66,49 ± 10,33	99,99%	0,39
97M0350S	S2	0,00007	0,00024	0,00005	0,15216	1,26766	50,14 ± 2,71	98,32%	313,01
97M0350U	S2	0,00006	0,00024	-0,00007	0,15799	1,60060	61,14 ± 1,77	98,89%	324,62
97M0350V	S2	0,00000	0,23058	0,00009	0,18458	1,40939	46,78 ± 1,57	99,99%	0,39
97M0350W	S2	0,00020	0,42454	-0,00027	0,36835	2,97466	48,45 ± 1,05	97,96%	0,43
97M0350X	S2	0,00005	0,53327	-0,00029	0,14443	1,64549	68,78 ± 2,75	99,15%	0,13

Irradiation values

J	0,003440
sd-J(1s)	0,000017

Sample Number = **Spot Fusion VU17-OS152** Irradiation Number = VU17
Material = white mica (aggregate) Location = W-Ossa

Datafile	fabric	$^{36}Ar(a)$	^{37}Ar	^{38}Ar	$^{39}Ar(K)$	$^{40}Ar(a+r)$	Age ± 2σ	$^{40}Ar(r)$	K/Ca
97M0349B	S2	0,00000	0,00000	-0,00001	0,00818	0,05281	46,06 ± 48,77	99,99%	NoCa
97M0349C	clast	0,00009	0,07616	-0,00002	0,01934	0,54169	182,63 ± 23,63	94,97%	0,12
97M0349D	S1	0,00008	0,00021	0,00004	0,01128	0,14628	76,45 ± 36,83	83,32%	26,12
97M0349F	S1	0,00000	0,00021	0,00012	0,00898	0,08293	65,50 ± 51,64	99,97%	20,78
97M0349G	S1	0,00013	0,00021	-0,00002	0,01678	0,25407	90,51 ± 29,53	84,86%	38,80
97M0349H	S1	0,00000	0,12378	0,00012	0,16173	1,16690	51,39 ± 3,12	99,99%	0,64
97M0349I	S1	0,00000	0,04714	-0,00003	0,02122	0,17843	59,74 ± 20,05	99,99%	0,22
97M0349K	S1	0,00004	0,00021	-0,00004	0,00277	0,04108	77,18 ± 172,0	73,55%	6,39
97M0349L	S1	0,00000	0,00021	0,00002	0,01466	0,08215	40,02 ± 34,69	99,97%	33,83
97M0349M	S1	0,00002	0,00021	-0,00001	0,00115	0,04700	248,48 ± 400,2	90,43%	2,66
97M0349N	S1	0,00000	0,00021	0,00002	0,01990	0,14396	51,53 ± 26,11	99,98%	45,86
97M0349Q	S2	0,00000	0,46425	0,00002	0,02360	0,22793	68,47 ± 17,01	99,99%	0,02
97M0349R	S2	0,00009	0,18188	0,00006	0,01401	0,21765	95,40 ± 27,91	87,28%	0,04
97M0349S	S2	0,00000	0,00022	0,00009	0,01724	0,15090	62,14 ± 27,58	99,98%	39,17
97M0349U	S2	0,00011	0,02554	0,00007	0,01142	0,15231	73,44 ± 48,60	77,80%	0,22
97M0349V	S2	0,00000	0,26106	-0,00007	0,05669	0,72890	90,59 ± 6,79	99,99%	0,11
97M0349W	S2	0,00006	0,24664	-0,00002	0,01686	0,20591	78,97 ± 29,40	91,49%	0,03
97M0349X	clast	0,00000	0,40890	-0,00007	0,01399	0,39216	191,89 ± 31,76	100,00%	0,02
97M0349Z	S2	0,00000	0,00022	-0,00006	0,04239	0,24387	41,09 ± 21,25	99,98%	95,93
97M0349!	S2	0,00016	0,00022	-0,00001	0,00814	0,07626	26,16 ± 52,14	38,89%	18,40
97M0349@	S2	0,00012	0,00022	-0,00012	0,01638	0,15281	50,41 ± 29,41	75,83%	37,03

Irradiation values	
J	0,004005
sd-J(1s)	0,000020

CHAPTER4,alldata

Sample Number = **VU12-A5-OS001** Irradiation Number = VU12
Material = white mica,coarse fraction Location = Ossa, Greece

Datafile	$^{36}Ar(a)$	^{37}Ar	^{38}Ar	$^{39}Ar(K)$	$^{40}Ar(a+r)$	Age ± 2σ	$^{40}Ar(r)$	Fraction	K/Ca
95M0300B	0,00039	0,00000	-0,00013	0,01304	0,87921	216,76 ± 15,29	86,91%	0,72%	NoCa
95M0300C	0,00027	0,00000	0,00016	0,01782	1,31746	254,01 ± 12,90	93,87%	0,99%	8228,2
95M0300E	0,00040	0,00000	-0,00003	0,03058	2,32615	263,63 ± 8,35	94,93%	1,69%	14108,9
95M0300F	0,00042	0,00000	0,00001	0,11267	8,52774	271,72 ± 4,66	98,55%	6,24%	51964,4
95M0300H	0,00038	0,00890	0,00039	0,42817	33,65712	284,35 ± 4,31	99,67%	23,70%	23,6
95M0300I	0,00038	0,00000	0,00012	0,21834	17,28811	285,44 ± 4,67	99,35%	12,08%	94983,4
95M0300K	0,00002	0,00357	0,00032	0,24128	18,93710	284,75 ± 4,58	99,97%	13,35%	33,1
95M0300L	0,00010	0,00431	0,00024	0,23674	18,52353	283,58 ± 4,59	99,84%	13,10%	26,9
95M0300N	0,00016	0,00325	0,00013	0,17048	13,61101	288,45 ± 4,67	99,66%	9,44%	25,7
95M0300O	0,00069	0,00457	0,00019	0,16226	13,13830	288,91 ± 4,77	98,44%	8,98%	17,4
95M0300R	0,00000	0,00238	0,00007	0,03727	2,93463	285,69 ± 6,97	100,00%	2,06%	7,7
95M0300S	0,00002	0,00000	-0,00002	0,01841	1,46108	286,45 ± 13,37	99,50%	1,02%	7692,3
95M0300T	0,00001	0,00534	0,00007	0,11981	9,54275	288,67 ± 5,13	99,98%	6,63%	11,0

Irradiation values		*Results*	$^{40}*/39K$ ±2σ	Age	2σ
J	0,002179	Weighted Mean of Plateau	78,6715 ± 0,5488	285,44	4,61
sd-J(1s)	0,000017	Total Fusion	78,1397 ± 0,3248	283,66	4,70

Sample Number = **VU17-H13-OS001** Irradiation Number = VU17
Material = white mica, fine fraction Location = Ossa,Greece

Datafile	$^{36}Ar(a)$	^{37}Ar	^{38}Ar	$^{39}Ar(K)$	$^{40}Ar(a+r)$	Age ± 2σ	$^{40}Ar(r)$	Fraction	K/Ca
96M0345B	0,00002	0,00000	0,00015	0,03394	0,21747	48,73 ± 9,06	97,33%	3,34%	NoCa
96M0345C	0,00000	0,00000	-0,00002	0,04073	0,27017	51,78 ± 9,31	99,98%	4,00%	10784,3
96M0345D	0,00000	0,00000	0,00002	0,05311	0,35396	52,02 ± 6,41	99,98%	5,22%	14056,4
96M0345F	0,00000	0,00287	0,00003	0,11669	0,80394	53,76 ± 2,91	99,99%	11,47%	19,9
96M0345G	0,00003	0,00278	0,00009	0,13410	0,94184	54,33 ± 2,60	99,15%	13,18%	23,7
96M0345H	0,00001	0,00000	0,00001	0,11086	0,76473	53,52 ± 4,23	99,41%	10,90%	29303,5
96M0345J	0,00009	0,00543	-0,00014	0,19198	1,36975	54,60 ± 1,71	98,08%	18,87%	17,3
96M0345K	0,00000	0,00095	-0,00005	0,10338	0,70517	53,23 ± 4,36	99,99%	10,16%	53,5
96M0345L	0,00001	0,00271	-0,00008	0,09549	0,66166	53,72 ± 4,40	99,35%	9,39%	17,2
96M0345N	0,00028	0,00000	-0,00002	0,05936	0,51037	56,09 ± 6,05	83,65%	5,84%	15658,3
96M0345O	0,00048	0,00404	-0,00008	0,07751	0,69859	56,04 ± 3,67	79,74%	7,62%	9,4

Irradiation values		Results	$^{40}*/^{39}K$ ±2σ	Age	2σ
J	0,004390	Weighted Mean of Plateau	6,9472 ± 0,3538	54,20	2,77
sd-J(1s)	0,000021	Total Fusion	6,9058 ± 0,2547	53,88	3,90

Sample Number = **OS003-VU12-A6** Irradiation Number = VU12
Material = white mica, fine fraction Location = Ossa, Greece

Datafile	$^{36}Ar(a)$	^{37}Ar	^{38}Ar	$^{39}Ar(K)$	$^{40}Ar(a+r)$	Age ± 2σ	$^{40}Ar(r)$	Fraction	K/Ca
95M0304A	0,00000	0,00000	0,00015	0,01160	0,17143	57,19 ± 20,35	99,99%	0,96%	NoCa
95M0304B	0,00000	0,00461	0,00020	0,01126	0,14423	49,67 ± 24,50	99,99%	0,94%	1,2
95M0304D	0,00000	0,00000	0,00023	0,01522	0,18940	48,01 ± 16,57	99,43%	1,27%	6344,3
95M0304G	0,00017	0,00000	0,00033	0,15482	1,84290	44,96 ± 1,71	97,28%	12,88%	64491,9
95M0304H	0,00021	0,00000	0,00016	0,22923	2,74181	45,39 ± 1,36	97,76%	19,06%	95450,2
95M0304J	0,00017	0,00079	0,00016	0,26698	3,16924	45,34 ± 1,34	98,38%	22,20%	166,6
95M0304K	0,00009	0,00000	0,00040	0,29424	3,49617	45,76 ± 1,19	99,22%	24,47%	122388
95M0304M	0,00000	0,00000	0,00006	0,05383	0,63755	45,96 ± 5,30	99,99%	4,48%	22378,1
95M0304N	0,00013	0,00000	0,00002	0,02526	0,33165	45,19 ± 10,14	88,67%	2,10%	10498,0
95M0304P	0,00016	0,00000	0,00005	0,06196	0,77248	45,36 ± 3,78	93,72%	5,15%	25729,2
95M0304Q	0,00006	0,00285	-0,00002	0,07805	0,96175	46,95 ± 3,83	98,18%	6,49%	13,4

Irradiation values		Results	$^{40}*/^{39}K$ ±2σ	Age	2σ
J	0,002179	Weighted Mean of Plateau	11,7104 ± 0,2973	45,46	1,35
sd-J(1σ)	0,000017	Total Fusion	11,7801 ± 0,3155	45,72	2,50

Sample Number = **OS004-VU12-A7** Irradiation Number = VU12

Material = white mica, coarse fraction Location = Ossa, Greece

Datafile	$^{36}Ar(a)$	^{37}Ar	^{38}Ar	$^{39}Ar(K)$	$^{40}Ar(a+r)$	Age ± 2σ	$^{40}Ar(r)$	Fraction	K/Ca
95M0288B	0,00020	0,00000	0,00005	0,01030	0,30096	89,84 ± 20,58	80,17%	0,91%	NoCa
95M0288C	0,00000	0,00049	0,00010	0,01246	0,33815	103,65 ± 17,12	100,00%	1,10%	12,5
95M0288E	0,00027	0,00036	0,00020	0,03234	0,89064	95,82 ± 9,60	90,90%	2,85%	44,3
95M0288F	0,00000	0,00000	0,00008	0,06411	1,91844	113,96 ± 3,96	100,00%	5,65%	NoCa
95M0288H	0,00023	0,00000	0,00012	0,12200	3,62251	111,00 ± 2,88	98,08%	10,76%	NoCa
95M0288I	0,00006	0,00000	0,00008	0,11744	3,31681	107,17 ± 2,57	99,45%	10,36%	NoCa
95M0288L	0,00009	0,00000	0,00015	0,10394	2,91504	106,06 ± 3,12	99,08%	9,17%	NoCa
95M0288M	0,00023	0,00000	0,00016	0,11411	3,00399	98,41 ± 2,63	97,73%	10,06%	NoCa
95M0288P	0,00267	0,00000	0,00011	0,12587	4,34815	107,83 ± 2,74	81,83%	11,10%	NoCa
95M0288Q	0,00016	0,00000	0,00013	0,04974	1,45497	107,88 ± 5,40	96,68%	4,39%	NoCa
95M0288S	0,00515	0,00000	0,00019	0,14323	5,57967	108,07 ± 2,83	72,72%	12,63%	NoCa
95M0288T	0,00036	0,00000	0,00017	0,09416	2,66841	103,88 ± 3,03	95,98%	8,30%	NoCa
95M0288X	0,00014	0,00070	0,00000	0,11577	3,37113	109,65 ± 2,42	98,75%	10,21%	81,6
95M0288Y	0,00000	0,00249	-0,00003	0,01100	0,32001	110,92 ± 16,93	100,00%	0,97%	2,2
95M0288Z	0,00000	0,00092	-0,00011	0,01739	0,50130	109,87 ± 11,06	100,00%	1,53%	9,2

Irradiation values		Results	$40^*/39K$ ±2σ	Age	2σ
J	0,002179	Weighted Mean of Plateau	28,2899 ± 0,7355	107,92	3,20
sd-J(1σ)	0,000017	Total Fusion	27,9732 ± 0,4332	106,74	3,60

Sample Number = **VU17-H14-OS004** Irradiation Number = VU17

Material = white mica, fine fraction Location = Ossa, Greece

Datafile	$^{36}Ar(a)$	^{37}Ar	^{38}Ar	$^{39}Ar(K)$	$^{40}Ar(a+r)$	Age ± 2σ	$^{40}Ar(r)$	Fraction	K/Ca
96M0346B	0,00037	0,00000	-0,00003	0,06693	0,73245	72,19 ± 6,64	84,98%	6,41%	NoCa
96M0346C	0,00009	0,00020	-0,00015	0,11827	1,31166	84,16 ± 3,30	98,08%	11,33%	282,9
96M0346D	0,00020	0,00037	-0,00008	0,18224	2,05488	84,77 ± 2,33	97,18%	17,45%	238,9
96M0346F	0,00006	0,00132	-0,00012	0,10534	1,18127	85,42 ± 3,53	98,49%	10,09%	39,1
96M0346G	0,00002	0,00000	-0,00012	0,06672	0,73912	84,94 ± 5,27	99,11%	6,39%	17292,6
96M0346H	0,00010	0,00071	-0,00003	0,10348	1,16511	84,86 ± 3,35	97,44%	9,91%	71,0
96M0346J	0,00000	0,00000	-0,00006	0,15449	1,64513	82,42 ± 4,11	99,99%	14,80%	39996,0
96M0346K	0,00004	0,00000	-0,00023	0,12745	1,30601	78,72 ± 3,63	99,13%	12,21%	32984,6
96M0346L	0,00006	0,00103	0,00005	0,06523	0,65975	76,18 ± 7,48	97,14%	6,25%	31,1
96M0346N	0,00009	0,00601	-0,00018	0,05398	0,59810	81,88 ± 8,10	95,45%	5,17%	4,4

Irradiation values		Results	$40^*/39K$ ±2σ	Age	2σ
J	0,004390	Weighted Mean of Plateau	10,9286 ± 0,4243	84,54	3,30
sd-J(1σ)	0,000021	Total Fusion	10,6207 ± 0,2696	82,21	4,23

Sample Number = **OS005-VU12-A13**
Material = white mica, coarse fraction

Irradiation Number = VU12
Location = Ossa, Greece

Datafile	$^{36}Ar(a)$	^{37}Ar	^{38}Ar	$^{39}Ar(K)$	$^{40}Ar(a+r)$	Age ± 2σ	$^{40}Ar(r)$	Fraction	K/Ca
95M0289B	0,00179	0,00000	0,00005	0,06369	1,67372	69,25 ± 3,96	68,33%	2,08%	NoCa
95M0289C	0,00017	0,00000	-0,00014	0,08671	2,22779	96,13 ± 2,90	97,76%	2,84%	NoCa
95M0289E	0,00088	0,00203	0,00004	0,35454	10,44473	109,53 ± 1,89	97,50%	11,59%	85,6
95M0289F	0,00066	0,00170	0,00020	0,55494	16,71595	113,39 ± 1,86	98,83%	18,15%	159,8
95M0289H	0,00578	0,00331	0,00044	0,79055	24,57964	110,29 ± 1,81	93,05%	25,85%	117,1
95M0289I	0,00041	0,00000	-0,00014	0,17553	4,99237	105,90 ± 2,03	97,55%	5,74%	NoCa
95M0289K	0,00060	0,00000	0,00017	0,22999	6,61521	106,79 ± 2,05	97,30%	7,52%	NoCa
95M0289L	0,00021	0,00000	0,00002	0,27324	7,85275	108,72 ± 1,91	99,19%	8,94%	NoCa
95M0289N	0,00013	0,00000	0,00000	0,16190	4,76163	111,21 ± 2,26	99,21%	5,29%	NoCa
95M0289O	0,00023	0,00000	0,00009	0,13075	3,89391	111,47 ± 2,48	98,22%	4,28%	NoCa
95M0289S	0,00015	0,00000	0,00013	0,23619	7,02928	112,68 ± 2,02	99,38%	7,72%	NoCa

Irradiation values		Results	$^{40}*/39K$ ±2σ	Age	2σ
J	0,002179	Weighted Mean of Plateau	28,9907 ± 0,2402	110,51	1,93
sd-J(1s)	0,000017	Total Fusion	28,6228 ± 0,1301	109,15	1,86

Sample Number = **VU12-A9-OS005**
Material = biotite

Irradiation Number= VU12
Location = Ossa, Greece

Datafile	$^{36}Ar(a)$	^{37}Ar	^{38}Ar	$^{39}Ar(K)$	$^{40}Ar(a+r)$	Age ± 2σ	$^{40}Ar(r)$	Fraction	K/Ca
95M0290C	0,00320	0,00000	0,00025	0,02295	1,06533	20,60 ± 13,80	11,36%	1,06%	NoCa
95M0290D	0,00669	0,00000	0,00020	0,05254	2,31628	25,24 ± 6,85	14,67%	2,42%	NoCa
95M0290F	0,00527	0,00000	0,00007	0,06665	2,38240	47,94 ± 4,05	34,57%	3,07%	NoCa
95M0290G	0,00424	0,00000	0,00016	0,06759	2,32173	61,07 ± 4,43	46,00%	3,12%	NoCa
95M0290I	0,00627	0,00000	0,00003	0,12691	4,14192	69,51 ± 2,31	55,23%	5,85%	NoCa
95M0290J	0,00541	0,00000	0,00007	0,13854	4,37231	77,05 ± 2,38	63,45%	6,39%	NoCa
95M0290L	0,00380	0,00268	-0,00008	0,11519	3,49858	79,30 ± 2,52	67,90%	5,31%	21,1
95M0290M	0,00327	0,00252	-0,00010	0,11679	3,49850	83,27 ± 3,05	72,37%	5,38%	22,7
95M0290O	0,00289	0,00216	0,00002	0,10040	2,98439	81,52 ± 3,71	71,36%	4,63%	22,8
95M0290P	0,00230	0,00078	0,00003	0,08800	2,62506	84,88 ± 3,12	74,11%	4,06%	55,0
95M0290R	0,00282	0,00341	-0,00009	0,09384	2,81829	81,28 ± 3,26	70,42%	4,33%	13,5
95M0290S	0,00348	0,00421	-0,00003	0,10854	3,26913	79,41 ± 2,80	68,56%	5,00%	12,6
95M0290U	0,01348	0,00361	0,00008	0,37577	11,87400	80,71 ± 1,55	66,45%	17,32%	51,1
95M0290V	0,00537	0,00396	0,00002	0,13894	4,41287	78,25 ± 2,28	64,05%	6,40%	17,2
95M0290X	0,00302	0,00396	0,00003	0,08620	2,66728	79,18 ± 3,45	66,54%	3,97%	10,7
95M0290Y	0,00326	0,00603	-0,00006	0,09368	2,89550	79,35 ± 3,23	66,76%	4,32%	7,6
95M0290Z	0,01290	0,00475	0,00006	0,37709	11,90657	82,47 ± 1,61	67,98%	17,38%	38,9

Irradiation values		Results	$^{40}*/39K$ ±2σ	Age	2σ
J	0,002179	Weighted Mean of Plateau	21,0334 ± 0,4690	80,85	2,17
sd-J(1σ)	0,000017	Total Fusion	19,8847 ± 0,2982	76,52	2,50

Sample Number = **VU12-C9-OS024** Irradiation Number = VU12
Material = white mica, coarse fraction Location = Ossa, Greece

Datafile	$^{36}Ar(a)$	^{37}Ar	^{38}Ar	$^{39}Ar(K)$	$^{40}Ar(a+r)$	Age ± 2σ	$^{40}Ar(r)$	Fraction	K/Ca
96M0067B	0,00060	0,00000	0,00007	0,01393	0,78842	170,98 ± 22,95	77,33%	0,52%	NoCa
96M0067C	0,00063	0,00000	-0,00003	0,02856	1,79715	217,41 ± 12,52	89,62%	1,07%	2933,4
96M0067E	0,00100	0,01387	0,00018	0,18641	13,18075	263,06 ± 3,05	97,76%	6,96%	6,6
96M0067F	0,00068	0,05152	0,00041	0,66981	50,59373	284,57 ± 3,11	99,60%	24,99%	6,4
96M0067G	0,00052	0,10115	0,00060	0,60617	46,80776	290,61 ± 2,98	99,67%	22,62%	2,9
96M0067I	0,00010	0,02258	0,00030	0,25393	19,45332	288,98 ± 3,50	99,85%	9,48%	5,5
96M0067J	0,00032	0,00620	0,00035	0,10754	8,52791	295,71 ± 3,99	98,90%	4,01%	8,5
96M0067L	0,00034	0,02272	0,00026	0,29597	23,85515	302,06 ± 3,44	99,58%	11,04%	6,4
96M0067M	0,00006	0,00412	0,00019	0,08536	6,81352	299,81 ± 4,86	99,73%	3,19%	10,2
96M0067N	0,00001	0,01075	0,00022	0,11960	9,54428	300,37 ± 4,10	99,96%	4,46%	5,5
96M0067O	0,00013	0,13124	0,00059	0,31257	24,48524	294,96 ± 2,99	99,84%	11,66%	1,2

Irradiation values		Results	40*/39K ±2σ	Age	2σ
J	0,002271	Weighted Mean of Plateau	77,6145 ± 0,5308	292,88	3,28
sd-J(1σ)	0,000011	Fusion	76,3280 ± 0,2746	288,39	3,30

Sample Number = **VU12-C14-OS026** Irradiation Number = VU12
Material = white mica, coarse fraction Location = Ossa, Greece

Datafile	$^{36}Ar(a)$	^{37}Ar	^{38}Ar	$^{39}Ar(K)$	$^{40}Ar(a+r)$	Age ± 2σ	$^{40}Ar(r)$	Fraction	K/Ca
96M0081A	0,00124	0,00000	0,00033	0,06476	2,11588	107,45 ± 5,01	82,70%	4,47%	NoCa
96M0081B	0,00061	0,00300	0,00023	0,19041	5,66022	114,24 ± 2,04	96,83%	13,14%	31,1
96M0081D	0,00044	0,00001	0,00015	0,40950	12,34680	118,26 ± 1,52	98,94%	28,25%	36380,6
96M0081E	0,00033	0,00001	0,00020	0,28537	8,52529	117,11 ± 1,61	98,85%	19,69%	25344,4
96M0081F	0,00033	0,00101	0,00004	0,14764	4,26391	112,10 ± 2,41	97,74%	10,18%	71,7
96M0081J	0,00011	0,00001	-0,00006	0,03061	0,87947	109,99 ± 10,15	96,35%	2,11%	2532,8
96M0081K	0,00000	0,00504	-0,00007	0,04546	1,29652	113,21 ± 7,36	100,00%	3,14%	4,4
96M0081M	0,00000	0,00727	0,00007	0,16719	4,76580	113,17 ± 2,42	100,00%	11,53%	11,3
96M0081N	0,00000	0,00001	0,00043	0,05981	1,68222	111,70 ± 4,91	100,00%	4,13%	4942,4
96M0081O	0,00000	0,00300	0,00024	0,04888	1,35847	110,41 ± 7,38	100,00%	3,37%	8,0

Irradiation values		Results	40*/39K ±2σ	Age	2σ
J	0,002271	Weighted Mean of Plateau	29,3070 ± 0,4819	116,25	2,17
sd-J(1σ)	0,000011	Tota lFusion	28,9678 ± 0,2983	114,94	2,21

Sample Number = **VU12-C16-OS029** Irradiation Number = VU12
Material = white mica, coarse fraction Location = Ossa, Greece

Datafile	$^{36}Ar(a)$	^{37}Ar	^{38}Ar	$^{39}Ar(K)$	$^{40}Ar(a+r)$	Age ± 2σ	$^{40}Ar(r)$	Fraction	K/Ca
96M0088A	0,00064	0,00000	-0,00015	0,04361	1,53518	122,29 ± 9,05	87,72%	1,47%	NoCa
96M0088B	0,00010	0,00201	0,00002	0,08570	2,67472	122,22 ± 4,65	98,90%	2,90%	20,8
96M0088C	0,00074	0,03918	0,00007	0,99105	31,90258	126,45 ± 1,40	99,31%	33,48%	12,4
96M0088E	0,00084	0,07611	0,00010	0,50516	15,73256	121,40 ± 2,55	98,42%	17,07%	3,3
96M0088F	0,00006	0,00001	-0,00001	0,40970	13,17727	127,02 ± 1,68	99,86%	13,84%	33763,8
96M0088G	0,00017	0,00973	0,00004	0,43833	14,08718	126,66 ± 1,63	99,65%	14,81%	22,1
96M0088I	0,00007	0,00211	0,00000	0,09161	2,89165	124,10 ± 4,65	99,33%	3,09%	21,3
96M0088J	0,00022	0,00760	-0,00008	0,20802	6,25447	117,97 ± 2,30	98,97%	7,03%	13,4
96M0088L	0,00005	0,00001	0,00017	0,05957	1,79066	118,18 ± 6,40	99,17%	2,01%	4898,9
96M0088M	0,00025	0,01559	-0,00004	0,12742	3,89593	118,90 ± 3,44	98,11%	4,30%	4,0

Irradiation values		Results	40*/39K ±2σ	Age	2σ
J	0,002271	Weighted Mean of Plateau	31,9224 ± 0,3426	124,40	2,90
sd-J(1σ)	0,000011	Total Fusion	31,4232 ± 0,2234	124,36	2,94

Sample Number = **VU17-E2-OS030**
Material = white mica, coarse fraction

Irradiation Number = VU12
Location = Ossa, Greece

Datafile	$^{36}Ar(a)$	^{37}Ar	^{38}Ar	$^{39}Ar(K)$	$^{40}Ar(a+r)$	Age ± 2σ	$^{40}Ar(r)$	Fraction	K/Ca
96M0351A	0,00055	0,00000	-0,00009	0,04624	0,73639	96,46 ± 9,94	78,06%	3,35%	NoCa
96M0351B	0,00016	0,00000	-0,00001	0,04715	0,66271	101,17 ± 11,42	92,89%	3,42%	10630,6
96M0351D	0,00027	0,00145	0,00009	0,14985	2,07719	103,27 ± 2,68	96,19%	10,86%	50,6
96M0351E	0,00023	0,00000	0,00009	0,21278	2,88300	102,53 ± 2,07	97,68%	15,42%	47925,8
96M0351F	0,00000	0,00000	0,00002	0,12334	1,60299	100,72 ± 3,56	99,99%	8,94%	27771,5
96M0351H	0,00011	0,00000	0,00005	0,16999	2,28025	102,43 ± 2,50	98,57%	12,32%	38252,8
96M0351I	0,00012	0,00000	0,00009	0,14539	1,97700	103,41 ± 2,58	98,20%	10,54%	32706,1
96M0351J	0,00008	0,00000	0,00008	0,12850	1,73154	102,91 ± 2,73	98,60%	9,31%	28896,3
96M0351L	0,00000	0,00001	0,00003	0,15627	2,06095	102,16 ± 2,57	99,99%	11,33%	5659,3
96M0351M	0,00005	0,00000	0,00003	0,19999	2,65235	102,13 ± 1,88	99,39%	14,50%	44933,2

Irradiation values		Results	$^{40}*/^{39}K$ ±2σ	Age	2σ
J	0,004418	Weighted Mean of Plateau	13,2321 ± 0,3253	102,50	2,45
sd-J(1σ)	0,000003	Tota lFusion	13,1945 ± 0,2018	102,21	3,06

Sample Number = **VU17-E3-OS030**
Material = relic biotite

Irradiation Number = VU17
Location = Ossa, Greece

Datafile	$^{36}Ar(a)$	^{37}Ar	^{38}Ar	$^{39}Ar(K)$	$^{40}Ar(a+r)$	Age ± 2σ	$^{40}Ar(r)$	Fraction	K/Ca
96M0352B	0,00136	0,00000	0,00000	0,05946	0,50409	13,81 ± 9,57	20,52%	9,65%	NoCa
96M0352C	0,00056	0,00000	-0,00010	0,03224	0,29649	32,33 ± 16,46	44,49%	5,23%	7152,6
96M0352D	0,00250	0,00000	-0,00002	0,17372	1,88936	52,07 ± 2,92	60,94%	28,20%	38532,1
96M0352F	0,00119	0,00260	0,00000	0,08114	1,13795	75,73 ± 5,18	69,19%	13,17%	15,3
96M0352G	0,00047	0,00051	0,00001	0,03102	0,47286	84,05 ± 15,19	70,82%	5,04%	29,7
96M0352H	0,00063	0,00218	0,00006	0,04986	0,79978	95,67 ± 11,77	76,84%	8,09%	11,2
96M0352J	0,00043	0,00280	-0,00003	0,03466	0,51240	86,82 ± 18,65	75,48%	5,63%	6,1
96M0352K	0,00188	0,00501	0,00020	0,15384	2,37388	91,76 ± 3,76	76,53%	24,98%	15,1

Irradiation values		Results	$^{40}*/^{39}K$ ±2σ	Age	2σ
J	0,004418	Weighted Mean of Plateau	11,8332 ± 0,8038	91,93	6,09
sd-J(1σ)	0,000003	Total Fusion	8,6489 ± 0,4539	67,65	6,98

Sample Number = **VU17-E7-OS106**
Material = white mica,coarse fraction

Irradiation Number = VU17
Location = Ossa, Greece

Datafile	$^{36}Ar(a)$	^{37}Ar	^{38}Ar	$^{39}Ar(K)$	$^{40}Ar(a+r)$	Age ± 2σ	$^{40}Ar(r)$	Fraction	K/Ca
96M0353B	0,00044	0,00000	-0,00007	0,01931	0,31107	73,55 ± 23,05	58,46%	1,14%	NoCa
96M0353C	0,00000	0,00000	-0,00001	0,01257	0,16234	100,12 ± 40,55	99,98%	0,74%	2677,3
96M0353D	0,00005	0,00131	-0,00002	0,01768	0,22752	93,91 ± 30,98	93,96%	1,05%	6,6
96M0353F	0,00007	0,00794	-0,00025	0,14698	2,19300	114,15 ± 3,59	99,08%	8,71%	9,1
96M0353G	0,00009	0,00363	-0,00004	0,17564	2,57933	112,23 ± 3,25	98,93%	10,41%	23,7
96M0353H	0,00052	0,00211	-0,00080	0,87536	13,39246	116,69 ± 0,64	98,85%	51,88%	203,0
96M0353J	0,00001	0,00039	-0,00009	0,30195	4,46266	114,01 ± 1,87	99,90%	17,89%	384,1
96M0353K	0,00009	0,00000	0,00007	0,13795	2,05232	113,34 ± 4,94	98,64%	8,18%	29320,4

Irradiation values		Results	$^{40}*/^{39}K$ ±2σ	Age	2σ
J	0,004418	Weighted Mean of Plateau	15,0578 ± 0,1695	116,19	1,28
sd-J(1σ)	0,000003	Fusion	14,8181 ± 0,1717	114,40	2,58

Sample Number = **VU17-E12-OS109** Irradiation Number = VU17
Material = white mica,coarse fraction Location = Ossa, Greece

Datafile	$^{36}Ar(a)$	^{37}Ar	^{38}Ar	$^{39}Ar(K)$	$^{40}Ar(a+r)$	Age ± 2σ	$^{40}Ar(r)$	Fraction	K/Ca
96M0354A	0,00030	0,00000	0,00005	0,00709	0,13985	57,96 ± 78,67	37,44%	0,85%	NoCa
96M0354B	0,00041	0,00000	-0,00004	0,00444	0,16746	79,77 ± 146,2	27,11%	0,53%	942,1
96M0354C	0,00075	0,00000	0,00011	0,02267	0,42540	70,22 ± 25,37	47,88%	2,72%	4812,7
96M0354E	0,00026	0,00000	-0,00013	0,09014	1,18164	95,06 ± 6,26	93,42%	10,83%	19123,7
96M0354F	0,00035	0,00000	0,00007	0,25581	3,37380	99,09 ± 2,35	96,90%	30,72%	54252,6
96M0354G	0,00012	0,00199	0,00010	0,17038	2,22571	99,67 ± 3,88	98,42%	20,46%	41,9
96M0354I	0,00004	0,00164	0,00015	0,10871	1,42551	100,75 ± 5,85	99,13%	13,06%	32,6
96M0354J	0,00013	0,00286	0,00015	0,17338	2,25335	99,00 ± 3,62	98,24%	20,82%	29,7

Irradiation values		Results	40*/39K ±2σ	Age	2σ
J	0,004418	Weighted Mean of Plateau	12,8103 ± 0,4461	99,32	3,37
sd-J(1σ)	0,000003	Total Fusion	12,6016 ± 0,3843	97,74	5,80

Sample Number = **VU17-F7-OS138** Irradiation Number = VU17
Material = white mica, fine fraction Location = Ossa,Greece

Datafile	$^{36}Ar(a)$	^{37}Ar	^{38}Ar	$^{39}Ar(K)$	$^{40}Ar(a+r)$	Age ± 2σ	$^{40}Ar(r)$	Fraction	K/Ca
97M0009B	0,00340	0,00000	-0,00004	0,12637	1,51286	31,44 ± 4,33	33,59%	11,31%	NoCa
97M0009C	0,00141	0,00800	0,00017	0,09213	0,93897	44,06 ± 3,69	55,49%	8,24%	5,6
97M0009E	0,00094	0,01117	0,00002	0,07522	0,74257	48,08 ± 5,08	62,58%	6,73%	3,3
97M0009F	0,00134	0,00887	-0,00002	0,07607	0,88764	50,33 ± 6,30	55,47%	6,81%	4,2
97M0009H	0,00130	0,00635	0,00002	0,08985	0,99390	52,76 ± 5,56	61,37%	8,04%	6,9
97M0009I	0,00098	0,00775	-0,00017	0,09921	0,96715	52,96 ± 5,03	69,91%	8,88%	6,3
97M0009J	0,00068	0,00000	-0,00005	0,07526	0,70767	52,23 ± 6,02	71,47%	6,73%	11456,7
97M0009L	0,00081	0,01248	-0,00006	0,09918	0,93693	54,72 ± 3,67	74,57%	8,87%	3,9
97M0009M	0,00081	0,01326	-0,00011	0,13575	1,18624	54,14 ± 3,94	79,76%	12,14%	5,0
97M0009N	0,00129	0,03977	0,00000	0,24877	2,09638	53,55 ± 2,39	81,79%	22,26%	3,1

Irradiation values		Results	40*/39K ±2σ	Age	2σ
J	0,004371	Weighted Mean of Plateau	6,9063 ± 0,4267	53,65	3,59
sd-J(1σ)	0,000062	Total Fusion	6,3859 ± 0,2520	49,67	3,98

Sample Number = **VU17-F18-OS146** Irradiation Number = VU17
Material = white mica, coarse fraction Location = Ossa, Greece

Datafile	$^{36}Ar(a)$	^{37}Ar	^{38}Ar	$^{39}Ar(K)$	$^{40}Ar(a+r)$	Age ± 2σ	$^{40}Ar(r)$	Fraction	K/Ca
97M0012A	0,00036	0,00000	-0,00003	0,01951	0,33387	89,58 ± 25,40	68,04%	2,46%	NoCa
97M0012B	0,00004	0,00000	0,00003	0,03155	0,45296	107,07 ± 15,46	97,42%	3,99%	4700,7
97M0012C	0,00026	0,00000	-0,00001	0,17670	2,77460	116,61 ± 3,93	97,28%	22,32%	26319,9
97M0012E	0,00012	0,00000	0,00003	0,23545	3,56612	114,52 ± 3,68	98,99%	29,75%	35049,8
97M0012F	0,00013	0,00000	0,00014	0,10500	1,61868	114,89 ± 5,09	97,58%	13,27%	15626,1
97M0012G	0,00030	0,00451	-0,00002	0,16653	2,59111	114,77 ± 3,95	96,58%	21,04%	18,1
97M0012I	0,00016	0,01454	0,00017	0,05676	0,89017	113,49 ± 7,24	94,71%	7,17%	1,9

Irradiation values		Results	40*/39K ±2σ	Age	2σ
J	0,004371	Weighted Mean of Plateau	15,0757 ± 0,3538	115,13	4,11
sd-J(1σ)	0,000062	Total Fusion	14,9379 ± 0,2553	114,11	5,01

Sample Number = **VU17-G3-OS146** Irradiation Number = VU17
Material = white mica, fine fraction Location = Ossa, Greece

Datafile	$^{36}Ar(a)$	^{37}Ar	^{38}Ar	$^{39}Ar(K)$	$^{40}Ar(a+r)$	Age ± 2σ	$^{40}Ar(r)$	Fraction	K/Ca
97M0043A	0,00922	0,00000	0,00019	0,35631	4,88156	46,17 ± 1,46	44,20%	7,35%	NoCa
97M0043B	0,00421	0,00898	0,00012	0,26074	2,97924	50,63 ± 1,84	58,19%	5,38%	14,2
97M0043C	0,00506	0,01195	0,00022	0,49636	5,15837	56,09 ± 1,01	70,99%	10,24%	20,4
97M0043E	0,00344	0,00436	0,00011	0,43244	4,17901	55,61 ± 1,20	75,68%	8,92%	48,6
97M0043F	0,00404	0,01066	0,00015	0,51939	4,92202	54,57 ± 1,82	75,71%	10,72%	23,9
97M0043G	0,00525	0,00067	0,00005	0,79097	7,25455	54,84 ± 1,67	78,62%	16,32%	580,1
97M0043I	0,00409	0,01113	-0,00007	0,75285	6,69862	55,46 ± 1,61	81,96%	15,54%	33,2
97M0043J	0,00324	0,00366	0,00001	0,58627	5,20407	55,10 ± 1,68	81,62%	12,10%	78,5
97M0043K	0,00724	0,06602	-0,00003	0,65034	6,96417	56,40 ± 1,77	69,28%	13,42%	4,8

Irradiation values		Results	$^{40}*/^{39}K$ ±2σ	Age	2σ
J	0,004280	Weighted Mean of Plateau	7,2863 ± 0,1105	55,40	1,70
sd-J(1σ)	0,000001	Total Fusion	7,1636 ± 0,0633	54,48	1,80

Sample Number = **VU17-G4-OS149** Irradiation Number = VU17
Material = white mica, coarse fraction Location = Ossa, Greece

Datafile	$^{36}Ar(a)$	^{37}Ar	^{38}Ar	$^{39}Ar(K)$	$^{40}Ar(a+r)$	Age ± 2σ	$^{40}Ar(r)$	Fraction	K/Ca
97M0049A	0,00026	0,00000	-0,00001	0,03194	0,44305	86,73 ± 17,38	82,94%	2,54%	NoCa
97M0049C	0,00019	0,01019	-0,00020	0,23096	3,31670	105,80 ± 3,55	98,26%	18,35%	11,1
97M0049D	0,00015	0,00662	-0,00008	0,22856	3,27918	106,14 ± 3,45	98,68%	18,16%	16,9
97M0049F	0,00021	0,00319	-0,00018	0,33217	4,53409	101,08 ± 3,11	98,63%	26,40%	51,1
97M0049G	0,00008	0,00001	0,00005	0,26779	3,74384	104,19 ± 3,34	99,35%	21,28%	23850,1
97M0049H	0,00019	0,00358	-0,00016	0,16692	2,32958	102,26 ± 3,99	97,62%	13,26%	22,9

Irradiation values		Results	$^{40}*/^{39}K$ ±2σ	Age	2σ
J	0,004280	Weighted Mean of Plateau	13,8158 ± 0,2662	103,64	3,39
sd-J(1σ)	0,000059	Total Fusion	13,7716 ± 0,1615	103,32	3,60

Sample Number = **VU17-G8-OS149** Irradiation Number = VU17
Material = white mica, fine fraction Location = Ossa, Greece

Datafile	$^{36}Ar(a)$	^{37}Ar	^{38}Ar	$^{39}Ar(K)$	$^{40}Ar(a+r)$	Age ± 2σ	$^{40}Ar(r)$	Fraction	K/Ca
97M0044B	0,00030	0,00000	0,00005	0,03409	0,31070	49,90 ± 11,92	71,89%	4,49%	NoCa
97M0044C	0,00022	0,00760	-0,00021	0,03659	0,30895	50,85 ± 10,95	79,10%	4,82%	2,4
97M0044D	0,00015	0,00042	-0,00009	0,07848	0,59254	53,04 ± 6,56	92,31%	10,34%	92,3
97M0044F	0,00012	0,00001	-0,00001	0,11380	0,84298	53,97 ± 5,45	95,77%	15,00%	10594,5
97M0044G	0,00008	0,00912	-0,00006	0,09023	0,68089	55,28 ± 5,20	96,33%	11,89%	4,8
97M0044H	0,00015	0,00398	-0,00017	0,16811	1,28660	56,14 ± 3,05	96,48%	22,16%	20,7
97M0044J	0,00018	0,00775	0,00003	0,12388	0,95129	55,10 ± 3,90	94,35%	16,33%	7,8
97M0044K	0,00040	0,01847	0,00011	0,11354	0,96269	56,59 ± 5,53	87,80%	14,96%	3,0

Irradiation values		Results	$^{40}*/^{39}K$ ±2σ	Age	2σ
J	0,004280	Weighted Mean of Plateau	7,3401 ± 0,4904	55,80	3,97
sd-J(1σ)	0,000059	Total Fusion	7,1999 ± 0,3376	54,75	5,20

Sample Number = **VU17-G9-OS152** Irradiation Number = VU17
Material = white mica, coarse fraction Location = Ossa, Greece

Datafile	$^{36}Ar(a)$	^{37}Ar	^{38}Ar	$^{39}Ar(K)$	$^{40}Ar(a+r)$	Age ± 2σ	$^{40}Ar(r)$	Fraction	K/Ca
97M0046A	0,00000	0,00000	0,00006	0,00401	0,07446	138,04 ± 95,90	99,96%	0,39%	NoCa
97M0046C	0,00002	0,00001	-0,00002	0,00143	0,03040	123,70 ± 262,1	77,78%	0,14%	131,9
97M0046D	0,00031	0,00001	-0,00003	0,00930	0,28641	154,14 ± 48,03	67,67%	0,89%	859,8
97M0046E	0,00000	0,00001	-0,00001	0,02872	0,98483	247,08 ± 17,03	99,99%	2,76%	2654,0
97M0046F	0,00008	0,00001	0,00010	0,09109	3,66464	285,00 ± 8,35	99,38%	8,76%	8415,2
97M0046H	0,00005	0,00349	-0,00006	0,13755	5,40445	279,72 ± 7,72	99,73%	13,23%	19,3
97M0046I	0,00000	0,00001	0,00025	0,14568	5,75046	281,62 ± 7,75	100,00%	14,02%	13446,1
97M0046J	0,00029	0,01369	0,00020	0,62158	25,33624	289,21 ± 7,54	99,66%	59,80%	22,2

Irradiation values		Results	40*/39K ±2σ	Age	2σ
J	0,004280	Weighted Mean of Plateau	40,1250 ± 0,3656	285,92	7,68
sd-J(1σ)	0,000059	Total Fusion	39,7465 ± 0,2520	283,42	8,00

Sample Number = **VU17-G12-OS152,S1** Irradiation Number = VU17
Material = white mica, fine fraction Location = Ossa, Greece

Datafile	$^{36}Ar(a)$	^{37}Ar	^{38}Ar	$^{39}Ar(K)$	$^{40}Ar(a+r)$	Age ± 2σ	$^{40}Ar(r)$	Fraction	K/Ca
97M0045A	0,00051	0,00000	0,00016	0,21027	1,32840	42,72 ± 2,30	88,61%	10,01%	NoCa
97M0045B	0,00017	0,00330	0,00023	0,16911	1,19313	51,46 ± 2,90	95,81%	8,05%	25,1
97M0045C	0,00025	0,00094	0,00023	0,36288	3,04176	62,05 ± 2,06	97,52%	17,28%	188,7
97M0045E	0,00034	0,00768	0,00011	0,37295	3,53925	69,82 ± 2,16	97,14%	17,76%	23,8
97M0045F	0,00026	0,00991	0,00003	0,26811	2,73737	75,01 ± 2,45	97,15%	12,77%	13,3
97M0045G	0,00034	0,01487	-0,00001	0,22838	2,46003	78,09 ± 2,54	95,94%	10,87%	7,5
97M0045I	0,00025	0,00645	0,00029	0,20622	2,43682	86,37 ± 2,80	96,96%	9,82%	15,7
97M0045J	0,00038	0,05359	0,00026	0,28233	5,58777	143,85 ± 4,26	97,98%	13,44%	2,6

Irradiation values		Results	40*/39K ±2σ	Age	2σ
J	0,004280	Weighted Mean of Plateau			
sd-J(1σ)	0,000059	Total Fusion	10,2764 ± 0,1035	77,65	2,60

Sample Number = **VU17-G13-OS152,S2** Irradiation Number = VU17
Material = white mica, fine fraction Location = Ossa, Greece

Datafile	$^{36}Ar(a)$	^{37}Ar	^{38}Ar	$^{39}Ar(K)$	$^{40}Ar(a+r)$	Age ± 2σ	$^{40}Ar(r)$	Fraction	K/Ca
97M0047B	0,00105	0,00000	0,00016	0,19111	1,23253	36,84 ± 2,18	74,74%	6,52%	NoCa
97M0047C	0,00071	0,00001	0,00003	0,17608	1,27498	46,07 ± 2,14	83,44%	6,01%	16041,0
97M0047E	0,00057	0,00668	-0,00031	0,25581	2,12515	58,14 ± 2,68	92,11%	8,73%	18,8
97M0047F	0,00098	0,01315	-0,00024	0,48792	4,59596	66,88 ± 2,06	93,67%	16,64%	18,2
97M0047G	0,00029	0,00201	-0,00017	0,20730	2,25143	78,92 ± 2,84	96,19%	7,07%	50,5
97M0047I	0,00061	0,00117	-0,00013	0,43491	4,73546	79,09 ± 2,49	96,16%	14,83%	182,4
97M0047J	0,00016	0,00001	-0,00001	0,16982	1,89088	81,91 ± 3,39	97,46%	5,79%	15437,6
97M0047K	0,00086	0,00489	0,00001	0,34257	4,28834	88,73 ± 2,70	94,09%	11,69%	34,3
97M0047M	0,00170	0,03093	0,00007	0,66614	12,93452	138,63 ± 3,73	96,11%	22,72%	10,6

Irradiation values		Results	40*/39K ±2σ	Age	2σ
J	0,004280	Weighted Mean of Plateau			
sd-J(1σ)	0,000059	Total Fusion	11,3513 ± 0,0892	85,59	2,60

Sample Number = **VU17-H6-OS159** Irradiation Number = VU17

Material = white mica, coarse fraction Location = Ossa, Greece

Datafile	$^{36}Ar(a)$	^{37}Ar	^{38}Ar	$^{39}Ar(K)$	$^{40}Ar(a+r)$	Age ± 2σ	$^{40}Ar(r)$	Fraction	K/Ca
96M0332A	0,00000	0,00000	-0,00003	0,00676	0,12271	138,32 ± 122,6	100,00%	0,43%	NoCa
96M0332B	0,00001	0,00146	-0,00007	0,00720	0,22764	231,72 ± 76,11	98,73%	0,46%	2,4
96M0332C	0,00020	0,00029	-0,00019	0,01618	0,51090	208,79 ± 35,22	88,49%	1,02%	27,3
96M0332E	0,00001	0,00000	0,00002	0,02719	1,09629	293,27 ± 21,18	99,72%	1,72%	9468,3
96M0332F	0,00040	0,00000	-0,00018	0,08970	3,80969	299,52 ± 7,24	96,86%	5,68%	31228,5
96M0332G	0,00001	0,00252	-0,00026	0,04878	1,92780	288,04 ± 13,31	99,77%	3,09%	9,5
96M0332I	0,00000	0,00000	-0,00026	0,43075	16,34076	277,90 ± 3,57	100,00%	27,29%	149820
96M0332J	0,00019	0,00000	-0,00066	0,64018	24,80270	282,79 ± 3,06	99,77%	40,56%	222593
96M0332K	0,00017	0,00539	-0,00010	0,31167	12,44473	290,30 ± 3,33	99,59%	19,75%	28,3

Irradiation values		Results	$^{40}*/^{39}K$ ±2σ	Age	2σ
J	0,004390	Weighted Mean of Plateau	38,9307 ± 0,4251	284,64	3,82
sd-J(1σ)	0,000021	Total Fusion	38,6395 ± 0,2932	282,67	3,19

Sample Number = **VU17-H7-OS159** Irradiation Number = VU17

Material = white mica, fine fraction Location = Ossa, Greece

Datafile	$^{36}Ar(a)$	^{37}Ar	^{38}Ar	$^{39}Ar(K)$	$^{40}Ar(a+r)$	Age ± 2σ	$^{40}Ar(r)$	Fraction	K/Ca
96M0333B	0,00067	0,00000	0,00006	0,06110	0,36793	22,04 ± 9,18	46,49%	2,78%	NoCa
96M0333C	0,00013	0,00050	0,00025	0,04088	0,23041	36,77 ± 13,88	83,21%	1,86%	39,9
96M0333E	0,00018	0,00065	-0,00009	0,05847	0,33999	38,51 ± 9,12	84,52%	2,66%	44,1
96M0333F	0,00005	0,00000	0,00004	0,04977	0,27645	41,38 ± 8,97	95,13%	2,26%	17056,7
96M0333G	0,00011	0,00000	-0,00002	0,10434	0,62821	44,70 ± 4,79	94,89%	4,74%	35749,3
96M0333I	0,00011	0,00000	0,00015	0,11648	0,73883	47,39 ± 4,76	95,58%	5,29%	39884,5
96M0333J	0,00010	0,00000	-0,00018	0,20967	1,84832	67,40 ± 3,66	98,35%	9,53%	71773,2
96M0333K	0,00018	0,00147	-0,00010	0,31747	2,93049	70,36 ± 2,53	98,14%	14,43%	105,6
96M0333M	0,00014	0,00035	-0,00005	0,33044	2,75688	63,92 ± 2,00	98,46%	15,02%	468,7
96M0333N	0,00000	0,00000	-0,00001	0,23038	1,72274	58,27 ± 2,65	99,99%	10,47%	78736,0
96M0333O	0,00008	0,00233	-0,00034	0,28005	2,29739	63,15 ± 2,73	98,91%	12,73%	58,9
96M0333Q	0,00000	0,00291	0,00003	0,17855	1,59352	69,33 ± 3,58	99,99%	8,11%	30,1
96M0333R	0,00042	0,02461	0,00006	0,22282	3,41529	113,34 ± 3,26	96,36%	10,13%	4,4

Irradiation values		Results	$^{40}*/^{39}K$ ±2σ	Age	2σ
J	0,004390	Weighted Mean of Plateau			
sd-J(1s)	0,000021	Total Fusion	8,4095 ± 0,2363	65,40	3,60

CHAPTER5, all data

Location 1

Sample Number = **VU17-H2-AG156-coarse** Irradiation Number = VU17
Material = white mica, coarse fraction Location = Longa, Antihassia

Datafile	$^{36}Ar(a)$	^{37}Ar	^{38}Ar	$^{39}Ar(K)$	$^{40}Ar(a+r)$	Age ± 2σ	$^{40}Ar(r)$	Fraction	K/Ca
96M0330A	0,00004	0,00000	-0,00003	0,00192	0,01909	27,00 ± 191,0	34,63%	0,66%	NoCa
96M0330B	0,00001	0,00000	-0,00002	0,00117	0,02284	127,90 ± 284,4	85,63%	0,40%	431,0
96M0330D	0,00013	0,00000	-0,00006	0,00257	0,06355	72,85 ± 136,8	38,00%	0,88%	948,5
96M0330E	0,00008	0,00239	-0,00001	0,00691	0,11099	96,64 ± 52,30	77,99%	2,36%	1,4
96M0330F	0,00017	0,00022	-0,00011	0,04859	0,71270	104,86 ± 6,72	92,94%	16,60%	106,4
96M0330H	0,00028	0,00000	0,00010	0,02830	0,46156	103,27 ± 13,54	82,29%	9,67%	10422,6
96M0330I	0,00013	0,00000	0,00001	0,12661	1,82811	108,54 ± 3,13	97,82%	43,25%	46605,4
96M0330J	0,00000	0,00000	0,00004	0,04783	0,69285	111,21 ± 7,28	99,99%	16,34%	17602,1
96M0330M	0,00000	0,00000	0,00005	0,00587	0,08671	113,38 ± 76,26	99,96%	2,00%	2127,2
96M0330N	0,00008	0,00000	-0,00007	0,00449	0,06945	81,33 ± 80,98	67,91%	1,53%	1627,1
96M0330O	0,00011	0,00502	0,00011	0,01847	0,27383	100,74 ± 20,64	88,25%	6,31%	1,8

Irradiation values		Results	40*/39K ±2σ	Age	2σ
J	0,004390	Weighted Mean of Plateau	14,0745 ± 0,6673	108,16	5,08
sd-J(1σ)	0,000021	Total Fusion	13,7864 ± 0,9145	106,01	6,90

Sample Number = **VU17-H3-AG156** Irradiation Number = VU17
Material= white mica, fine fraction Location = Longa, Antihassia

Datafile	$^{36}Ar(a)$	^{37}Ar	^{38}Ar	$^{39}Ar(K)$	$^{40}Ar(a+r)$	Age ± 2σ	$^{40}Ar(r)$	Fraction	K/Ca
96M0331A	0,00085	0,00000	-0,00006	0,06405	0,62342	45,54 ± 6,20	59,82%	3,18%	NoCa
96M0331B	0,00031	0,00000	-0,00015	0,03661	0,40623	66,69 ± 15,95	77,30%	1,82%	13250,2
96M0331D	0,00015	0,00156	-0,00017	0,05305	0,60103	81,05 ± 8,71	92,39%	2,63%	16,6
96M0331E	0,00017	0,00000	-0,00006	0,07346	0,85012	84,19 ± 6,20	94,03%	3,65%	26562,1
96M0331F	0,00007	0,00000	0,00010	0,06237	0,71290	86,00 ± 6,49	97,29%	3,09%	22543,8
96M0331I	0,00019	0,00000	-0,00012	0,12778	1,50342	87,60 ± 3,35	96,32%	6,34%	44713,7
96M0331J	0,00019	0,00145	-0,00011	0,14834	1,77329	89,42 ± 3,95	96,82%	7,36%	50,2
96M0331L	0,00012	0,00000	0,00003	0,17918	2,11509	89,64 ± 2,65	98,30%	8,89%	62642,8
96M0331M	0,00018	0,00246	0,00004	0,23767	2,79969	89,31 ± 2,27	98,13%	11,79%	47,3
96M0331N	0,00002	0,00170	-0,00009	0,16355	1,91723	90,25 ± 3,54	99,67%	8,12%	47,1
96M0331P	0,00000	0,00122	-0,00001	0,10240	1,17311	88,52 ± 5,45	99,99%	5,08%	41,2
96M0331Q	0,00009	0,00123	-0,00002	0,25320	2,93323	88,70 ± 2,66	99,09%	12,56%	101,1
96M0331R	0,00036	0,00897	-0,00023	0,51350	5,96779	88,21 ± 1,91	98,21%	25,48%	28,1

Irradiation values		Results	40*/39K ±2σ	Age	2σ
J	0,004390	Weighted Mean of Plateau	11,5161 ± 0,3406	88,98	2,70
sd-J(1σ)	0,000021	Total Fusion	11,2048 ± 0,2251	86,63	1,88

Location 2

Sample Number = **VU17-F2-MV117** Irradiation Number = VU17
Material = coarse white mica in boudin Location =S W Mavrovouni, Greece

Datafile	$^{36}Ar(a)$	^{37}Ar	^{38}Ar	$^{39}Ar(K)$	$^{40}Ar(a+r)$	Age ± 2σ	$^{40}Ar(r)$	Fraction	K/Ca
97M0007B	0,00023	0,00000	0,00003	0,01551	0,31643	122,62 ± 27,20	78,85%	2,86%	NoCa
97M0007C	0,00010	0,00171	0,00007	0,01005	0,21379	139,73 ± 47,07	86,58%	1,85%	2,9
97M0007E	0,00015	0,00617	-0,00006	0,03199	0,65768	144,89 ± 14,29	93,06%	5,89%	2,5
97M0007F	0,00017	0,00412	0,00013	0,11241	2,20568	145,30 ± 6,12	97,78%	20,71%	13,4
97M0007G	0,00003	0,00000	0,00006	0,15371	3,05685	149,90 ± 5,18	99,66%	28,32%	23835,5
97M0007I	0,00000	0,00799	-0,00001	0,08398	1,68033	151,26 ± 6,65	100,00%	15,47%	5,2
97M0007J	0,00010	0,00547	-0,00018	0,13519	2,69958	149,36 ± 5,18	98,88%	24,90%	12,1

Irradiation values		Results	$^{40}*/39K$ ±2σ	Age	2σ
J	0,004371	Weighted Mean of Plateau	19,8195 ± 0,4953	149,89	5,44
sd-J(1σ)	0,000062	Total Fusion	19,5274 ± 0,4057	147,77	4,99

Sample Number = **VU17-F3-MV118** Irradiation Number = VU17
Material = mylonitic white mica, coarse fraction Location = SW Mavrovouni, Greece

Datafile	$^{36}Ar(a)$	^{37}Ar	^{38}Ar	$^{39}Ar(K)$	$^{40}Ar(a+r)$	Age ± 2σ	$^{40}Ar(r)$	Fraction	K/Ca
97M0006A	0,00010	0,00000	0,00021	0,00724	0,07859	52,41 ± 49,54	62,09%	0,75%	NoCa
97M0006B	0,00011	0,00000	0,00013	0,01050	0,12748	70,02 ± 30,48	74,56%	1,09%	1657,4
97M0006D	0,00008	0,00000	-0,00002	0,00687	0,09612	80,88 ± 46,30	74,98%	0,71%	1084,1
97M0006E	0,00015	0,00000	-0,00019	0,01365	0,21704	97,01 ± 29,87	79,49%	1,42%	2153,3
97M0006F	0,00005	0,00000	-0,00007	0,01776	0,30700	125,10 ± 17,32	95,01%	1,85%	2800,2
97M0006H	0,00006	0,00000	-0,00017	0,04941	0,92424	139,23 ± 9,16	98,12%	5,14%	7786,6
97M0006I	0,00014	0,00000	-0,00001	0,16083	3,08261	143,27 ± 4,76	98,65%	16,72%	25340,5
97M0006J	0,00025	0,00000	-0,00018	0,44185	8,44456	143,55 ± 4,00	99,14%	45,93%	69595,4
97M0006L	0,00006	0,00000	-0,00002	0,07067	1,33928	141,63 ± 5,92	98,59%	7,35%	11124,0
97M0006M	0,00004	0,00298	-0,00006	0,18325	3,43035	141,46 ± 4,23	99,68%	19,05%	30,2

Irradiation values		Results	$^{40}*/39K$ ±2σ	Age	2σ
J	0,004371	Weighted Mean of Plateau	18,8840 ± 0,2212	143,08	4,22
sd-J(1σ)	0,000062	Total Fusion	18,4408 ± 0,2452	139,85	4,22

Location 3

Sample Number = **VU17-F2-MV121** Irradiation Number = VU17
Material = white mica, coarse fraction Location = SW Mavrovouni, Greece

Datafile	$^{36}Ar(a)$	^{37}Ar	^{38}Ar	$^{39}Ar(K)$	$^{40}Ar(a+r)$	Age ± 2σ	$^{40}Ar(r)$	Fraction	K/Ca
97M0008A	0,00051	0,00000	0,00002	0,01557	0,34702	96,67 ± 38,38	56,51%	1,53%	NoCa
97M0008B	0,00010	0,00591	-0,00011	0,02918	0,46442	113,74 ± 16,16	93,54%	2,88%	2,4
97M0008C	0,00005	0,00000	-0,00010	0,12134	2,04998	127,61 ± 5,22	99,25%	11,96%	18777,7
97M0008E	0,00013	0,00000	-0,00007	0,19732	3,27629	124,98 ± 4,17	98,83%	19,45%	30517,8
97M0008F	0,00000	0,00000	0,00016	0,06988	1,12898	123,02 ± 7,51	99,93%	6,89%	10804,1
97M0008G	0,00003	0,00000	-0,00009	0,22858	3,46914	115,60 ± 4,02	99,74%	22,53%	35329,9
97M0008I	0,00032	0,00036	0,00036	0,35276	5,68868	120,89 ± 3,53	98,31%	34,77%	474,0

Irradiation values		Results	$^{40}*/39K$ ±2σ	Age	2σ
J	0,004371	Weighted Mean of Plateau	15,8976 ± 0,2892	121,20	3,95
sd-J(1σ)	0,000062	Total Fusion	15,8531 ± 0,2284	120,87	3,72

Location 4

Sample Number= **VU12-A16-NA007** Irradiation Number = VU12

Material = mylonitic white mica, coarse fraction Location = W-Volos, Greece

Datafile	$^{36}Ar(a)$	^{37}Ar	^{38}Ar	$^{39}Ar(K)$	$^{40}Ar(a+r)$	Age ± 2σ	$^{40}Ar(r)$	Fraction	K/Ca
95M0297B	0,00054	0,00000	0,00000	0,03146	0,96534	98,00 ± 7,46	83,49%	1,68%	NoCa
95M0297C	0,00011	0,00000	0,00016	0,03354	1,05743	116,18 ± 7,28	96,83%	1,79%	16012,4
95M0297E	0,00010	0,00000	0,00017	0,02627	1,30199	181,15 ± 8,10	97,82%	1,40%	12534,8
95M0297F	0,00007	0,00142	0,00018	0,11682	8,48509	264,47 ± 4,40	99,76%	6,23%	40,2
95M0297H	0,00017	0,00000	0,00010	0,11191	8,10218	262,74 ± 4,63	99,38%	5,97%	53337,1
95M0297I	0,00000	0,00000	0,00030	0,14656	10,96356	272,43 ± 4,47	100,00%	7,82%	69824,0
95M0297K	0,00004	0,00640	0,00041	0,15714	12,27375	283,33 ± 5,70	99,91%	8,38%	12,0
95M0297L	0,00005	0,00000	0,00035	0,26123	20,97492	290,68 ± 4,51	99,92%	13,93%	124337
95M0297N	0,00012	0,00000	0,00035	0,24475	19,10816	282,96 ± 4,47	99,82%	13,06%	116422
95M0297O	0,00002	0,00055	0,00000	0,17875	14,31618	290,11 ± 4,77	99,96%	9,54%	159,7
95M0297Q	0,00018	0,00000	0,00033	0,26403	22,60574	307,96 ± 4,89	99,77%	14,08%	125473
95M0297R	0,00000	0,00000	-0,00006	0,13459	11,10241	298,20 ± 4,91	100,00%	7,18%	63945,2
95M0297T	0,00000	0,00000	-0,00009	0,03994	3,31097	299,60 ± 7,51	100,00%	2,13%	18961,8
95M0297U	0,00000	0,00000	-0,00004	0,12765	10,56337	299,08 ± 4,84	100,00%	6,81%	60588,8

Irradiation values		*Results*	40*/39K ±2σ	Age	2σ
J	0,002179	Weighted Mean of Plateau	81,0914 ± 0,5675	293,55	4,73
sd-J(1σ)	0,000017	Total Fusion	77,1997 ± 0,3371	280,50	4,31

Location 5

Sample Number = **VU17-E14-PE111** Irradiation Number = VU17

Material = mylonitic white mica, coarse fraction Location = Pouri, Pelion, Greece

Datafile	$^{36}Ar(a)$	^{37}Ar	^{38}Ar	$^{39}Ar(K)$	$^{40}Ar(a+r)$	Age ± 2σ	$^{40}Ar(r)$	Fraction	K/Ca
97M0003B	0,00012	0,00000	-0,00005	0,01926	0,09702	25,03 ± 20,53	62,78%	1,51%	NoCa
97M0003C	0,00008	0,00000	-0,00007	0,03087	0,12656	26,07 ± 12,07	80,34%	2,42%	4989,6
97M0003D	0,00000	0,00267	-0,00008	0,10936	0,50516	36,45 ± 4,49	99,98%	8,56%	20,0
97M0003F	0,00012	0,00000	0,00015	0,43745	2,19052	38,87 ± 0,86	98,42%	34,25%	70630,5
97M0003G	0,00000	0,00750	0,00007	0,57669	2,59378	35,50 ± 0,78	99,98%	45,15%	37,7
97M0003H	0,00012	0,00992	0,00002	0,10376	0,55571	39,53 ± 3,85	93,60%	8,12%	5,1

Irradiation values		*Results*	40*/39K ±2σ	Age	2σ
J	0,004418	Weighted Mean of Plateau	4,6993 ± 0,1452	37,07	1,13
sd-J(1σ)	0,000003	Total Fusion	4,6486 ± 0,1241	36,68	0,97

Sample Number = **VU17-E18-PE114**
Materi l = white mica

Irradiation Number = VU17
Location = Pouri, Pelion, Greece

Datafile	$^{36}Ar(a)$	^{37}Ar	^{38}Ar	$^{39}Ar(K)$	$^{40}Ar(a+r)$	Age ± 2σ	$^{40}Ar(r)$	Fraction	K/Ca
96M0370B	0,00066	0,00000	0,00016	0,04862	0,24065	7,41 ± 7,11	18,83%	3,09%	NoCa
96M0370C	0,00012	0,00000	0,00006	0,03160	0,10030	16,63 ± 12,57	66,04%	2,01%	5321,2
96M0370E	0,00000	0,00209	-0,00004	0,03749	0,11697	24,70 ± 10,75	99,97%	2,38%	8,8
96M0370F	0,00000	0,00257	-0,00002	0,10861	0,26831	19,58 ± 5,03	99,97%	6,91%	20,7
96M0370G	0,00000	0,00000	0,00006	0,13262	0,33671	20,12 ± 2,82	99,96%	8,44%	22302,0
96M0370I	0,00000	0,00000	-0,00014	0,11724	0,31918	21,57 ± 3,82	99,96%	7,46%	19697,6
96M0370J	0,00000	0,00201	-0,00016	0,12779	0,34654	21,49 ± 3,09	99,97%	8,13%	31,2
96M0370K	0,00000	0,00480	-0,00009	0,18793	0,50492	21,29 ± 2,08	99,97%	11,95%	19,2
96M0370M	0,00000	0,00479	-0,00009	0,28043	0,74594	21,08 ± 1,40	99,97%	17,84%	28,7
96M0370N	0,00005	0,03492	0,00015	0,49981	1,39329	21,85 ± 1,18	98,92%	31,79%	7,0

Irradiation values		Results	$^{40}*/39K$ ±2σ	Age	2σ
J	0,004418	Weighted Mean of Plateau	2,7129 ± 0,2216	21,49	1,75
sd-J(1σ)	0,000003	Total Fusion	2,6262 ± 0,1714	20,81	1,35

Sample Number = **VU17-E16-PE113**
Material = white mica, fine fraction

Irradiation Number = VU17
Location = Pouri, Pelion, Greece

Datafile	$^{36}Ar(a)$	^{37}Ar	^{38}Ar	$^{39}Ar(K)$	$^{40}Ar(a+r)$	Age ± 2σ	$^{40}Ar(r)$	Fraction	K/Ca
96M0369A	0,00025	0,00000	0,00012	0,03440	0,15369	18,22 ± 13,18	51,43%	3,40%	NoCa
96M0369B	0,00020	0,00162	0,00002	0,05261	0,13554	11,42 ± 7,09	55,78%	5,19%	16,0
96M0369C	0,00000	0,01221	0,00016	0,10618	0,21370	15,97 ± 3,53	99,96%	10,48%	4,3
96M0369E	0,00020	0,00809	0,00002	0,13686	0,31093	14,59 ± 3,16	80,88%	13,51%	8,3
96M0369F	0,00006	0,00711	-0,00007	0,21047	0,44601	16,18 ± 2,31	96,19%	20,78%	14,5
96M0369G	0,00009	0,00510	-0,00005	0,12066	0,25653	15,11 ± 3,53	89,51%	11,91%	11,6
96M0369I	0,00000	0,00542	-0,00005	0,17322	0,33203	15,21 ± 2,69	99,96%	17,10%	15,7
96M0369J	0,00003	0,00229	-0,00008	0,09064	0,17820	14,88 ± 4,59	95,28%	8,95%	19,4
96M0369K	0,00064	0,03249	-0,00009	0,08786	0,36325	15,65 ± 4,28	47,68%	8,67%	1,3

Irradiation values		Results	$^{40}*/39K$ ±2σ	Age	2σ
J	0,004418	Weighted Mean of Plateau	1,9498 ± 0,4034	15,47	3,19
sd-J(1σ)	0,000003	Total Fusion	1,9291 ± 0,2373	15,31	1,88

Location 6

Sample Number = VU17-E19-PE115
Material = white mica

Irradiation Number = VU17
Location = W-Zagora, Pelion, Greece

Datafile	$^{36}Ar(a)$	^{37}Ar	^{38}Ar	$^{39}Ar(K)$	$^{40}Ar(a+r)$	Age ± 2σ	$^{40}Ar(r)$	Fraction	K/Ca
97M0002B	0,00033	0,00000	-0,00002	0,01604	0,12824	14,75 ± 28,77	23,24%	2,29%	NoCa
97M0002C	0,00017	0,00000	-0,00001	0,03954	0,22390	34,73 ± 5,75	77,67%	5,64%	6508,0
97M0002E	0,00002	0,00332	-0,00006	0,02952	0,14265	36,44 ± 13,22	95,56%	4,21%	4,4
97M0002F	0,00010	0,00000	0,00011	0,16336	0,78688	36,52 ± 1,73	96,09%	23,31%	26865,7
97M0002G	0,00000	0,00232	0,00025	0,18261	0,73827	31,94 ± 1,78	99,98%	26,06%	38,6
97M0002I	0,00013	0,00000	0,00014	0,07369	0,39449	37,98 ± 5,34	89,95%	10,52%	12108,0
97M0002J	0,00085	0,00000	-0,00005	0,19605	1,16055	36,59 ± 2,49	78,32%	27,97%	32201,2

Irradiation values		Results	$^{40}*/39K$ ±2σ	Age	2σ
J	0,004418	Weighted Mean of Plateau	4,4198 ± 0,3333	34,89	2,61
sd-J(1σ)	0,000003	Total Fusion	4,4214 ± 0,2337	34,90	1,83

Sample Number = **VU17-E5-PE102** Irradiation Number = VU17
Material = mylonitic white mica, coarse fraction Location = Pelion, Greece

Datafile	$^{36}Ar(a)$	^{37}Ar	^{38}Ar	$^{39}Ar(K)$	$^{40}Ar(a+r)$	Age ± 2σ	$^{40}Ar(r)$	Fraction	K/Ca
96M0356A	0,00019	0,00000	-0,00003	0,01681	0,03855	0,00 ± 36,01	-44,26%	1,69%	NoCa
96M0356B	0,00012	0,00659	0,00006	0,01955	0,03152	0,00 ± 24,95	-11,67%	1,96%	1,5
96M0356C	0,00000	0,00273	0,00005	0,01790	0,02639	11,71 ± 31,51	99,94%	1,80%	3,2
96M0356E	0,00000	0,00212	0,00005	0,04809	0,07094	11,72 ± 12,95	99,94%	4,83%	11,1
96M0356F	0,00005	0,00000	0,00001	0,04868	0,08366	11,14 ± 12,47	81,50%	4,89%	10136,4
96M0356G	0,00018	0,00000	-0,00004	0,11558	0,25906	14,05 ± 4,00	78,94%	11,60%	24060,4
96M0356I	0,00014	0,00000	0,00007	0,25847	0,55283	15,70 ± 1,70	92,43%	25,94%	53774,1
96M0356J	0,00022	0,00581	0,00017	0,26397	0,58010	15,53 ± 1,92	89,01%	26,49%	22,3
96M0356K	0,00006	0,00305	0,00027	0,20742	0,41475	15,18 ± 2,65	95,59%	20,82%	33,3

Irradiation values		Results	$^{40}*/39K$ ±2σ	Age	2σ
J	0,004418	Weighted Mean of Plateau	1,9580 ± 0,2515	15,54	1,99
sd-J(1σ)	0,000003	Total Fusion	1,7800 ± 0,3068	14,13	2,43

Location 7

Sample Number = **VU12-C5-PE013** Irradiation Number = VU12
Material = white mica, coarse fraction Location = Pelion Ridge, Greece

Datafile	$^{36}Ar(a)$	^{37}Ar	^{38}Ar	$^{39}Ar(K)$	$^{40}Ar(a+r)$	Age ± 2σ	$^{40}Ar(r)$	Fraction	K/Ca
96M0062A	0,00016	0,00000	0,00009	0,01937	0,27362	47,50 ± 16,11	83,14%	0,96%	NoCa
96M0062B	0,00000	0,01218	0,00009	0,10399	6,85407	251,65 ± 4,36	100,00%	5,15%	4,2
96M0062C	0,00001	0,02710	0,00014	0,28758	20,21286	267,14 ± 2,81	99,99%	14,23%	5,2
96M0062E	0,00025	0,00000	-0,00010	0,29072	23,00203	297,23 ± 3,24	99,67%	14,39%	31442,1
96M0062F	0,00017	0,00000	0,00022	0,43123	34,09925	297,55 ± 3,05	99,85%	21,34%	46623,1
96M0062I	0,00073	0,04393	0,00023	0,24239	18,81021	289,73 ± 3,46	98,85%	12,00%	2,7
96M0062J	0,00005	0,03326	0,00029	0,27489	20,37158	280,42 ± 3,18	99,92%	13,61%	4,1
96M0062L	0,00003	0,01315	0,00003	0,13762	10,70701	293,29 ± 3,66	99,91%	6,81%	5,1
96M0062M	0,00011	0,01596	0,00021	0,09096	7,20378	297,10 ± 4,72	99,54%	4,50%	2,8
96M0062N	0,00000	0,01302	-0,00015	0,03189	2,44451	289,57 ± 9,84	100,00%	1,58%	1,2
96M0062O	0,00000	0,00678	0,00013	0,10979	8,63263	296,40 ± 4,21	100,00%	5,43%	7,9

Irradiation values		Results	$^{40}*/39K$ ±2σ	Age	2σ
J	0,002271	Weighted Mean of Plateau	77,6725 ± 0,6142	293,08	3,45
sd-J(1σ)	0,000011	Total Fusion	75,3125 ± 0,3081	284,84	2,85

Sample Number = **VU17-H17-PE013**
Material = white mica, fine fraction

Irradiation Number = VU17
Location = Milies, Pelion, Greece

Datafile	$^{36}Ar(a)$	^{37}Ar	^{38}Ar	$^{39}Ar(k)$	$^{40}Ar(a+r)$	Age ± 2σ	$^{40}Ar(r)$	Fraction	K/Ca
96M0347B	0,00077	0,00000	-0,00009	0,26227	0,53642	9,26 ± 1,43	57,32%	15,67%	NoCa
96M0347C	0,00017	0,00081	-0,00002	0,10045	0,16989	9,36 ± 4,14	70,02%	6,00%	60,7
96M0347D	0,00007	0,00291	0,00001	0,13191	0,25429	14,03 ± 2,98	92,24%	7,88%	22,2
96M0347F	0,00000	0,00065	0,00006	0,14138	0,27605	15,40 ± 2,67	99,96%	8,45%	107,2
96M0347G	0,00001	0,00000	-0,00008	0,16690	0,35384	16,64 ± 2,89	99,51%	9,97%	42422,2
96M0347H	0,00000	0,00108	-0,00002	0,10489	0,24332	18,28 ± 4,49	99,96%	6,27%	47,5
96M0347J	0,00027	0,00009	-0,00005	0,19895	0,56928	19,33 ± 2,08	85,74%	11,88%	1119,1
96M0347K	0,00032	0,00000	0,00008	0,19616	0,85289	30,34 ± 2,49	88,84%	11,72%	49798,6
96M0347L	0,00029	0,00296	-0,00003	0,19035	0,76471	28,04 ± 1,76	88,80%	11,37%	31,5
96M0347N	0,00010	0,00176	-0,00002	0,06347	0,41670	47,59 ± 5,36	92,73%	3,79%	17,7
96M0347O	0,00038	0,00397	0,00011	0,11724	0,67726	37,74 ± 3,35	83,35%	7,00%	14,5

Irradiation values		Results	$^{40}*/^{39}K$ ±2σ	Age	2σ
J	0,004390	No Plateau			
sd-J(1σ)	0,000021	Total Fusion	2,6340 ± 0,1706	20,74	1,35

Sample Number = **VU17-H18-PE015**
Material = white mica, fine fraction

Irradiation Number = VU17
Location = Milies, Pelion, Greece

Datafile	$^{36}Ar(a)$	^{37}Ar	^{38}Ar	$^{39}Ar(K)$	$^{40}Ar(a+r)$	Age ± 2σ	$^{40}Ar(r)$	Fraction	K/Ca
96M0348B	0,00062	0,00000	0,00006	0,02489	0,19514	3,56 ± 15,96	5,73%	3,96%	NoCa
96M0348C	0,00011	0,02274	-0,00001	0,01626	0,06983	18,78 ± 21,57	55,50%	2,59%	0,4
96M0348D	0,00006	0,01606	-0,00004	0,01889	0,08203	26,57 ± 18,57	77,83%	3,00%	0,6
96M0348F	0,00011	0,01260	-0,00002	0,02941	0,11781	22,66 ± 11,99	71,85%	4,68%	1,1
96M0348G	0,00010	0,00980	-0,00002	0,05952	0,22754	26,13 ± 5,49	86,92%	9,46%	3,0
96M0348H	0,00016	0,01015	-0,00012	0,08298	0,31485	25,42 ± 5,05	85,18%	13,20%	4,0
96M0348J	0,00010	0,01067	-0,00010	0,11953	0,43899	26,98 ± 4,02	93,44%	19,01%	5,5
96M0348K	0,00005	0,00655	-0,00010	0,09115	0,30866	25,29 ± 4,27	94,94%	14,50%	6,8
96M0348L	0,00005	0,00192	0,00003	0,07772	0,25332	24,27 ± 5,35	94,61%	12,36%	19,9
96M0348N	0,00009	0,00414	0,00012	0,10848	0,42002	28,57 ± 2,72	93,90%	17,25%	12,8

Irradiation values		Results	$^{40}*/^{39}K$ ±2σ	Age	2σ
J	0,004390	Weighted Mean of Plateau	3,4106 ± 0,5224	26,81	4,08
sd-J(1σ)	0,000021	Total Fusion	3,1839 ± 0,3838	25,04	3,01

Location 8

Sample Number = **VU12-A18-PE009** Irradiation Number = VU12
Material = white mica, coarse fraction Location = Kalamaki, Pelion, Greece

Datafile	$^{36}Ar(a)$	^{37}Ar	^{38}Ar	$^{39}Ar(K)$	$^{40}Ar(a+r)$	Age ± 2σ	$^{40}Ar(r)$	Fraction	K/Ca
95M0299B	0,00026	0,00000	0,00011	0,00942	0,16168	35,20 ± 26,83	52,67%	0,32%	NoCa
95M0299C	0,00029	0,00465	-0,00003	0,04179	0,54420	42,70 ± 6,38	84,39%	1,44%	4,4
95M0299E	0,00000	0,00054	0,00006	0,02241	0,33646	58,08 ± 11,36	99,99%	0,77%	20,5
95M0299F	0,00007	0,00319	-0,00002	0,02867	0,95961	124,36 ± 12,13	97,85%	0,99%	4,4
95M0299H	0,00012	0,00395	0,00004	0,12568	8,66017	251,38 ± 4,32	99,58%	4,32%	15,6
95M0299I	0,00011	0,00100	0,00005	0,11199	8,80113	284,18 ± 4,89	99,63%	3,85%	54,7
95M0299K	0,00000	0,00324	-0,00001	0,24908	20,92947	303,33 ± 4,83	100,00%	8,56%	37,6
95M0299L	0,00029	0,00587	0,00063	0,65718	49,34167	272,91 ± 4,28	99,83%	22,59%	54,8
95M0299N	0,00010	0,00994	0,00041	0,40705	31,28495	279,10 ± 4,43	99,91%	13,99%	20,1
95M0299O	0,00008	0,00817	0,00033	0,19401	15,19410	283,85 ± 4,71	99,85%	6,67%	11,6
95M0299Q	0,00014	0,00636	0,00003	0,13645	11,57444	304,99 ± 4,88	99,65%	4,69%	10,5
95M0299R	0,00006	0,01543	-0,00002	0,40258	33,57393	301,09 ± 4,61	99,95%	13,84%	12,8
95M0299T	0,00007	0,01013	0,00005	0,02347	1,97927	301,21 ± 14,15	98,90%	0,81%	1,1
95M0299U	0,00004	0,01633	0,00038	0,49967	43,44749	312,95 ± 4,97	99,98%	17,17%	15,0

Irradiation values		Results	$^{40}*/^{39}K$ ±2σ	Age	2σ
J	0,002179	Weighted Mean of Plateau	84,4581 ± 0,5522	304,76	4,85
sd-J(1σ)	0,000017	Total Fusion	77,7841 ± 0,2816	282,46	4,29

Location 9

Sample Number = **VU17-F9-PE140** Irradiation Number = VU17
Material = white mica, coarse fraction Location = Neohori,CPelion,Greece

Datafile	$^{36}Ar(a)$	^{37}Ar	^{38}Ar	$^{39}Ar(K)$	$^{40}Ar(a+r)$	Age ± 2σ	$^{40}Ar(r)$	Fraction	K/Ca
97M0010A	0,00031	0,00000	-0,00001	0,00843	0,20048	99,26 ± 66,89	54,40%	1,09%	NoCa
97M0010B	0,00003	0,00056	-0,00003	0,03988	0,50840	96,35 ± 11,61	98,45%	5,15%	35,0
97M0010C	0,00026	0,00368	0,00016	0,26217	3,31462	94,82 ± 3,06	97,64%	33,84%	34,9
97M0010E	0,00006	0,00280	-0,00007	0,13898	1,73803	95,06 ± 4,23	98,98%	17,94%	24,3
97M0010F	0,00002	0,00131	0,00013	0,09366	1,18678	96,69 ± 4,90	99,39%	12,09%	34,9
97M0010G	0,00000	0,00262	0,00000	0,05387	0,66761	95,18 ± 8,30	99,99%	6,95%	10,1
97M0010I	0,00000	0,00000	0,00014	0,17773	2,22062	95,93 ± 3,44	99,99%	22,94%	26930,1

Irradiation values		Results	$^{40}*/^{39}K$ ±2σ	Age	2σ
J	0,004371	Weighted Mean of Plateau	12,4099 ± 0,3407	95,30	3,66
sd-J(1σ)	0,000062	Total Fusion	12,4362 ± 0,2663	95,49	3,31

Sample Number = **VU17-F12-PE140** Irradiation Number = VU17
Material = white mica, fine fraction Location = Neohori,Pelion,Greece

Datafile	$^{36}Ar(a)$	^{37}Ar	^{38}Ar	$^{39}Ar(K)$	$^{40}Ar(a+r)$	Age ± 2σ	$^{40}Ar(r)$	Fraction	K/Ca
97M0013B	0,00022	0,00000	0,00001	0,03979	0,20454	27,44 ± 9,91	68,20%	6,80%	NoCa
97M0013C	0,00009	0,00000	-0,00004	0,04973	0,26334	37,28 ± 6,44	90,20%	8,50%	7292,3
97M0013D	0,00000	0,00000	-0,00004	0,04875	0,30610	48,84 ± 10,56	99,98%	8,34%	7145,8
97M0013F	0,00005	0,00000	0,00003	0,07213	0,51146	53,59 ± 5,45	97,27%	12,33%	10567,4
97M0013G	0,00000	0,00000	0,00009	0,08429	0,54517	50,29 ± 5,15	99,98%	14,41%	12342,9
97M0013H	0,00000	0,00000	-0,00014	0,06352	0,42041	51,45 ± 6,57	99,98%	10,86%	9297,5
97M0013J	0,00013	0,00000	-0,00003	0,07590	0,58709	56,15 ± 5,43	93,49%	12,98%	11097,2
97M0013K	0,00004	0,00745	-0,00004	0,07017	0,55035	59,44 ± 5,49	97,70%	12,00%	4,6
97M0013L	0,00000	0,00000	-0,00010	0,08053	0,54484	52,57 ± 5,49	99,98%	13,77%	11767,0

Irradiation values		Results	$^{40}*/^{39}K$ ±2σ	Age	2σ
J	0,004371	Weighted Mean of Plateau	6,9216 ± 0,7373	53,77	5,84
sd-J(1σ)	0,000062	Total Fusion	6,4597 ± 0,4019	50,23	3,39

Sample Number = **VU17-F14-PE141** Irradiation Number = VU17
Material = mylonitic white mica, fine fraction Location = Neohori, Pelion, Greece

Datafile	$^{36}Ar(a)$	^{37}Ar	^{38}Ar	$^{39}Ar(K)$	$^{40}Ar(a+r)$	Age ± 2σ	$^{40}Ar(r)$	Fraction	K/Ca
97M0015B	0,00024	0,00000	0,00014	0,07019	0,28653	23,95 ± 5,98	74,88%	2,30%	NoCa
97M0015C	0,00026	0,00000	0,00006	0,11760	0,50723	28,60 ± 3,80	84,74%	3,85%	16906,7
97M0015D	0,00035	0,00000	0,00014	0,13603	0,63394	30,43 ± 2,90	83,49%	4,45%	19549,9
97M0015F	0,00015	0,00128	-0,00003	0,16129	0,77690	35,52 ± 2,55	94,43%	5,28%	61,7
97M0015G	0,00012	0,00099	0,00012	0,22262	1,06969	36,24 ± 2,33	96,59%	7,28%	110,6
97M0015H	0,00018	0,00000	0,00003	0,37924	1,88721	37,75 ± 1,56	97,20%	12,41%	54436,5
97M0015J	0,00035	0,00922	-0,00030	0,58049	3,10293	40,29 ± 1,34	96,65%	18,99%	30,9
97M0015K	0,00116	0,00161	0,00026	1,38932	8,25148	44,34 ± 1,30	95,83%	45,45%	421,7

Irradiation values		Results	40*/39K ±2σ	Age	2σ
J	0,004371	Weighted Mean of Plateau	5,0085 ± 0,1482	39,07	1,58
sd-J(1σ)	0,000062	Total Fusion	5,1307 ± 0,0727	40,01	1,25

Sample Number = **VU17-F17-PE142** Irradiation Number = VU17
Material = mylonitic white mica, fine fraction Location = Neohori, Pelion, Greece

Datafile	$^{36}Ar(a)$	^{37}Ar	^{38}Ar	$^{39}Ar(K)$	$^{40}Ar(a+r)$	Age ± 2σ	$^{40}Ar(r)$	Fraction	K/Ca
97M0014A	0,00136	0,00000	0,00008	0,13127	0,72519	19,37 ± 4,10	44,69%	3,93%	NoCa
97M0014B	0,00060	0,00000	0,00007	0,12604	0,59911	26,27 ± 3,84	70,59%	3,77%	18399,6
97M0014C	0,00040	0,00000	-0,00008	0,14065	0,68259	31,32 ± 4,06	82,54%	4,21%	20526,0
97M0014E	0,00045	0,00000	-0,00006	0,17968	0,91563	34,04 ± 2,53	85,50%	5,38%	26206,1
97M0014F	0,00052	0,00170	-0,00018	0,34343	1,81574	37,77 ± 1,72	91,53%	10,27%	99,1
97M0014G	0,00043	0,00000	-0,00020	0,29818	1,58231	38,06 ± 2,14	91,90%	8,92%	43462,0
97M0014I	0,00098	0,00000	-0,00030	0,67355	3,74002	39,95 ± 1,30	92,24%	20,15%	96518,4
97M0014J	0,00256	0,00171	-0,00037	1,44966	9,19628	45,34 ± 1,38	91,77%	43,37%	416,6

Irradiation values		Results	40*/39K ±2σ	Age	2σ
J	0,004371	Weighted Mean of Plateau	5,0519 ± 0,1257	39,40	1,47
sd-J(1σ)	0,000062	Total Fusion	5,1164 ± 0,0814	39,90	1,28

Location 10

Sample Number = **VU17-F8-PE139** Irradiation Number = VU17
Material = mylonitic white mica Location = Platania, S Pelion, Greece

Datafile	$^{36}Ar(a)$	^{37}Ar	^{38}Ar	$^{39}Ar(K)$	$^{40}Ar(a+r)$	Age ± 2σ	$^{40}Ar(r)$	Fraction	K/Ca
97M0011B	0,00113	0,00000	-0,00006	0,05963	0,46922	17,82 ± 6,80	28,85%	2,07%	NoCa
97M0011C	0,00037	0,00000	0,00012	0,06618	0,29974	22,69 ± 6,92	63,92%	2,29%	9910,6
97M0011E	0,00022	0,00000	0,00018	0,06180	0,25952	24,54 ± 5,53	74,58%	2,14%	9248,5
97M0011F	0,00018	0,00000	0,00013	0,09358	0,39373	28,46 ± 4,41	86,42%	3,24%	13999,4
97M0011G	0,00004	0,00183	0,00007	0,09345	0,40217	32,55 ± 4,66	96,76%	3,24%	25,0
97M0011I	0,00018	0,00256	0,00008	0,15107	0,66910	31,86 ± 4,25	92,01%	5,24%	29,0
97M0011J	0,00025	0,00000	0,00007	0,21447	0,95182	32,01 ± 2,03	92,25%	7,44%	32043,3
97M0011K	0,00009	0,00000	0,00013	0,13610	0,59885	32,77 ± 2,95	95,29%	4,72%	20328,2
97M0011M	0,00017	0,00000	0,00023	0,41600	1,79464	32,77 ± 1,27	97,18%	14,43%	62082,7
97M0011N	0,00024	0,00000	0,00009	0,64310	2,67394	31,64 ± 1,15	97,32%	22,30%	95942,2
97M0011O	0,00053	0,00000	-0,00016	0,94846	4,09198	32,42 ± 1,00	96,15%	32,89%	141455

Irradiation values		Results	40*/39K ±2σ	Age	2σ
J	0,004371	Weighted Mean of Plateau	4,1336 ± 0,1101	32,31	1,25
sd-J(1σ)	0,000062	Total Fusion	4,0216 ± 0,1038	31,44	1,20

Location 11

Sample Number = **VU17-G18-SK154** Irradiation Number = VU17
Material = white mica, coarse fraction Location = Skiathos, Greece

Datafile	$^{36}Ar(a)$	^{37}Ar	^{38}Ar	$^{39}Ar(K)$	$^{40}Ar(a+r)$	Age ± 2σ	$^{40}Ar(r)$	Fraction	K/Ca
97M0051A	0,00090	0,00000	0,00009	0,01644	0,54604	127,39 ± 33,33	51,46%	0,76%	NoCa
97M0051B	0,00013	0,00001	-0,00002	0,01770	0,46005	175,29 ± 30,05	91,73%	0,82%	1569,7
97M0051C	0,00101	0,00001	0,00005	0,04483	1,31251	166,72 ± 13,08	77,27%	2,07%	3974,3
97M0051D	0,00000	0,00001	-0,00001	0,09153	2,36462	189,20 ± 7,80	100,00%	4,23%	8110,8
97M0051G	0,00014	0,00001	0,00042	0,58381	16,00621	199,68 ± 5,39	99,74%	27,01%	51300,5
97M0051H	0,00024	0,00001	-0,00011	0,50885	15,46068	219,61 ± 5,81	99,54%	23,54%	44700,0
97M0051I	0,00018	0,00001	0,00038	0,89870	26,92588	217,27 ± 5,71	99,80%	41,57%	78919,0

Irradiation values		Results	40*/39K ±2σ	Age	2σ
J	0,004280	Weighted Mean of Plateau	30,0358 ± 0,1421	218,18	5,75
sd-J(1σ)	0,000059	Total Fusion	28,8228 ± 0,1381	209,86	5,54

Sample Number = **VU17-G17-SK154** Irradiation Number = VU17
Material = white mica, fine fraction Location = Skiathos, Greece

Datafile	$^{36}Ar(a)$	^{37}Ar	^{38}Ar	$^{39}Ar(K)$	$^{40}Ar(a+r)$	Age ± 2σ	$^{40}Ar(r)$	Fraction	K/Ca
97M0052A	0,00787	0,00000	0,00040	0,30156	4,73630	60,66 ± 3,00	50,87%	10,24%	NoCa
97M0052B	0,00564	0,00001	0,00026	0,21032	3,72021	73,88 ± 3,50	55,21%	7,14%	18452,9
97M0052C	0,00408	0,00001	0,00008	0,21247	3,57045	83,98 ± 4,15	66,25%	7,21%	18635,8
97M0052D	0,00280	0,00785	0,00000	0,31292	4,68956	92,89 ± 3,18	82,37%	10,62%	19,5
97M0052F	0,00190	0,00066	-0,00010	0,28819	4,18619	94,59 ± 3,18	86,58%	9,78%	214,0
97M0052G	0,00315	0,00666	0,00004	0,57088	8,05999	93,93 ± 2,70	88,44%	19,38%	42,0
97M0052H	0,00810	0,01427	0,00041	1,04960	15,27830	92,38 ± 2,55	84,33%	35,63%	36,0

Irradiation values		Results	40*/39K ±2σ	Age	2σ
J	0,004280	Weighted Mean of Plateau	12,3472 ± 0,1278	92,90	2,67
sd-J(1σ)	0,000059	Total Fusion	11,6533 ± 0,1007	87,81	2,48

CHAPTER 6, Incremental heating data

SECTION 6.2: RHODOPE MASSIF

Sample Number = **VU23-B15-Rh402** Irradiation Number = VU23
Material = white mica, coarse fraction Location = Chalkidiki, Rhodope, Greece

Datafile	$^{36}Ar(a)$	^{37}Ar	^{38}Ar	$^{39}Ar(K)$	$^{40}Ar(a+r)$	Age ± 2σ	$^{40}Ar(r)$	Fraction	K/Ca
97M0461A	0,00013	0,00000	0,00016	0,00127	0,06908	183,65 ± 243,0	43,31%	0,61%	NoCa
97M0461B	0,00000	0,00301	-0,00003	0,00248	0,03792	121,47 ± 205,4	99,99%	1,19%	0,4
97M0461D	0,00005	0,00219	-0,00010	0,00769	0,13350	121,50 ± 75,19	87,91%	3,67%	1,7
97M0461E	0,00013	0,00111	-0,00019	0,10039	1,85466	143,03 ± 3,45	97,86%	47,98%	44,4
97M0461F	0,00009	0,00228	-0,00038	0,05897	1,08050	141,65 ± 12,35	97,66%	28,18%	12,7
97M0461G	0,00003	0,00034	-0,00011	0,02523	0,46674	143,54 ± 30,85	98,08%	12,06%	35,9
97M0461I	0,00003	0,00000	-0,00010	0,01320	0,23969	139,19 ± 27,12	96,78%	6,31%	NoCa

Irradiation values		Results	40*/39K ±2σ	Age	2σ
J	0,004564	Weighted Mean of Plateau	18,0716 ± 0,5642	142,98	4,89
sd-J(1σ)	0,000039	Total Fusion	17,8996 ± 1,0679	141,67	8,45

Sample Number = **VU23-B17-Rh405** Irradiation Number = VU23
Material = white mica, coarse fraction Location = Chalkidiki, Rhodope, Greece

Datafile	$^{36}Ar(a)$	^{37}Ar	^{38}Ar	$^{39}Ar(K)$	$^{40}Ar(a+r)$	Age ± 2σ	$^{40}Ar(r)$	Fraction	K/Ca
97M0462B	0,00015	0,00000	-0,00017	0,03083	1,09580	261,12 ± 24,77	96,02%	8,26%	NoCa
97M0462C	0,00038	0,00000	-0,00018	0,16059	5,96031	277,45 ± 5,43	98,14%	43,02%	NoCa
97M0462E	0,00000	0,00033	0,00026	0,08821	3,13461	271,15 ± 7,10	100,00%	23,63%	130,0
97M0462F	0,00000	0,00000	0,00007	0,01523	0,46430	235,07 ± 50,91	99,99%	4,08%	NoCa
97M0462G	0,00000	0,00178	-0,00017	0,03342	1,16810	267,01 ± 17,56	100,00%	8,95%	9,2
97M0462H	0,00000	0,00026	-0,00018	0,04501	1,56903	266,36 ± 16,83	100,00%	12,06%	83,4

Irradiation values		Results	40*/39K ±2σ	Age	2σ
J	0,004564	Weighted Mean of Plateau	36,1187 ± 0,8613	275,28	7,48
sd-J(1σ)	0,000039	Total Fusion	35,4617 ± 0,7204	270,63	6,66

Sample Number = **VU23-B19-Rh410** Irradiation Number = VU23
Material = white mica, coarse fraction Location = Pangeo, Rhodope, Greece

Datafile	$^{36}Ar(a)$	^{37}Ar	^{38}Ar	$^{39}Ar(K)$	$^{40}Ar(a+r)$	Age ± 2σ	$^{40}Ar(r)$	Fraction	K/Ca
97M0464B	0,00098	0,00000	0,00007	0,13501	0,63727	21,11 ± 2,83	54,64%	9,30%	NoCa
97M0464C	0,00062	0,00000	0,00003	0,23456	0,82290	22,28 ± 5,20	77,61%	16,15%	NoCa
97M0464D	0,00086	0,00050	-0,00008	0,48058	1,38361	19,26 ± 1,15	81,67%	33,09%	473,6
97M0464F	0,00004	0,00000	0,00008	0,23424	0,60326	20,66 ± 2,30	97,95%	16,13%	NoCa
97M0464G	0,00020	0,00000	-0,00013	0,16746	0,43717	18,44 ± 13,74	86,22%	11,53%	NoCa
97M0464H	0,00000	0,00000	-0,00021	0,06305	0,14733	19,13 ± 8,23	99,94%	4,34%	NoCa
97M0464J	0,00000	0,00000	-0,00020	0,03377	0,07675	18,61 ± 11,99	99,92%	2,33%	NoCa
97M0464K	0,00000	0,00000	-0,00009	0,10351	0,24689	19,53 ± 3,62	99,95%	7,13%	NoCa

Irradiation values		Results	40*/39K ±2σ	Age	2σ
J	0,004564	Weighted Mean of Plateau	2,4121 ± 0,3066	19,75	2,52
sd-J(1σ)	0,000039	Total Fusion	2,4490 ± 0,2641	20,05	2,18

Sample Number = **VU23-F2-Rh411** Irradiation Number = VU23
Material = white mica, coarse fraction Location = Pangeo, Rhodope, Greece

Datafile	$^{36}Ar(a)$	^{37}Ar	^{38}Ar	$^{39}Ar(K)$	$^{40}Ar(a+r)$	Age ± 2σ	$^{40}Ar(r)$	Fraction	K/Ca
97M0466A	0,00069	0,00000	-0,00034	0,10108	0,44314	19,04 ± 3,13	53,99%	20,24%	NoCa
97M0466B	0,00000	0,00000	-0,00012	0,07129	0,19045	21,46 ± 10,19	99,95%	14,28%	NoCa
97M0466C	0,00000	0,00080	-0,00026	0,21427	0,59542	22,33 ± 2,71	99,97%	42,91%	131,8
97M0466E	0,00000	0,00000	-0,00033	0,04221	0,11382	21,66 ± 16,18	99,94%	8,45%	NoCa
97M0466F	0,00002	0,00000	-0,00022	0,01767	0,04528	18,06 ± 37,83	87,58%	3,54%	NoCa
97M0466G	0,00000	0,00000	-0,00019	0,05278	0,15297	23,27 ± 6,80	99,95%	10,57%	NoCa

Irradiation values		Results	40*/39K ±2σ	Age	2σ
J	0,004481	Weighted Mean of Plateau	2,7836 ± 0,6701	22,36	5,36
sd-J(1σ)	0,000040	Total Fusion	2,6668 ± 0,4166	21,43	3,35

Sample Number = **VU23-F4-Rh413**
Material = white mica

Irradiation Number = VU23
Location = Vrondou, Rhodope, Greece

Datafile	$^{36}Ar(a)$	^{37}Ar	^{38}Ar	$^{39}Ar(K)$	$^{40}Ar(a+r)$	Age ± 2σ	$^{40}Ar(r)$	Fraction	K/Ca
97M0470A	0,00012	0,00000	0,00011	0,00054	0,03976	71,42 ± 803,5	12,19%	0,09%	NoCa
97M0470B	0,00000	0,00719	0,00004	0,00095	0,01537	125,62 ± 460,8	99,99%	0,16%	0,1
97M0470C	0,00000	0,00000	0,00028	0,00406	0,02590	50,10 ± 104,3	98,57%	0,70%	NoCa
97M0470D	0,00000	0,00000	0,00011	0,01451	0,06516	35,94 ± 30,93	99,94%	2,49%	NoCa
97M0470F	0,00000	0,00000	0,00000	0,02637	0,09071	27,59 ± 19,28	99,94%	4,53%	NoCa
97M0470G	0,00000	0,00142	0,00018	0,05474	0,16582	24,32 ± 14,32	99,97%	9,41%	18,9
97M0470H	0,00021	0,00000	-0,00014	0,09103	0,34239	24,79 ± 6,93	82,08%	15,64%	NoCa
97M0470I	0,00000	0,00000	-0,00007	0,38985	1,18137	24,33 ± 1,74	99,97%	66,98%	NoCa

Irradiation values		Results	40*/39K ±2σ	Age	2σ
J	0,004481	Weighted Mean of Plateau	3,0363 ± 0,4076	24,38	3,28
sd-J(1σ)	0,000040	Total Fusion	3,1437 ± 0,4651	25,24	3,73

Sample Number = **VU23-F5-Rh414**
Material = white mica, coarse fraction

Irradiation Number = VU23
Location = Vrondou, Rhodope, Greece

Datafile	$^{36}Ar(a)$	^{37}Ar	^{38}Ar	$^{39}Ar(K)$	$^{40}Ar(a+r)$	Age ± 2σ	$^{40}Ar(r)$	Fraction	K/Ca
97M0468A	0,00048	0,00000	-0,00003	0,12959	0,38760	15,19 ± 1,77	63,08%	30,07%	NoCa
97M0468B	0,00019	0,00000	0,00018	0,13970	0,31841	15,18 ± 3,75	82,68%	32,42%	NoCa
97M0468C	0,00000	0,00102	0,00004	0,02228	0,04684	16,92 ± 23,01	99,96%	5,17%	10,7
97M0468E	0,00000	0,00000	-0,00009	0,05133	0,10477	16,42 ± 12,67	99,93%	11,91%	NoCa
97M0468F	0,00000	0,00000	-0,00031	0,06245	0,13446	17,32 ± 8,59	99,94%	14,49%	NoCa
97M0468G	0,00000	0,00000	-0,00018	0,02556	0,05639	17,74 ± 35,17	99,91%	5,93%	NoCa

Irradiation values		Results	40*/39K ±2σ	Age	2σ
J	0,004481	Weighted Mean of Plateau	1,8869 ± 0,2801	15,19	2,26
sd-J(1σ)	0,000040	Total Fusion	1,9733 ± 0,4849	15,88	3,90

Sample Number = **VU23-F6-Rh414**
Material = biotite

Irradiation Number = VU23
Location = Vrondou, Rhodope, Greece

Datafile	$^{36}Ar(a)$	^{37}Ar	^{38}Ar	$^{39}Ar(K)$	$^{40}Ar(a+r)$	Age ± 2σ	$^{40}Ar(r)$	Fraction	K/Ca
97M0469A	0,00052	0,00000	0,00025	0,24434	0,60508	14,87 ± 3,40	74,56%	21,25%	NoCa
97M0469B	0,00000	0,00000	0,00022	0,24812	0,48288	15,66 ± 1,97	99,95%	21,58%	NoCa
97M0469C	0,00000	0,00000	0,00018	0,17303	0,33058	15,35 ± 3,43	99,79%	15,05%	NoCa
97M0469E	0,00003	0,00001	-0,00001	0,05498	0,10682	14,39 ± 5,43	91,94%	4,78%	1942,8
97M0469F	0,00000	0,00000	-0,00009	0,08216	0,15799	15,48 ± 7,05	99,94%	7,15%	NoCa
97M0469G	0,00000	0,00069	-0,00009	0,18926	0,35509	15,10 ± 3,39	99,95%	16,46%	134,5
97M0469H	0,00000	0,00000	0,00027	0,15772	0,30600	15,62 ± 2,28	99,95%	13,72%	NoCa

Irradiation values		Results	40*/39K ±2σ	Age	2σ
J	0,004481	Weighted Mean of Plateau	1,9220 ± 0,3691	15,47	2,97
sd-J(1σ)	0,000040	Total Fusion	1,8976 ± 0,2048	15,28	1,66

Sample Number = **VU23-F7-Rh418**
Material = white mica, coarse fraction

Irradiation Number = VU23
Location = N Drama, Rhodope, Greece

Datafile	$^{36}Ar(a)$	^{37}Ar	^{38}Ar	$^{39}Ar(K)$	$^{40}Ar(a+r)$	Age ± 2σ	$^{40}Ar(r)$	Fraction	K/Ca
97M0471B	0,00029	0,00000	-0,00027	0,03071	0,24331	40,88 ± 11,45	64,55%	6,16%	NoCa
97M0471C	0,00000	0,00016	-0,00043	0,22901	1,04129	36,39 ± 3,48	99,98%	45,94%	693,1
97M0471E	0,00000	0,00116	-0,00037	0,15139	0,67282	35,57 ± 5,37	99,98%	30,37%	64,0
97M0471F	0,00000	0,00000	0,00011	0,02603	0,11575	35,59 ± 22,26	99,96%	5,22%	NoCa
97M0471G	0,00000	0,00000	0,00019	0,00641	0,02834	35,38 ± 91,40	99,88%	1,28%	NoCa
97M0471H	0,00000	0,00000	-0,00019	0,05496	0,24864	36,20 ± 13,06	99,97%	11,02%	NoCa

Irradiation values		Results	40*/39K ±2σ	Age	2σ
J	0,004481	Weighted Mean of Plateau	4,5156 ± 0,6240	36,14	4,99
sd-J(1σ)	0,000040	Total Fusion	4,5412 ± 0,4839	36,34	3,89

Sample Number = **VU23-F9-Rh427**
Material = white mica, coarse fraction

Irradiation Number = VU23
Location = N Kavala, Rhodope, Greece

Datafile	$^{36}Ar(a)$	^{37}Ar	^{38}Ar	$^{39}Ar(K)$	$^{40}Ar(a+r)$	Age ± 2σ	$^{40}Ar(r)$	Fraction	K/Ca
97M0472A	0,00072	0,00000	0,00028	0,03069	0,34925	35,71 ± 16,49	39,20%	2,88%	NoCa
97M0472B	0,00025	0,00358	0,00016	0,12450	0,53214	29,44 ± 3,56	85,89%	11,70%	17,1
97M0472C	0,00000	0,00019	0,00011	0,22362	0,80804	28,98 ± 2,20	99,97%	21,01%	585,4
97M0472E	0,00000	0,00170	-0,00015	0,18610	0,67585	29,12 ± 3,67	99,98%	17,48%	53,5
97M0472F	0,00000	0,00404	-0,00006	0,19598	0,71382	29,21 ± 2,45	99,98%	18,41%	23,8
97M0472G	0,00000	0,00021	0,00006	0,06425	0,23660	29,52 ± 12,84	99,97%	6,04%	153,2
97M0472H	0,00000	0,00000	-0,00013	0,05606	0,19666	28,13 ± 14,05	99,96%	5,27%	NoCa
97M0472J	0,00000	0,00000	-0,00015	0,18321	0,62985	27,58 ± 1,83	99,97%	17,21%	NoCa

Irradiation values		Results	40*/39K ±2σ	Age	2σ
J	0,004481	Weighted Mean of Plateau	3,5616 ± 0,3541	28,56	2,86
sd-J(1σ)	0,000040	Total Fusion	3,6215 ± 0,2658	29,04	2,18

Sample Number = **VU23-F12-Rh430**
Material = white mica, coarse fraction

Irradiation Number = VU23
Location = N Xanthi, Rhodope, Greece

Datafile	$^{36}Ar(a)$	^{37}Ar	^{38}Ar	$^{39}Ar(K)$	$^{40}Ar(a+r)$	Age ± 2σ	$^{40}Ar(r)$	Fraction	K/Ca
97M0473B	0,00006	0,00000	-0,00003	0,00157	0,03336	79,18 ± 168,3	47,13%	0,10%	NoCa
97M0473C	0,00014	0,00185	-0,00004	0,00136	0,05296	59,46 ± 251,8	19,21%	0,08%	0,4
97M0473E	0,00008	0,00000	-0,00005	0,00271	0,04110	54,13 ± 196,9	44,80%	0,17%	NoCa
97M0473F	0,00037	0,00020	-0,00021	0,17014	0,87511	35,99 ± 2,75	87,41%	10,47%	413,2
97M0473G	0,00005	0,00081	0,00030	0,56794	2,57559	36,10 ± 0,84	99,43%	34,97%	343,6
97M0473H	0,00000	0,00000	-0,00001	0,42996	1,94870	36,27 ± 1,28	99,98%	26,47%	NoCa
97M0473J	0,00004	0,00077	-0,00021	0,35986	1,64400	36,29 ± 1,32	99,25%	22,16%	230,4
97M0473K	0,00003	0,00134	-0,00002	0,02475	0,11417	33,79 ± 22,00	91,45%	1,52%	9,1
97M0473L	0,00000	0,00036	-0,00041	0,06599	0,29912	36,28 ± 4,93	99,98%	4,06%	88,9

Irradiation values		Results	40*/39K ±2σ	Age	2σ
J	0,004481	Weighted Mean of Plateau	4,5170 ± 0,1127	36,15	1,10
sd-J(1σ)	0,000040	Total Fusion	4,5282 ± 0,1420	36,24	1,29

Sample Number = **VU23-F13-Rh432** Irradiation Number = VU23
Material = white mica, coarse fraction Location = N Xanthi, Rhodope, Greece

Datafile	$^{36}Ar(a)$	^{37}Ar	^{38}Ar	$^{39}Ar(K)$	$^{40}Ar(a+r)$	Age ± 2σ	$^{40}Ar(r)$	Fraction	K/Ca
97M0474A	0,01219	0,00000	-0,00006	0,08079	3,99058	38,57 ± 10,63	9,76%	14,40%	NoCa
97M0474B	0,00980	0,02123	0,00024	0,05971	3,19112	39,43 ± 12,06	9,23%	10,64%	1,4
97M0474C	0,00191	0,01069	-0,00008	0,16167	1,36108	39,44 ± 5,02	58,59%	28,81%	7,4
97M0474D	0,00131	0,00820	0,00001	0,15179	1,16634	40,99 ± 5,32	66,74%	27,05%	9,1
97M0474F	0,00060	0,00434	0,00009	0,06696	0,50851	39,58 ± 2,01	65,18%	11,93%	7,6
97M0474G	0,00053	0,00388	-0,00010	0,04015	0,36561	41,37 ± 17,40	56,84%	7,16%	5,1

Irradiation values		Results	40*/39K ±2σ	Age	2σ
J	0,004481	Weighted Mean of Plateau	4,9662 ± 0,3655	39,71	2,97
sd-J(1σ)	0,000040	Total Fusion	4,9894 ± 0,4307	39,89	3,48

Sample Number = **VU23-F14-Rh437** Irradiation Number = VU23
Material = white mica, coarse fraction Location = N Alexandr., Rhodope, Greece

Datafile	$^{36}Ar(a)$	^{37}Ar	^{38}Ar	$^{39}Ar(K)$	$^{40}Ar(a+r)$	Age ± 2σ	$^{40}Ar(r)$	Fraction	K/Ca
97M0475B	0,00015	0,00000	-0,00001	0,00870	0,08257	35,86 ± 74,03	47,20%	1,88%	NoCa
97M0475C	0,00010	0,00000	-0,00037	0,07826	0,40426	38,32 ± 5,38	92,72%	16,91%	NoCa
97M0475E	0,00000	0,00000	-0,00017	0,06971	0,35305	40,48 ± 6,12	99,97%	15,06%	NoCa
97M0475F	0,00059	0,00031	-0,00018	0,19399	1,12965	39,33 ± 3,39	84,45%	41,91%	305,4
97M0475G	0,00000	0,00000	-0,00003	0,05348	0,25134	37,59 ± 8,74	99,97%	11,56%	NoCa
97M0475H	0,00000	0,00000	-0,00037	0,05868	0,30180	41,10 ± 10,12	99,97%	12,68%	NoCa

Irradiation values		Results	40*/39K ±2σ	Age	2σ
J	0,004481	Weighted Mean of Plateau	4,9113 ± 0,6742	39,27	5,38
sd-J(1σ)	0,000040	Total Fusion	4,9136 ± 0,4353	39,29	3,51

Sample Number = **VU23-F15-Rh437** Irradiation Number = VU23
Material = white mica, fine fraction Location = N Alexandr., Rhodope, Greece

Datafile	$^{36}Ar(a)$	^{37}Ar	^{38}Ar	$^{39}Ar(K)$	$^{40}Ar(a+r)$	Age ± 2σ	$^{40}Ar(r)$	Fraction	K/Ca
97M0476A	0,00041	0,00000	-0,00023	0,02842	0,24495	34,67 ± 13,14	50,23%	6,01%	NoCa
97M0476B	0,00008	0,00000	-0,00007	0,04211	0,23481	40,15 ± 14,81	90,04%	8,90%	NoCa
97M0476C	0,00016	0,00032	-0,00042	0,12095	0,57752	35,17 ± 2,68	92,00%	25,57%	182,8
97M0476E	0,00012	0,00025	-0,00006	0,11248	0,53114	35,27 ± 3,75	93,27%	23,78%	219,4
97M0476F	0,00004	0,00000	-0,00015	0,05898	0,27817	36,07 ± 9,10	95,55%	12,47%	NoCa
97M0476G	0,00006	0,00000	0,00005	0,03702	0,17797	34,64 ± 8,93	89,99%	7,83%	NoCa
97M0476H	0,00010	0,00015	0,00001	0,07310	0,36482	36,67 ± 7,58	91,81%	15,45%	238,6

Irradiation values		Results	40*/39K ±2σ	Age	2σ
J	0,004481	Weighted Mean of Plateau	4,4115 ± 0,5510	35,31	4,41
sd-J(1σ)	0,000040	Total Fusion	4,4866 ± 0,4195	35,91	3,38

Sample Number = **VU23-F16-Rh438** Irradiation Number = VU23

Material = white mica, coarse fraction Location = N Alexandr., Rhodope, Greece

Datafile	$^{36}Ar(a)$	^{37}Ar	^{38}Ar	$^{39}Ar(K)$	$^{40}Ar(a+r)$	Age ± 2σ	$^{40}Ar(r)$	Fraction	K/Ca
97M0477A	0,00013	0,00000	-0,00019	0,01333	0,09933	36,68 ± 29,68	61,51%	1,95%	NoCa
97M0477B	0,00020	0,00000	0,00002	0,11270	0,71668	46,50 ± 4,09	91,61%	16,48%	NoCa
97M0477C	0,00016	0,00000	-0,00041	0,11168	0,64943	42,98 ± 3,58	92,51%	16,33%	NoCa
97M0477E	0,00005	0,00000	-0,00008	0,33734	1,79960	42,25 ± 1,39	99,10%	49,32%	NoCa
97M0477F	0,00000	0,00031	-0,00013	0,03785	0,19191	40,53 ± 16,15	99,98%	5,53%	59,6
97M0477G	0,00000	0,00129	-0,00003	0,07106	0,39053	43,89 ± 5,82	99,98%	10,39%	27,0

Irradiation values		*Results*	$^{40}*/39K$ ±2σ	Age	2σ
J	0,004481	Weighted Mean of Plateau	5,3031 ± 0,2751	42,37	2,30
sd-J(1σ)	0,000040	Total Fusion	5,3874 ± 0,2454	43,04	2,08

Sample Number = **VU23-F17-Rh438** Irradiation Number = VU23

Material = white mica, fine fraction Location = N Alexandr., Rhodope, Greece

Datafile	$^{36}Ar(a)$	^{37}Ar	^{38}Ar	$^{39}Ar(K)$	$^{40}Ar(a+r)$	Age ± 2σ	$^{40}Ar(r)$	Fraction	K/Ca
97M0480A	0,00173	0,00000	-0,00003	0,06913	0,81435	35,24 ± 18,94	37,37%	4,08%	NoCa
97M0480B	0,00016	0,00354	-0,00002	0,04000	0,23833	37,97 ± 22,86	79,67%	2,36%	5,5
97M0480C	0,00032	0,00098	-0,00035	0,25504	1,21091	35,01 ± 6,49	92,09%	15,07%	128,0
97M0480E	0,00031	0,00269	0,00000	0,22947	1,12758	36,15 ± 5,26	91,91%	13,56%	41,8
97M0480F	0,00027	0,00001	-0,00008	0,29966	1,43872	36,32 ± 3,81	94,50%	17,70%	12992,8
97M0480G	0,00032	0,00245	-0,00022	0,34115	1,60608	35,47 ± 3,16	94,10%	20,15%	68,2
97M0480H	0,00004	0,00272	-0,00025	0,22581	1,03928	36,42 ± 3,26	98,86%	13,34%	40,7
97M0480J	0,00000	0,00219	-0,00004	0,09104	0,41950	36,87 ± 13,44	99,98%	5,38%	20,4
97M0480K	0,00000	0,00595	-0,00010	0,14139	0,66308	37,52 ± 4,60	99,98%	8,35%	11,6

Irradiation values		*Results*	$^{40}*/39K$ ±2σ	Age	2σ
J	0,004481	Weighted Mean of Plateau	4,5200 ± 0,5364	36,17	4,30
sd-J(1σ)	0,000040	Total Fusion	4,5062 ± 0,3666	36,07	2,97

Sample Number = **VU23-F18-Rh442** Irradiation Number = VU23

Material = white mica, coarse fraction Location = W Paranesti, Rhodope, Greece

Datafile	$^{36}Ar(a)$	^{37}Ar	^{38}Ar	$^{39}Ar(K)$	$^{40}Ar(a+r)$	Age ± 2σ	$^{40}Ar(r)$	Fraction	K/Ca
97M0481A	0,00021	0,00000	0,00024	0,03140	0,22785	41,94 ± 13,87	72,33%	7,31%	NoCa
97M0481B	0,00006	0,00057	0,00004	0,08269	0,38800	35,87 ± 6,14	95,49%	19,24%	71,7
97M0481D	0,00000	0,00083	0,00002	0,15812	0,70947	35,91 ± 7,47	99,98%	36,80%	93,1
97M0481E	0,00000	0,00296	-0,00005	0,11313	0,50083	35,44 ± 5,23	99,98%	26,33%	18,7
97M0481F	0,00000	0,00000	-0,00034	0,04434	0,20657	37,27 ± 32,03	99,97%	10,32%	NoCa

Irradiation values		*Results*	$^{40}*/39K$ ±2σ	Age	2σ
J	0,004481	Weighted Mean of Plateau	4,4581 ± 0,7636	35,68	6,08
sd-J(1σ)	0,000040	Total Fusion	4,5435 ± 0,6057	36,36	4,84

Sample Number = **VU23-F19-Rh442** Irradiation Number = VU23
Material = white mica, fine fraction Location = W Paranesti, Rhodope, Greece

Datafile	$^{36}Ar(a)$	^{37}Ar	^{38}Ar	$^{39}Ar(K)$	$^{40}Ar(a+r)$	Age ± 2σ	$^{40}Ar(r)$	Fraction	K/Ca
97M0482B	0,00030	0,00000	-0,00022	0,07216	0,40417	35,09 ± 5,71	78,25%	15,05%	NoCa
97M0482C	0,00014	0,00000	-0,00009	0,14580	0,66569	34,34 ± 5,30	93,91%	30,40%	64980,1
97M0482E	0,00004	0,00000	-0,00006	0,12607	0,57012	35,42 ± 4,21	97,82%	26,29%	56155,9
97M0482F	0,00000	0,00000	-0,00039	0,05399	0,24150	35,80 ± 11,22	99,97%	11,26%	24039,8
97M0482G	0,00000	0,00000	-0,00028	0,02284	0,10105	35,41 ± 55,97	99,95%	4,76%	10165,5
97M0482H	0,00000	0,00024	-0,00034	0,05869	0,27095	36,94 ± 6,85	99,98%	12,24%	117,6

Irradiation values		Results	$^{40}*/39K$ ±2σ	Age	2σ
J	0,004481	Weighted Mean of Plateau	4,4136 ± 0,7858	35,33	6,26
sd-J(1σ)	0,000040	Total Fusion	4,4058 ± 0,5240	35,27	4,20

SECTION 6.3: KAZDAG MASSIF

Sample Number = **VU23-B2-KD303** Irradiation Number = VU23
Material = white mica, coarse fraction Location = gneiss, Kazdag, NW Turkey

Datafile	$^{36}Ar(a)$	^{37}Ar	^{38}Ar	$^{39}Ar(K)$	$^{40}Ar(a+r)$	Age ± 2σ	$^{40}Ar(r)$	Fraction	K/Ca
97M0449A	0,00000	0,00000	0,00006	0,01055	0,05976	46,01 ± 89,06	99,94%	2,80%	NoCa
97M0449B	0,00000	0,00056	-0,00038	0,20543	0,57469	22,89 ± 4,55	99,97%	54,46%	179,2
97M0449C	0,00000	0,00087	-0,00017	0,15285	0,38429	20,58 ± 5,05	99,97%	40,52%	86,5
97M0449D	0,00000	0,00000	-0,00001	0,00837	0,01846	18,05 ± 104,7	99,80%	2,22%	NoCa

Irradiation values		Results	$^{40}*/39K$ ±2σ	Age	2σ
J	0,004564	Weighted Mean of Plateau	2,6706 ± 0,5858	21,86	4,78
sd-J(1σ)	0,000037	Total Fusion	2,7496 ± 0,5749	22,50	4,69

Sample Number = **VU23-B3-KD303** Irradiation Number = VU23
Material = biotite Location = gneiss, Kazdag, NW Turkey

Datafile	$^{36}Ar(a)$	^{37}Ar	^{38}Ar	$^{39}Ar(K)$	$^{40}Ar(a+r)$	Age ± 2σ	$^{40}Ar(r)$	Fraction	K/Ca
97M0450A	0,00007	0,00000	-0,00027	0,02150	0,14205	46,05 ± 58,85	85,72%	5,62%	NoCa
97M0450B	0,00000	0,00000	-0,00050	0,05007	0,13697	22,38 ± 13,83	99,95%	13,09%	NoCa
97M0450C	0,00008	0,00000	-0,00065	0,16734	0,45283	20,99 ± 4,43	94,74%	43,75%	NoCa
97M0450E	0,00017	0,00000	-0,00032	0,12899	0,32929	17,64 ± 3,50	84,29%	33,73%	NoCa
97M0450F	0,00000	0,00002	-0,00012	0,01017	0,02498	20,08 ± 88,17	99,85%	2,66%	224,1
97M0450G	0,00000	0,00000	-0,00005	0,00438	0,02124	39,45 ± 140,9	99,84%	1,14%	NoCa

Irradiation values		Results	$^{40}*/39K$ ±2σ	Age	2σ
J	0,004564	Weighted Mean of Plateau	2,3259 ± 0,5708	19,05	4,66
sd-J(1σ)	0,000037	Total Fusion	2,6452 ± 0,7523	21,65	6,13

Sample Number = **VU23-B5-KD304**
Material = biotite

Irradiation Number = VU23
Location = Evciler GRD, Kazdag, NW Turkey

Datafile	$^{36}Ar(a)$	^{37}Ar	^{38}Ar	$^{39}Ar(K)$	$^{40}Ar(a+r)$	Age ± 2σ	$^{40}Ar(r)$	Fraction	K/Ca
97M0452A	0,00058	0,00000	0,00010	0,01052	0,25046	60,34 ± 54,83	31,31%	1,76%	NoCa
97M0452B	0,00045	0,00450	-0,00007	0,17636	0,57146	20,36 ± 4,39	76,72%	29,46%	19,2
97M0452C	0,00000	0,00180	-0,00013	0,11944	0,36687	25,11 ± 13,82	99,97%	19,95%	32,4
97M0452E	0,00009	0,00297	0,00038	0,08115	0,25475	22,93 ± 7,61	89,27%	13,56%	13,4
97M0452F	0,00004	0,00403	-0,00006	0,04127	0,12825	23,19 ± 16,38	91,19%	6,89%	5,0
97M0452G	0,00008	0,00551	-0,00015	0,06984	0,21198	22,04 ± 5,94	88,69%	11,67%	6,2
97M0452H	0,00000	0,00187	0,00007	0,07092	0,21390	24,66 ± 6,82	99,97%	11,85%	18,6
97M0452J	0,00000	0,00168	0,00009	0,01480	0,04449	24,59 ± 54,39	99,97%	2,47%	4,3
97M0452K	0,00000	0,00000	0,00024	0,01432	0,04470	25,50 ± 50,58	99,91%	2,39%	NoCa

Irradiation values		Results	$^{40}*/^{39}K$ ±2σ	Age	2σ
J	0,004564	Weighted Mean of Plateau	2,6974 ± 0,8406	22,07	6,85
sd-J(1σ)	0,000037	Total Fusion	2,8722 ± 0,6915	23,50	5,63

Sample Number = **VU23-B6-KD305**
Material = white mica, fine fraction

Irradiation Number = VU23
Location = mylonite, Kazdag, NW Turkey

Datafile	$^{36}Ar(a)$	^{37}Ar	^{38}Ar	$^{39}Ar(K)$	$^{40}Ar(a+r)$	Age ± 2σ	$^{40}Ar(r)$	Fraction	K/Ca
97M0453A	0,00015	0,00000	0,00018	0,02288	0,17607	47,24 ± 27,21	75,54%	20,19%	NoCa
97M0453C	0,00010	0,02713	0,00019	0,05779	0,38390	49,86 ± 10,24	92,42%	50,99%	1,0
97M0453D	0,00000	0,02891	0,00004	0,00736	0,05657	62,16 ± 81,48	99,99%	6,50%	0,1
97M0453E	0,00000	0,00023	-0,00006	0,00523	0,03859	59,76 ± 133,8	99,96%	4,61%	11,2
97M0453F	0,00000	0,00149	-0,00001	0,00493	0,03391	55,78 ± 144,4	99,99%	4,35%	1,6
97M0453H	0,00000	0,07128	0,00008	0,01515	0,11498	61,43 ± 58,29	99,99%	13,37%	0,1

Irradiation values		Results	$^{40}*/^{39}K$ ±2σ	Age	2σ
J	0,004564	Weighted Mean of Plateau	6,0994 ± 1,6872	49,54	13,54
sd-J(1σ)	0,000037	Total Fusion	6,4571 ± 2,2723	52,40	18,19

Sample Number = **VU23-B8-KD315**
Material = white mica, coarse fraction

Irradiation Number = VU23
Location = eclogite, Kazdag, NW Turkey

Datafile	$^{36}Ar(a)$	^{37}Ar	^{38}Ar	$^{39}Ar(K)$	$^{40}Ar(a+r)$	Age ± 2σ	$^{40}Ar(r)$	Fraction	K/Ca
97M0455A	0,00000	0,00000	0,00000	0,00178	0,04049	177,71 ± 359,2	99,92%	1,12%	NoCa
97M0455B	0,00020	0,00000	0,00042	0,07271	0,97889	101,11 ± 8,80	93,81%	45,57%	NoCa
97M0455C	0,00000	0,00000	0,00059	0,05128	0,63728	99,52 ± 15,17	99,99%	32,14%	NoCa
97M0455E	0,00000	0,00000	0,00038	0,00257	0,03300	102,59 ± 243,0	99,90%	1,61%	NoCa
97M0455F	0,00000	0,00000	0,00020	0,00210	0,02867	109,17 ± 371,9	99,89%	1,31%	NoCa
97M0455G	0,00000	0,00000	0,00010	0,02911	0,36466	100,28 ± 30,04	99,99%	18,25%	NoCa

Irradiation values		Results	$^{40}*/^{39}K$ ±2σ	Age	2σ
J	0,004564	Weighted Mean of Plateau	12,5772 ± 2,0879	100,70	16,34
sd-J(1σ)	0,000039	Total Fusion	12,6744 ± 1,7504	101,45	13,73

Sample Number = **VU23-B9-KD316** Irradiation Number = VU23
Material = white mica, fine fraction Location = S Kazdag, Turkey

Datafile	$^{36}Ar(a)$	^{37}Ar	^{38}Ar	$^{39}Ar(K)$	$^{40}Ar(a+r)$	Age ± 2σ	$^{40}Ar(r)$	Fraction	K/Ca
97M0456B	0,00000	0,00000	0,00015	0,00196	0,04811	191,37 ± 363,8	100,00%	1,77%	NoCa
97M0456C	0,00009	0,11963	0,00015	0,00213	0,05758	117,71 ± 465,8	54,63%	1,92%	0,0
97M0456E	0,00003	0,22987	-0,00004	0,00322	0,04352	88,23 ± 380,4	81,21%	2,90%	0,0
97M0456F	0,00000	0,15026	0,00016	0,00479	0,03453	58,44 ± 122,9	99,99%	4,31%	0,0
97M0456G	0,00000	0,27492	0,00022	0,01394	0,06723	39,29 ± 33,31	99,98%	12,55%	0,0
97M0456I	0,00000	0,22037	-0,00017	0,05659	0,17200	24,85 ± 17,70	99,97%	50,95%	0,1
97M0456J	0,00000	0,01341	0,00004	0,01842	0,05173	22,98 ± 50,96	99,97%	16,59%	0,7
97M0456K	0,00000	0,02421	0,00017	0,00679	0,02184	26,31 ± 112,4	99,97%	6,11%	0,1
97M0456L	0,00000	0,09818	0,00011	0,00323	0,02402	60,22 ± 295,8	99,99%	2,91%	0,0

Irradiation values		Results	$^{40}*/^{39}K$ ±2σ	Age	2σ
J	0,004564	Weighted Mean of Plateau	3,4246 ± 4,0561	27,98	32,89
sd-J(1σ)	0,000039	Total Fusion	4,3786 ± 4,4284	35,70	35,75

SECTION 6.4: MENDERES MASSIF

Sample Number = **VU23-B14-MD319** Irradiation Number = VU23
Material = white mica, fraction 1 Location = Buyuk Menderes, W Turkey

Datafile	$^{36}Ar(a)$	^{37}Ar	^{38}Ar	$^{39}Ar(K)$	$^{40}Ar(a+r)$	Age ± 2σ	$^{40}Ar(r)$	Fraction	K/Ca
97M0458B	0,00010	0,00000	0,00004	0,05708	0,32797	42,41 ± 8,67	90,69%	33,61%	NoCa
97M0458C	0,00000	0,00067	-0,00001	0,06162	0,32106	42,40 ± 9,11	99,98%	36,28%	45,3
97M0458E	0,00000	0,00000	-0,00008	0,00645	0,03215	40,53 ± 71,27	99,89%	3,80%	NoCa
97M0458F	0,00000	0,00000	0,00005	0,01787	0,09579	43,58 ± 35,38	99,95%	10,52%	NoCa
97M0458G	0,00000	0,00000	-0,00009	0,02681	0,12405	37,69 ± 31,91	99,96%	15,79%	NoCa

Irradiation values		Results	$^{40}*/^{39}K$ ±2σ	Age	2σ
J	0,004564	Weighted Mean of Plateau	5,2110 ± 1,1005	42,40	8,88
sd-J(1σ)	0,000039	Total Fusion	5,1252 ± 1,0972	41,71	8,86

Sample Number = **VU23-B15-MD319** Irradiation Number = VU23
Material = white mica, fraction 2 Location = Buyuk Menderes, W Turkey

Datafile	$^{36}Ar(a)$	^{37}Ar	^{38}Ar	$^{39}Ar(K)$	$^{40}Ar(a+r)$	Age ± 2σ	$^{40}Ar(r)$	Fraction	K/Ca
97M0459A	0,00004	0,00000	-0,00007	0,05437	0,29045	41,88 ± 6,85	96,31%	16,19%	NoCa
97M0459B	0,00000	0,00038	-0,00002	0,09427	0,53479	46,12 ± 4,84	99,98%	28,07%	120,5
97M0459C	0,00000	0,00154	-0,00040	0,06370	0,35107	44,82 ± 9,13	99,98%	18,97%	20,3
97M0459E	0,00000	0,00000	-0,00019	0,09946	0,52117	42,63 ± 8,99	99,98%	29,62%	NoCa
97M0459F	0,00000	0,00165	-0,00023	0,02403	0,10421	35,36 ± 27,44	99,98%	7,16%	7,1

Irradiation values		Results	$^{40}*/^{39}K$ ±2σ	Age	2σ
J	0,004564	Weighted Mean of Plateau	5,4646 ± 0,8304	44,44	6,71
sd-J(1σ)	0,000039	TotalFusion	5,3332 ± 0,5461	43,39	4,45

Sample Number = **VU23-B12-MD318** Irradiation Number = VU23
Material = white mica, fraction 1 Location = Gediz, Menderes, W Turkey

Datafile	$^{36}Ar(a)$	^{37}Ar	^{38}Ar	$^{39}Ar(K)$	$^{40}Ar(a+r)$	Age ± 2σ	$^{40}Ar(r)$	Fraction	K/Ca
97M0457A	0,00000	0,00000	-0,00044	0,07825	0,09972	10,46 ± 11,56	99,93%	15,66%	NoCa
97M0457B	0,00000	0,00000	0,00009	0,05712	0,05769	8,29 ± 15,81	99,86%	11,43%	NoCa
97M0457C	0,00000	0,00015	-0,00007	0,17036	0,14276	6,89 ± 3,43	99,88%	34,09%	575,3
97M0457E	0,00000	0,00000	0,00006	0,04739	0,03840	6,65 ± 19,68	99,82%	9,48%	NoCa
97M0457F	0,00000	0,00000	-0,00001	0,05459	0,04301	6,47 ± 12,77	99,82%	10,92%	NoCa
97M0457G	0,00001	0,00000	0,00012	0,09206	0,07303	6,22 ± 5,74	95,24%	18,42%	NoCa

Irradiation values		Results	40*/39K ±2σ	Age	2σ
J	0,004564	Weighted Mean of Plateau	0,8149 ± 0,6913	6,70	5,67
sd-J(1σ)	0,000039	Total Fusion	0,9026 ± 0,5551	7,42	4,55

Sample Number = **VU23-B13-MD318** Irradiation Number = VU23
Material = white mica, fraction 2 Location = Gediz, Menderes, W Turkey

Datafile	$^{36}Ar(a)$	^{37}Ar	^{39}Ar	$^{39}Ar(K)$	$^{40}Ar(a+r)$	Age ± 2σ	$^{40}Ar(r)$	Fraction	K/Ca
97M0460A	0,00000	0,00000	-0,00035	0,04019	0,05382	10,99 ± 26,92	99,94%	20,71%	NoCa
97M0460B	0,00000	0,00087	-0,00036	0,06411	0,05890	7,55 ± 15,63	99,91%	33,03%	36,0
97M0460C	0,00000	0,00222	-0,00013	0,03887	0,04889	10,33 ± 18,07	99,93%	20,03%	8,6
97M0460E	0,00000	0,00152	-0,00018	0,05089	0,04784	7,72 ± 25,46	99,91%	26,22%	16,4

Irradiation values		Results	40*/39K ±2σ	Age	2σ
J	0,004564	Weighted Mean of Plateau	1,0822 ± 2,4312	8,89	19,92
sd-J(1σ)	0,000039	Total Fusion	1,0793 ± 1,2836	8,86	10,52

CHAPTER 6, Spot fusion data

Sample Number = **Spot Fusion Rhodopian samples** Irradiation Number = VU23
Material = white mica Location = Rhodope

Datafile	sample	$^{36}Ar(a)$	^{37}Ar	^{38}Ar	$^{39}Ar(K)$	$^{40}Ar(a+r)$	Age ± 2σ	$^{40}Ar(r)$	K/Ca
97M0504B	Rh411	0,00000	0,00000	-0,00006	0,11146	0,25486	19,25 ± 4,30	99,95%	NoCa
97M0504C	Rh413	0,00055	0,02012	-0,00008	0,57247	1,66175	22,04 ± 1,00	90,24%	13,9
97M0504F	Rh414m	0,00041	0,00086	-0,00008	0,48749	1,04571	16,00 ± 1,58	88,49%	277,7
97M0504G	Rh427	0,00005	0,00075	0,00028	0,20471	0,74263	29,83 ± 1,52	97,94%	133,3
97M0504J	Rh430	0,00130	0,00111	-0,00041	2,45979	11,44968	36,09 ± 0,45	96,62%	1083,1
97M0504K	Rh432	0,00000	0,00224	-0,00001	0,21730	0,96378	37,11 ± 2,38	99,85%	47,5
97M0504L	Rh437	0,00071	0,00339	0,00015	0,73678	3,51461	37,57 ± 1,94	94,00%	106,5
97M0504O	Rh438c	0,00036	0,00498	-0,00025	0,45066	2,36664	41,94 ± 1,18	95,44%	44,4
97M0504P	Rh438f	0,00381	0,01333	-0,00024	1,05825	5,67604	36,04 ± 0,74	80,16%	38,9
97M0504Q	Rh442c	0,00159	0,00190	-0,00001	0,74574	3,62870	35,50 ± 1,00	87,02%	192,5
97M0504R	Rh442f	0,00084	0,00154	0,00013	0,57292	2,61254	34,61 ± 1,10	90,52%	182,5

Irradiation values	
J	0,004692
sd-J(1s)	0,000027

Sample Number = **Spot Fusion Rhodopian, Kazdag, Menderes samples** Irradiation Number = VU23

Material = white mica Location = Greece & Turkey

Datafile	sample	$^{36}Ar(a)$	^{37}Ar	^{38}Ar	$^{39}Ar(K)$	$^{40}Ar(a+r)$	Age ± 2σ	$^{40}Ar(r)$	K/Ca
97M0502A	KD303	0,00147	0,00000	0,00005	0,16294	0,84456	21,51 ± 2,37	48,62%	NoCa
97M0502B	KD303btt	0,00104	0,00116	-0,00024	0,35193	1,14420	20,27 ± 1,61	73,00%	149,2
97M0502C	KD304	0,00072	0,00000	-0,00038	0,21448	0,78743	22,88 ± 2,43	73,03%	95111,4
97M0502D	KD304btt	0,00068	0,00358	0,00021	0,34324	1,12017	22,85 ± 2,08	82,04%	47,0
97M0502F	KD305	0,00032	0,09368	0,00002	0,07603	0,58988	55,05 ± 6,20	83,89%	0,4
97M0502H	KD315	0,00028	0,00355	-0,00004	0,40928	4,94964	99,33 ± 2,34	98,32%	56,5
97M0502I	KD316	0,00114	1,14374	0,00014	0,13047	0,74570	26,72 ± 2,81	54,84%	0,1
97M0502K	MD318-I	0,00018	0,00000	-0,00057	0,44333	0,39905	6,70 ± 1,10	86,77%	196023
97M0502L	MD318-II	0,00037	0,00254	-0,00006	0,23291	0,28756	6,56 ± 2,46	61,95%	44,9
97M0502M	MD319-I	0,00000	0,02387	-0,00006	0,27463	1,07038	35,50 ± 1,54	99,98%	5,6
97M0502N	MD319-II	0,00011	0,00482	-0,00023	0,30396	1,40406	38,31 ± 2,40	97,60%	30,9
97M0502Q	Rh402	0,00019	0,01079	0,00020	0,30322	5,45894	146,89 ± 2,99	98,99%	13,8
97M0502R	Rh405	0,00085	0,00089	-0,00045	0,45822	16,44799	280,53 ± 5,46	98,46%	251,8
97M0502T	Rh410	0,00043	0,00222	-0,00031	0,90786	2,15917	19,13 ± 0,78	94,13%	200,0

Irradiation values	
J	0,004760
sd-J(1s)	0,000048

Dankbetuiging

Allereerst gaat mijn dank uit naar mijn begeleider en promotor Stan White. Ik heb eigenlijk nooit de kans gehad om te zien hoe goed zijn kennis van de Nederlandse taal is ontwikkeld, zodat ik graag mijn laatste mogelijkheid tijdens mijn promotie wil aangrijpen om dit toch nog even te controlleren en dit dankwoord in het Nederlands vervolg. Stan heeft niet alleen het project geinitieerd, hij heeft mij bovendien goede argumenten aangedragen om te solliciteren naar dit onderzoek, terwijl ik met mijn gedachten nog ruimschoots tussen de granulieten van Broken Hill zat, welke in de P-T-t ruimte al gauw zo'n 400°C warmer en bijna 1400 miljoen jaar ouder zijn. Tijdens het onderzoek was Stan een prettige begeleider, waarbij op alle momenten serieuze discussies konden worden afgewisseld met gezellige anekdotes. Ook mijn tweede begeleider en co-promotor Jan Wijbrans ben ik dankbaar voor de aangename samenwerking, waarbij Jan mij niet alleen het functioneren van de laserprobe heeft bij kunnen brengen maar waarbij ook Jan's kennis van het Egeïsche basement goed van pas kwam.
I would like to thank the reviewers of this thesis Prof. Jean-Pierre Brun, Prof. Kip Hodges, Prof. Gordon Lister, Prof. Johan Meulenkamp and Prof. Rinus Wortel and my two supervisors for their critical reading and the constructive comments on the thesis. Also constructive reviews of Dr. Dov Avigad, Dr. José-Maria Azañon, Dr. John Dixon, Dr. Pierre Gautier, Prof. Laurent Jolivet, Dr. Malcolm Pringle, Prof. Alastair Robertson and an anonymous reviewer have helped to improve two publications which have been presented in chapters 4 and 5.
Rachel wil ik heel graag bedanken voor de prettige herinneringen aan de samenwerking en de ontspannen avonden in het veld in Griekenland en Turkije en de discussies op de faculteit. De gezellige tijd in Griekenland werd ook versterkt door de hartelijkheid van de familie Panteli van camping Sikia in Kato Gatzea.
Op de beide faculteiten was er voldoende gezelligheid tijdens het dagelijkse werk dankzij mijn beider kamergenoten; Govert, die bereid was na onze verhuizing naar F062 mijn "belangen te behartigen" wanneer ik niet op de VU aanwezig was, en Arjan, die er mede voor zorgde dat onze ruime kamer zo nu en dan nog te klein was voor de gemoedelijke werksfeer.
Ik wil de AV dienst van de faculteit Aardwetenschappen bedanken voor het verzorgen van de opmaak van het proefschrift. Het mineraalscheidingslab van de VU (Lodewijk, Roel, Peter) wil ik bedanken voor de onovertreffelijke set-up. Ook de gesteentepreparatie in Utrecht en Amsterdam wil ik bedanken voor het maken van slijpplaten en laserprobeplaten. Magda en Marnella worden bedankt voor hun goede en opgewekte bijdrage aan, en organisatie van, allerlei administratieve zaken.
I would like to thank my teammembers of the Anatolian project; Daniel Cassard, Jean-Pierre Milesi, Hasan Sözbilir, the Eurogold Geologists and especially John Wright and Jean-Luc Lescuyer (La Source) for the invitation to participate in the project.
Vanwege het gevaar dat ik mensen ga vergeten wil ik in het algemeen graag iedereen

bedanken voor de samenwerking en de gezelligheid in de laatste 4 jaar; alle (oud)promovendi en stafleden van STG en HPT in Utrecht, Arjan, Fraukje, en Bart worden bedankt voor het kritisch doornemen van delen van mijn proefschrift; alle (oud)promovendi en stafleden van PI in Amsterdam, met name mijn oud kamergenoten op F222, Govert, Jan-Marten, Lieselotte, Martijn, Mélanie, René en Rick; alle medebegeleiders van het Jumilla '96 rescueteam; Harm, Taco, Anna, Thijs, Karen, Frank, Bernd, Ceciel, Gerco, Dick; al mijn teamgenoten van de Ouwe Manne; alle deelnemers aan de HPT/STG competities; Tree-hanging, How low can you go (Limbo), How far can you wheel en Throw-Up; en, voor het zwart-wit geblokt valt, alle mede VUCKers, met name Super Mario, de VUCK Gameboy, Burny, de VUCK secretaris, Notorious F.A.S.T., Speedo Guido, Duftig Gummi en Rocketeer voor de competitie aan de kop van het klassement.

Rest mij om mijn naaste familie, mijn goede vrienden en mijn lieve vriendin te bedanken voor al hun steun en voor hun geduld, aangezien ik de laatste jaren zo nu en dan wat minder tijd voor ze vrij kon maken dan dat ik had gewenst.

Curriculum Vitae

5-3-1971	Geboren te Breda
1983-1989	Voorbereidend Wetenschappelijk Onderwijs aan het Stedelijk Gymnasium te Breda
1989-1994	Doktoraal Examen Geologie (Cum Laude) aan de Universiteit Utrecht
1994-1998	Onderzoeker in Opleiding aan de faculteiten Aardwetenschappen van de Universiteit Utrecht en de Vrije Universiteit Amsterdam